University of Southampton

School of Engineering Sciences

Bioengineering Science Research Group

The Computational Assessment of Mechanical Fixation Failure in Cemented Total Hip Arthroplasty

By

Oliver J Coultrup

A thesis submitted in partial fulfilment of the requirements for the degree of:

Engineering Doctorate

April 2010

UNIVERSITY OF SOUTHAMPTON

ABSTRACT

FACULTY OF ENGINEERING, SCIENCE & MATHEMATICS,
SCHOOL OF ENGINEERING SCIENCES,
BIOENGINEERING SCIENCE RESEARCH GROUP

Engineering Doctorate

THE COMPUTATIONAL ASSESSMENT OF MECHANICAL FIXATION FAILURE IN CEMENTED TOTAL HIP ARTHROPLASTY

By Oliver J Coultrup

Total hip arthroplasty is a remarkably successful procedure for elderly patients. As a consequence, the procedure is increasingly offered to younger patients with high expectations for postoperative quality of life. Engineers and heath care professionals must rise to the challenge of meeting these expectations. The dominant indication for revision for cemented total hip arthroplasties is aseptic loosening, which may be postponed by optimising the design of prostheses.

This thesis uses computational and experimental methods to better-understand the failure processes for cemented total hip arthroplasties, with a view to developing methods for evaluating the efficacy of medical devices at the design stage. In particular, this study characterises the fatigue failure process for bone cement via acoustic emission monitoring of experimental specimens, revealing discontinuous damage evolution in multiple locations prior to failure. Tomographic methods are used to verify the presence of fatigue damage at these locations. Additionally, a novel computational method is described, and demonstrated to accurately predict the fatigue life of experimental specimens by incorporating internal defects.

These data are used to develop simulations of medical devices. The first such analysis investigates the factors which influence the stress state in the acetabular cement mantle, finding the magnitude of load, cup penetration depth and cement mantle thickness to be the most critical. Fatigue simulations are used to quantify the effect of these variables on the mechanical fatigue life of the cement mantle. These simulations suggest that aseptic loosening for a cemented polyethylene cup is mainly biological in nature, but where there is high cup wear or a thin cement mantle the mechanical effect on loosening may contribute. Also, a novel homogenisation method is used to determine the stresses generated in interdigitated bone cement in femoral arthroplasty components during gait, revealing them to be far higher than previously thought; this verifies the formation of cement cracking in the interdigitated region of cemented prostheses. In the final chapter, a homogenisation method is trialled as a possible method of representing trabeculae in accurate large-scale fatigue simulations of interdigitated trabeculae. Stress concentrations in cement adjacent to trabeculae are found to determine the fatigue life and failure method in the structure, though the computational expense of the method may present a significant obstacle to its acceptance in industry.

Contents

List of Figures

List of Tables

Abbreviations

AE - Acoustic emission

ASTM - American standard test method

BS - British standard

$BaSO_4$ - Barium sulphate

CDM - Continuum damage mechanics

CT - Computed tomography

DGB - Discontinuous growth band

FE - Finite element

PMMA - Polymethylmethacrylate

MMA - Methylmethacrylate

ROM - Range of motion

SEM - Scanning electron microscopy

THA - Total hip arthroplasty

UHMWPE – Ultra high molecular weight polyethylene

WT - Working time

ZnO_2 - Zirconium oxide

µCT - Micro-computed tomography

%BW – Percent body weight

Declaration of Authorship

I, Oliver J Coultrup, declare that the thesis entitled 'The Computational Assessment of Mechanical Fixation Failure in Cemented Total Hip Arthroplasty' and the work presented in the thesis are both my own, and have been generated by me as a result of my own original research. I confirm that:

- This work was done wholly or mainly while in candidature for a research degree at this University;
- Where any part of this thesis has previously been submitted for a degree or any other qualification at this University or any other institution, this has been clearly stated;
- Where I have consulted the published work of others, this is always clearly attributed;
- Where I have quoted from the work of others, the source is always given. With the exception of such quotations, this thesis is entirely my own work;
- I have acknowledged all main sources of help;
- Where the thesis is based on work done by myself jointly with others, I have made clear exactly what was done by others and what I have contributed myself;
- Parts of this work have been published, as stated in Chapter 11 (Appendix A).

Signed: __________________________________

Date: __________________________________

Acknowledgements

There were few occasions when I wasn't sure if I would ever get to this stage. A few dark moments, when I was frustrated, low on motivation, and thought it might be all beyond me. Of course, the buzz of learning, getting everything to work, putting your own ideas into action and presenting your conclusions to your peers (preferably in some glamorous far-flung destination) all make up for these lows in abundance. But it was my supervisors, colleagues, family and friends who supported me in the hard times, and deserve some acknowledgement.

I couldn't go any further without mentioning my supervisors: Mark Taylor, Martin Browne and Chris Hunt. Mark was my primary supervisor and I must thank him for giving me the opportunity to conduct this research. Mark's enthusiasm and wisdom was an inspiration for me, whilst his guidance helped me develop as a researcher. I should probably mention Mark's tolerance too (he certainly could have blown a fuse when we got lost on Skafel Pike in the rain, resulting in us climbing it twice). Martin's help was invaluable with the experimental side of this research, while his sense of humour certainly kept me on my toes! After two years in Southampton, Chris made the transition t'up north to Leeds remarkably easy, and helped me settle in at DePuy. His interest in my research never waned, and his guidance was always spot on. I owe you all a million thanks.

There are a plethora of other people who made this thesis a reality, and deserve a mention. Jonathan Jeffers for all his instruction in the labs, Chris Williams for building my lab fixtures, Mark Mavrogordato for being the king of AE, Ian Sinclair for help with all the CT scanning, Sunchai Wang for help with the SEM, Mike Wroblewski for his surgical experience and input, James Brookes at DePuy for helping me design my studies, Sonia Davy and Dawn Attree in finance for working their way through Venezuelan financial bureaucracy for me, Alex Dickinson for all his assistance with my simulations, Becky Bryan, Toby Balla and Duncan Crump for putting a roof over my head on far too many occasions... I must also mention Mike Strickland, who on one fateful winter's night helped me to get my first finite element models working when I was on the verge of losing my sanity: I remain in your debt.

I can't forget my family, who offered me support and guidance throughout, which I probably accepted all too easily. Thanks also to my brother Ed for having a penchant for exotic holidays, which became perfect get-away from EngD fever.

I've never been great at saying thanks, and there are lots of other people who deserve a mention, so to everyone in the Bioengineering and Materials engineering research groups at Southampton, the bio, design and test engineers at DePuy, all my various housemates (Frank, Basil, Andy, Mark, Pete, Steph, Rob, Olly and Sophia), all the gang from Colchester, the lads at Southampton University Fencing Club and the boys from Smokeskill, cheers for the good times!

1 INTRODUCTION

1.1 MOTIVATION

Historically, candidates for total hip arthroplasty (THA) were the elderly and infirm, seeking pain reduction and the restoration of some limited hip function. Early failure modes for arthroplasties were largely related to implant fracture and fixation failure induced by cup wear (Learmonth, 2006). Since then, advances in engineering materials and improvements in prosthesis design have eliminated stem fracture and reduced wear debris generation, while improvements in surgical technique have helped to tackle cement mantle weaknesses. Modern tapered and proximal cementless stems with textured bioactive coatings can also produce durable long-term fixation without large-scale bone resorption (Shah and Porter, 2005; Learmonth, 2006).

Hip registers reveal that the long-term survival of modern total hip arthroplasties is generally excellent: 90% survival at 10 years postoperatively and 75% at 20 years postoperatively is now expected of THAs (Furnes et al, 2007; Karrholm et al, 2008). Indeed, THA is the most successful joint replacement procedure currently available (knee = 90% survival at 10 years; metacarpophalangeal = 88%; elbow = 86%; shoulder = 78%; Furnes et al, 2007). However, this success has brought about a change in the patient demographic. Today, THA is being offered to increasingly young patients with high activity levels, who have high expectations for quality of life after surgery (Learmonth, 2006). This led Poss et al (1992) to comment that THA is ’threatened by its own success’.

With these high patient expectations in mind, prosthesis survival may be regarded as a crude measure of prosthesis performance. Patient mobility, range of motion, pain, disfigurement and confidence are also important considerations. Many methods have been devised to help ‘score’ an arthroplasty upon patient follow-up, incorporating not only survival time, but also patient feedback and activity (Merle d'Aubigne and Postel, 1954; Harris, 1969; Klassbo et al, 2003). Currently no system has been universally accepted (Kermit et al, 2005; Learmonth and Cavendish, 2005), but clinical studies reveal that patients may suffer moderate pain and limited activity, even through the arthroplasty is not classified as 'failed' (Britton et al, 1996; Garellick et al, 1998). This patient condition is increasingly considered as unacceptable.

There has been continuous development of new treatments from manufactures to meet these high patient expectations. However, while there have been significant improvements in terms of surgical technique and infection control, the improvement in prosthesis system long-term (+20 years) survivorship has been limited since the widespread use of the Charnley low-friction arthroplasty (Huiskes, 1993a). Learmonth (2006) described the 'law of diminishing returns' for new product development: as arthroplasties become more successful, exponentially greater investment is required to achieve further improvement. Indeed, Huiskes (1993a) hypothesised on the existence of a natural endurance limit for THA for a general patient population. Since then, improved mid-term clinical data for hip systems such as the Exeter (Stryker, Newbry, UK) and the C-Stem (DePuy International Ltd, Leeds, UK) have suggested that if this limit does indeed exist, it has not been reached yet. However, further development required to deliver optimum performance to a target audience with increasing expectations of medical devices.

One of the major factors hindering the development of improved medical devices is the time taken for good performance to be realised. Many modern prostheses perform well for the first 10 years, after which problems with aseptic loosening become apparent and prostheses may be differentiated in terms of longevity (Wroblewski et al, 2004; Karrholm et al, 2008). The development of improved medical devices would be very slow indeed if each novel product would have to prove its value over a 10 to 15 year clinical trial period before widespread market release. In fact, clinical trials commonly last one to two years, meaning some novel arthroplasties are no better than (or sometimes inferior to) predicate devices

(Huiskes, 1993a). Where there is long-term clinical data, it is often difficult to interpret failure processes: clinical follow-up occurs radiographically between large time intervals, making it difficult to track subtle bone and soft tissue changes and cement mantle damage which may reflect the genesis of implant failure (Jacobs et al, 1989; Reading et al, 1999). This means that failure processes are sometimes not well understood. Failure is generally multi-factorial, and without accurately determining the effect of different independent variables, one may not fully-understand its various manifestations. Additionally, it is incredibly difficult to assess the effect of implant design features on the longevity of the arthroplasty (Huiskes, 1993a).

Product developers need methods for quickly predicting the long-term performance of medical devices. Experimental methods exist (for example, ISO 7206), but generally cannot account for biological processes and variations in surgical technique, patient bone quality and loading conditions. Novel methods are required to track the progress of mechanical and biological failure processes through the lifetime of a medical device if they are to be fully understood. Computational methods are useful to help understand the failure processes of medical devices due to the high degree of control the user has over independent variables and the ability to record results throughout a structure during simulations (Huiskes, 1993b). The speed and reproducibility of computational approaches are also considerable advantages. Computational models can be used to determine stress distributions and predict the longevity of medical devices for a range of implant, patient and surgeon variables. This would help to avoid the release of potentially disastrous medical devices (Janssen et al, 2005c), such as Boneloc cement (Abdel-Kadar et al, 2001) and the Capital Hip (Massoud et al, 1997). However, finite element methods frequently require skilled operators and lack experimental validation. Also, more research is required to identify valid assumptions of in vivo conditions (Jeffers, 2005).

This thesis concentrates on cemented THA. Cement fixation of the prosthesis was first introduced by Sir John Charnley in the 1960's, and soon became the accepted best practice. Today however, the percentage of hip arthroplasties using cement fixation is slowly decreasing in favour of cementless devices, in both Europe and the USA. Cementless arthroplasties are considered as the 'luxury' product for young patients, while cemented products are generally reserved for the elderly (Spitzer, 2005). Despite this trend, a role remains for cemented THA for the foreseeable future. Cemented fixation allows the patient to return to mobility much sooner, which is a considerable advantage for elderly patients (Spitzer, 2005). Cost is another issue in the favour of cemented THA. In the UK, the average cost of prostheses and associated paraphernalia for a cemented arthroplasty is estimated at £900, while the matching cost for a cementless arthroplasty is estimated to be up to £3000 (Learmonth, 2006). This makes cemented prostheses the prime choice for elderly patients, especially for state-funded health care providers. Finally, the low cost of cemented prostheses also makes their adoption a realistic preposition for some emerging orthopaedic markets, such as China and India.

The number of revision procedures conducted per year is also slowly increasing, due to the increase in yearly primary procedures (Karrholm et al, 2008). In 2006, 5,821 revision procedures were reported in the UK (NJR, 2007). The average total cost to healthcare providers for a primary THA procedure has been estimated at approximately $11,100, while the cost for each revision procedure is estimated at $14,900 (Iorio et al, 1999). By maximising the longevity of primary arthroplasties, the total cost of revision procedures may be reduced. Revision arthroplasties typically exhibit shorter survival than primaries (Engelbrecht et al, 1990; McLaughlin and Harris, 1996), meaning some patients will receive multiple revisions. Revision is both traumatic and dangerous for the patient, and expensive for the healthcare service.

It is evident from this discussion that prosthesis longevity, amongst other factors, must be improved to meet the challenges presented by a younger, more-active target group. There are a number of ways to do this:

1. Conduct research to better-understand the failure methods associated with THA failure, and design against these occurrences.

2. Develop methods to assess the long-term performance of medical devices prior to clinical use.
3. Improve surgical instruments and techniques to reduce surgeon variation (e.g. computer assisted surgery).
4. Design prostheses to be more-tolerant to surgical and patient variation.
5. Develop better methods of allocating the best treatment method to different patients (Huiskes, 1993a).

1.2 OBJECTIVES

This thesis uses the experimental and computational expertise at the University at Southampton to elucidate failure processes for THA prostheses, and identify critical performance variables and design inputs. This includes the use of fatigue testing and acoustic emission monitoring to record fatigue processes, and the use of both scanning electron microscopy and synchrotron tomography to validate results. There is a significant computational methodology to this research. In particular, a parametric design-of-experiments approach is to identify the most important variables to prosthesis longevity, using data derived from static simulations. Additionally, novel fatigue simulation methods are used in this study to simulate the failure of both acetabular and femoral THA prostheses.

The main aims of this research are summarised as follows:

- To use novel experimental and computational methods to better-understand the fatigue failure process of bone cement.
- To draw on clinical evidence and computational methods to help understand the multi-factorial process of aseptic loosening in cemented polyethylene acetabular cups.
- To explore the validity of the widespread assumption that individual trabeculae have little effect on cement mantle stresses, and develop a novel computational method to identify their effect on the fatigue failure process.

This research is the result of corroboration with the University of Southampton and the medical device manufacturer DePuy International Ltd. Much of the thesis was driven by technical questions raised by DePuy International Ltd, related to products in the market or in development. The common theme is the exploration of aseptic loosening in cemented THA devices. However, not all research chapters directly follow on from each other.

2 LITERATURE REVIEW

This section discusses the key principles of the multi-disciplinary research presented in this thesis. It is split into the following five sections:

- **Section 2.1:** The natural geometry of hip and the mechanism of load transfer through the pelvis and the femur are considered. Cortical and cancellous bone are introduced in the context of engineering materials. Finally, the measured joint contact forces at the hip are discussed.
- **Section 2.2:** The key considerations for total hip arthroplasty, the success of existing procedures and their clinical failure scenarios are discussed, providing a background to discuss current trends in orthopaedic research and development.
- **Section 2.3:** Bone cement is characterised as an engineering material, with a focus on its fatigue performance and failure mechanisms.
- **Section 2.4:** Experimental and computational methods of reproducing the fixation failure of cemented total hip arthroplasties are introduced. A thorough discussion of how the understanding of fatigue failure in total hip arthroplasties has been advanced using such methods follows.
- **Section 2.5:** Other relevant techniques used in this thesis are discussed, comprising computed and synchrotron tomography, and acoustic emission monitoring.

2.1 THE NATURAL HIP JOINT

The hip is a synovial joint formed by the femoral head and the acetabular cavity in the pelvis. The articulating surfaces are covered by a layer of cartilage. The joint is surrounded by the synovium which contains lubricating synovial fluid (figure 2.1b).

On a macro-structural level, bone is organised into two main types: compact cortical bone and spongy cancellous bone (figure 2.1a). Dense cortical bone in found along the shafts of long bones (up to 5 mm thick), and forms a shell around the ends (0.5 to 2 mm thick). This shell is filled with cancellous bone, an irregular porous (typically

75 to 95 % volume porosity) structure of trabeculae (Figure 2.1a; Gray, 1997). These trabeculae are disposed along lines of greatest stress; figure 2.1b shows trabeculae arranged perpendicular to the articular surface in the femoral head (Wolff, 1892).

Movements at the hip are controlled and restricted by a combination of ligaments, capsular fibres, the bony constraint and surrounding muscles. The articular capsule is reinforced by the iliofemroal, pubofemoral, ischiofemoral and transverse acetabular ligaments (figure 2.2), while the ligamentum teres also provides stabilisation during flexion (figure 2.1b) (Kapandji, 1987). However, the bulk of support at the hip joint is provided by the surrounding muscles, providing flexion, extension, adduction, abduction and rotation at the hip : the range of motion (ROM) of articulations of the hip are given in (table 2.1).

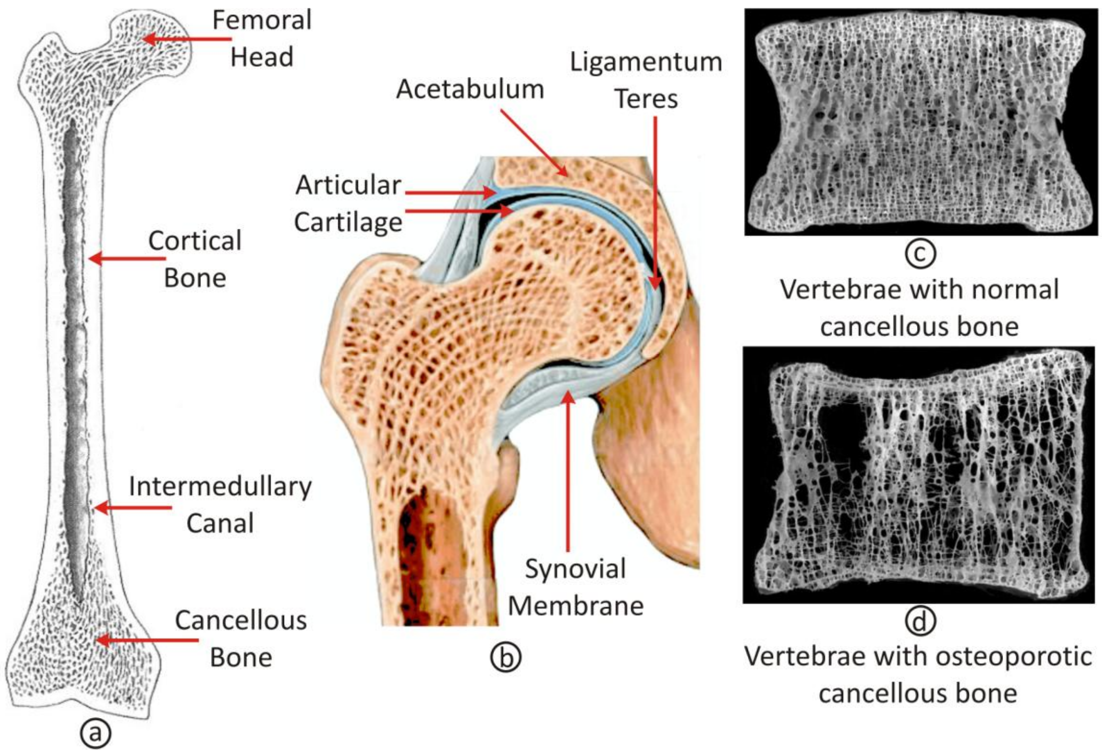

Figure 2.1: Cortical and cancellous bone in the femur (a); the bony and ligamentous tissue at the hip joint (b) (Gray, 1997); sections of vertebrae showing trabeculae structures in normal (c) and osteoporotic (d) cancellous bone (McCormick, 2010).

Movement	Active ROM	Passive ROM
Flexion	120°	145°
Extension	20°	30°
Abduction	60°	90°
Adduction	30°	30°
Lateral Rotation	60°	60°
Medial Rotation	40°	40°

Table 2.1: The range of motions achievable in the natural hip (Kapandji, 1987).

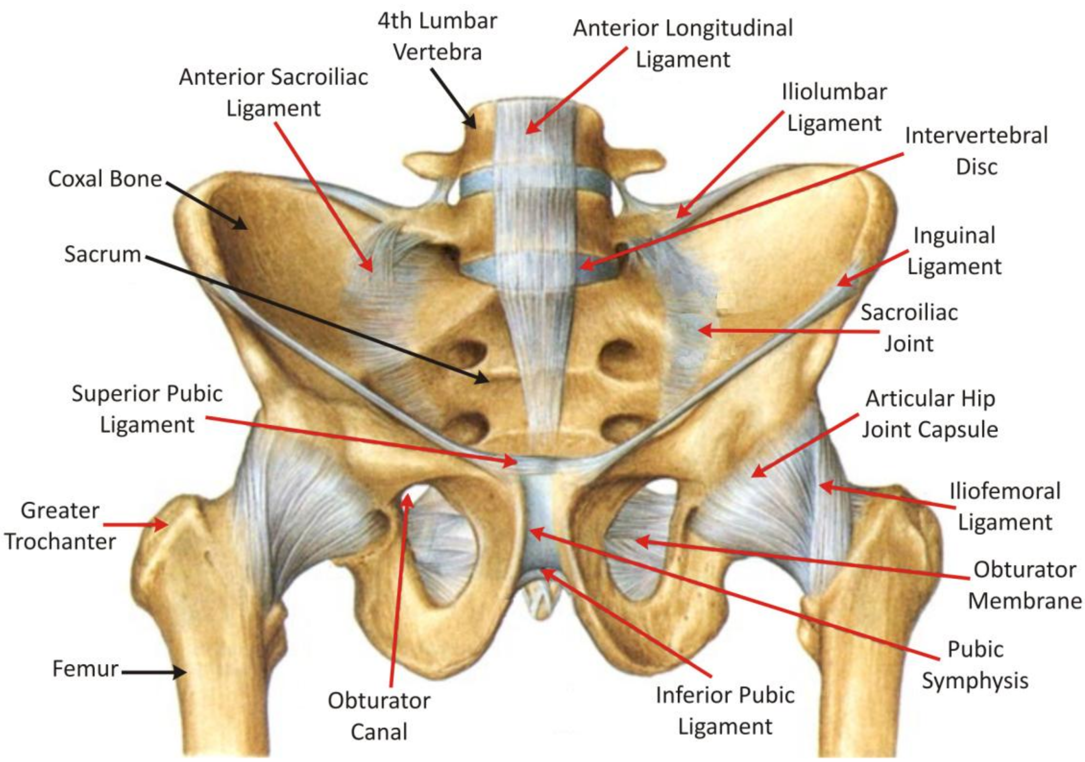

Figure 2.2: The anatomy of the pelvis, and associate ligaments (Kapandji, 1987).

The pelvis consists of the left and right coxal (hip) bones anteriorly, and the sacrum posteriorly (figure 2.2). The synovial sacro-iliac joints connect the hip bones to the sacrum through an interlocking geometry which constricts motion, providing stable load transfer from the vertebrae to the pelvis. The two hip bones are connected anteriorly by the superior and inferior pubic ligaments, and interposed by the fibro-cartilaginous inter-pubic disc. Mechanically, the pelvis transmits load from the upper-body to the lower limbs. It also affords muscle attachments to allow relative motion in the lower limbs. The wedge-shaped sacrum transfers load to the two hip bones. This tendency to separate the hip bones is resisted by the irregular shape of the bones at the sacro-iliac joint, the sacro-iliac ligaments, and superior and inferior public ligaments (Gray, 1997). After experimental testing, Dakin et al (2001) reported the pubic ligaments to have a tensile spring stiffness of 700 N/mm, while the inter-pubic disc was found to have a compressive spring stiffness of 1500 N/mm.

The cortex layer on the coxal bones is reported to be 0.44 to 4.00 mm thick (Dalstra et al, 1995; Anderson et al, 2005), forming an effective ‘sandwich structure’ filled with cancellous bone; the majority of load is born by the cortex (Gray, 1997). The thickest cortical bone regions are associated with high load transfer at the superior-lateral acetabulum and the anterior of the sacro-iliac joint (Dalstra et al, 1995).

2.1.1 The Mechanical Properties of Cancellous and Cortical Bone

By mechanical testing, the elastic modulus of cortical bone has been found to vary between 15.0 to 18.6 GPa, with a Poisson’s ratio of 0.3 (Choi et al, 1990; Katsamanis et al, 1990; Rho et al, 1993; Anderson et al, 2005). Since the architecture of trabeculae is highly varied, the mechanical properties of cancellous bone are highly variable. In low loading-bearing locations, the elastic modulus of bulk cancellous bone is reported to range between 1 and 186 MPa, with a Poisson’s ratio of approximately 0.2 (Dalstra et al, 1993). At areas of high load, however, cancellous bone may be much denser. For example, cancellous bone adjacent to the pelvic acetabulum (termed subchondral bone) is reported to have an elastic modulus between 132 and 2155 MPa (Dalstra et al, 1993), while Anderson et al (2005) found the elastic modulus to be as high as 3829 MPa. The degenerative bone disease osteoporosis, which results in the resorption of trabeculae and a general loss of cancellous bone density (figure 2.2), is frequently associated with bone fragility (ARC, 2004). Li and Aspden (1995) reported a 30% reduction in the elastic modulus of bulk cancellous bone in patients with this condition compared to normal patients.

	Ulrich et al (1999)	Majumdar et al (1998)	Majumdar et al (1998)	Ulrich et al (1999)	Nicholson et al (1997)	Majumdar et al (1998)	Ulrich et al (1999)
Specimen Location	Femoral Head	Proximal Femur	Distal Femur	Lumbar Spine	Vertebrae Spine	Vertebrae Spine	Iliac Crest
Bv/Tv	0.207	0.27	0.27	0.082	0.076	0.17	0.152
Tb.Sp (mm)	0.706	0.65	0.45	0.80	-	1.11	0.754
Tb.Th (mm)	0.172	0.19	0.2	0.123	-	0.17	0.15
E_1 (MPa)	114.33	130.2	118.8	33.42	164.7	65.8	66.5
E_2 (MPa)	71.6	51.2	59.6	14.04	51.6	30.2	48.59
E_3 (MPa)	50.01	56.7	42.2	9.59	42.9	29.7	35.08
v_{12}	0.31	-	-	0.226	-	-	0.259
v_{23}	0.333	-	-	0.381	-	-	0.315
v_{13}	0.313	-	-	0.399	-	-	0.301
G_{12} (MPa)	21.65	-	-	4.37	-	-	14.97
G_{23} (MPa)	27.43	-	-	5.12	-	-	17.35
G_{13} (MPa)	37.52	-	-	6.11	-	-	23.22

Table 2.2: The architectural parameters and bulk mechanical properties of human cancellous bone. Where Bv = bone volume, Tv = total specimen volume, Tb.Sp = trabeculae spacing, Tb.Th = trabeculae thickness, E_i = elastic modulus, v_{ij} = Poisson's ratio and G_{ij} = shear modulus. The subscripts 1, 2 and 3 indicate the superior-inferior, anterior-posterior and medial-lateral planes respectively.

By mechanically loading cubic specimens in non-destructive tests, the mechanical properties of cancellous bone have been more-accurately defined as orthotropic (table 2.2.1; Nicholson et al, 1997; Majumdar et al, 1998). The elastic modulus of femoral, tibial and vertebral cancellous bone is significantly higher in the load-bearing superior-inferior direction that other directions, though there is considerable inter-patient and inter-location variation. Image analysis of micro-focus computed tomography (μCT) scans of cancellous bone has enabled the architecture of cancellous bone to be characterised (table 2.2; Majumdar et al, 1998; Ulrich et al, 1999). Experimental and computational analyses have returned significant variation in mechanical properties dues to local trabecular size, trabecular orientation, specimen preparation and the evaluation method / test protocol used (table 2.2; Van Rietbergen et al, 1995; Majumdar et al, 1998; Ulrich et al, 1999).

In order to represent structures of trabeculae, several authors have used mechanical testing and computational evaluation to determine the elastic modulus of individual trabeculae. Using three-point bend tests, Choi et al (1990) reported the elastic modulus of individual trabeculae from the proximal tibia to average 4.59 GPa. Using an ultrasonic technique, Nicholson et al (1997) found the average elastic modulus of individual lumbar spine trabeculae to be 9.98 GPa (7.28 – 13.02 GPa). The physical size of trabeculae and testing fixtures can bring the accuracy of such experimental methods into question. Van Rietbergen et al (1995) attempted to overcome this problem by validating a computational method against experimental data, reporting an elastic modulus of 5.91 GPa (2.23 - 10.10 GPa) for proximal tibia trabeculae. In all studies, where was considerable inter-specimen variability.

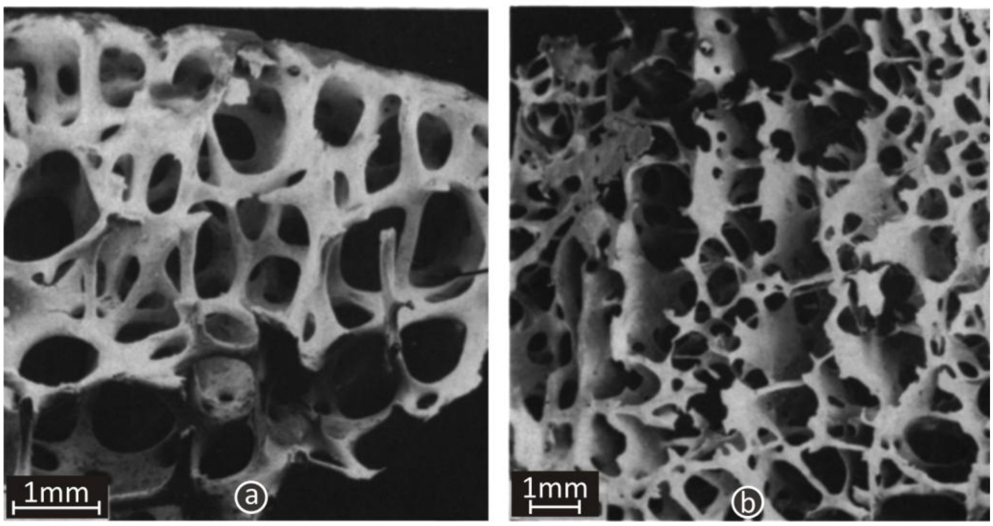

Figure 2.3: The low density, rod-like trabecular structure seen at low load-bearing locations (a); the plate-like structure seen in high-density cancellous bone (b) (Gibson, 1985).

The geometry of individual trabeculae can vary markedly, due to local boundary conditions (Wolff, 1892). Upon investigating the structure of cancellous bone specimens, Gibson (1985) reported that where the density of cancellous bone was less than 0.13, an open, rod-like structure is found. However where the density of cancellous bone exceeds 0.2, a closed-cell plate-like structure results. At intermediate densities, the structure is a combination of these types (figure 2.3). Kowalzyck (2003) defined computational models of cancellous architecture using the description of Gibson (1985), reporting elastic moduli comparable to those found from experimental testing.

2.1.2 Hip Contact Forces

An understanding of joint contact forces is required to evaluate the performance of medical devices. In a landmark study, Rydell et al (1966) implanted patients with femoral prostheses instrumented with strain gauges in order to determine hip joint loading. More-recent analyses of hip joint loading have used ground force plates and telemeterised hip prostheses to record joint contact forces throughout the gait cycle for a variety of activities (Bergmann et al, 1993; Bergmann et al, 1995; Bergmann et al, 2001; figure 2.4). The characteristic 'double peak' force curve can be seen in all activities; these peaks correspond to the flat foot and toe-off phases of gait. The peak contact forces for various activities are also given in table 2.3.

Activity	Hip Contact Force (%BW)			
	F_X	F_Y	F_Z	F_{TOT}
Walking Normally	52	32	225	233
Fast Walking	51	30	243	251
Stair Ascent	59	61	237	252
Stair Descent	48	37	253	261

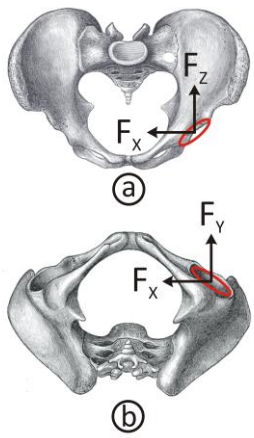

Table 2.3: The peak joint contact force at the acetabulum, measured for a range of activities. The pelvis coordinate system is shown for the coronal (a) and transverse (b) planes. F_{TOT} denotes the magnitude of the force vector (Bergmann et al, 2001).

The peak hip contact forces given here are similar for a range of activities (figure 2.4), with the exception of stumbling, which is thought to generate hip contact forces approaching double those of walking (Bergmann et al, 1993). The hip contact forces reported by Bergmann et al (2001) are also lower in magnitude than previously thought (Bergmann et al, 1993; Bergmann et al, 1995), due to an improvement in the definition of gait models and telemeterised prostheses, and by taking measurements from patients with fully-restored gait (Bergmann et al, 2001).

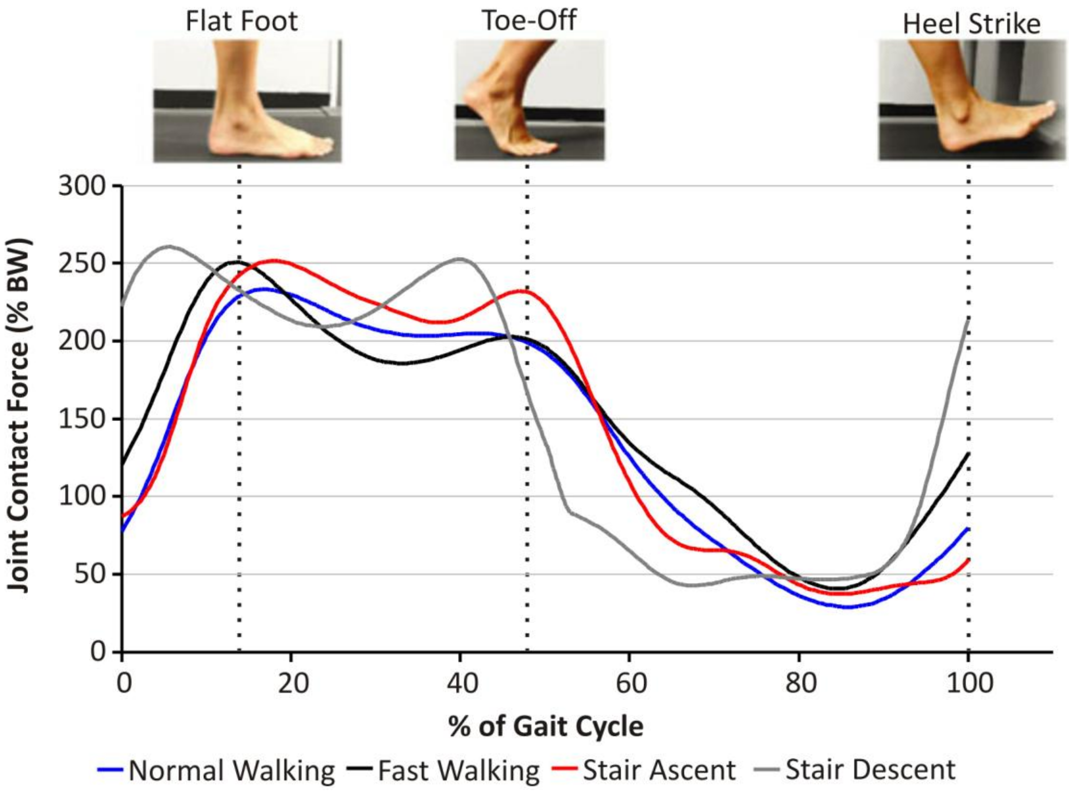

Figure 2.4: The average contact force curve (in terms of percentage of body weight (%BW)) for patients walking 'normally', walking fast, ascending stairs and descending stairs. The segment of gait is indicated at the top (Bergmann et al, 2001).

The loading exerted on the prosthesis in one year is also based on the number of applied loading cycles, and the weight of the patient. Silva et al (2002) instrumented 33 THA patients with ankle-mounted accelerometers to determine the number of loading cycles experienced in a given time period. The authors recorded an average of 1.90 (0.63-4.31) million loading cycles per year, though there was considerable inter-patient variability. The US Department of Health and Human Services (2004) report high variability in the weight of Americans, with an average of 80 kg for males and females between the ages of 20 and 74.

2.2 INTRODUCING TOTAL HIP ARTHROPLASTY

A number of problems can develop in the healthy hip joint involving the degradation of soft tissue and bone, which can cause significant pain, loss of motion, and general deterioration in quality of life (Brandt, 2004). Where there is partial damage, drug therapy or physiotherapy may be effective, or it may be possible to repair damaged areas with minor surgical procedures. Where these measures are ineffective at improving patient symptoms, joint replacement is the last-resort treatment to restore quality of life (Brandt, 2004). Either a single (hemi-arthroplasty), or both (arthroplasty) joint surfaces may be replaced, depending on the damage. This thesis will concentrate on arthroplasty of the entire hip, termed total hip arthroplasty (THA) (Learmonth, 2006).

In practice, THA involves replacing damaged articulating surfaces with inorganic material. There are three main goals for this procedure:

- To remove joint pain.
- The restore adequate joint kinematics and range of motion.
- To provide a means of transferring load between the pelvis and femur in a manner that prolongs the longevity of joint (Learmonth, 2006).

2.2.1 Indications for Total Hip Arthroplasty

National joint registries record details of procedures conducted in large patient cohorts in individual countries. Of interest to this thesis are indications for surgery, records of prosthesis longevity, and reasons for revision. This thesis will principally refer to the Swedish and Norwegian joint registers, because they have the longest follow-up durations and present the most complete data. This document also draws upon the National Joint Registry for England and Wales for a national perspective. The occurrence rates for the most-common THA indications are reported below

(Furnes et al 2007; Karrholm et al 2007; NJR 2007), accompanied by a description of each condition:

Osteoarthritis (indication rate 77%): the acute degradation of articular cartilage when the articular wear rate exceeds the rate of repair. When cartilage is removed, painful bone-on-bone articulation, swelling and joint disfiguration occurs (figure 2.5; ARC, 2005).

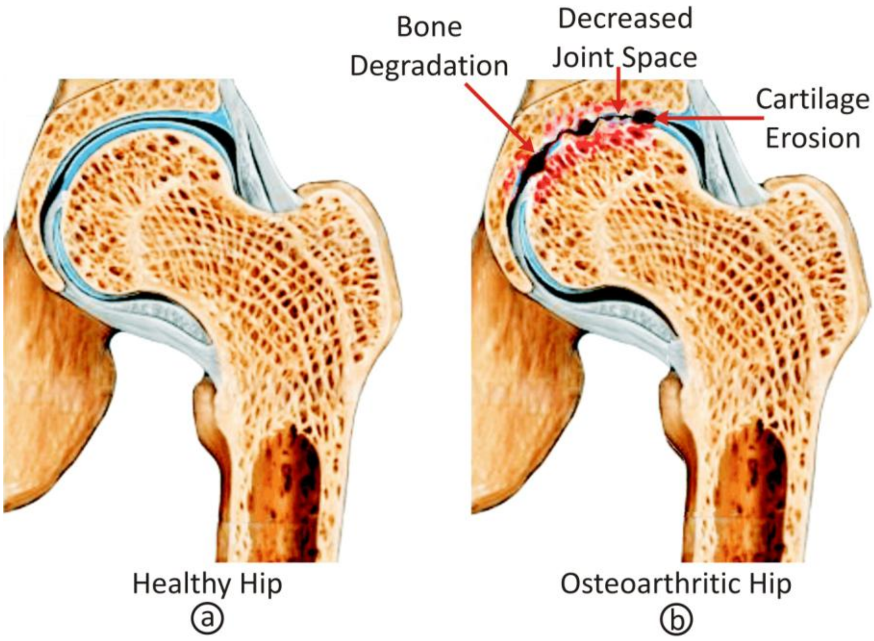

Figure 2.5: A normal hip (a) and an osteoarthritic hip (a) (ARC, 2005)

Femoral Neck Fracture (indication rate 7%): the bone degeneration disease osteoporosis leads to a loss of trabeculae (figure 2.1), making the femoral neck at risk to fracture during a fall. This is most common in elderly women (ARC, 2004).

Avascular Necrosis (indication rate 3%): the loss of blood supply to bone extremities can inhibit the natural ability for self-repair, which can lead to the collapse of the joint surface (Coombs and Thomas, 1994).

Rheumatoid Arthritis (indication rate 3%): a chronic auto-immune response to an unknown stimulation, where all soft tissues are indiscriminately attacked, again causing pain and swelling of the joint. Joints are typically attacked symmetrically (ARC, 2006).

Congenital Dysplasia (indication rate 2%): the abnormal development of the hip during gestation and subsequent joint instability which can cause regular dislocation of the hip (Sherk et al, 1981). Reconstruction of articular surfaces may be required.

2.2.2 The Evolution of the Art of Total Hip Arthroplasty

The first total hip arthroplasties were developed in the early 20th century, using components made from ivory and polymethylmethacrylate to separate the articulating surfaces at the hip. Despite anecdotal evidence of good long-term efficacy, the performance of these devices was generally unacceptable (Le Vay, 1990). The Austin Moore prosthesis (which articulates on the natural acetabulum; figure 2.6) and McKee-Farrar prosthesis were the first femoral components to be fitted into the femoral intermeduallary canal, with an angled offset head to mimic the anatomic geometry. This was a significant step forward, as it allowed stress to be transferred to the femoral shaft and better-replicate natural bone strains in the long-term. (Murphy et al, 1984; Shah and Porter, 2005).

Figure 2.6: The early Austin Moore femoral THA prosthesis (Corin, Cirencester, UK).

Sir John Charnley is regarded as the pioneer of successful cemented THA. After experimenting with cementless fixation, Charnley realised the potential to achieve prosthesis fixation with dental acrylic (bone) cement (Le Vay, 1990; Shah and Porter, 2005). This material acts as a grout, rather than a glue, to give fixation by mechanical interlock. He also chose to use polyethylene for the acetabular bearing surface, and his selection of a small diameter femoral head to minimise cup wear revolutionised hip replacement. Arthroplasties in the 1960's were plagued by fatigue failure of the femoral component, and it was Charnley who proposed the use of a proximal flange and shorter neck, as well as the introduction of fatigue-resistant steels and cold working to counter this problem (Shah and Porter, 2005). The description of a cemented THA procedure is given in section 2.2.4.

Cemented THA has a history of excellent long-term performance in the elderly (Furnes et al, 2007; Karrholm et al, 2008). However, some critics viewed the 'inherent weakness' of bone cement as the limiting factor to the long-term success of cemented THAs in younger patients; as a result cementless arthroplasties became popular again in the 1970s. Improvements in manufacturing processes meant that metal-on-metal bearing couples could be adopted, achieving fixation with screws or bone in-growth (Shah and Porter, 2005). Modern cementless designs are coated with hydroxyapatite, the inorganic content of bone, to encourage the in-growth of bone into a porous surface. The surgical procedure for cementless THA involves precise reaming of the intermeduallary canal to ensure a tight press-fit before bone in-growth can be achieved. It is also essential that the patient has a good bone stock, and is suitable for the lengthy recovery time involved (Huiskes, 1993a).

A more modern concept, hip resurfacing, was firstly widely accepted with the introduction of the Birmingham Hip Resurfacing in the 1990's (Ebied and Journeaux, 2002). This procedure involves shaving the femoral head and reaming the acetabulum, and replacing the articulating surfaces (figure 2.7a). Hip resurfacing is an attractive option for young patients, as much of the femoral bone stock is retained, and due to the large femoral component, a larger range of motion and higher stability can result (McDonald, 2008). While excellent short-term results have been recorded for this procedure (Ebied and Journeaux, 2002; Amstutz et al, 2004), the surgical technique is considered much more demanding than conventional THA due to the complex muscle release and accurate femoral cuts required, meaning poor performance has been seen where the procedure is conducted infrequently (Parvizi, 2008). There has also been a high rate of failure due to femoral neck fracture, especially for patients with poor femoral bone condition, osteoporosis or osteopenia: as such resurfacing is not recommended for women, or men older than

65 (MacDonald, 2008). These problems have fuelled to the development of short-stem femoral components which also allow proximal bone stock to be retained (Stulberg and Dolan, 2008), such as the Proxima femoral component (DePuy International Ltd., Leeds, UK) (figure 2.7).

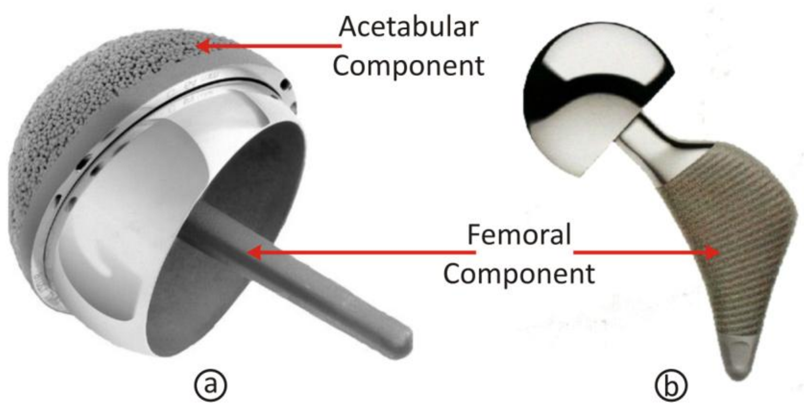

Figure 2.7: Bone-preserving joint reconstruction. The Birmingham Hip Resurfacing (Smith and Nephew, London, UK), the most prevalent hip resurfacing in the UK (NJR, 2007) (a); The Proxima femoral prosthesis (DePuy International Ltd., Leeds, UK) (b).

The development of alternative THA products has not stopped innovation in cemented devices. There have been radical improvements in cementing techniques in the last 30 years, with the inception of the cement gun, distal plugs and stem centralisers, pulsatile lavage and vacuum mixing (section 2.3.2). In terms of prostheses, the major development has involved the use of double or triple tapered femoral stems (figure 2.8b and 2.8c). Released in the 1970's, the double-taper Exeter stem (Stryker, Newbury, UK) allows the stem to subside in the cement mantle to continually engage the cement, ensuring loading in the proximal femur is not lost. A polished surface finish is crucial to allow subsidence and prevent significant cement damage upon stem-cement debonding. Based on this success, the C-Stem (DePuy International, Leeds, UK) features three tapers, and has enjoyed excellent mid-term clinical results (Wroblewski et al, 2005). In contrast to femoral components, the acetabular component has evolved little since the adoption of the ultra high molecular weight polyethylene (UHMWPE) cup. Modern polyethylene cups feature a flange to enhance cement pressurisation. With improvements in manufacturing methods, metal and ceramic cups may also be used, which offer better wear characteristics, though issues with the biocompatibility of metal wear debris (Jacobs, 2008) and the fracture of ceramic cups (Masonis et al, 2004) have hindered their acceptance on the general market.

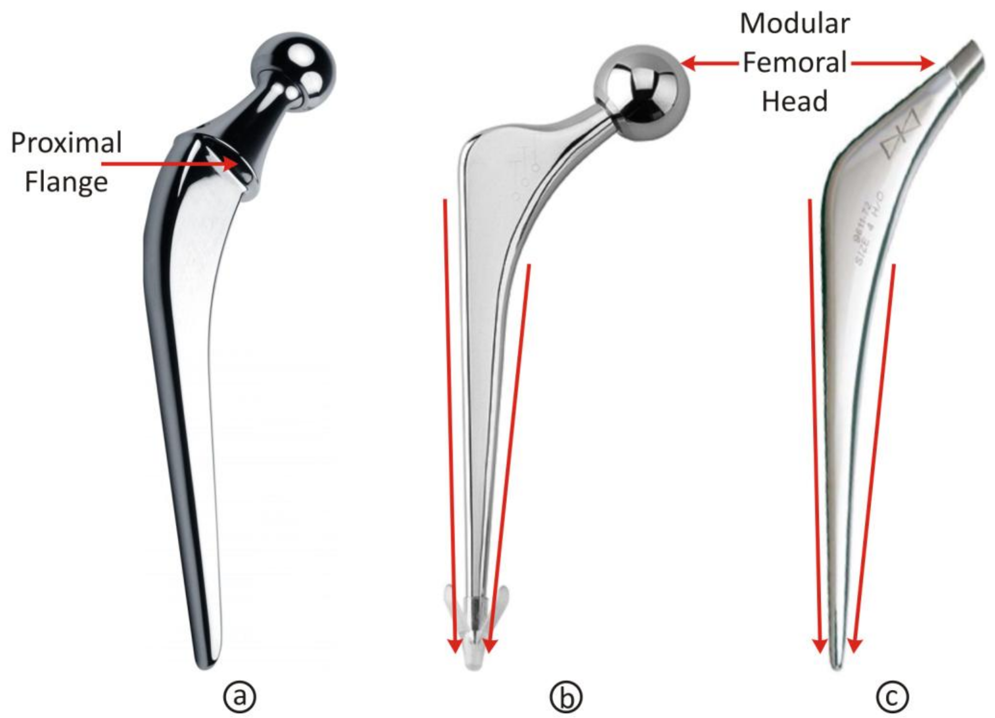

Figure 2.8: The three most commonly-used cemented stems used in the UK (NJR, 2007); The collared Charnley cemented stem (a) (DePuy International Ltd., Leeds, UK); The Exeter Universal cemented stem (b) (Stryker, Newbury, UK); The C-Stem cemented stem (c) (DePuy International Ltd., Leeds, UK). For the Exeter and C-Stem the proximal-distal taper is highlighted with red arrows.

2.2.3 Modern Cemented Stem Philosophies

The optimal stem should transmit torsional and axial load to the cement and bone without creating excessive damaging peak stresses or micromotion, while also maintaining good bony support (Sheelinck and Casterlyn, 2006). Changing ideas about femoral stem design have lead to two well-established femoral stem philosophies: “force-closed” and “shape-closed”.

Force-closed stems (e.g. Exeter, C-Stem, figure 2.8) feature tapers in two or three planes, which allow subsidence due to the presence of a distal cement void. Retrieval studies have shown that debonding at the cement-stem interface is inevitable with time (Jasty et al, 1991; Kawate et al, 1998). However, a taper appears to force the stem further into the cement mantle, enabling re-fixation (Verdonschot and Huiskes, 1996) and preventing osteolysis (Hook et al, 2006). This subsidence may also prevent the flow of cement and polyethylene debris to the joint capsule and the associated bodily macrophage response to debris of a given morphology (osteolysis) (Scheerlinck and Casteleyn, 2006). Additionally, stem subsidence reduces the risk of distal fixation, and dangerous proximal bone resorption. It is critical that force-closed stems have a polished finish, or significant cement damage (Verdonschot and Huiskes, 1998) and osteolysis (Anthony et al, 1990) may result on stem-cement debonding.

Shape-closed stems (e.g. Lubinus, Charnley, figure 2.8) aim to maintain stem-cement bonding for as long as possible, thus minimising subsidence (Scheerlinck and Casteleyn, 2006). These stems usually feature grit-blasted or vaquasheen surface finishes to create a strong cement interface bond. Stems may also feature a proximal collar to prevent adverse subsidence and maintain proximal bone loading. Shape-closed stems require a thick (2-5mm), continuous cement mantle with good interdigitation of cement into cancellous bone, and as such may be less tolerant to sub-optimal cementing, as they cannot subside into the cement mantle to achieve good support (Kawate et al, 1998).

A third option has been developed in France, where the custom is to remove as much cancellous bone as possible with a large broach, and then implant a stem of the same size (Langlais et al, 2003). The result is that the majority of cement is forced into any remaining cancellous bone (up to 3mm). The advantage of these “line-to-line” stems is that the majority of mechanically-weak cancellous bone is removed, and the stem is directly apposed to the cortex in some locations, reducing cement stresses. Load is also spread over larger, ovular profile, developing lower cement stresses and providing better torsional support (Janssen et al, 2007). Surgery may also be simpler for the surgeon, as alignment is achieved by the broach shape, and cement pressures are very high ensuring good interdigitation. The method of leaving a very thin cement mantle, however, contradicts traditional cemented THA philosophies (Kawate et al, 1998), and as such has been slow to catch on outside of France, despite excellent reported performance (97% survival at 10 years, 85-95% survival at 20 years; Hamadouche et al, 2002; Kerboull et al, 2004).

2.2.4 Cemented Total Hip Arthroplasty Surgical Procedure

The steps for a straight-forward cemented THA procedure are now explained for the force-closed C-Stem (DePuy International Ltd., Leeds, UK) (figure 2.9); the procedure may vary for different hip systems. First, the size of the femoral prostheses is gauged from the stem template and the anterior / posterior radiograph (figure 2.9a). The acetabular cavity is reamed until a hemispherical dome of healthy, bleeding subchondral bone is achieved (figure 2.9b). Cement holes are drilled into the roof of the acetabulum to promote cement proliferation.

For the stem, a probe establishes the long axis of the femur, and the femoral neck is removed. The femoral canal is drilled and progressively broached until the broach is well-seated: this should confirm the stem size. Trial sizes are used to establish neck length, acetabular cup size and femoral head size, and to confirm stability (figure 2.9c). Cement is commonly applied by hand to the acetabulum, and the cup is then introduced in approximately 45° of abduction and 15° of anteversion. The broach is removed and a cement restrictor is added to the bottom of the intermedullary canal, which is then washed and dried. Cement is inserted with a cement gun and the stem is placed retrospectively. For the C-Stem a 2mm cement mantle is recommended, as is 20mm of distal cement (figure 2.9d). Finally, the femoral head is impacted onto the stem, before the range of motion is again checked and the incision is closed (DePuy International Ltd, 2007).

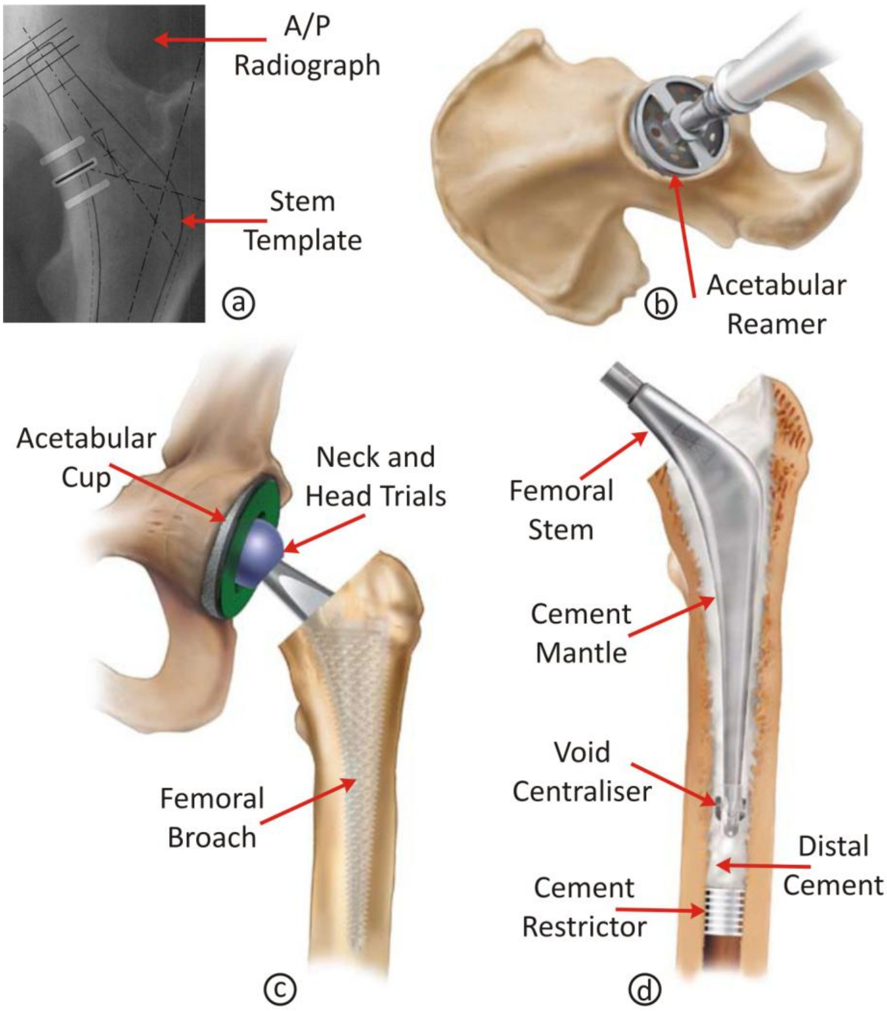

Figure 2.9: Surgical technique for the cemented C-Stem THA (DePuy International Ltd., Leeds, UK). Templating the femur (a); reaming the acetabulum (b); trial sizing the stem and femoral head with the femoral broach (c); the cemented stem (d) (DePuy International Ltd, 2007).

2.2.5 Clinical Performance

Commonly 'centres of excellence' will track patients postoperatively to measure the longevity of an implant and patient satisfaction. Reports from such studies may be compared to elucidate the relative success of given procedures in given patient cohorts. However, the true test for a hip system is where it is used by surgeons with a range of clinical proficiency, in both the public and private sector. Thus, for an overview of the performance of THA procedure types, national joint registers are referred to here.

In 2006, 55,352 THA produces were conducted in England and Wales (NJR, 2007). 48% of THAs implanted were fully cemented, 30% were cementless, 12% were hybrid (cementless acetabular fixation with a cemented femoral component) or reverse hybrid (a cemented cup with a cementless femoral component) and the remaining 10% were hip resurfacings. The relative age ranges of patients receiving these devices are given in figure 2.10. Fully cemented THA is commonly selected for patients over 65 who are generally less active, while bone-preserving resurfacing devices are usually selected for younger patients with good bone stock (Macdonald, 2008). There has been a steady increase in THAs implanted (e.g. an increase from 4,900 procedures in 1979 to 15,600 procedures in 2007 in Sweden; Karrholm et al, 2008). The Swedish Hip Arthroplasty Register reports a decrease in average patient age from 70 to 68 years over the last 10 years, due to THA being offering to younger patients. This is reflected in an increased demand for cementless, hybrid and resurfacing arthroplasties in the last 5 years (Karrholm et al, 2008).

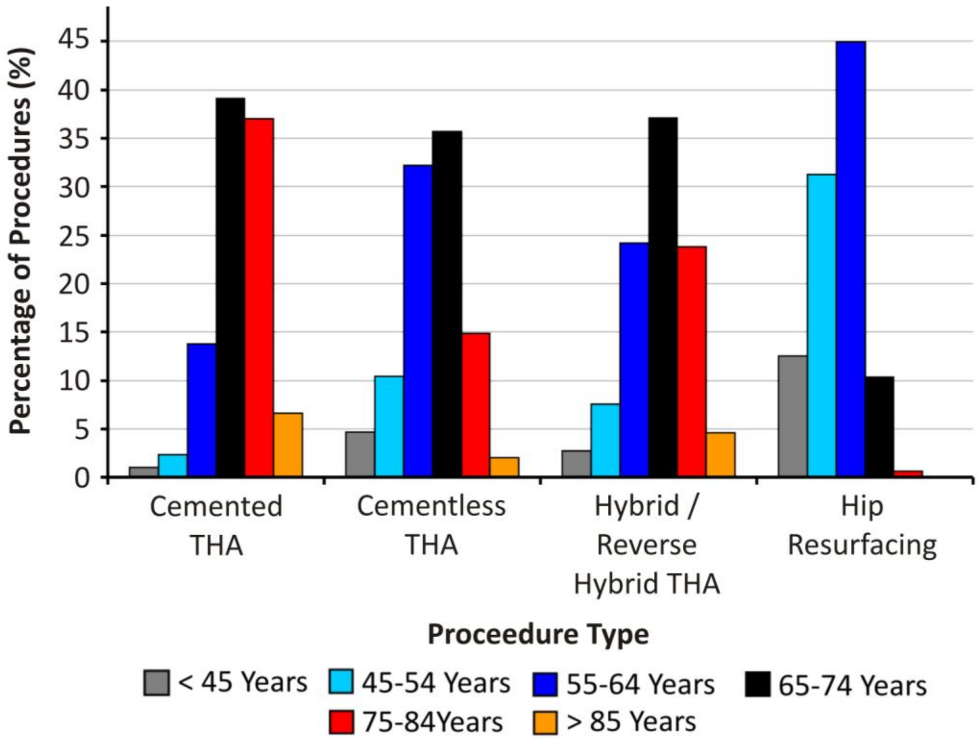

Figure 2.10: The relative percentages of hip arthroplasty types implanted in different age groups in England and Wales in 2006 (NJR, 2007).

Prosthesis survival until revision is used here as a success indicator of arthroplasty. Despite the popularity of cementless devices in the USA, it is clear that superior long-term survival is achieved with cement fixation (figure 2.11). This may be partly explained by the fact that cemented arthroplasties are typically implanted in older, less-active patients (figure 2.10; Karrholm et al, 2008). An improvement in longevity for both fixation methods is apparent over the last 30 years (figure 2.12), which may be related to improved surgical technique, prosthesis design and patient selection. The growing challenge in hip arthroplasty is to meet the demand of increasingly young patients. Figure 2.12 shows survival rates for patients younger than 50, revealing that cemented fixation still appears to be superior to cementless. Crucially though, for this age range survival is significantly poorer than the population average (86.8% survival compared to 93.8% survival at 10 years; Karrholm et al, 2008). These observations illustrate the need to improve THA survival for younger patients.

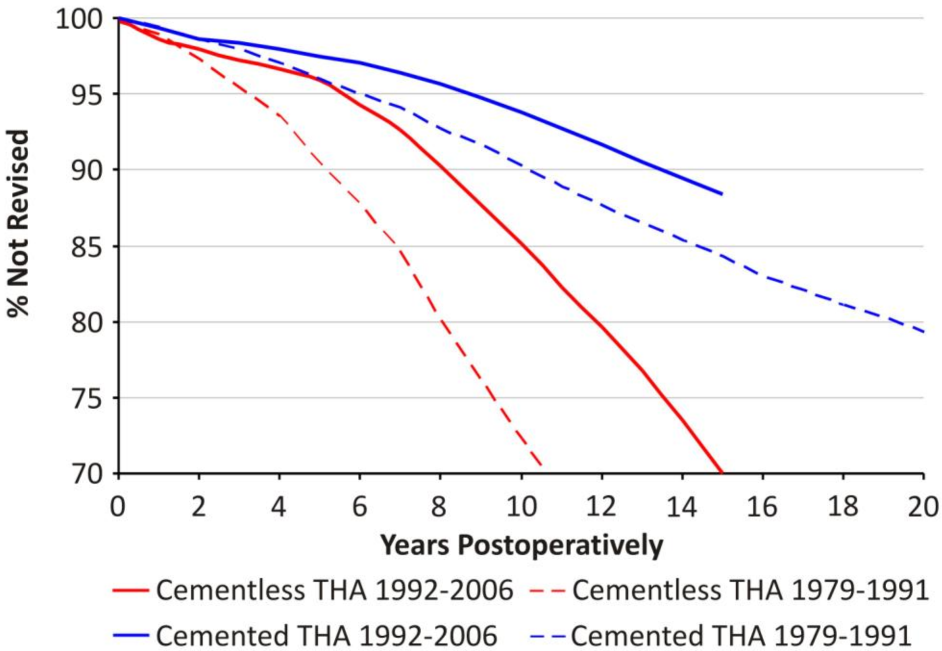

Figure 2.11: The survival of cemented and cementless prosthesis types in Sweden (Karrholm et al, 2008).

The assessment of the long-term performance of THAs is a matter of some controversy (Learmonth and Cavendish, 2005). Clinical studies generally report the number of years postoperatively before arthroplasties are revised, excluding patients who die or are lost to follow-up. Such data may be misleading, as the time and indications for revision can vary between centres, and some patients may refuse or be denied revision for a variety of reasons (Learmonth and Cavendish, 2005). In section 2.2, the principle aims of THA were established: to remove pain and restore a functional range of motion to the patient. Many methods have been established to include patient feedback in the assessment of medical devices, though one has never been universally accepted (Merle d'Aubigne and Postel, 1954; Harris, 1969; Klassbo et al, 2003; Kermit et al, 2005). In this thesis, prostheses are compared on postoperative survival to revision, but it should be remembered that a patient may suffer from unacceptable pain or a loss of function without receiving a revision procedure (Stauffer, 1982).

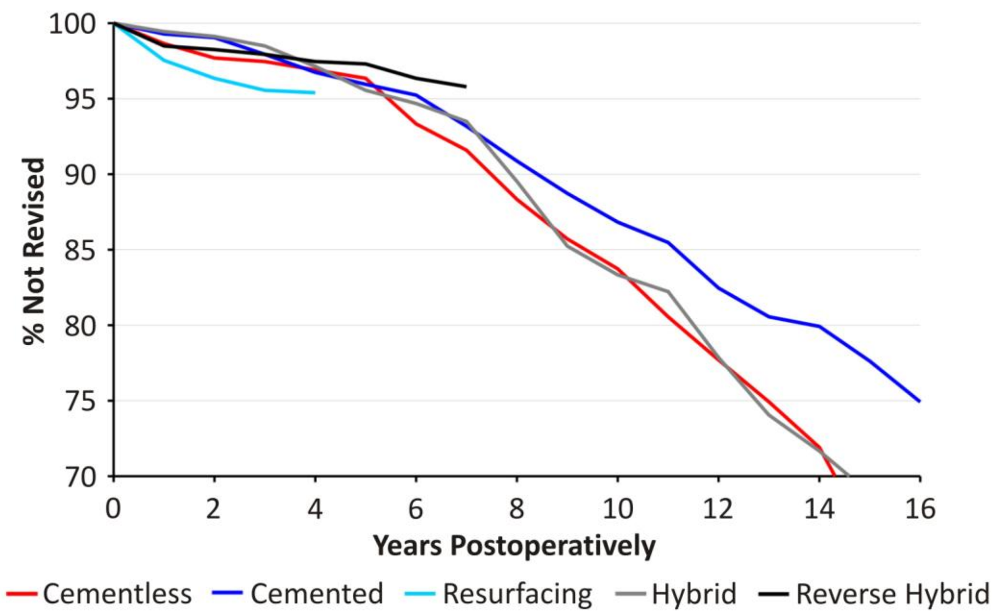

Figure 2.12: The survival of different types of prosthesis for patients younger than 50 (Karrholm et al, 2008).

2.2.6 Failure Scenarios

From a clinical perspective, excessive pain and impaired function are indications for revision. It may be possible for failure to be radiologically defined due to high prosthesis migration or marked bone resorption, even though the patient remains asymptomatic (Stauffer, 1982). Some surgeons have recognised that the 'early revision' approach is best in some instances to ensure long-term patient satisfaction, meaning good patient care may involve one or more revision procedures (Wroblewski et al, 2004). Failure is generally manifested as a process, not an event, as clinical and radiological symptoms develop over time. The most prevalent failure processes for cemented THA are listed in table 2.4.

Reason for Revision	Furnes et al, 2007	Karrholm et al, 2008
Aseptic loosening	69.2%	64.7%
Deep Infection	12.5%	8.5%
Dislocation / Subluxation	19.3%	14.2%
Femur fracture	6.2%	9.0%
Pain	11.9%	0.6%

Table 2.4: THA failure processes taken from the Norwegian and Swedish National Hip Registers (Furnes et al, 2007; Karrholm et al, 2008). Note: reasons for revision are not mutually exclusive in Furnes et al (2007).

Aseptic loosening is clearly the most prevalent failure. This phrase refers to the mechanical failure of prosthesis fixation due to repeated dynamic loading. The aseptic loosening processes differ for cemented and cementless THA. This thesis will concentrate solely on aseptic loosening in cemented prostheses, which involves fatigue crack initiation in the cement mantle at stress concentrations, and crack propagation under further loading. The coalescence of cracks, increased micromotion and bone resorption eventually result in the gross loosening of the implant (Jasty et al, 1991; Huiskes, 1993b; Race et al, 2003). Clinical studies annually record the radiological and symptomatic conditions of patients; feedback from such studies help elucidate in vivo failure processes to be elucidated, and allow improvements or changes to surgical techniques and prosthesis design to be suggested. It is important to consider the long-term (>20 years) clinical follow-up of medical devices if the full aseptic loosening process is to be understood. This process is now explained for acetabular and femoral components in more depth.

2.2.7 Cemented Femoral Stem Aseptic Loosening: Clinical Studies

Stem-cement debonding is generally the first significant stage of aseptic loosening in cemented THA (Jasty et al, 1991; Wroblewski et al, 2009b). Partial debonding has been reported after as little as 15 days, and consistently after 3 years in vivo (Jasty et al, 1991). While a rough stem surface finish appears to postpone debonding, it appears to be inevitable (Race et al, 2002). For the majority of patients this event is not symptomatic (Jasty et al, 1991; Schulte et al, 1993; Carrington et al 2009), though for some patients pain has been experienced after radiographic loosening, which may be due to increased intermedullary pressure upon stem pistoning (Wroblewski et al 2009b). Osteolysis due to polyethylene wear debris may cause the deterioration of supporting proximal bony tissue, but there is evidence that wear-induced osteolysis is only significant after through-cracking in the cement mantle allows wear particles to access the mid-stem and distal cement-bone interface (Schulte et al, 1993; Carrington et al 2009).

Damage has been found to accumulate in the cement mantle in the form of micro-cracks under continued dynamic loading. Cracks may be progressive, and increase in length and number with increasing loading cycles (Jasty et al, 1991). Crack growth and formation is associated with cement pores, though not at the stem-cement interface: it appears that the bone-cement interface or pores in the bulk cement mantle may be more significant in the failure process (Kawate et al, 1998). Jasty et al (1991) found cement micro-cracks after 5 years postoperatively, and complete through-cracks after 10-17 years in vivo. Evidence of this process is shown in figure 2.13 for shape-closed stems in autopsy studies, and has been replicated for force-closed stems and modern cementing techniques in laboratory assessments (section 2.4.3.5)

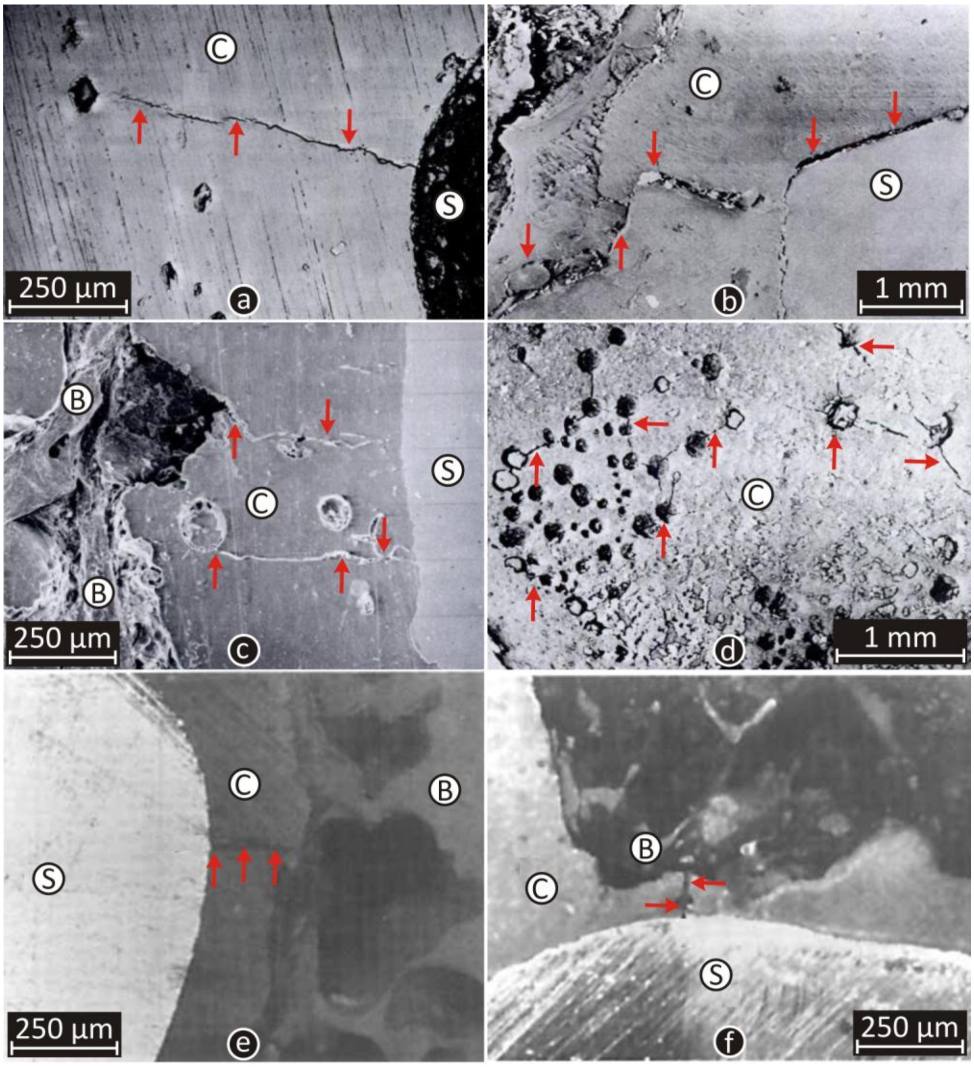

Figure 2.13: Scanning electron microscopy (a to d) and photomicrograph (e and f) images of cement cracks in autopsy specimens; cement cracks (a, b, e and f) and lucency (b) caused at the interface of a femoral stem; cement cracks emerging from the bone-cement interface and pores (b and c); diffuse cement cracking at small pores in distal cement (d) (Jasty et al, 1991; Kawate et al, 1998). B = bone, C = cement, S = stem, red arrows indicate cracks.

For shape-closed stems, through-cracking appears to be a significant event, as it allows the ingress of wear-debris to the bone, which provokes bone resorption (osteolysis) and soft tissue formation. This event may be less-significant for force-closed stems, because subsidence of the stem ensures that the bone-cement interface remains sealed from wear debris, except for the proximal region of the arthroplasty. Osteolysis is indeed an infrequent event for these stems (Schulte et al, 1993; Carrington et al 2009; Hook et al, 2006). Therefore, for force-closed stems, subsidence may not be considered deleterious (Young et al, 2009). The continued growth of cracks and bone resorption where applicable eventually causes a loss of prosthesis support, advances the breakdown of the cement mantle, and results in gross loosening of the implant (figure 2.14; Jasty et al, 1991).

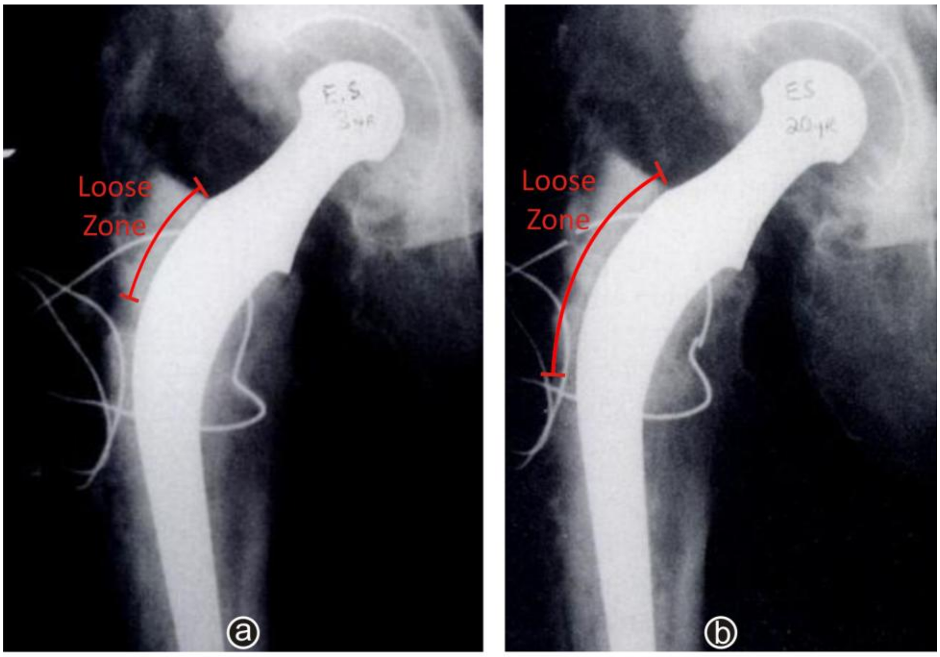

Figure 2.14: Progressive femoral loosening; postoperative radiograph 3-year radiograph showing superio-latoral radiolucency (a); 20-year radiograph with sufficient radiolucency to classify the stem as loose (b) (Schulte et al, 1993).

The thickness and completeness of the cement mantle is identified as key to stem longevity (Jasty et al, 1991; Kawate et al, 1998). Cement of a thickness less than 1mm has been identified as particularly vulnerable to crack formation (Kawate et al, 1998). In many cases, areas of thin or inconsistent cement may not be visible on radiographs, while cement cracks or debonding may not be visible until they are substantial (Jacobs et al, 1989; Reading et al, 1999). These findings support the argument for early revision if bone resorption or soft tissue degradation is to be avoided, especially for young patients (Wroblewski et al, 2009b).

2.2.8 Cemented Acetabular Cup Aseptic Loosening: Clinical Studies

Aseptic loosening in the acetabular component has been identified in many studies as the major problem for cemented THA (Schulte et al, 1993; Madey et al, 1997; Callaghan et al, 2000; Furnes et al, 2007), leading to revision between 2 and 4 times more often than aseptic loosening for the femoral component. The Norwegian Arthroplasty Register also reports a higher revision rate in cemented cups than cemented femoral stems (Furnes et al, 2007). The aseptic loosening process is poorly understood in the acetabulum, as the phenomenon has received little research attention. Short-term loosening (<5 years) is associated with poor interdigitation of cement in cancellous bone and the failure to remove articular cartilage (Garcia-Cimbrelo et al, 1997). Long-term loosening occurs primarily at the bone-cement interface, and is accompanied by the formation of soft-tissue. This is apparent on radiographs as a lucent line, due to the low density of soft tissue (Hodgkinson et al, 1988). The genesis of this soft tissue, however, is the subject of debate. Loosening at the cement-cup interface is not reported in clinical literature, though it may be difficult in practice to identify demarcation at this location using radiographs.

Schmalzried et al (1992) suggested that acetabular aseptic loosening is mainly biological. Liberated polyethylene wear particles find their way to exposed bone and bone-cement interface in the synovial capsule, causing an osteolytic response which results in bone resorption. The destruction of bone allows further particle ingress into the bone-cement interface, and progressive resorption towards the pole of the cup (figure 2.15). The identification of polyethylene wear debris, macrophages and cytokines at the resorbed interface appears to confirm this theory (Zicat et al, 1995; Mai et al, 1996; Jones et al, 1999). A number of clinical studies have not related osteolysis to the aseptic loosening process (Schulte et al, 1993; Wroblewski et al, 2004; Wroblewski et al, 2009b; Young et al, 2009), although osteolytic effects may be difficult to detect in radiographs.

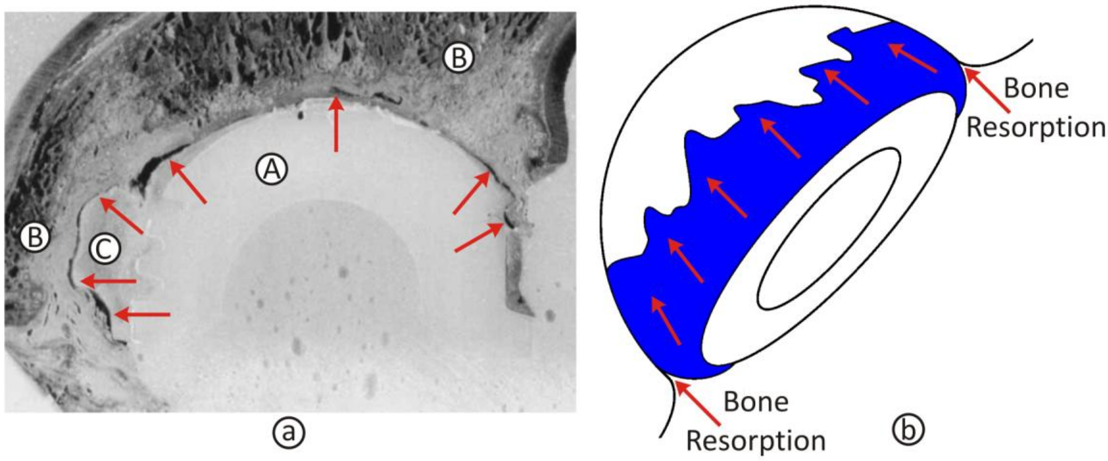

Figure 2.15: Biological cup aseptic loosening theory; visible debonding and soft tissue formation in an autopsy specimen (a); schematic of resorption initiation at exposed bone and progression towards the pole of the cup (b) (Schmalzried et al, 1992). A = acetabular cup, B = bone, C = cement, red arrows indicate debonding.

A second suggested failure method is mechanical. The removal of subchondral bone and insertion of a polyethylene cup is thought to raise stresses in superior cancellous bone and cement, which result in micro-fractures in these regions (Schmalzried et al, 1992). This method may produce the radiographic loosening seen clinically, creating high adjacent bone and cement stresses, thus causing progressive deterioration of fixation. Evidence of fatigue failure in the acetabular cement mantle has not, however, been reported in clinical literature.

A third possible hypothesis is that the offset of the femoral head due to cup wear enables the mechanical impingement of the femoral stem onto the acetabular cup rim (Wroblewski et al, 2009a). This is thought to exert high loads onto the cup, wrenching it from the socket. An additional effect may be the deformation of a heavily-worn cup to ‘pinch’ the femoral head, raising torques applied to cement and subchondral bone (Schmalzried et al, 1992). However, the occurrence of loosening without high wear depths means impingement cannot always be the cause of failure (Schmalzried et al, 1992).

There is a clear relationship between aseptic loosening and polyethylene cup penetration depth, though no link with osteolysis has been defined (Schulte et al, 1993; Garcia-Cimbrelo et al, 1997). Wroblewski et al (2004) separated patients into high wear (>0.2mm per year) and low wear (<0.02mm per year) groups, showing that the revision rate in the high-wear group was 8 times that of the low wear group (figure 2.16a). The authors reasoned that if osteolysis was the cause of the high failure rate, it should also effect the femoral component comparably: as the survival of the femoral component does not appear to be linked to cup wear, Wroblewski et al (2004) suggested that the high acetabular loosening rate cannot be due to osteolysis, and suggested an alternative mechanical process, whereby material lost from the cup raises cement mantle stresses.

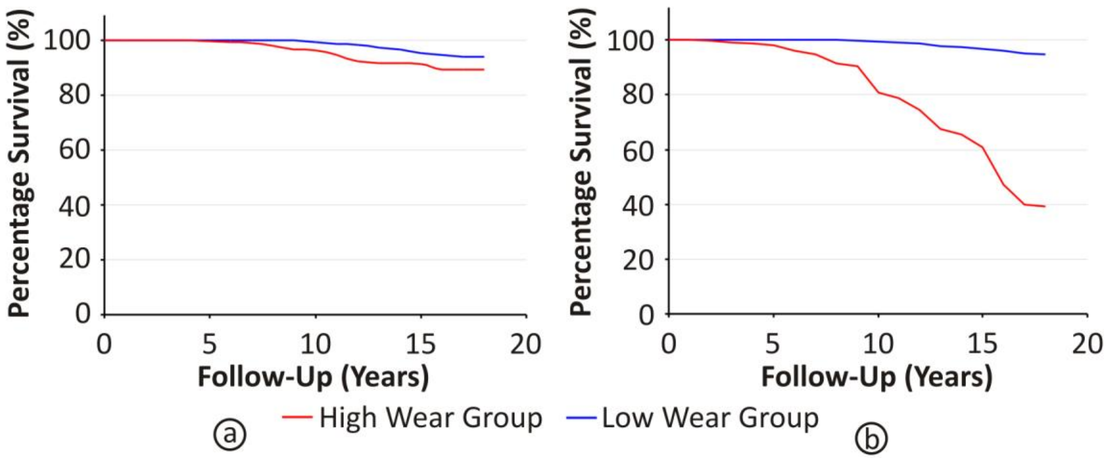

Figure 2.16: The survival to revision of femoral stems (a) and acetabular cups (b) for patients experiencing high cup wear and low cup wear. While the survival of the femoral component is largely unaffected by the cup wear state, there is a marked effect in the survival of the acetabular component (Wroblewski et al, 2004).

The method of aseptic loosening in the cemented acetabular component is not fully-understood. Three methods of loosening have been suggested, and may be valid for different patients, depending on a myriad of mechanical and biological factors.

2.3 CHARACTERISING BONE CEMENT

2.3.1 The Composition of Bone Cement

Bone cement mainly consists of polymethylmethacrylate (PMMA), with added components to control polymerisation and maintain shelf life. It is supplied in two components; a power and a liquid. The powder ingredient mainly consists of pre-polymerised PMMA beads with a polymerisation initiator. A radio-pacifier such as barium sulphate ($BaSO_4$) is commonly added to enable the cement to be seen in radiographs. The liquid component is primarily composed of methylmethacrylate (MMA) monomer, with hydroquinone added to ensure long shelf life and N,N-dimethyl-p-toludine as a polymerisation initiator. Gentamicin may also be added to reduce the risk of patient infection. There are a plethora of bone cement brands available, with constituents mainly varied to control the working time and viscosity of cement. All experimental and computational analyses in this thesis use CMW-1 bone cement (DePuy-CMW, Blackpool, UK); the ingredients of this brand are given in table 2.5 (DePuy-CMW, 2007).

Powder Constituent		Liquid Constituent	
Polymethylmethacrylate (%w/w)	88.85	Methylmethacrylate (%w/w)	99.18
Benzol peroxide (%w/w)	2.05	N,N-dimethyl-p-toludine (%w/w)	≥ 0.82
Barium sulphate (%w/w)	9.10	Hydroquinone (ppm)	25

Table 2.5: The constituents of CMW-1 bone cement (DePuy-CMW, 2007).

2.3.2 Cementing Technique

Cementing techniques have changed markedly since bone cement was first used by Sir John Charnley to achieve fixation in orthopaedic devices. Early (first generation) cementing involved hand-mixing and simple finger packing into cavities. This method permits air, blood and debris to become entrained in the cement, it allows laminations to form, it does not guide the positioning of prostheses and prohibits good interdigitation of cement into cancellous bone. Retrieval studies have revealed that a complete cement mantle and good cement interdigitation are prerequisites for fixation longevity (Jasty, 1991; Kawate et al, 1998). These discoveries led to the development of second generation techniques, involving cleaning to remove blood and debris from the cavity, the use of an inter-medullary plug to contain cement, and retrograde cement insertion to reduce lamination and cement pore formation (Learmonth 2005).

Later, third generation techniques (table 2.6) allowed the surgeon to achieve greater cement pressurisation and therefore improved cement interdigitation in cancellous bone. This is now achieved by using a cement gun to introduce cement, with a seal around the proximal femur. In this manner the inter-medullary canal may be completely sealed. Vacuum mixing has also been introduced in the third generation, to remove noxious fumes from the operating room and minimise cement porosity. Modern techniques for femoral prostheses involve the use of both distal and proximal stem centralisers, to prevent thin areas of cement and leave distal cement voids where desirable (Learmonth, 2005).

Feature	1st Generation	2nd Generation	3rd Generation
Distal femoral plug	No	Yes	Yes
Proximal femoral seal	No	No	Yes
Acetabular pressurisation	No	No	Yes
Hand mixing cement	Yes	Yes	No
Vacuum mixing cement	No	No	Yes
Brushing	No	Yes	Yes
Pulsatile lavage	No	No	Yes

Table 2.6: The three generations of cementing in THA (Learmonth, 2005).

2.3.3 Using CMW-1 Cement: Practicalities

Upon mixing the liquid and powder constituents of cement, an exothermic free-radical polymerisation process begins. For CMW-1 bone cement, the manufacturers recommend a mixing duration of 60 seconds, followed by a holding time of 20 seconds. This leaves approximately 200 seconds working time before the cement begins to set (at an ambient temperature of 21°C) (DePuy-CMW Ltd, 2007). Several authors have recorded the temperature profile of curing bone cement, reporting peak temperatures between 50 and 80°C (figure 2.17; Lennon and Prendergast, 2002; Roques et al, 2004a; Mavrogordato et al, 2008).

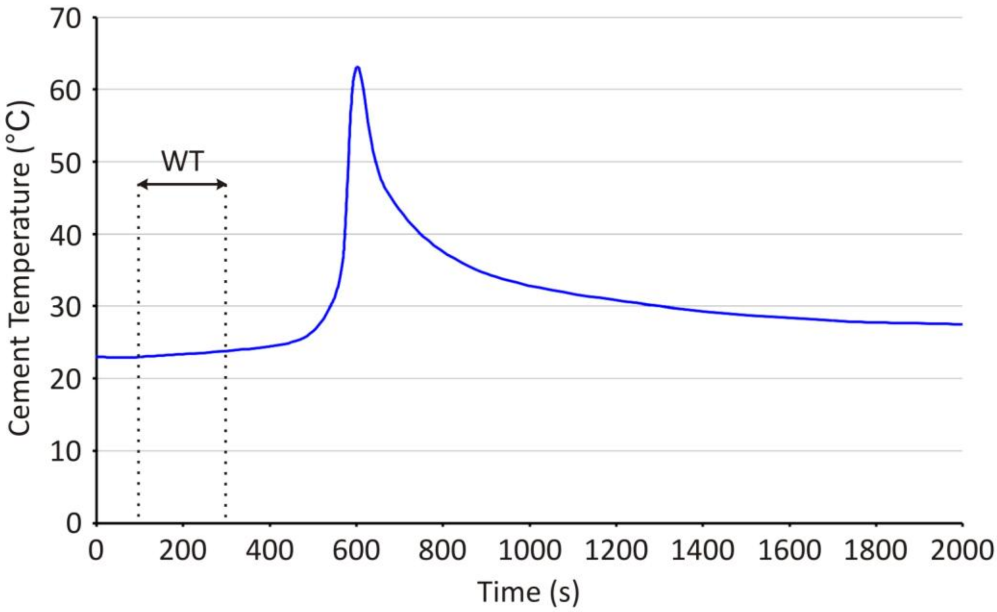

Figure 2.17: The temperature profile for polymerising CMW-1 cement, showing the working time (WT) (Roques et al, 2004a).

2.3.4 The Microstructure of Bone Cement

Micro-tomography and scanning electron microscopy (SEM) has revealed bone cement to be a highly inhomogeneous material, comprising a continuous matrix interspersed with radiopaque $BaSO_4$ particles surrounding pre-polymerised PMMA beads (Sinnett-Jones et al, 2005). Multiple features have been reported in specimens of bone cement (figure 2.18; Wang et al, 1996; Sinnett-Jones et al, 2005):

- Pre-polymerised beads between 10 and 60 µm in diameter.
- $BaSO_4$ powder particles up to 2 µm in diameter.
- Agglomerates of $BaSO_4$ up to 200 µm in diameter.
- Cement pores up to 2 mm in diameter, commonly grouped in clusters.
- Voids between 2 and 20 µm in diameter within approximately 2% of pre-polymerised beads.

Since both cement pores and radiopaque agglomerates have been implicated in the fatigue failure process for bone cement, their formation and effect is explored here in detail.

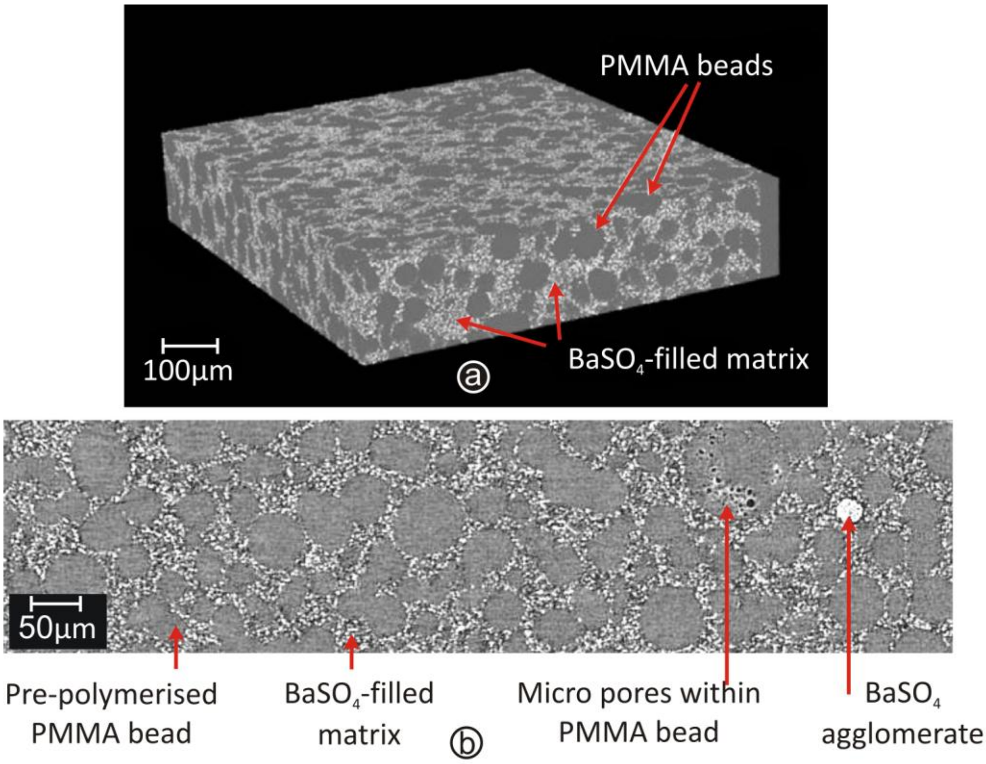

Figure 2.18: The microstructure of CMW-1 cement observed via synchrotron tomography (a) and scanning electron microscopy (b) (Sinnett-Jones et al, 2005).

2.3.4.1 *Cement Porosity*

Cement pores may occur in bone cement either due to the entrainment of air on mixing, or due to a volumetric shrinkage during cement polymerisation:

- Cement polymerisation is an exothermic process; cement expands and flows before the peak temperature is reached, yet contracts upon cooling. The constraint of cured cement at surrounding geometry means pores must form within cement to account for shrinkage.
- There is a reduction in monomer density on polymerisation, which results in a volumetric shrinkage of bone cement. Again, where cement extremities are constrained, the contraction must be taken up internally in pores (figure 2.19).

Gilbert et al (2000) theoretically determined the polymerisation shrinkage of one brand of cement to be 7.8%, and used the Archimedes' principle to record shrinkage between 5 and 6.5% experimentally.

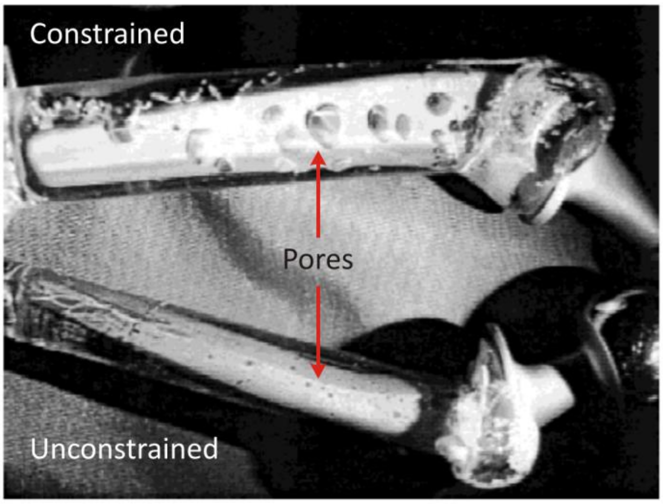

Figure 2.19: The external constraint of cement forces cement contraction on polymerisation to occur through pore growth, resulting in large pores for a rigid mould (top). Where a flexible mould is used (bottom), cement is free to contract from the extremity, resulting in smaller pores (Gilbert et al, 2000).

The number and size of pores has been closely linked to the mixing method used. Several studies have shown that vacuum mixing is effective in reducing porosity (increasing specimen apparent density) in a range of bone cements (Wang et al, 1996; Dunne and Orr, 2001; Lewis, 1999). The higher the applied vacuum, the lower the porosity found. Dunne and Orr (2001) reported a reduction from 16.4% to 1.4% porosity by using vacuum mixing, while Lewis (1999) reported the reduction to be from 6.9% to 0.5%. However, upon sectioning specimens Wang et al (1996) reported that vacuum mixing had been effective in removing small pores (diameter < 0.5 mm), yet some larger pores (diameter > 0.5 mm) remained. Vacuum mixing minimises entrained air bubbles, which may become micro-pores. Where the cement exterior is constrained by a mould, volumetric contraction is shared internally amongst pores during curing: thus, fewer micro-pores from mixing may result in a small number of larger macro-pores after polymerisation (Murphy and Prendergast, 2000). The porosity in specimens is also reported to vary with bone cement type, and the temperature of the monomer prior to mixing (Lewis, 1997).

The number, distribution and size of cement pores have not been adequately described yet. Wang et al (1996) determined the number of macro-pores (> 1 mm in diameter) from radiographs of vacuum-mixed specimens, finding between 0.1 and 1 pore per cm^3, depending on the preparation method and cement type; for hand-mixed specimens, between 1.2 and 1.8 macro-pores per cm^3 were found.

2.3.4.2 Barium Sulphate

Barium sulphate ($BaSO_4$) is commonly used as a radio-pacifying agent, though zirconium oxide (ZnO_2) is also used in some cement brands. $BaSO_4$ particles appear not to be well-bonded to the surrounding matrix, and may be accompanied by small voids at their surface (figure 2.20; Molino and Topoleski, 1996; Sinnett-Jones, 2007). There is evidence that the fine distribution of $BaSO_4$ results in improved fatigue properties of polymers, since cracks deflect between $BaSO_4$ particles, creating a longer crack path (Molino and Topoleski, 1996; Ginebra et al, 2002; Lewis, 2003).

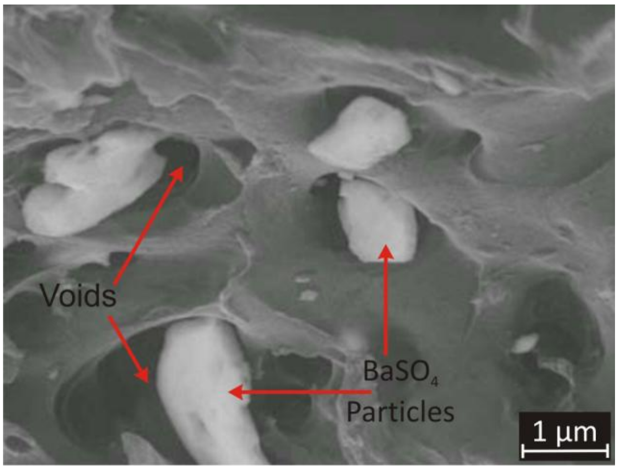

Figure 2.20: Scanning electron micrograph showing limited bonding between the matrix and barium sulphate particles, and the associated voids (Sinnett-Jones, 2007).

Agglomerates of $BaSO_4$ have also been found in specimens, and are thought to relate to insufficient mixing; however, their prevalence suggests they cannot be avoided with current preparation methods. The degree of bonding between individual particles in these agglomerates, and the bulk material properties of whole agglomerates, is currently unknown (Sinnett-Jones et al, 2005).

2.3.5 The Static Mechanical Properties of Bone Cement

Knowledge of the static mechanical properties of bone cement is required to conduct computational simulations of bone cement. In a state-of-the-art review, Lewis (1997) found huge variation in the static performance of bone cement, depending on the method of specimen preparation and test configuration (table 2.7). As this thesis concerns the performance of vacuum-mixed CMW-1 bone cement, specific properties for this preparation are also provided in table 2.7.

Static Mechanical Property	General (Lewis, 1997)	Vacuum-Mixed CMW-1 (Roques, 2003)
Tensile elastic modulus	1.58 – 3.08 GPa	2.8 GPa
Compressive elastic modulus	1.95 – 3.18 GPa	-
Ultimate tensile strength	23.6 – 47.0 MPa	41.3 – 47.0 MPa
Ultimate compressive strength	72.6 – 117.0 MPa	96.0 MPa
Ultimate shear strength	32.0 – 69.0 MPa	63.0 MPa
Poisson's ratio	0.3	-

Table 2.7: The static mechanical properties of bone cement.

2.3.6 The Fatigue Failure of Bone Cement

Many experimental studies have attempted to characterise the fatigue failure process in bone cement using dog-bone-shaped specimens (figure 2.21; Murphy and Prendergast, 2000; Roques et al, 2004b; Jeffers et al, 2005; Coultrup et al, 2009). The following section presents the results of these characterisation analyses.

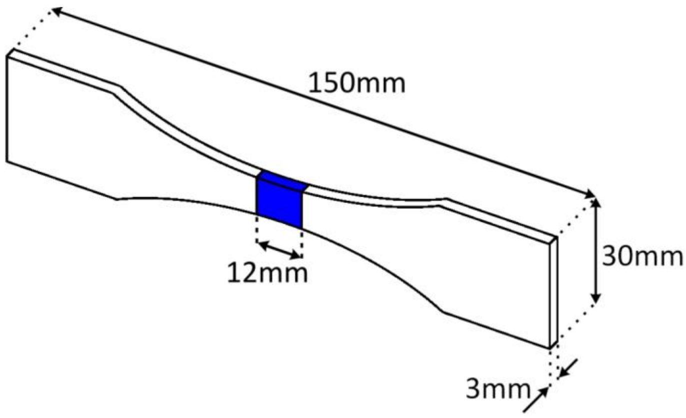

Figure 2.21: The geometry of dog-bone-shaped fatigue specimens used by Jeffers et al (2005). The gauge length is shown in blue, 12 mm wide.

2.3.6.1 Wöhler Curves for Bone Cement

By testing specimens to failure under fatigue loading at different peak stresses, the fatigue performance of a polymer may be defined by a Wöhler (S-N) curve (figure 2.22). Phase 1 occurs where the applied load in the first cycle is high enough to form craze zones in the polymer, meaning the fatigue life is highly dependent on the applied load. Phase 2 shows a reduced dependence of fatigue life on applied load, and represents the enhanced role of microscopic crack growth in fatigue failure. Phase 3 forms the endurance limit, where the number of cycles to failure approaches infinity and has a low dependence on the peak applied stress (Suresh, 2004).

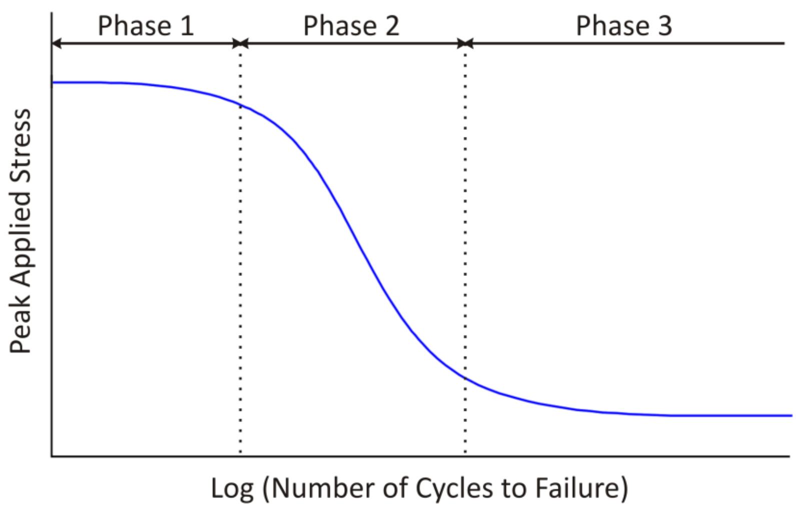

Figure 2.22: Schematic of the typical variation of peak stress to the number of cycles to failure for polymers (Suresh, 2004).

Jeffers et al (2005) and Murphy and Prendergast (2000) have both collected fatigue data for vacuum-mixed cement, enabling the authors to determine the slope of phase 2 of the Wöhler curve with regression lines of average fatigue life (N_F) at each applied stress level (σ, MPa) (figure 2.23; equations 2.1 and 2.2). These data are characterised by highly variable fatigue lives for a given stress level. In most cases, pores and/or $BaSO_4$ agglomerates were found on the fracture surfaces of specimens.

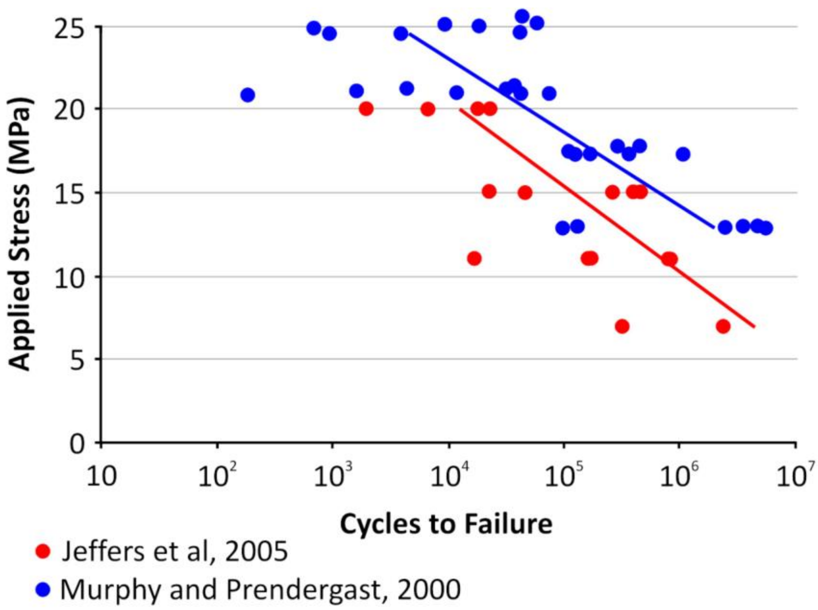

Figure 2.23: Fatigue data for two different stuides of vacuum-mixed dog-bone-shaped specimens. Regression lines are shown for average fatigue life at each stress level (Murphy and Prendergast, 2000; Jeffers et al, 2005).

$\sigma=41.99-5.13\cdot\log(N_F)$ Equation 2.1 (Jeffers et al, 2005)

$\sigma=40.40-4.40\cdot\log(N_F)$ Equation 2.2 (Murphy and Prendergast, 2000)

2.3.6.2 Effect of Porosity on Fatigue of Bone Cement

A number of studies have reported superior fatigue performance of vacuum-mixed dog-bone-shaped fatigue specimens over hand-mixed, though this improved performance is accompanied with significant variation (Lewis, 1999; Murphy and Prendergast, 2000; Dunne et al, 2003). The presence of pores in the gauge length (figure 2.24b) and their relative distribution appear to dictate crack initiation and the fatigue life of specimens, as well as inter-specimen variability (Lewis et al, 1999; Murphy and Prendergast, 2000; Dunne et al, 2003; Jeffers et al, 2005; Sinnett-Jones et al, 2005). These authors have associated very early fatigue failure with the presence of macro-pores (>1 mm diameter) on the fracture surface.

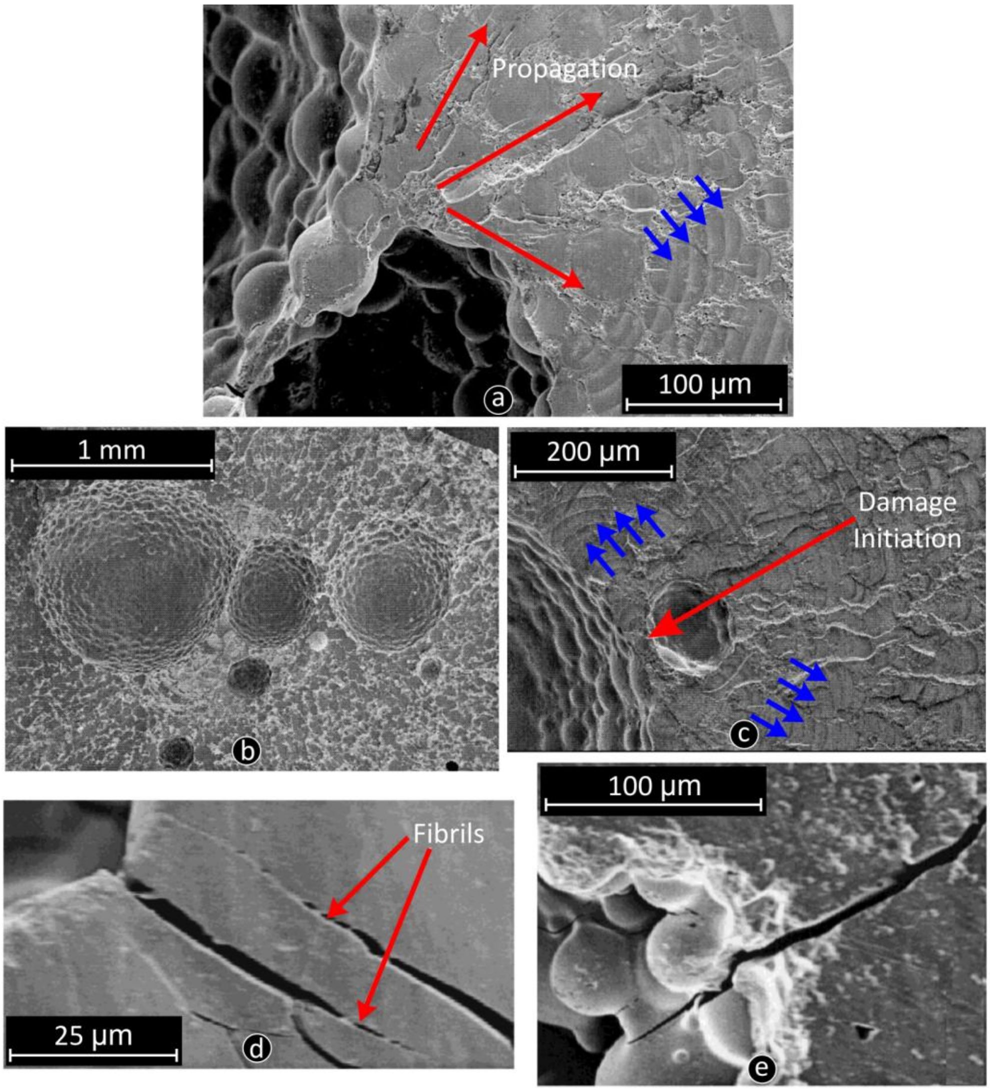

Figure 2.24: The morphology of fatigue specimen fracture surfaces (Murphy and Prendergast, 2000; Murphy and Prendergast, 2001). Discontinuous growth bands (blue arrows) from fatigue failure at pores (a and c); pores from hand-mixed specimens (b); fibrils left spannning cracks after propagation (d); crack initiation between pre-polymerised beads at a pore surface (e).

Pores reduce the cross-sectional area of specimens and thus increase the apparent stress level. Additionally, stress amplification by a factor of 2.045 also occurs at pores (Timoshenko and Goodier, 1970). This is compounded where pores are clustered as stress amplifications are superimposed. On a microscopic scale, crack initiation is seen at the further stress concentration created between adjacent pre-polymerised beads on the surface of pores (figure 2.24e; Murphy and Prendergast, 2000; Murphy and Prendergast, 2001; Sinnett-Jones et al, 2005). Using synchrotron tomography, Sinnett-Jones (2007) also identified crack initiation at micro-voids associated with $BaSO_4$ particles in the amplified stress region near larger pores (figure 2.25).

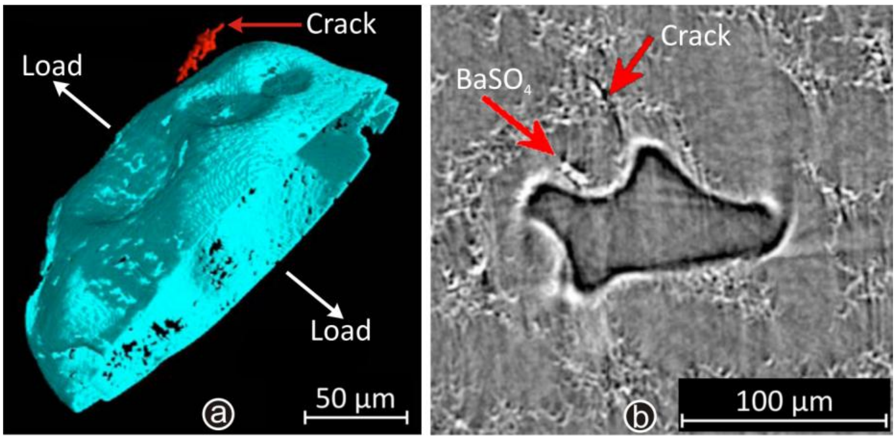

Figure 2.25: Cement cracking at $BaSO_4$ voids in the high-stress region near a pore. Synchrotron scanning allowed the crack to be visualised as a 3D segmented model (a) and on a micrograph (b) (Sinnett-Jones, 2007).

Several authors have theorised that the presence of pores may be beneficial in some respects. Topoleski et al (1993) proposed that the prevalence of small pores (<0.5 mm) in hand-mixed cement may be beneficial to the fatigue life of specimens, as they blunt cracks that propagate into them, reducing the stress intensity at the crack tip. They may also deflect the crack tip, increasing the fatigue crack length, and thus increasing fatigue life (Topoleski et al, 1993). Janssen et al (2005a) also stressed the importance of the location of pores. If pores are next to cracks but do not deflect them, non-critical damage-induced strain at the pore may reduce the stress at the crack tip, thus increase the fatigue life. This theory currently lacks validation.

2.3.6.3 The Effect of Barium Sulphate on Fatigue in Bone Cement

In the absence of macro-pores, $BaSO_4$ agglomerates have been seen on the fracture surfaces of uni-axial fatigue specimens, and thought to be locations for crack initiation (Sinnett-Jones et al, 2005; Coultrup et al, 2009). Fatigue crack propagation has also been observed through agglomerates (figure 2.26b), suggesting they do posses some mechanical integrity, rather than being a collection of loose powder. Compressive stresses in the surrounding matrix may contribute to this integrity (Sinnett-Jones, 2007).

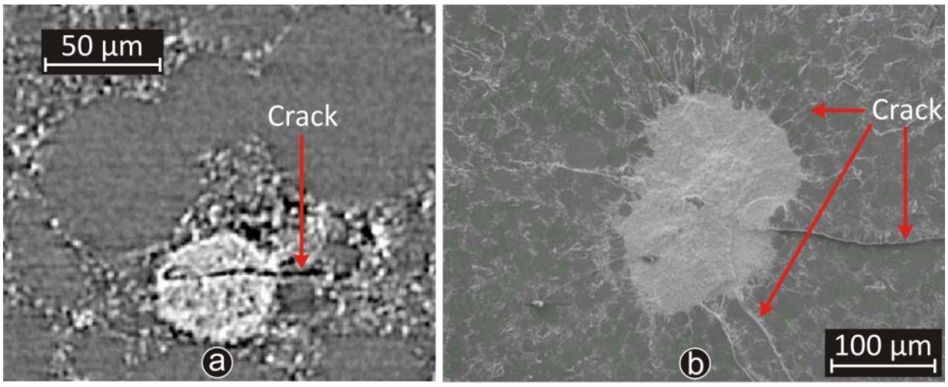

Figure 2.26: Cracks propagating through barium sulphate agglomerates found with synchrotron tomography (a) and by scanning electron microscopy of a specimen fracture surface (b) (Sinnett-Jones, 2007).

In contrast, where $BaSO_4$ is well-distributed upon mixing, it appears to result in increased fatigue life compared to where is it not added (Molino and Topoleski, 1996). $BaSO_4$ powder ensures many microscopic pores (<1 µm in diameter) form as curing shrinks away from particles during polymerisation (figure 2.20), creating a preferential crack path around pre-polymerised beads which may otherwise not be present (Topoleski et al, 1990; Molino and Topoleski, 1996; Sinnett-Jones, 2007). This longer failure path, plus the arrest of cracks at pre-polymerised PMMA beads, results in increased cement fatigue life. Using synchrotron tomography, Sinnett-Jones et al (2007) found evidence that crack initiation may also occur at micro-voids in the high-stress region near large pores in some cases.

Other authors have noted that other factors which contribute to the variation in cement specimen fatigue performance include cement type (Lewis, 1997), cement age (Roques et al, 2004b) and the loading regime (Verdonschot and Huiskes, 1996).

2.3.6.4 The Microscopic Fatigue Failure Process of Bone Cement

There is some disagreement over the location of reported cracking in bone cement during stable fatigue crack progression. Relevant literature reveals examples of stable crack propagation preferentially though the inter-bead matrix (Topoleski et al, 1993; Molino and Topoleski et al, 1996; Murphy and Prendergast, 2001), and commonly through both the matrix and pre-polymerised beads (figure 2.24a and 2.24c; Topoleski et al, 1993; Molino and Topoleski, 1996; Murphy and Prendergast, 2000; Sinnett-Jones et al, 2005). The local path of least resistance to cracking is probably determined by a number of variables in reality. Fracture surfaces commonly feature areas with discontinuous growth bands (DGBs), indicating the crack initiation location.

Analyses of the fatigue failure of dog-bone shaped specimens using acoustic emission (AE) monitoring (section 2.52) have recorded stop-start AE activity, suggesting the fatigue process is discontinuous (Roques et al, 2004b; Jeffers et al, 2005). This ties up well with observations of DGBs on the failure surfaces of fatigue specimens (figures 2.24a and 2.24c; Murphy and Prendergast, 2000; Jeffers et al, 2005). AE may be generated during crack initiation and propagation, and craze formation; unfortunately, given AE have not been able to be directly linked to given damage events. Jeffers et al (2005) found DGBs on the surface of specimens (~80 µm) to be too thick to be fatigue striations, thus supporting the discontinuous damage accumulation theory.

Such observations allow one to propose a theory for the process of fatigue failure in bone cement. Porosity, $BaSO_4$ agglomerates and individual $BaSO_4$ particles may act together to initiate cracks. DGBs on fracture surfaces correspond to crack tip advance in a single spurt after multiple fatigue cycles (they should not be confused with striations, which result from crack advance on every loading cycle). Suresh (2004) associated DGBs with low stress intensity factor ranges (ΔK) at the crack tip. In this condition, energy is absorbed within a craze zone at the crack tip by microscopic deformation. During cyclic loading, damage accumulates within the craze zone in the form of micro-cracking, which increases the opening of the craze zone (figure 2.27a). The load is borne by remaining fibrils. When the opening reaches a critical size, crack growth occurs through the craze zone in one spurt (a stretch zone), along the craze-matrix interface and through fibrils (figure 2.27b). The crack becomes arrested due to closure of the craze zone. The DGBs are locations of successive crack tips which are repeatedly blunted, advanced, and arrested (Suresh, 2004). This theory explains the association of DGBs (figures 2.24a and 2.24c) with fatigue cracks in specimens subjected to physiological fatigue loading. Additionally, Murphy and Prendergast (2001) claimed to identify fibrils spanning cracks propagating in specimens, as in figure 2.24d; it appears that these fibrils are too sparsely spaced to signify a craze zone (Suresh, 2004), but it is possible that the resolution of this image prevents closely-spaced fibrils being seen at the crack tip.

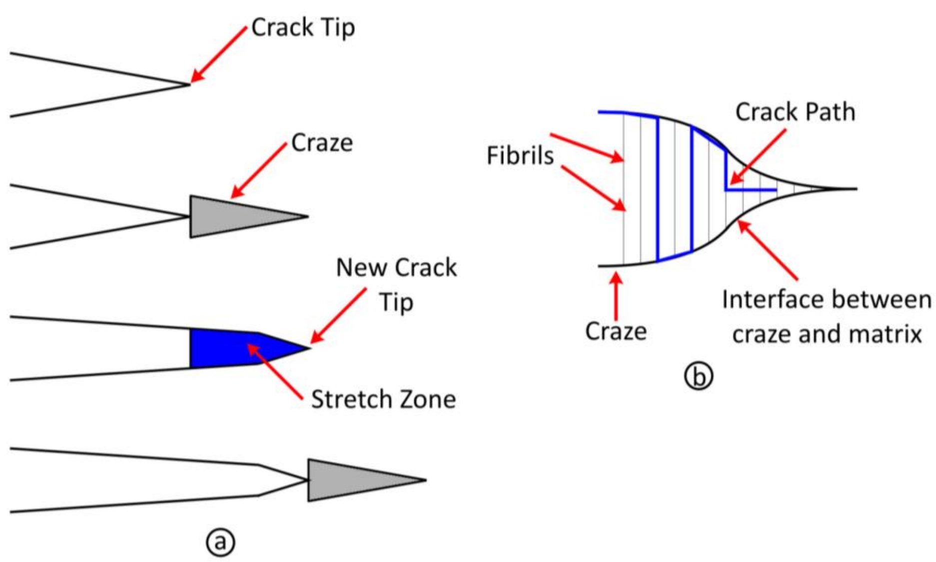

Figure 2.27: A schematic representation of crack progression in bone cement (a); a schematic of crack propagation through a craze zone (b) (Suresh, 2004).

2.3.7 Bone Cement Creep

Creep refers to a change in the strain of specimens for a state of constant static or dynamic stress: this is applicable to bone cement, since it is a viscoelastic material. This phenomenon may account for the subsidence of the femoral stem reported clinically, as cement deforms in areas of high stress imparted by the prosthesis (section 2.4.3.2). Stress relaxation refers to a reduction in cement stresses with time in a sample held at constant static or dynamic strain (Lee et al, 2002). Stress relaxation is relevant to the in vivo case during extended periods of unloading (e.g. resting) or loading (e.g. standing), reducing the magnitude of stresses in the cement mantle.

Under static four-point bending, Lee et al (2002) reported that stress relaxation may reduce cement stresses from 25MPa to 13MPa over 8 hours. Chwirut (1984) reported that static creep strains equalled elastic strains after 200 hours loading at physiological uni-axial tensile stresses. The author reported that the power-law stress function in equation 2.3 approximated the relationship between static strain (ε_{STAT}), time (T, s) and applied stress (σ, MPa). These authors reported the creep rate reduced with time, and was initially higher for higher applied stress, younger cement, the presence of fat, and increasing temperature.

$$\varepsilon_{STAT} = 1.79\text{x}10^{-6} \cdot T^{0.283} \cdot \sigma^{1.858}$$ Equation 2.3 (Chwirut, 1984)

During uni-axial fatigue loading of dog-bone-shaped cement specimens, creep strains approaching 50% of elastic strains have been reported after only 250,000 cycles of physiological loading (Verdonschot and Huiskes, 1994; Verdonschot and Huiskes, 1995). The dynamic strain rate exhibited reduces as tests progress, and is higher for higher applied stresses. For a high load condition, the creep process may be split into three phases (figure 2.28). Phases 1 and 2 are thought to refer to the disentanglement of polymer chains under initial loading, and the sliding of polymer chains thereafter, and are theoretically reversible upon unloading. The third phase of creep comprises irreversible mechanical damage, resulting in an unstable increase in creep rate prior to failure. Where the applied strain level is below the endurance limit of cement, phase 3 does not occur, and the creep strain rate approaches zero as loading continues (figure 2.28). The creep rates seen under tensile loading were 5 to 10 times higher than those for compressive loading (Verdonschot and Huiskes, 1994; Verdonschot and Huiskes, 1995).

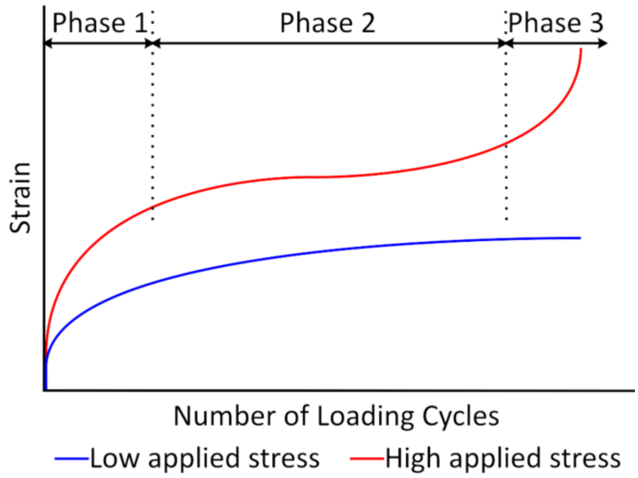

Figure 2.28: Creep profiles in dog-bone-shaped specimens under uni-axial tensile fatigue stress. The three phases of cement creep are highlighted for cement under high applied stress (Verdonschot and Huiskes, 1994).

$$\varepsilon^{C}_{DYN} = 7.985\text{x}10^{-7} \cdot N^{0.4113} \cdot \sigma_{DYN}^{\ 1.9063} \cdot N^{-0.116\log\sigma_{DYN}}, \text{ where } \sigma > 0 \qquad \text{Equation 2.4}$$

$$\varepsilon^{C}_{DYN} = 1.225\text{x}10^{-5} \cdot N^{0.314} \cdot 10^{0.033\sigma_{DYN}}, \text{ where } \sigma < 0 \qquad \text{Equation 2.5}$$

By determining the strain response for specimens under a range of applied loads, the dynamic creep strain (ε^{C}_{DYN}) may be related to the number of loading cycles (N) and peak dynamic stress (σ_{DYN}, MPa), for both tensile (equation 2.4) and compressive (equation 2.5) stresses (Verdonschot and Huiskes, 1994; Verdonschot and Huiskes, 1995).

2.4 EXPERIMENTAL AND COMPUTATIONAL ANALYSES OF THE FATIGUE FAILURE OF ARTHROPLASTIES

Controlled laboratory and computational analyses of fatigue failure in arthroplasties are vital to understanding the genesis and progression of failure processes, which may not be elucidated clinically. Analyses of the femoral component are considered here first, while a discussion of the acetabular component follows afterwards. The conclusions of these analyses are discussed separately to the methods involved, to allow a concise summary of the failure processes reported.

2.4.1 Experimental Methods of Elucidating the Aseptic Loosening Processes in the Femoral Component of Cemented THA

The clinical evidence of the aseptic loosening process for the femoral THA component involves stem-cement debonding, cement fatigue damage, osteolysis and stem subsidence (section 2.2.7; Jasty et al, 1991; Schulte et al, 1993; Kawate et al, 1998; Wroblewski et al, 2009b). However, suitable methods do not currently exist to determine the processes pertaining to the initiation of these events in vivo (Jacobs et al, 1989; Reading et al, 1999). Also, retrieval and autopsy studies only show the condition of the construct at one time point for each arthroplasty. Researchers have implanted prostheses in cadavers and measured cement strains, stem-cement micromotion, stem migrations, and sectioned specimens to reveal the state of the cement mantle (Stolk et al, 2002; Stolk et al, 2003b; Race et al, 2003). Again though, this approach reveals the condition of the arthroplasty at one time point, not the whole process of loosening. To allow monitoring of complete failure processes, experimental models which mimic the stress distribution in the cement mantle, yet leave cement exposed to allow visual monitoring of cement fatigue failure have been developed (McCormack et al, 1996; Hertzler et al, 2002). Such analyses can also be devised to allow good control of independent variables. By deviating from the natural geometry and loading of the arthroplasty, some fidelity to the in-vivo case is inherently lost; this must be considered when interpreting results (Huiskes, 1993a). Additionally, biological processes cannot generally be accurately replicated in experimental analyses. In spite of these limitations, experimental analyses can provide important conclusions for the aseptic loosening process and prosthesis design. Of particular relevance to this thesis are the experimental protocols of McCormack et al (1996) and Hertzler et al (2002), as these are used in multiple studies to reach important conclusions on the failure of cemented THA implants.

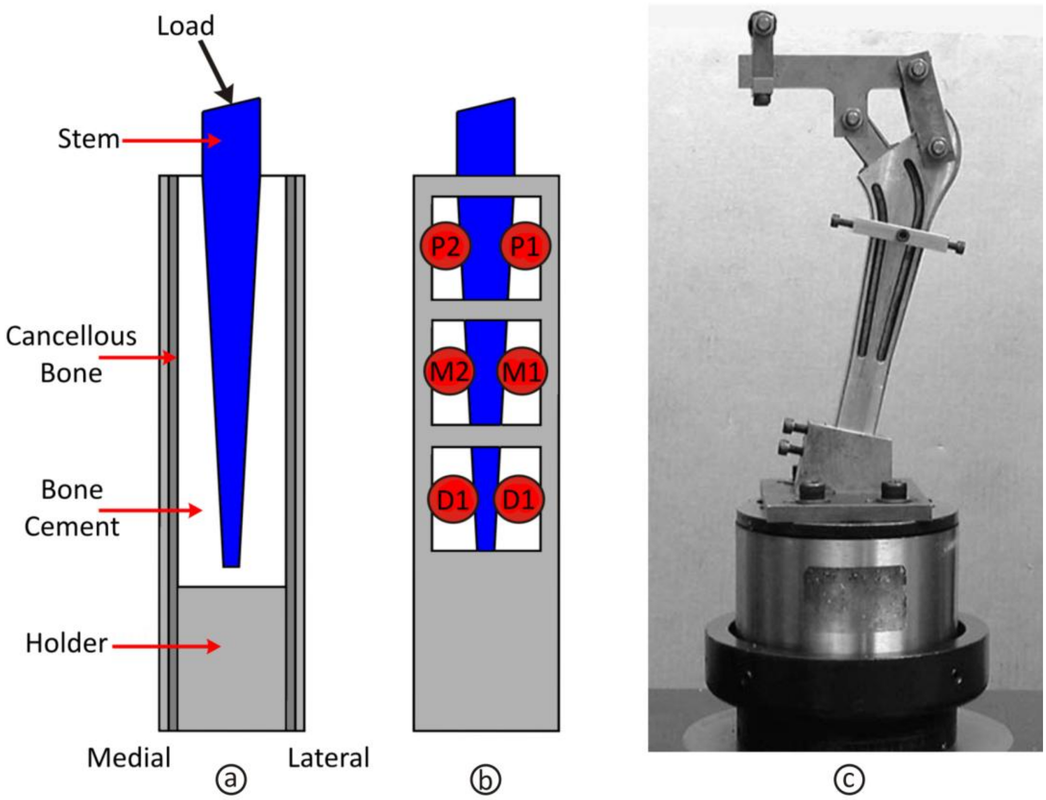

Figure 2.29: A schematic of the experimental configuration of McCormack et al (1996) where P = proximal, M = medial and D = distal (a and b); a similar construction with bending and axial load applied to the stem (c) (Lennon et al, 2003).

McCormack et al (1996) first presented a longitudinal section configuration of a cemented femoral stem, consisting of a cement mantle and tapered stem, surrounded by an aluminium case to simulate the cortex: this shall be referred to as a 2½D model (figure 2.29). Windows in the aluminium casing allowed developing cracks and flaws to be measured every 500,000 cycles, thereby allowing a step-based understanding of the loosening process. Dye penetrant was used to highlight cracks, though this has the disadvantage that only cracks close to the surface may be detected. While this configuration constrains the cement in a physiological geometry, the sectional geometry means that hoop and radial stresses are not imparted upon the cement mantle. Other studies have exploited this test configuration to explore different aspects of the damage accumulation process, and to allow the validation of computational methods (McCormack and Prendergast, 1999; Lennon and Prendergast, 2002; Lennon et al, 2003; Jeffers et al, 2007).

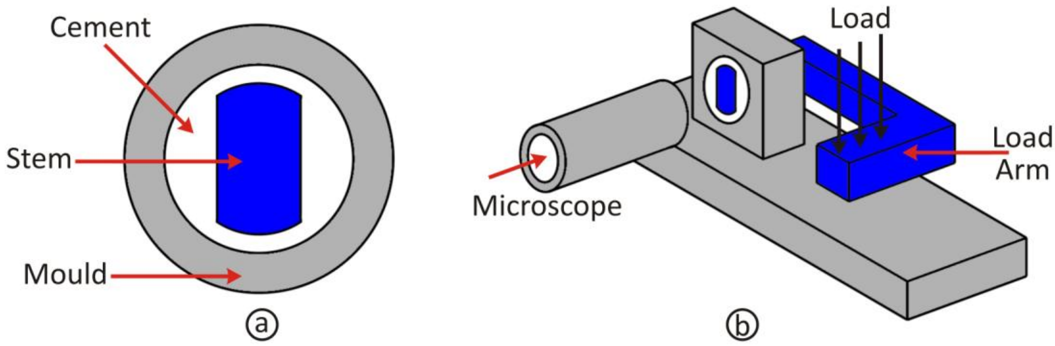

Figure 2.30: The mould (a) and torsional loading mechanism (b) used in the study of Hertzler et al (2002).

Hertzler et al (2002) used a model representing transverse slices of the THA reconstruction at the mid-stem level, with applied torsional load (figure 2.30). The cement mantle was left exposed to microscopically monitor crack propagation in the cement mantle caused by stress concentrations in the stem profile. The exposure of the cement mantle again reduces the accuracy of the model to the in vivo load case. In particular, only torsional loading was applied to the model, and despite statements concerning the dominance of torsional loads in vivo (Mann et al, 1995), the omission of axial and bending loads may significantly affect the crack propagation mechanism reported. Additionally, the load-transfer mechanism at the bone-cement interface was not well-represented, while stress concentration generated at the sharp stem edge was far higher than should be expected with modern cemented stems. Hertzler et al (2002) used the configuration to record the cement crack propagation rate in cement mantles of varying thickness, while others have used it to determine the accuracy of findings from computational models of cement fatigue (Stolk et al, 2003b; Janssen et al, 2005b).

2.4.2 Computational Methods of Elucidating The Aseptic Loosening Processes in the Femoral Component of Cemented THA

A range of static finite element analyses have been used to predict cement mantle stresses for a range of different prostheses and patient conditions. In some instances, these models represent a simplified stress state of the cement mantle in order to explore specific phenomena (Verdonschot and Huiskes, 1996) or replicate experimental models (Hertzler et al, 2002; Jeffers et al, 2007). State of the art methods revolve around segmenting computed-tomography scans of host bones, and determining the correct prosthesis size, orientation and location. The required cortical and cancellous bone is then removed, prosthesis geometries are imported and the bulk cement mantle is determined from the space between the prosthesis and remaining cancellous bone. By applying joint contact forces to the femoral head of the prosthesis and constraining the distal femur, stresses in the bulk cement mantle may be calculated (Jeffers, 2005; Stolk et al, 2007; Janssen et al, 2007).

Static simulations of the reconstructed hip are, unfortunately, of limited use. The aseptic loosening scenario has already been explained as a combination of mechanical and biological processes, the effect of which change with time postoperatively (sections 2.2.7 and 2.2.8). For instance, bone necrosis, bone resorption, stem-cement debonding, cement creep and partial cement damage are thought to all have an effect on the stress state within the cement mantle (Schmalzried et al, 1992; Huiskes, 1993a). Thus, a complete computational method should also represent a processes influenced by these effects.

2.4.2.1 Cement Damage Accumulation

A number of studies (Verdonschot and Huiskes, 1997a; Stolk et al, 2003a; Stolk et al, 2004; Janssen et al, 2006; Stolk et al, 2007; Jeffers et al, 2007) have used a continuum damage mechanics (CDM) method for modelling damage accumulation in finite element simulations of bone cement which was originally published by Verdonschot and Huiskes (1997a). Fatigue loading cycles are simulated incrementally in batches. Each cement element in the finite element model is allocated a 3D global damage tensor (D^{GLOBAL}), which is initially 0 in all directions (D_1, D_2, D_3; equation 2.6). The finite element model is solved, and for each cement element, the principle stresses and rotations from the global coordinate system are determined. For tensile stresses, cracks are assumed to develop perpendicular to the stress plane. The fatigue life for cement (N_F) for each principle stress value (σ_i, MPa) is determined from S-N data (equation 2.7, or alternatively equations 2.1 or 2.2). The number of cycles simulated in each increment (ΔN) is determined as the minimum required to result in a damage tensor value of 1 in any element. For this increment size, the change in damage for each tensor in each element (ΔD_i) is found using equation 2.8, and rotated into the global coordinate system and added to existing damage tensor values. Where global tensor values exceed a value of 0.95, a crack is assumed to have occurred perpendicular to the damage direction. Cracking can be modelled with special finite element options, by reducing orthotropic stiffness constants or through element death. Once the mechanical state of the cement mantle has been updated, a new increment begins. These authors counted cement cracks as a measure of the damage state of the cement mantle: a crack refers to every damage tensor value exceeding a value of 0.95 (i.e. each cement element can support three perpendicular cracks).

$$D^{GLOBAL} = \begin{pmatrix} D_1 & 0 & 0 \\ 0 & D_2 & 0 \\ 0 & 0 & D_3 \end{pmatrix} \qquad \text{Equation 2.6}$$

$$\sigma_i = -4.68 \cdot \log(N_F) + 8.77 \qquad \text{Equation 2.7}$$

$$\Delta D_i^{LOCAL} = \left(\frac{\Delta N}{N_F} \right) \qquad \text{Equation 2.8}$$

It should be noted that the CDM method represents a significant departure from the traditional fracture mechanics approach: however, the simplifications involved result in the computational efficiency required to assess whole implant systems in an expedient time frame for this highly-inhomogeneous material. It is shown later that the method has been used successfully to predict the comparable performance of implants: however, for a given condition it cannot precisely replicate the clinical failure method as the constituent laws do not directly reflect crack initiation, propagation and coalescence mechanisms in vivo.

2.4.2.2 Simulating Cement Creep

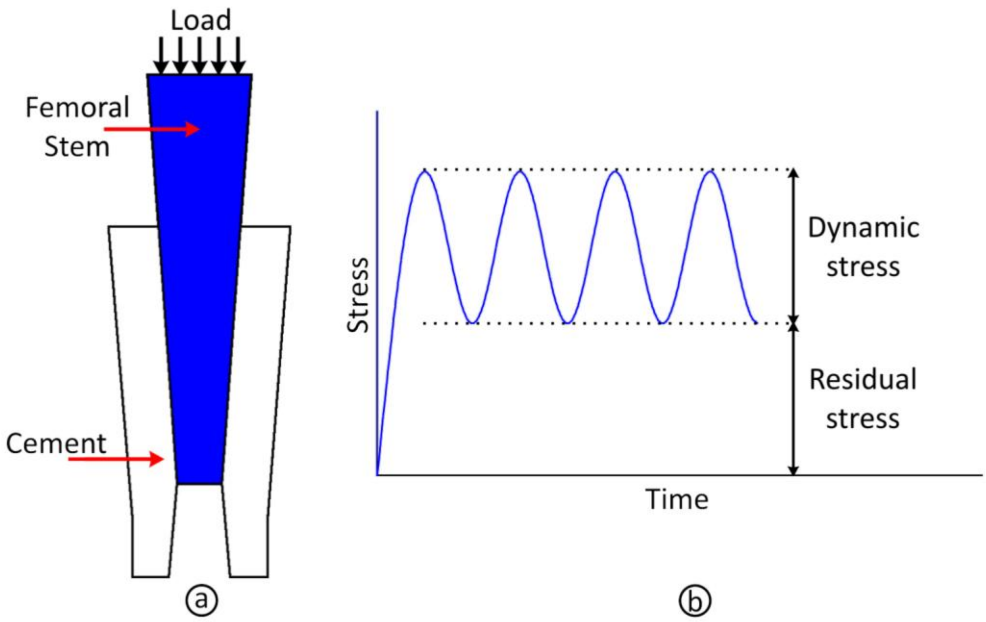

Figure 2.31: A cross-section of the cylindrical stem-cement model of Verdonschot and Huiskes (1996) (a); the cement stress response under dynamic loading (b).

Verdonschot and Huiskes (1996) presented a method for simulating bone cement creep around prostheses. Fatigue cycles are again simulated incrementally in batches. Like the damage accumulation calculation, each cement element has an individual creep strain tensor associated with it. The authors explained that under fatigue loading, creep comprises of dynamic and residual (static) strain components (figure 2.31b) which are dependent upon the residual stress (σ_{RES}, MPa) and peak dynamic stress (σ_{DYN}, MPa) components; these are related to the element Von Mises stress (σ_{VM}, MPa) in equation 2.9. If one assumes a loading frequency of 1 Hz, the residual creep component (ε^{C}_{RES}) may be determined from the number of loading cycles (N) using equation 2.10 (Chwirut, 1984). Depending on the principle stress, both tensile and compressive dynamic creep laws may be used to determine the dynamic creep component (ε^{C}_{DYN}) in equations 2.4 and 2.5. The number of cycles in the increment are determined as the number required to achieve a maximum creep strain in any element which is equal to 5% of the elastic strain in the same element. After Von Mises stresses have been determined, the change in individual creep tensors are found from equation 2.11 and added to existing creep strains, and a new increment can begin.

$$\sigma_{VM} = \sigma_{DYN} + \sigma_{RES} \qquad \text{Equation 2.9}$$

$$\varepsilon^{C}_{RES} = 1.798\text{x}10^{-6} \cdot N^{0.283} \cdot \sigma_{RES}{}^{1.858} \qquad \text{Equation 2.10}$$

$$\Delta\varepsilon^{C}_{ij} = \Delta\varepsilon^{C} \frac{\partial\sigma_{VM}}{\partial\sigma_{ij}} \qquad \text{Equation 2.11}$$

2.4.2.3 Simulating Cement Pores

It was shown in section 2.3.6.2 that pores have a significant effect on the fatigue performance of uni-axial specimens of bone cement. However, the anticipated benefits in the clinical survival of prostheses implanted with vacuum-mixed cement have not been seen (Malchau and Herberts, 1996; Ling and Lee, 1998). Several authors have included cement pores in fatigue simulations of cemented THAs in an attempt to explain this. Janssen et al (2005b) represented porosity in simulations by assigning near-zero stiffness to elements randomly. Lennon et al (2003) and Jeffers et al (2007) determined the number of pores in specimens using Monte Carlo methods. They randomly designated pores to cement elements and used the theoretical elastic solution for a spherical cavity in an infinite medium to simulate the stress concentration arising due to the pore (Timoshenko and Goodier, 1970). This solution is accurate so long as another pore or the edge of the cement is not within 3 radii of the centre of the pore (Jeffers et al, 2007). While these methods are computationally efficient, they mean the size of pores is regulated by the size of elements. Also, pore distributions and geometries may not be clinically accurate when this method is used.

The previous S-N data detailed (equations 2.1 and 2.2) pertains to cement with porosity. However, if pores are individually modelled in cement, the Wöhler curve for specimens without porosity is required. In practice it is not possible to produce such specimens. Both Janssen et al (2005b) and Jeffers (2005) explained an iterative computational method to determine a theoretic Wöhler curve for pore-free bone cement. Existing experimental S-N data is used to drive fatigue predictions of small specimens without pores. Calculated fatigue lives can be used to determine a new Wöhler curve, from which simulations can be re-run. By repeating this process multiple times, a converged Wöhler curve is derived for pore-free cement. For the experimental data of Jeffers (2005), the theoretically pore-free Wöhler curve is given in equation 2.12.

$$\mathrm{Log}(N_F)=(78.39-\sigma)/11.22 \qquad \text{Equation 2.12}$$

2.4.3 Findings from Experimental and Computational Studies of Cemented THA

2.4.3.1 Residual Stress and Pre-Load Damage

Before investigating the damage process recorded experimentally and computationally, one must consider the state of the cement mantle prior to loading. Cement shrinkage occurs on polymerisation (section 2.3.4.1), generating stresses which are high enough to cause local cracking. Prior to any loading, several authors have identified diffuse damage around a femoral stem, with some cracks spanning the whole thickness of the cement mantle (McCormack et al, 1996; McCormack and Prendergast, 1999; Lennon and Prendergast, 2002; Race et al, 2003). Both Roques et al (2004a) and Mavrogordato et al (2008) used acoustic emission monitoring to confirm that these cracks occur during cement cure around the femoral stem.

Computational models by Lennon and Prendergast (2002) and Roques et al (2004a) reported peak cement stress upon polymerisation in a simplified cement mantle to be in the range of 4 to 10MPa; significantly lower than the fracture strength of bone cement (table 2.6). The authors concluded that other factors must cause cracking, aside from the volume and temperature change. Porosity is one such factor, since pores impose a stress-raising factor of approximately 2 for an infinite medium, and more at the exterior (Timoshenko and Goodier, 1970). This may account for the discovery of pre-load cracks at bulk cement pores (McCormack and Prendergast, 1999). In reality, the location and severity of cracking may be a function of the polymerisation process and boundary conditions that determine the direction and magnitude of shrinkage (Bishop et al, 1996).

2.4.3.2 Cement Creep

Verdonschot and Huiskes (1997c) simulated the effect of long-term cement creep in the reconstructed femur under fatigue loading of constant peak load. While peak cement stresses at singularities were not reduced over 5 million fatigue cycles, average cement stresses were reduced by up to 50% due to creep, and interfacial shear stresses were also reduced, thus diminishing the chance of stem-cement debonding.

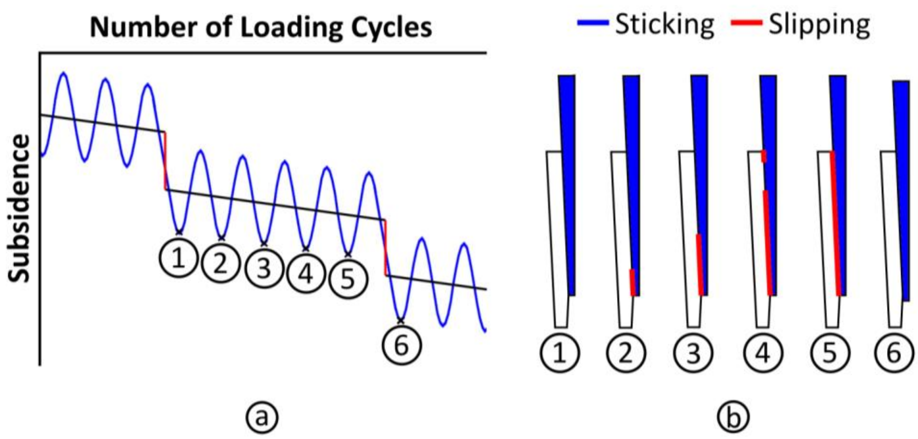

Figure 2.32: The subsidence pattern of a tapered cemented stem under uni-axial fatigue loading, revealing a stick-slip pattern (a); the slipping area (red) initiates distally at high shear stresses, and propagates proximally until the entire interface starts to slip, so the stem subsides in one step (Verdonschot and Huiskes, 1996) (b).

Computational and experimental methods have shown creep to account for stem subsidence; for a polished stem this is manifested as a stick-slip process at the stem-cement interface (figure 2.32; Mann et al, 1991; Verdonschot and Huiskes, 1996). Where the stem is completely stuck, distal stresses become very high, resulting in local cement creep and a reduction in resistance to axial load, changing the interface mode from stuck to slipping in this region. The slipping mode grows proximally, until the whole stem displaces distally in one step, and returns to a completely stuck condition (figure 2.32). Computational simulations have suggested the phenomenon is sensitive to the stem-cement condition, where a higher coefficient of friction results in a decrease in the frequency of step subsidence frequency. This finding was verified in experimental models by different step subsidence frequencies and overall subsidence rates, which may be related to differing stem roughness and interfacial porosity (Verdonschot and Huiskes, 1996). Other studies have suggested, however, that creep alone cannot account for the degree of stem subsidence seen clinically (Verdonschot and Huiskes, 1997c; Verdonschot and Huiskes, 1998); in reality, subsidence probably occurs due to a combination of cement creep, damage and porosity.

2.4.3.3 The Stem-Cement Interface

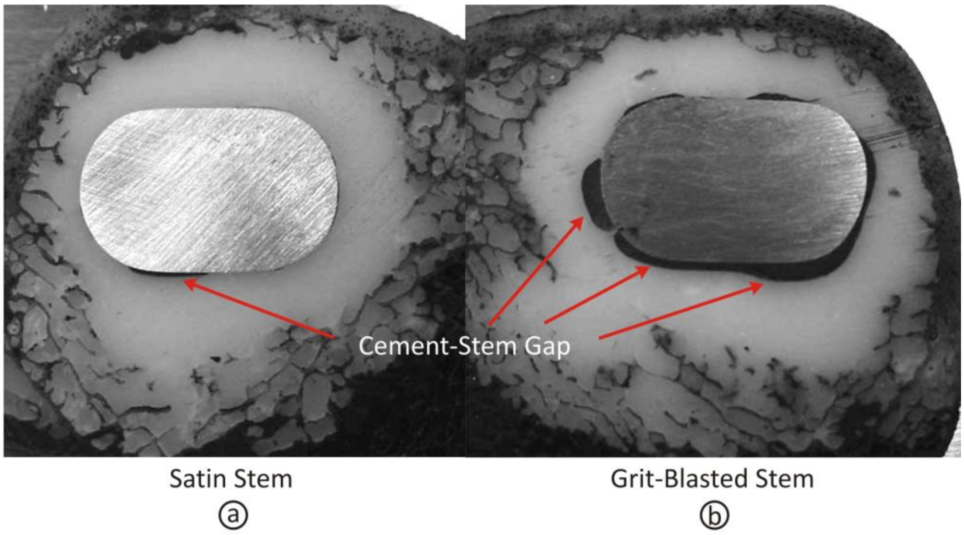

Figure 2.33: Stem-cement gaps for satin (a) and grit-blasted (b) femoral stems observed by Race et al (2002).

Upon polymerisation, no chemical bond forms between the prosthesis and cement: fixation is achieved is solely by mechanical interlock with irregularities in the stem surface. This interface is the weakest part of the femoral reconstruction (Huiskes, 1993a). While experimenting with bars of titanium set in bone cement, Mann et al (2004b) found that cement porosity which inherently forms at the interface is the source of this weakness, particularly for grit-blasted stems where air entrapment appears to aid void nucleation (figure 2.33; Race et al, 2002). This finding agrees with James et al (1993), who found shrinkage porosity to cover up to 30% of the stem-cement interface upon the sectioning of experimental and clinical specimens. The formation porosity at this interface may at least partially overcome the fixation advantage due to the rough surface finish (Race et al, 2002).

Several authors have investigated methods of strengthening this interface. Increasing the roughness of the stem and introducing macro-features into its design are two ways of achieving this (Chen et al, 1999; Crowninshield, 2001). Bishop et al (1996) showed that by heating the stem, interfacial cement can be forced to cure first, and thus porosity can be driven to other parts of the cement mantle. However, this method has not been widely adopted clinically. Mann et al (2004b) attempted to increase the strength of the stem-cement interface by implanting the stem early in the polymerisation process, but no significant increase in debond energy was achieved. Other researchers experimented with pre-coated stems to ensure a defect-free interface; while initial results seemed promising (Raab et al, 1982), clinically-suitable methods are not thought to offer any improved long-term performance (Ling, 1992). There appears to be no easy way to significantly increase the strength of this interface. Additionally, partial debonding has been found after as little as two weeks in vivo (Jasty et al, 1991). Since debonding of the stem-cement interface seems to be inevitable, engineers should design prostheses to perform well in the debonded state (Ling, 1992).

Debonding at the stem-cement interface can radically change the stress state in the cement mantle. While a bonded stem can transfer tensile, compressive and shear stresses, an unbonded stem can only transfer compressive stresses, and shear stresses to a limited degree via friction (Huiskes, 1993a; Crowninshield, 2001). Verdonschot and Huiskes (1997b) recorded an increase in peak cement stresses by a factor of 2.6 upon stem-cement debonding in a computational model: this has implications for cement fatigue and subsidence to mal-positioning. High stresses in cancellous bone along the length of the stem may also cause the resorption of trabeculae in the interdigitated region (Mann et al, 2009). Micro-motion at the stem-cement interface causes cement abrasion: this effect is more significant for a rougher stem (Crowninshield, 2001). Debonding and cement damage may allow wear debris to access the bone-cement interface, causing osteolysis in the long-term (Collis and Mohler, 1998).

The stick-slip pattern of stem subsidence has already been explained in section 2.4.3.2 for force-closed stems. Because the stem becomes wedged in the cement mantle, cement stresses are not fully removed on unloading: there is evidence that this maintained low stress may actually increase the longevity of the cement mantle (Verdonschot and Huiskes, 1996). A rough debonded stem cannot subside due to asperities on the stem surface, and subsequent cement damage and debris generation appear to be greater for a loose rough stem than a loose smooth stem (Verdonschot and Huiskes, 1998).

In summary, it appears that debonding of a polished tapered stem is not a catastrophic event, and creep and subsidence may reduce cement damage, minimise osteolysis, and help to re-distribute cement stresses. A rough stem may take longer to debond, but causes more damage to the construct after loosening. Verdonschot and Huiskes (1998) concluded that, since debonding cannot be avoided indefinitely, the smooth tapered stem is preferable to a rough stem.

2.4.3.4 The Cement-Bone Interface

The cement-bone interface has been implicated in the aseptic loosening process due to the observance of pre-load cracks, fatigue cracking and trabeculae resorption at this location (Schmalzried et al, 1992). Experimental studies have characterised the load-transfer mechanism in cancellous bone interdigitated with cement by varying loading cases to cubic specimens and measuring the resulting displacement (Kim et al, 2004a; Kim et al, 2004b; Race et al, 2007; Janssen et al, 2008; Miller et al, 2008; Mann et al, 2009). Specimens are typically prepared by implanting a mock stem into a cadaver femur with cement, and then sectioning to obtain rectangular specimens containing four regions: bulk cement, trabecular bone interdigitated with cement, the cement penetration extent, and cortical bone (figure 2.34).

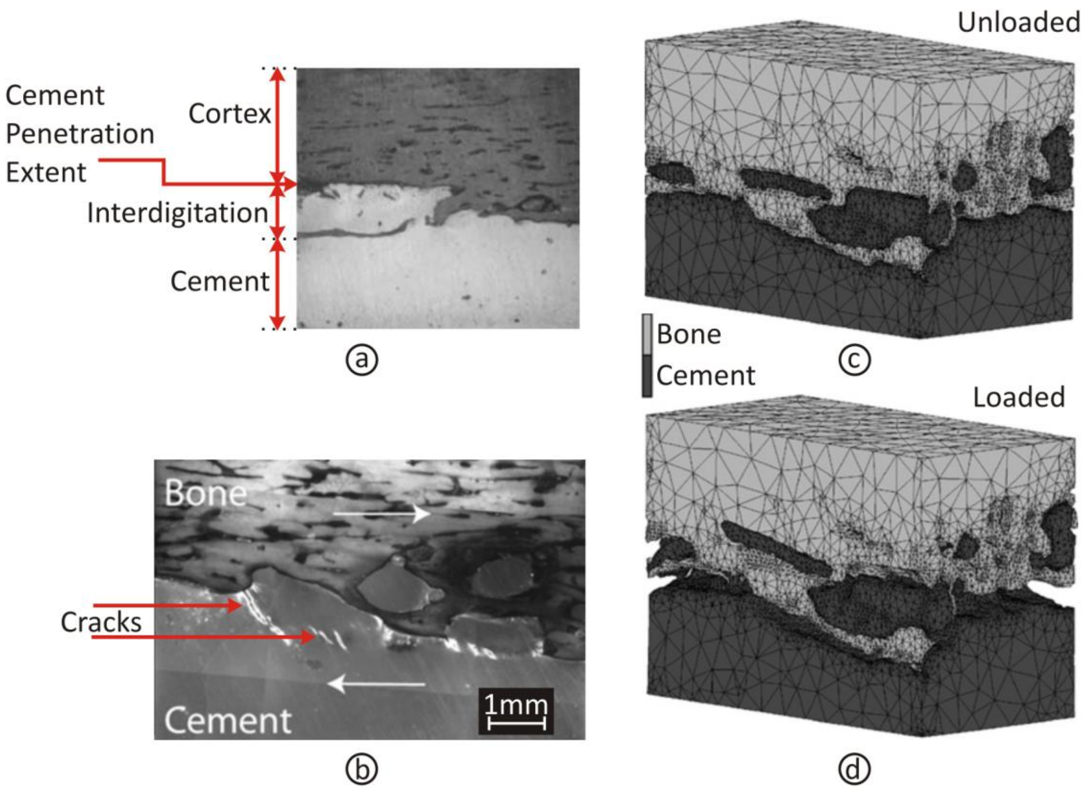

Figure 2.34: The zones of the bone-cement mantle (Kim et al, 2004a) (a); cement cracking upon shear fatigue loading (Miller et al, 2008) (b); the finite element model of Janssen et al (2008) (c); the bulk of strain under loading occurs at the cement-bone interface due to separation at the contact interface (d).

Race et al (2007) determined the tensile elastic modulus (2.1-2.8 GPa) and compressive elastic modulus (2.3-3.0 GPa) of vertebral cancellous bone interdigitated with bone cement. Elastic moduli values were generally lower than the moduli of pure cement (2.8 MPa). This is because cement does not chemically bond to bone, meaning load transfer occurs by mechanical interlock only (interface compression and friction). Sliding between cement and bone effectively reduce the elastic modulus of the composite below that of pure cement. The load transfer mechanism probably also explains the difference in compressive and tensile elastic moduli (Race et al, 2007). A further study of bovine specimens found the elastic modulus in the major trabecular alignment direction (superior-inferior) to be slightly higher than the modulus of pure cement, which may be due to the thickness of trabeculae in this direction (Williams and Johnson, 1989; Majumdar et al, 1998).

Experimental analyses have determined the response of cement-bone specimens under tensile (Kim et al, 2004b) and shear (Kim et al, 2004a; Miller et al, 2008) fatigue loading. The failure process comprised of three phases: a high initial strain rate phase, followed by a stable process of strain accumulation, finishing in rapid failure. For both loading modes the majority of strain occurred due to debonding of bone and cement and relative sliding, resulting from the lack of chemical bonding between cement and bone. While no damage was found in trabeculae, there was evidence of some cement cracking at bone interfaces accompanying the failure process (figure 2.34b; Miller et al, 2008). Further to this, Leung et al (2008) recorded cracking initiation at the interface with trabeculae in four-point bend fatigue specimens with acoustic emission monitoring, and verified the presence of damage in µCT scans. Upon tensile fatigue loading, Kim et al (2004b) reported bone-cement micro-motions in the order of 50 to 150 µm under fatigue loading, which may be tolerated by the body without the formation of fibrous tissue (Szmukler-Moncler et al, 1998).

Janssen et al (2008) attempted to computationally mimic the response of interdigitated cancellous bone to cyclic loading using geometrical models segmented from µCT scans (figure 2.34 a and c). The authors found the best stiffness predictions were achieved with a cement-bone coefficient of friction of 0.3 (rather than bonded contact). As may be expected, the stiffness of the structure is heavily reliant on the depth of cement penetration into cancellous bone (Janssen et al, 2008).

2.4.3.5 Fatigue Failure of the Femoral Cement Mantle

The discussion of mechanical cement failure in the reconstructed femur shall begin by considering simplified models of the in-vivo case. A 2½D model of the implanted proximal femur (figure 2.29) has been used by several authors to study the location and progression of cement cracks (McCormack et al, 1996; McCormack and Prendergast, 1999; Lennon et al, 2003; Jeffers et al, 2007). Upon fatigue loading of the stem, new cracks mainly form in the bulk cement mantle, and have been associated with cement pores (McCormack et al, 1996; McCormack and Prendergast, 1999), though Jeffers et al (2007) also reported cracking at both the stem-cement and cement-bone interface. Where distal cement is present, distal punch-out occurs after a few thousand cycles (figure 2.35); a finite element model by Jeffers et al (2007) of the reconstructed femur under gait fatigue loading reported distal cement stresses approaching 30MPa, suggesting distal fracture is inevitable where no distal void is left. After this, damage continuously occurs in diffuse patterns, mainly in regions M2, D1 and D2 (figure 2.29; McCormack et al, 1996; McCormack and Prendergast, 1999). The damage patterns which develop are diffuse. There is evidence that both pre-load cracks and new cracks propagate at the same rate; this makes pre-load cracks especially deleterious, as they have longer to become through-cracks (McCormack and Prendergast, 1999). Lennon et al (2003) reported that short-term (< 2 million loading cycles) damage patterns were similar for both polished and grit-blasted stems, though a difference in damage patterns may become evident in longer tests. Jeffers et al (2007) reported far less short-term damage for bonded stems over unbonded stems.

In addition, Jeffers et al (2007) simulated the mechanical failure of the cement mantle in this configuration with a damage accumulation-based finite element model. They were able to account for some of the considerable variation in experimental specimens and simulate diffuse damage by modelling cement pores and the residual stress field. In one simulation, through-cracking was unexpectedly caused proximo-medially at 2 million cycles, due to a cluster of cement pores and the associated stress amplification (figure 2.35). This implies that the local stress concentration at pores makes them favourable sites for crack initiation and progression, especially if located at stress singularities caused by local geometry.

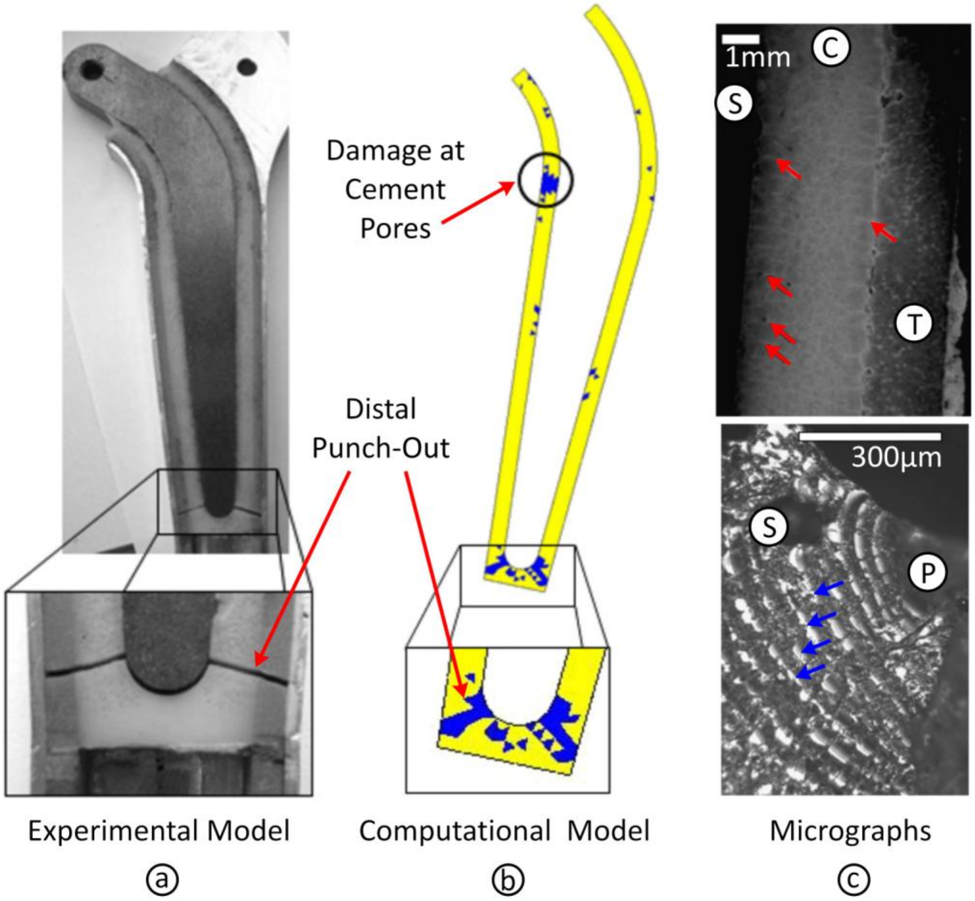

Figure 2.35: Experimental punch-out (a) and accurate damage accumulation simulation distally and at cement pores (b); pre-load cement micro-cracks (red arrows) and DGBs around a pore after fatigue failure (blue arrows) (c) (Jeffers et al, 2007. Cement (C), pores (P), the stem (S) and trabecular bone (T) are indicated.

This 2½D configuration does not include hoop or radial cement mantle stresses. In order to model these stresses, other authors have set stems in cylindrical cement mantles and recorded crack growth under torsional loading (figure 2.30; Hertzler et al, 2002; McCormack et al, 1999). In this case, cracks are found to initiate at the stem-cement interface, particularly at interfacial porosity (McCormack et al, 1999; Hertzler et al, 2002). The process was only unstable where there were pores at thin cement cross-sections. Otherwise, Hertzler et al (2002) reported the crack propagation rate to be independent of cement mantle thickness, inferring that a thin cement mantle is deleterious though since through-cracking occurs after fewer loading cycles.

A finite element study of the same configuration confirmed the stress concentration at the stem-cement interface (Janssen et al, 2005b). Using a computational damage accumulation method, Janssen et al (2005b) found pores to have a negligible effect on the fatigue failure process of the construct. This is probably because, for the configuration used, the high-stress region is sharply-defined by the stem geometry, and is very small; if a pore is not found in this region it has no effect. For a homogenous stress distribution, however, the highest stress will occur by a pore, so porosity causes huge variation in the performance of specimens (Jeffers et al, 2005). The reconstructed hip and multidirectional loading creates a complex stress distribution, meaning only pores located at stress singularities influence the cement failure process (Jeffers et al, 2007). Unfortunately, Janssen et al (2005b) did not confirm this idea by modelling pores at the stress singularity created by the stem.

Analyses of the whole reconstructed hip are more relevant to the in-vivo case, and help to determine if the findings of these simplified constructs are clinically relevant (Huiskes, 1993a). Race et al (2003) and Mann et al (2004a) assessed the condition of the Charnley Flanged (DePuy International Ltd, Leeds, UK) cement mantle in cadavers by sectioning after gait loading. These studies have revealed that crack growth rates are similar for thin and thick cement regions, and for pre-load and load-induced cracks, leading authors to cite the importance of pre-load cracks in thin cement regions (Race et al, 2003; Mann et al, 2004a). Through-cracking at pre-load cracks creates local stress amplification, and may allow osteolysis (Mann et al, 2004a). In contrast with other studies (Jasty et al, 1991), the majority of damage was found at the bone-cement interface, and few cracks were associated with cement pores (figure 2.36). This led the authors to postulate that the mechanical loosening process may be very different for different stem types and cementing techniques. In both of these analyses only 300,000 loading cycles were applied, so only the early damage mechanism was discerned.

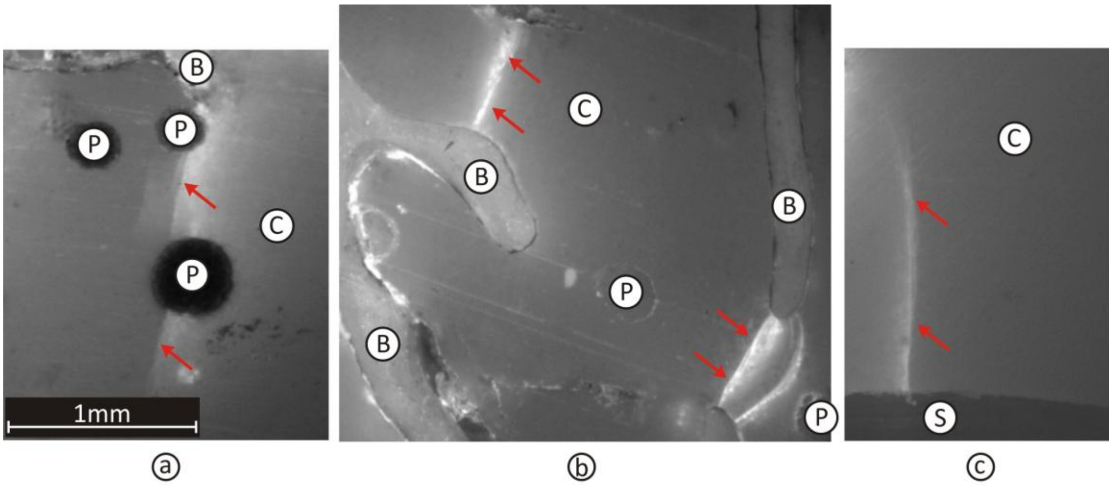

Figure 2.36: Cement damage in sections of an implanted cadaver after fatigue loading, showing cement damage initiation from trabeculae through pores (a); cement damage between trabeculae (b); and cement damage initiation at the stem-cement interface (c) (Race et al, 2003). B = bone, C = cement, P = pore, S = stem. Cracks are indicated with red arrows.

The research group at the University of Nijmegen have used the CDM computational damage accumulation method (section 2.4.2.1) in several analyses to reveal different failure patterns for different cemented femoral stems. Stolk et al (2003a) and Stolk et al (2004) simulated the mechanical failure of the cement mantle for Lubinus SPII and Mueller Curved femoral stems, with the method correctly identifying the Mueller Curved as the clinically inferior by determining the total number of ‘cracks’ in simulations. Stolk et al (2004) reported that damage and creep effects should be simulated in combination: creep relaxes high cement stresses, reducing the damage accumulation rate.

Using similar methods, other studies have assessed the impact of various factors on the long-term mechanical failure of the cement mantle. Verdonschot and Huiskes (1997a) found more cracks were formed for an unbonded stem-cement mantle than a bonded one for a given number of loading cycles. The bonded stem caused moderate damage at the lateral bone-cement interface, while an unbonded stem caused more damage along the stem-cement interface. Jeffers (2005) determined the effects of toggling cement creep, porosity and residual stresses on and off in fatigue simulations of the force-closed C-Stem (DePuy International, Leeds, UK). Porosity led to the development of diffuse damage seen by other authors, and had the most significant effect on the number of cycles required to achieve failure, followed by cement residual stress and creep respectively (Jeffers, 2005).

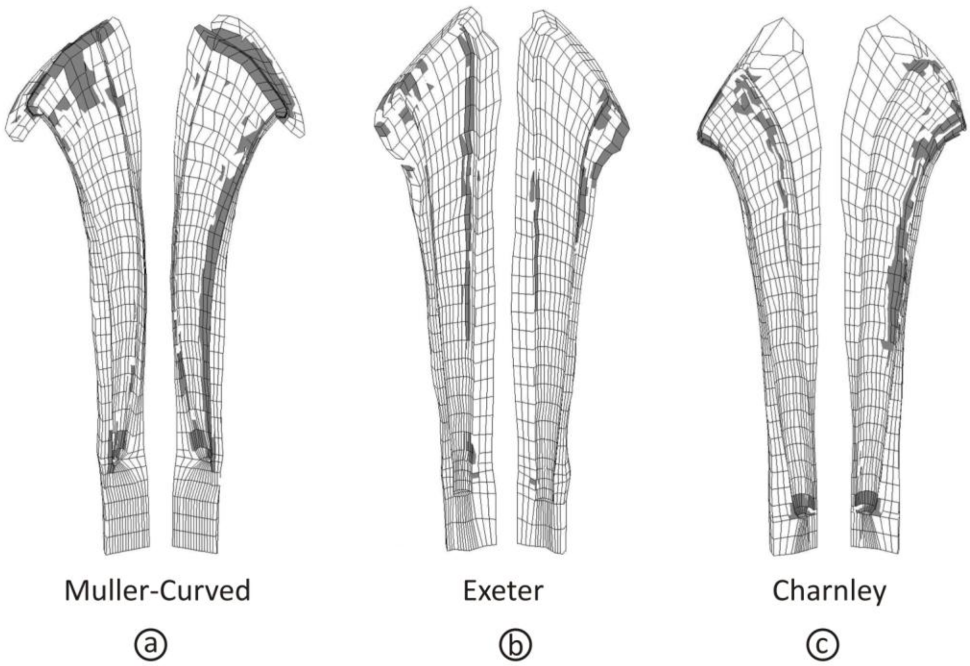

Figure 2.37: A comparison of simulated damage (grey) in the cement mantles of three different femoral stems after 20 million walking cycles (Stolk et al, 2007).

While computational methods have identified clinically representative damage patterns (Stolk et al, 2004; Jeffers, 2005; Stolk et al, 2007), they have not been able to adequately determine the number of cycles to achieve failure, despite the apparent accuracy of mechanical strain determination (Stolk et al, 2002). The reasons for this are not clear, though the under-prediction of fatigue lives may be because cement stresses are over-predicted at stress singularities (Stolk et al, 2003). It should also be remembered that biological processes also contribute to the aseptic loosening failure process, and have not been included so far.

The only existing preclinical test for cemented THA stem performance relates to fatigue failure of the stem (ISO 7206); it has been proposed that the computational technique described here can be used to diagnose the mechanical failure method for cemented arthroplasties, and via comparison with predicate devices with known clinical success, one may estimate the clinical performance of a new device (Stolk et al, 2004). To test this hypothesis, Stolk et al (2007) simulated the mechanical aspect of aseptic loosening in four different cemented stems. The method successfully predicted that an Exeter stem subsides without causing significant damage, while the collar on the Mueller-Curved prevents its subsidence at the cost of high proximal cement damage. Different damage patterns were predicted for different stem types (figure 2.37). By determining the total number of cracks, the stems were successfully ranked in order of their clinical success, confirming the value of this tool to predict the performance of novel hip stems.

2.4.4 Analyses of the Cemented Acetabular THA Component

The discrepancies between clinical theories of aseptic loosening in the cemented polyethylene acetabular components (section 2.2.8) reveals that the failure process is not well understood, with both mechanical and biological processes proposed (Schmalzried et al, 1992; Huiskes, 1993a; Wroblewski et al, 2004). The effects of biological parameters on cemented cup loosening have not been reported yet. Thus, this section will only consider analyses of the mechanical factors, though the reader should not forget that osteolysis and subchondral bone resorption appear to both contribute significantly to the failure scenario (Schmalzried et al, 1992). Compared to the femoral component, very few analyses have considered the acetabular component.

Zant et al (2007) represented the polyethylene-cement-bone structure in a simplified multi-layer experimental reconstruction, finding fatigue failure of the cement mantle due to radial stresses of the order of 9MPa. However, studies of polyethylene cups implanted in sawbone (Heaton-Adegbile et al, 2006) and dry bovine (figure 2.38; Tong et al, 2008; Wang et al, 2009) pelvises under multi-axial fatigue loading have demonstrated a different failure process. In all specimens, loosening occurred due to the failure of the bone-cement interface, beginning at the superior-posterior region and propagating towards the periphery. The failure of this interface is consistent with the failure mode documented in clinical literature, though the process may be different, since clinical analyses have reported cup-cement demarcation initially at the cup periphery, before propagation to the dome of the cup (Schmalzried et al, 1992). This difference may occur because biological loosening processes are not replicated in experimental tests. Tong et al (2008) applied various load cases to experimental specimens, recording cement-bone demarcation after 15 million loading cycles for normal walking loads, but after only 2.2 million cycles for stair descent loading. Wang et al (2009) simulated different patient weights, unsurprisingly finding significantly shorter survival for increased patient weight.

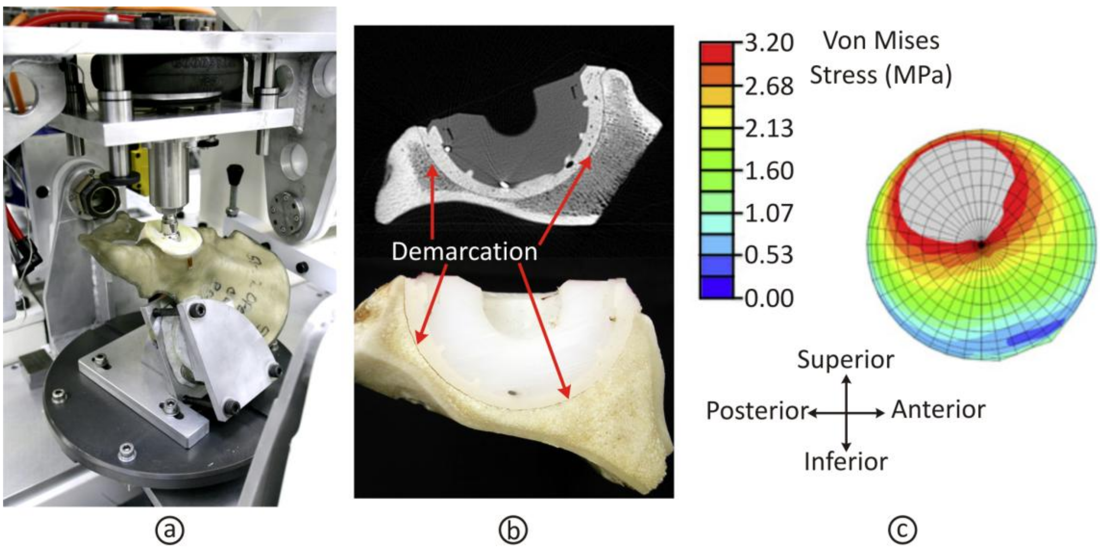

Figure 2.38: The hip simulator of Tong et al (2008) (a); cement-bone demarcation in a CT scan and a sectioned experimental specimen (b); the Von Mises stress distribution at the cement-bone interface (c) (Tong et al, 2008).

Tong et al (2008) used a static finite element model to evaluate stresses at the bone-cement interface, finding them to be approximately 3.8 MPa for normal walking, rising to 5.4 MPa for stair descent (figure 2.38). The location of peak stresses correlated with the location of demarcation initiation in experimental specimens. However, Janssen et al (2008) simulated mechanical failure of the acetabular cement mantle, predicting failure at the cup-cement interface due to the stiffness mis-match. This failure mode again differs from that observed clinically (Schmalzried et al, 1992; Garcia-Cimbrelo et al, 1997), though one should note that clinical methods rely on the use of radiographs, which may not be acceptable for indentifying lucency at the cup-cement interface (Reading et al, 1999). Also the low magnitude of predicted stresses relative to cement fatigue data (Murphy and Prendergast, 2001; Jeffers et al, 2005) suggest that failure is not solely mechanical. Thus, Tong et al (2008) suggest that a good cement-bone interface is preferable to a good cement mantle.

For computational studies, some authors have stressed the importance of using accurate pelvic geometries and location-based material properties to return accurate pelvis strain distributions (Dalstra et al, 1995; Anderson et al, 2006). Zannoni et al (1998) presented a method of determining the stiffness of cancellous bone from CT (computed tomography) scan voxel density values to achieve this. The mechanical properties determined for the pelvis have already been discussed (section 2.1.1) and are not repeated here. Additionally, by modelling local cortex thicknesses found in CT scans these authors have found superior strain predictions over uniform cortex thicknesses (Dalstra et al, 2005; Anderson et al, 2006).

While most models constrain the coxal bones at the sacro-iliac joint and pubis, Phillips et al (2007) also modelled both coxal bones and femurs, 42 muscles and 7 ligaments at the pelvis to observe differences in the stress state in cancellous and cortical bone (figure 2.39). For the second case, load transfer in the muscular and ligamentous model was significantly different with less stress concentration superior of the acetabulum. However, stresses at the acetabulum for both boundary condition sets were comparable, suggesting the fixed pelvis model is suitable for simulating the integrity of acetabular prostheses.

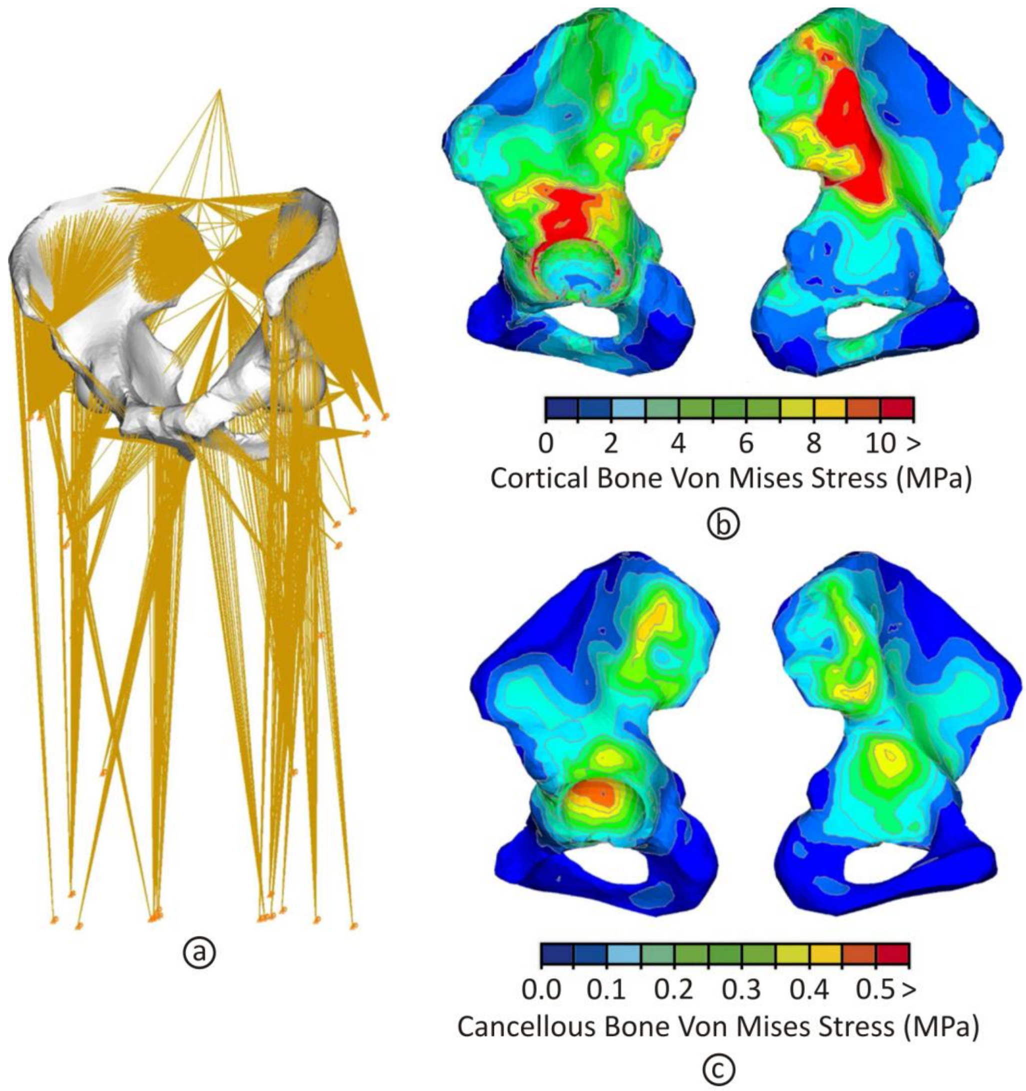

Figure 2.39: The muscular and ligamentous finite element model of Phillips et al (2007) (a); calculated cortical (b) and cancellous bone (c) Von Mises stress distributions in the natural hip.

2.5 OTHER TECHNIQUES RELEVANT TO THIS THESIS

This thesis uses several additional cutting-edge imaging and analysis techniques which required a significant level of technical understanding. These methods are outlined here.

2.5.1 Micro-Focus Computed and Synchrotron Scanning Tomography

Micro-focus computed tomography (μCT) and synchrotron scanning tomography were used by this author to form computational models of bone cement specimens, and to visualise cement damage in non-invasively. This section is contains a brief introduction of the key principles of using these techniques: for a more thorough discussion, the reader is directed to ASTM Standard E1441-00 (ASTM, 2000).

2.5.1.1 Micro-Focus Computed Tomography of Bone Cement

X-rays with a fine focus and low energy (10-100eV) may be generated in an X-ray tube. This is achieved by accelerating electrons from a wire cathode onto a focused spot on a metallic target (typically molybdenum or tungsten). Upon incidence, electron energy is lost to the target, producing heat and X-rays as a by-product. These X-rays may be directed through a subject and onto an X-ray sensitive camera, which produces an enlarged radiograph of the object. The degree of magnification is determined by the ratio of distances between the tube and the target, and the tube and the detector. Using this method, the optimum resolution achievable is less than 1 μm (Sasov and Van Dyck, 1998). As the X-rays pass through the subject, they are attenuated due to scattering and absorption effects. Where the subject is composed of several different materials, an X-ray attenuation map is generated.

Computed tomography takes this process one stage further, by acquiring multiple radiographs of the subject from multiple viewing angles. For engineering applications, this commonly involves fixing the radiation source and rotating the specimen about a fixed central axis (figure 2.40). After these radiographs are obtained, a suitable algorithm (e.g. filtered back-projection) enables the average attenuation at each discrete 3D location to be determined (figure 2.41). As more images are taken at more numerous viewing angles, the clearer the image becomes (Sasov and Dyck, 1998; ASTM, 2000).

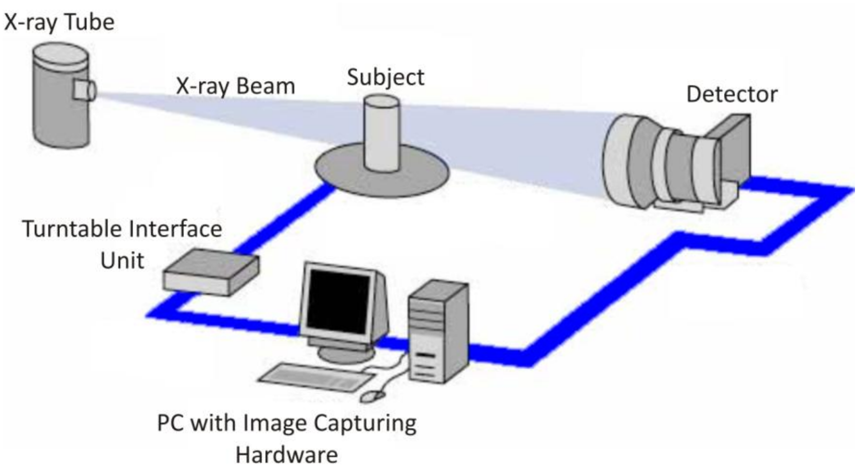

Figure 2.40: A schematic of a CT scanning system

Several authors have shown that aluminium, steel and bone cement may be differentiated in that µCT scans (Jeffers et al, 2007; Mavrogordato et al, 2008). Also, µCT scanning has been used to reveal the microstructure of bone cement, differentiating between cement, pores, pre-polymerised beads, and $BaSO_4$ agglomerates (Jeffers et al, 2007; Sinnett-Jones, 2007). Since the maximum resolution achieved in these studies is 1 µm, individual $BaSO_4$ particles and cement cracks may not be discernable in scans (Sinnett-Jones, 2007).

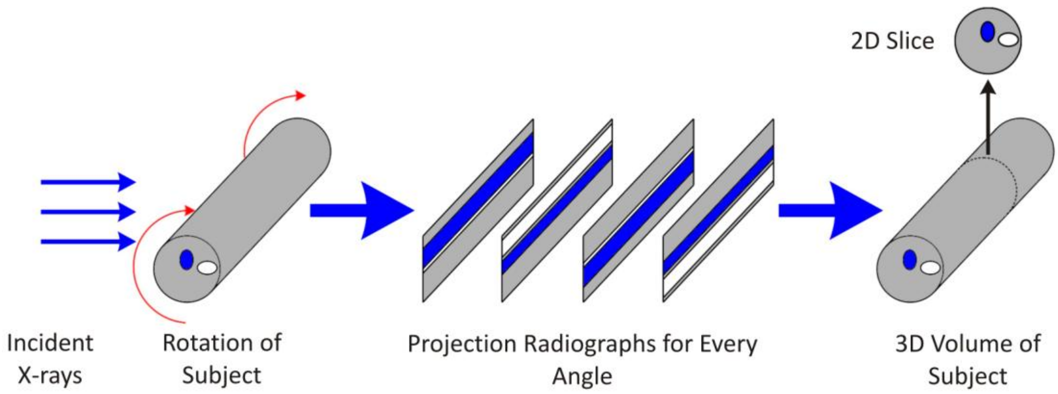

Figure 2.41: Data manipulation to produce a 3D volume of a specimen from a series of radiographs taken at different viewing angles of the subject.

2.5.1.2 Synchrotron Tomography of Bone Cement

To obtain images of finer resolution than μCT, an intense source of short-wavelength X-rays is required. Such radiation may be generated in a synchrotron (figure 2.42), allowing a resolution of lower than 100 nm to be achieved (ESRF, 2008). Within a synchrotron, X-ray radiation is generated from a beam of electrons, which are evaporated from the cathode of an electron gun by thermionic emission. These liberated electrons are accelerated by a linear accelerator and further by a booster synchrotron until the beam is stable enough for release into the storage ring (figure 2.42). The electron beam within the storage ring has an energy between 0.5 and 7000 TeV; in practice high beam energies may only be achieved with a very large radius accelerator, such as the Large Hadron Collider in Switzerland (DLS, 2009).

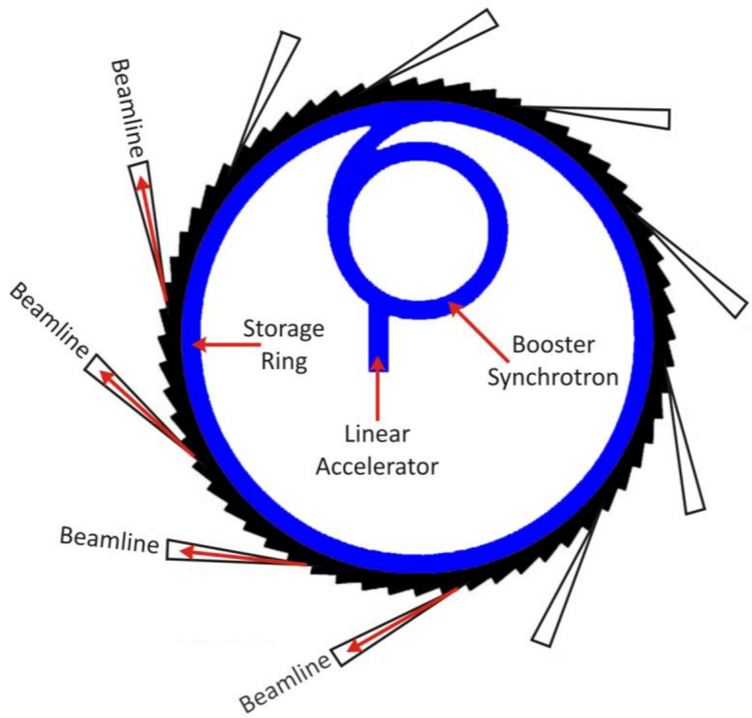

Figure 2.42: A schematic of a synchrotron (ESRF, 2008).

The storage ring is not a true circle, but a polygon, made of straight sections angled together with bending magnets. These bending magnets are used to steer the electrons around the ring. They circulate around the storage ring in a near-vacuum to minimise energy loss to collision with air molecules. As electrons travel around the storage ring at very high speed, they emit synchrotron light. This light can be channelled out of the storage ring wall and into the experimental stations called beamlines, by using bending magnets. Within the beamline, light is filtered and focussed, before being directed onto specimens for tomographic analysis (ESRF, 2008).

Synchrotron tomography has been previously used to visualise the microstructure of bone cement, and to identify non-catastrophic fatigue cracks in specimens (Sinnett-Jones et al, 2005).

2.5.2 Acoustic Emission Monitoring

The experimental assessment of simple and complex cement configurations has already been discussed in section 2.4.1. Most require visual inspection, and have the limitations that the cement mantle must be exposed, that only surface damage may be traced, or that tests must be paused to measure damage. Acoustic emission monitoring enables the mechanical failure process to be followed non-invasively throughout specimens in real-time (Browne et al, 2005). A significant limitation of this technique, however, is the difficulty in verifying the sources of emissions. A brief overview of the technique, the equipment required, and the design of suitable tests now follows. This is not intended to be an exhaustive discussion of the method: those interested in understanding more are directed to the publications of Beattie (1983) and Kohn (1995).

2.5.2.1 Acoustic Emissions

Acoustic emissions can be defined as oscillating strain waves moving within a body (Beattie, 1983). At an atomic level, they comprise the deflection of atoms from their equilibrium point as kinetic energy is transferred within a specimen. Acoustic emissions may be detected within a substrate using piezoelectric sensors. The piezoelectric effect describes a material which generates charge under applied strain, and vice-versa. When firmly attached to the substrate a piezoelectric sensor undergoes microscopic strain due to an incident acoustic emission. The output of such sensors can be used to determine various parameters of the emission (figure 2.43). This thesis considers acoustic emissions released during fracture events within specimens. Strain waves released from different types of fracture events posses different characteristics; by recording these characteristics for all emissions, researchers may determine the evolution of failure in specimens in real time (Beattie, 1983).

A typical response from an acoustic emission sensor is given in figure 2.43. The threshold voltage, marking the amplitude level above which emissions are recorded, is also plotted. The wave parameters highlighted in the figure are defined below:

Peak amplitude: The maximum amplitude of the waveform.

Rise time: The time between the first threshold crossing and peak amplitude.

Ring down counts: The number of times the signal exceeds the threshold level.

Duration: The time between the first and last threshold crossings

Energy: The energy of the emission (area between the waveform and time-axis).

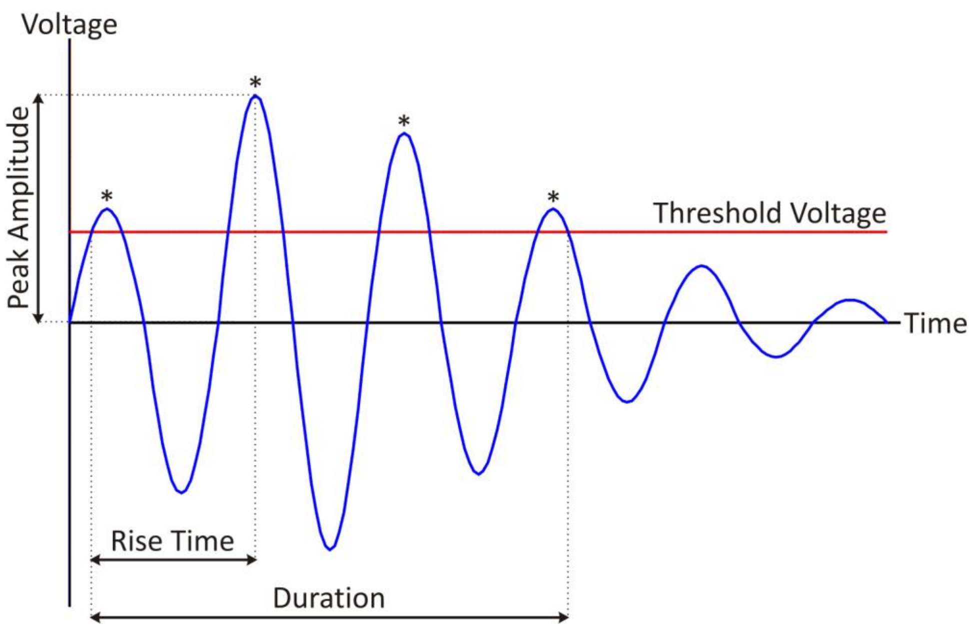

Figure 2.43: The parameters of a typical acoustic emission sensor response to an incident emission; ring down counts are indicated with * (Roques et al, 2004).

2.5.2.2 The Acoustic Emission Monitoring System

The main requirements for a simple AE system are given in figure 2.44. In practice, the magnitude of the output signals from piezoelectric sensors is small, so they must be amplified to reduce IR losses. The pre-amplifier typically includes a frequency-based filter for noise rejection. The signal is recorded and converted into a digital electronic data set by the event detector. As already mentioned, the event detector has a front-end threshold filter, again to remove extraneous noise signals. Later, a computer is used to manipulate the data.

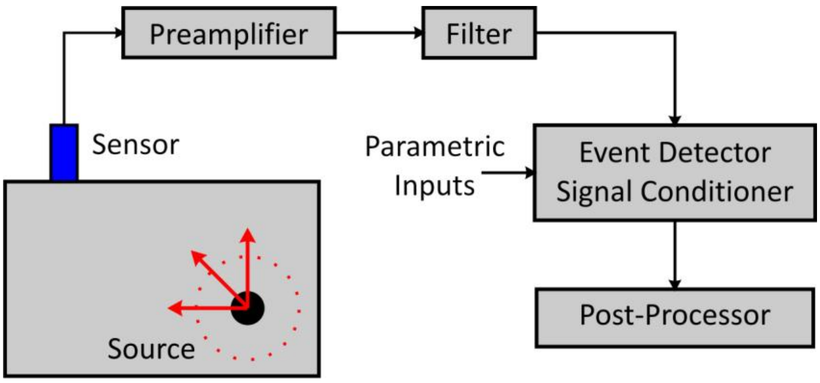

Figure 2.44: The components of a basic acoustic emission monitoring system.

The following factors must also be determined to define an acoustic emission:

Hit Definition Time - the time after the last crossing of the threshold after which an emission is declared as finished.

Hit Lockout Time - the time after a previous event before the acquisition system re-arms to record the next event.

Peak Definition Time - the time within which the system identifies a signal peak.

2.5.2.3 Locating Acoustic Emission Sources

The relative location of AE sources can be determined using a multiple sensor array. At least two sensors are required for linear-based location (figure 2.45), three for area-based location and four for volume-based (Beattie, 1983). In figure 2.45, the distance between the emission source and sensor 2 (d_2, m) is determined by considering the distance between sensors (d, m), the times at which the emissions were received by each sensor (t_1 and t_2, s), and the speed of sound in the substrate (V, m/s) (equation 13). The accuracy of source location is limited by the physical size of sensors (usually a few mm), though tests in bone cement have shown that accuracy of as low as 0.4mm is attainable, depending upon the sensor array (Browne et al, 2005).

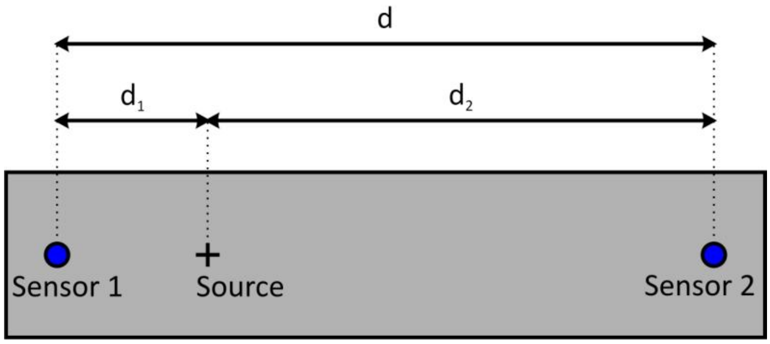

Figure 2.45: The linear location of acoustic emissions.

$$d_2 = \frac{V(t_2 - t_1) + d}{2} \qquad \text{Equation 13}$$

As waves propagate in a three-dimensional body, the expansion of the wave-front means the energy of the wave decreases proportionally to the square of the distance from the source. In practice, emission energy is also lost to dissipative and scattering mechanisms in inhomogeneous bodies (Beattie, 1983). Prior to testing, the wave attenuation, the accuracy of source location, the speed of sound in the medium and the attachment of sensors should be checked with a pencil-lead break test (BS EN 1330-9, 2000). Roques (2003) reported the speed of sound in vacuum-mixed CMW-1 bone cement to be 3000 m/s, and recorded an attenuation of 2dB/cm.

2.5.2.4 Analyses of Bone Cement using Acoustic Emission Monitoring

Several authors have used AE to monitor the accumulation of cement damage in dog-bone shaped bone cement specimens under fatigue loading (Roques et al, 2004b; Jeffers et al, 2005; Sinnett-Jones, 2007). These authors have recorded a discontinuous damage accumulation process under fatigue loading, which may represent the craze failure method observed by other authors (section 2.3.6.4).

Using high-load boundary conditions, Roques et al (2004b) related durations exceeding 200 μs to crack propagation events. In a uni-axial fatigue study, Jeffers et al (2005) identified an increasing rate of emission generation during tests, relating this to the study of Murphy and Prendergast (2001), who identified an increasing rate of crack propagation during fatigue loading of comparable radiolucent specimens. Crack propagation was also recorded early in high-load tests (>15MPa), showing that some cement damage can be maintained without catastrophic failure. As damage progresses, events of higher duration and energy were detected, allowing Jeffers et al (2005) to predict imminent specimen failure. Sinnett-Jones (2007) matched significant AE data to cement pore locations, and found evidence of associated cement cracking upon sectioning and microscopy. These observations show that AE has an application for determining critical and non-critical damage in cement specimens.

Acoustic emission monitoring has also been used in full cement mantle configurations. Roques et al (2004a) and Browne et al (2005) recorded emissions characteristic of cement cracking in polymerising bone cement, while Mavrogordato et al (2008) confirmed this phenomenon by matching AE data with cement damage on dye-penetrant μCT scans. Acoustic emission sensors have even been used to identify radiolucent femoral hip stems in clinical patients (Kohn, 1995). Despite this progress however, there is still much to be done with regards to distinguishing between different types of emissions, understanding the effects of interfaces, rejecting noise, and reducing sensor size to improve emission source location in such studies (Qi et al, 2004).

3 ACCOUNTING FOR DEFECTS ALLOWS THE PREDICTION OF TENSILE FATIGUE LIFE OF BONE CEMENT

3.1 INTRODUCTION

The dominant cause of failure in cemented total hip arthroplasty (THA) is aseptic loosening of the prosthesis (Furnes et al, 2007; Karrholm et al, 2008). The failure of stem-cement interface and subsequent crack initiation and propagation in the cement mantle are understood to be critical stages in the failure of femoral prostheses. Stress shielding, osteolysis and stem micro-motion may all contribute to the loss of bony support to the implant and the accumulation of damage in the cement mantle, prior to gross loosening of the implant (Jasty et al, 1991; Kawate et al, 1998; Schmalzried and Callaghan, 1999). For the acetabular component, osteolysis appears to be the dominant cause of failure at the cement-bone interface, although mechanical effects may also contribute to gross loosening at this interface (Schmalzried et al, 1992; Wroblewski et al, 2009b).

Numerous studies have commented on the highly-variable mechanical properties of bone cements, with many authors identifying porosity as the key driver (Lewis, 1999; Murphy and Prendergast, 2000; Dunne and Orr, 2001; Lewis, 2003; Dunne et al, 2003). The introduction of modern cementing techniques has been shown to reduce porosity in bone cement (Lewis, 2003). However, is has been reported that the improved mechanical properties due to porosity reduction are far more apparent in nominal dog-bone-shaped cement specimens subjected to uni-axial loading than the cement mantle in vivo (Janssen et al, 2005b). This is because the geometry of the cement mantle in cemented THA creates a highly inhomogeneous stress distribution, due to stress singularities generated at the prosthesis and bone: such singularities are believed overwhelm the effect of individual pores (Janssen et al, 2005b), unless the pores themselves are present at a stress singularity (Jeffers et al, 2007). The effect of radiopaque barium sulphate ($BaSO_4$) agglomerates on the longevity of the cement mantle has received little attention, though they are believed to act as crack initiation sites, and form favourable paths for crack propagation (Topoleski et al, 1993; Sinnett-Jones et al, 2005).

Novel experimental methods are required to elucidate the fatigue failure process in bone cement in real-time. Other researchers have used dye penetrant to track the propagation of fatigue cracks (Murphy and Prendergast, 2001), but this method has the disadvantage that the test must be stopped for analysis, and only surface damage may be detected. Acoustic emission (AE) monitoring is a viable technique for detecting fatigue in bone cement, as damage throughout the specimen can be monitored continuously and non-invasively in real time (Browne et al, 2005), and a change in nature of damage may be detected as the characteristics of emissions change during a test (Jeffers et al, 2005).

Experimental characterisation of bone cement is required to drive computational simulations of cement performance. In simulations of two different prostheses, Stolk et al (2004) used a continuum damage mechanics (CDM) damage accumulation method to identify the clinically inferior of two THA stems. However, a much shorter component life was predicted than was measured experimentally. Another theoretical study (Jeffers, 2005) found that porosity influenced the stress distribution and damage patterns in the cement mantle, facilitating the growth of through-cracks, due to highly-localised peak stresses. Damage was particularly prevalent at clusters of pores. Again, the time-scale to failure was much shorter than that seen in vivo.

There were several aims to this study. The first was to provide quantitative data concerning the size and quantity of pores and $BaSO_4$ agglomerates in dog-bone-shaped specimens of bone cement. The second was to import defect geometries into finite element simulations of bone cement from micro-computed-tomography (µCT) scans, to see if the degree of variability in fatigue performance seen in vitro could be reproduced computationally. This was achieved by conducting experimental uni-axial tension fatigue tests in corresponding specimens. Finally, this chapter aimed to assess whether the simulations could predict the fatigue life of specimens, and whether the simulated damage accumulation patterns corresponded to those seen experimentally.

3.2 MATERIALS AND METHODS

3.2.1 Specimen Preparation

16 dog-bone shaped specimens (figure 3.1) were formed by injecting CMW-1 radiopaque bone cement (DePuy CMW, Blackpool, UK) into polyethylene moulds at 23 ± 1 °C. Vacuum mixing was performed using VacuMix vacuum mixing apparatus (DePuy CMW, Blackpool, UK), with 100 seconds allowed between first monomer-polymer contact until injection into a polyethylene mould. After injection, the top of the mould was covered in a polyethylene sheet, before the whole construct was clamped rigidly between external steel plates. Specimens were left to cure for two hours before specimens were aged for 18 to 30 days in Ringer's solution at 37°C prior to testing (Jeffers et al, 2005). Excess flash was removed from specimens using polishing paper, but no other surface finishing was administered, as this would remove surface porosity from specimens which may be relevant in vivo (Lewis, 2003). Specimens which failed to fill the mould were discarded, but all others were included in testing, regardless of porosity, to capture the true variation of cement conditions in vivo.

3.2.2 Micro Computed Tomography (μCT) Scanning and Segmentation

Prior to experimental testing, specimens were scanned by μCT (Benchtop Scanner, X-Tek Systems Ltd., Tring, UK). The volume scanned was 5 mm x 50 mm x 15 mm, located at the mid-span of specimens, at a voxel resolution of 90 μm. μCT scans were first vertically orientated using VGStudio Max 1.2 (Volume Graphics GmbH, Heidelberg, Germany), then imported into Amira 3.1 (ZIB, Berlin, Germany). Voxels relating to cement, $BaSO_4$ and pores were segmented based on grey-scale values, and converted into a tetrahedral mesh.

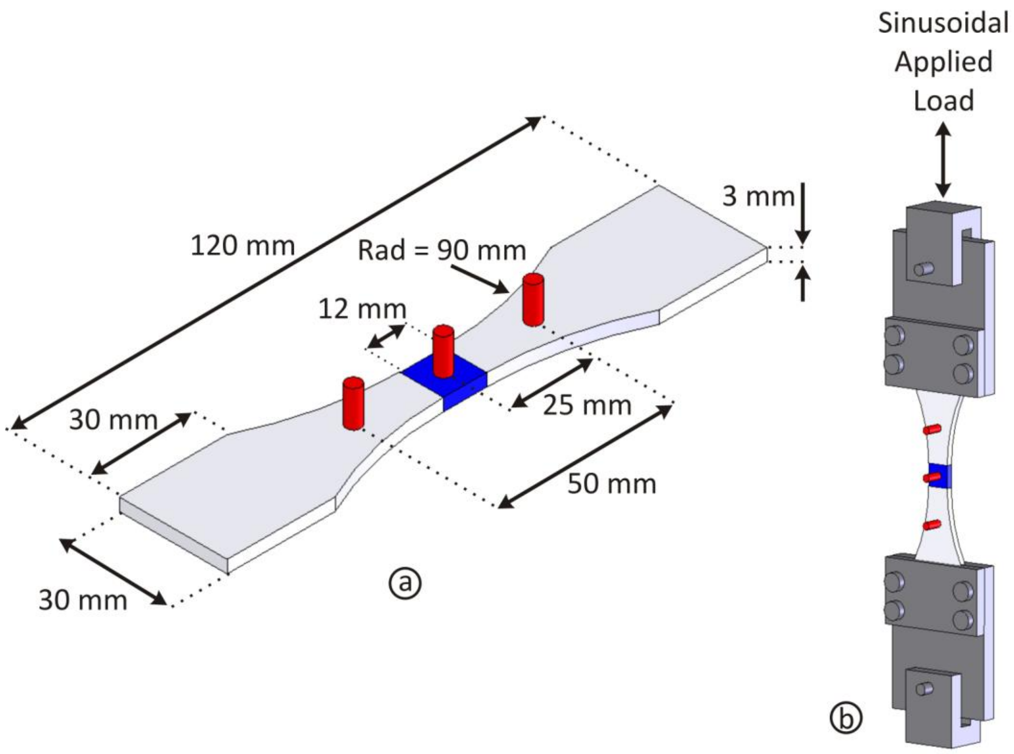

Figure 3.1: Specimen geometry (a) highlighting the gauge length (blue) and AE sensors (red). The width of the gauge length is 12 mm. The test configuration is also shown (b).

3.2.3 Acoustic Emission Monitoring

Although one-dimensional emission location only requires a minimum of two sensors, three Z-Series miniature sensors (Vallen Systeme GmbH, Munich, Germany) were used in a linear set-up (figure 3.1), to overcome signal attenuation effects noted when using two sensors in this polymeric material (Jeffers et al, 2005). To allow good transfer of acoustic emissions from specimens, sensors were attached with clear silicone rubber compound (RS Components, Corby, UK). Signals were preamplified by 40 dB and band-pass filtered outside the range of 100 kHz to 1 MHz. Signals were recorded and analysed using an AMSY4 PC-based data acquisition system (Vallen Systeme GmbH). Where AE were located by more than one sensor, the first threshold crossing method was used to determine emission location (Beattie, 1983), giving a measured accuracy of location of approximately 2.5 mm. These AE are referred to as ‘hits’. For an event occurring between two sensors, numbered one and two, the distance of the source from sensor two (b) was computed from the velocity of the wave in the medium (V), the time of detection at each sensor (t_1 and t_2), and the distance between the sensors (d), using equation 3.1.

$$b = \frac{V(t_2 - t_1) + d}{2} \qquad \text{Equation 3.1}$$

Extraneous noise was excluded from detection by setting a suitable threshold as a front-end filter of the AE instrumentation. A screening test revealed the test rig generated acoustic activity of up to 32 dB, so the threshold was set at 40 dB. Before tests, the peak amplitude response of sensors was checked with two Hsu-Nielsen (pencil lead break) source tests (BS, 2000) located equidistantly between the sensors; if the emission amplitude was below 90dB, it was considered that sensors may be defective or poorly attached to the substrate. Hsu-Nielsen sources also confirmed that the speed of sound through the specimens was 3000 mm/ms. For events passing the front-end threshold filter, the amplitude, duration, and time of emission detection were recorded (Roques et al, 2004b).

3.2.4 Experimental Testing

Testing was conducted on an Instron 8874 servohydraulic testing machine, equipped with an environmental chamber, containing distilled water at 37°C. Specimens were clamped in custom-made grips, and coupled to the machine via a pin linkage system to ensure pure tensile loading (figure 3.1). Specimens were loaded in uni-axial tensile fatigue at peak stresses of 20 MPa (6 specimens), 15 MPa (6 specimens), 11 MPa (3 specimens) and 7 MPa (1 specimen). These applied loads correspond to the range in peak tensile stresses found in simulations of cement mantle fatigue under walking load (Stolk et al, 2004). An R-ratio (ratio of minimum to maximum load) of 0.1 was used to reflect the ratio of maximum and minimum loads seen *in vivo* during gait (Bergmann et al, 2001). Loading was sinusoidal, at a frequency of 5Hz. Where specimen fatigue life exceeded 3 million cycles (approximately 7 days testing), tests were terminated.

3.2.5 Computational Model

Computational models contained cement, pore and $BaSO_4$ regions from segmented µCT scans. Only regions corresponding to volumes larger than the resolution of µCT scans (90 µm) were captured: distributed $BaSO_4$ particles were not modelled. It has been shown that a fine distribution of $BaSO_4$ powder may improve the fatigue performance of bone cement (Lewis, 2003; Ginebra et al, 2002; Molino and Topoleski, 1996). However, less is known about the effects of agglomerates (large, unmixed clusters) of $BaSO_4$ powder. Large agglomerates of radiopacifier powder left after mixing are reported to be deleterious to fatigue performance, sometimes leading to catastrophic failure, as they create stress concentrations and crack initiation sites (Jeffers et al, 2005; Kurtz et al, 2005; Harper and Bonfield, 2000). However, Sinnett-Jones (2007) observed crack growth through $BaSO_4$ agglomerates in fatigue tests, concluding that while individual particles in agglomerates appear to be poorly bonded, cracking through agglomerates was possible due to residual stresses in the surrounding matrix created during polymerisation.

To evaluate the effect of $BaSO_4$ agglomerate mechanical properties on the longevity of specimens, they were modelled in four different methods:

A: By deleting $BaSO_4$ elements from specimens; this is analogous to the theory that because particles are poorly bonded, agglomerates offer the structure no mechanical integrity.

B: By modelling $BaSO_4$ agglomerates with an arbitrarily-chosen elastic modulus of one tenth of that of bone cement.

C: By assuming that $BaSO_4$ agglomerates have the same mechanical properties as the surrounding bone cement, thus do not act as stress raisers.

D: By modelling $BaSO_4$ agglomerates with an arbitrarily-chosen elastic modulus of ten times that of bone cement, meaning they have a reinforcing effect.

Material properties for all materials in these four types of analysis are given in table 3.1. It was anticipated that a comparison between experimental and computational results would reveal the most appropriate method of computationally modelling $BaSO_4$ agglomerates. Fatigue simulations were conducted in MSC MARC 2005 (MSC Software Corporation, Santa Ana, USA). Cement was meshed with first-order tetrahedral elements of an edge length of approximately 1mm, while better-definition was ensured around internal defects by using an edge mesh length between 0.2 mm and 0.1 mm (figure 3.2). Mesh dependency tests of 6 different mesh sizes showed that doubling the number of elements altered the predicted fatigue life by 3.8%, justifying the ability of the chosen mesh size to compute an accurate solution. An elastic foundation method was chosen to model the boundary condition at the un-modelled distal end of the specimen; this effectively modelled the rest of the specimen as a distributed spring with the same stiffness as bulk cement. Loads were applied to a distant node attached to proximal end by nodal ties, which represented the proximal end of the specimen (figure 3.2).

Material Property	Cement	$BaSO_4$ (A)	$BaSO_4$ (B)	$BaSO_4$ (C)	$BaSO_4$ (D)
Elastic Modulus (MPa)	2800	Deleted	280	2800	28000
Poisson's Ratio	0.3	Deleted	0.3	0.3	0.3
Shear Modulus (MPa)	1077	Deleted	1077	1077	1077

Table 3.1: Mechanical properties of materials simulated (Harper and Bonfield, 2000; Roques, 2003).

Damage was simulated in finite element models of uni-axial tensile fatigue specimens using the CDM approach originally outlined by Verdonschot and Huiskes (1997a). A damage scalar, d, was allocated to all elements, which was initially zero, and accumulated during simulations. Tests were simulated iteratively, with each iteration representing between 500 and tens of thousands of loading cycles (ΔN), depending on the highest stress (σ, MPa) in all elements. From the stress in each element, the number of cycles to failure (N_F) was calculated using S-N data. Since cement defects were directly modelled, a theoretically pore-free S-N curve (equation 3.2) was adopted.

$$\mathrm{Log}(N_F) = \frac{(78.38 - \sigma)}{11.22}$$ Equation 3.2 (Jeffers, 2005)

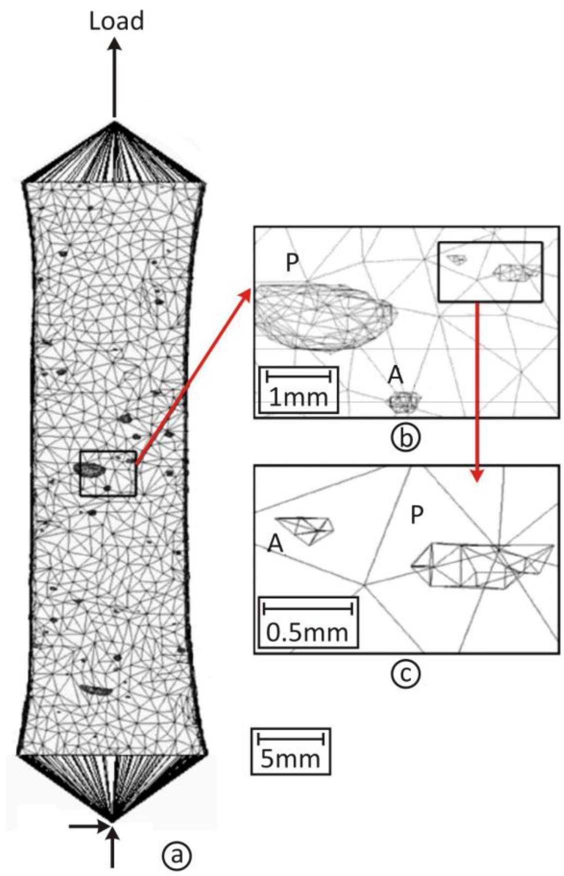

Figure 3.2: Finite element meshes formed in Amira 3.1, showing the relative edge lengths of the cement, pore (P) and $BaSO_4$ agglomerate (A) elements. The boundary conditions are also shown (a), with a linked elastic foundation at the base of specimens, and loading applied to one node linked to the specimen by nodal ties.

The linear Palmgren-Miner rule (equation 3.3) was used identify the fraction of fatigue life spent by each element in an iteration (ΔD). This fraction was then summed with that from previous iterations to give a scalar total damage, D, for the element. Elements were identified as ‘critically damaged’ when the damage scalar exceeded 0.9. Crack propagation was simulated by reducing the elastic modulus for critically damaged elements from 2.8GPa to 28 MPa. This marked the end of the iteration. Creep effects were not included in simulations.

$$\Delta D = \frac{\Delta N}{N_F} \qquad \text{Equation 3.3}$$

It took many loading cycles for any damage to initiate: however, thereafter damage was found to accumulate rapidly in adjacent elements. This phenomenon meant that the specimen load-end deflection remained consistent until failure was imminent, when a sharp rise in deflection occurred. This allowed the failure of computational specimens to be defined as when the load-end deflection increased by one tenth of the undamaged deflection (figure 3.3). Four specimens failed outside the μCT scanned volume, meaning their failure could not be traced back to internal defects, so simulations were not conducted for these specimens.

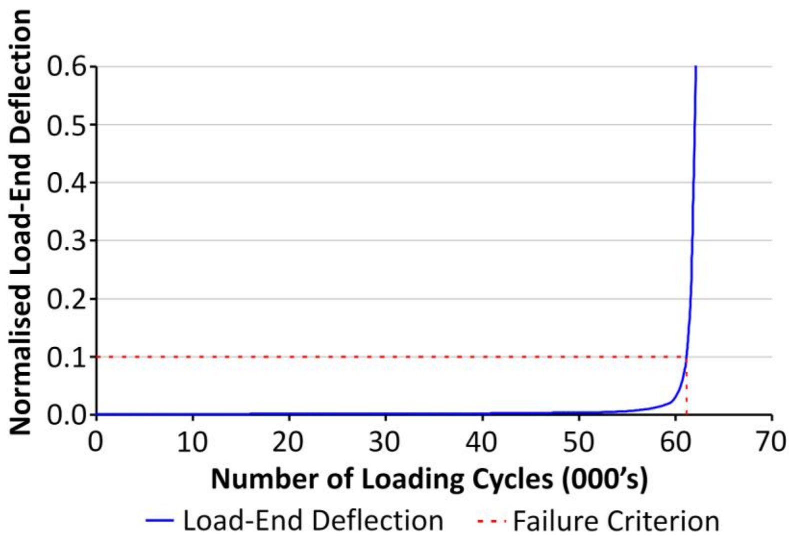

Figure 3.3: Normalised load-end deflection of specimens with increasing number of fatigue cycles. The failure criterion of 0.1 is highlighted.

3.3 RESULTS

3.3.1 Defect Populations in µCT Scans

In total, 1544 defects were found in the 16 specimens: an average of 1.62×10^{-3} pores per mm^3 (standard deviation = 3.14×10^{-3}) and 4.46×10^{-2} $BaSO_4$ agglomerates per mm^3 (standard deviation = 4.92×10^{-2}) of bone cement. A histogram of pore and $BaSO_4$ agglomerate volumes is given in figure 3.4, showing the distribution of defect sizes is not normal. The median pore volume was 8.26×10^{-3} mm^3 (maximum = 16.62 mm^3), whilst the median $BaSO_4$ agglomerate volume was 2.32×10^{-2} mm^3 (maximum = 0.69 mm^3). The smallest pore and $BaSO_4$ agglomerate sizes were limited by the voxel size (0.0003 mm^3). Approximately 13% of pores had a volume larger than 0.7 mm^3, which represents a reduction of 9% or greater of the load-bearing cross-sectional area if found in the gauge length (figure 3.4). Pores of this volume were found on the fracture surfaces of 5 specimens. This data pertains to internal defects, so does not include the porosity seen along the sides of specimens, resulting from the constraint of the mould.

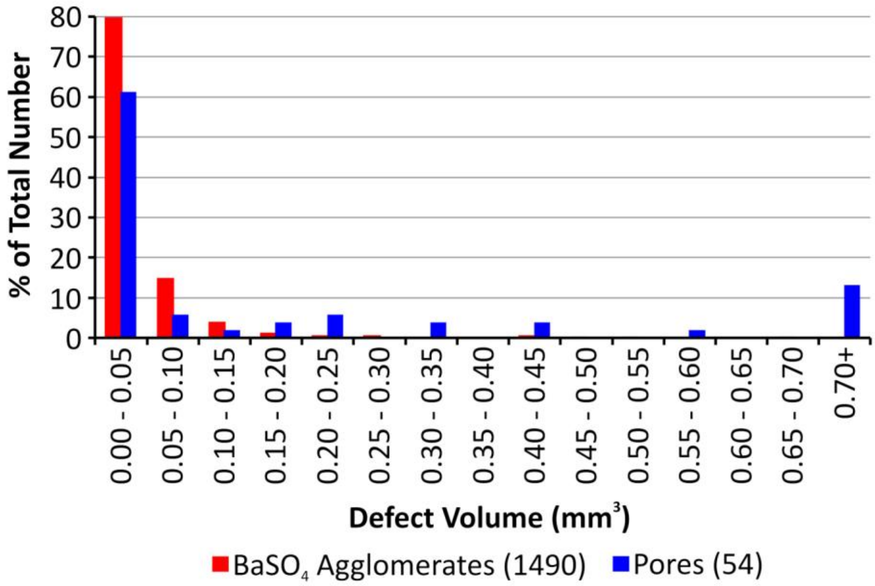

Figure 3.4: The occurrence of $BaSO_4$ agglomerates and pores in 16 specimens of average volume 2.09 $\times 10^{-6}$ m^3.

3.3.2 Experimentally Measured Fatigue Life and Fracture Surfaces

The experimental results were characterised by large variations in fatigue life, at all stress levels (figure 3.5). As has been previously reported (Roques et al, 2004b), AE plots generally showed that damage accumulation occurs in multiple locations, and was discontinuous in time, before sudden failure occurred in a location which may have seen very little AE previously (figure 3.6). Failure was always characterised by several high-energy events.

$BaSO_4$ agglomerates were found on the fracture surfaces of five specimens, whilst pores were found on the fracture surfaces of a further five specimens. In the remaining specimens, failure could not be traced back to specific internal defects There was no correlation between the type of defect found on the fracture surface, and the specimen fatigue life (see full results table in Chapter 11, Appendix B).

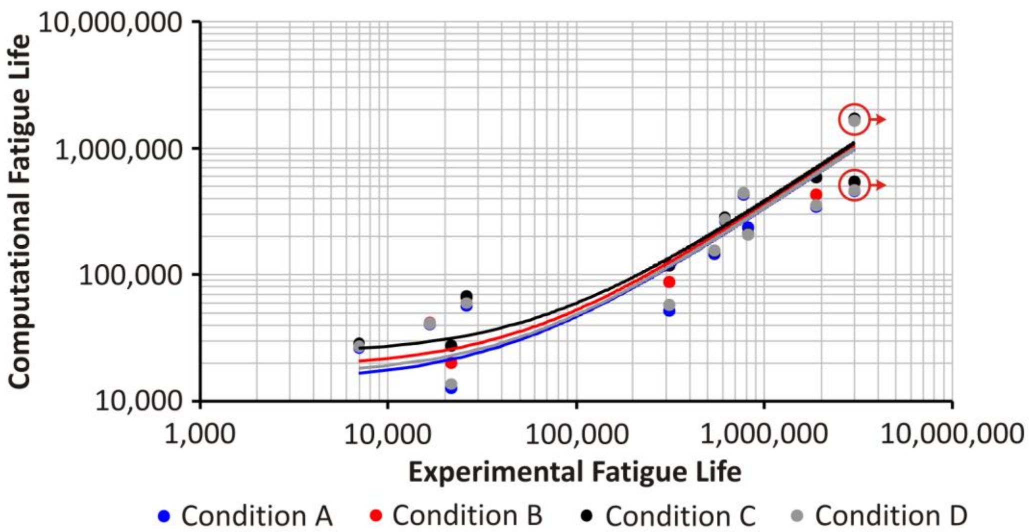

Figure 3.5: A comparison of specimen fatigue life from experimental tests and computational simulations. Linear trendlines are shown for the four $BaSO_4$ conditions. Where applicable, experimental tests were terminated at three million cycles: these results are circled in red on the figure.

3.3.3 Predicted Fatigue Life

A comparison between experimental and computational fatigue life, for all four methods of modelling $BaSO_4$ agglomerates, is given in figure 3.5 and Chapter 11 (Appendix B). The best correlation between computational and experimental results was found when $BaSO_4$ agglomerates were modelled with the same mechanical properties as bone cement (condition C; linear R^2 = 0.7, p=0.0252). The model appears to over-predict the fatigue lives of specimens at the highest stress levels, but under-predict at low stress levels. A paired T-test showed that changing the stiffness of $BaSO_4$ in simulations did not have a significant effect on the fatigue life of specimens to a level of p=0.05. The most significant effect was when $BaSO_4$ elements were deleted (p=0.0604).

3.3.4 Comparison of Predicted and Measured Damage Zones

In computational simulations, the failure zone was considered to be accurately predicted if it occurred within 2.5 mm of the experimental failure site. Of the 12 specimens considered, the failure location was only correctly identified in four simulations (figure 3.6; Chapter 11, Appendix B). In five other cases, significant damage was predicted in multiple locations, including the area of failure, even though failure was predicted in another location (figure 3.7). In the majority of examples, the simulations were able to locate several areas where acoustic emissions were generated.

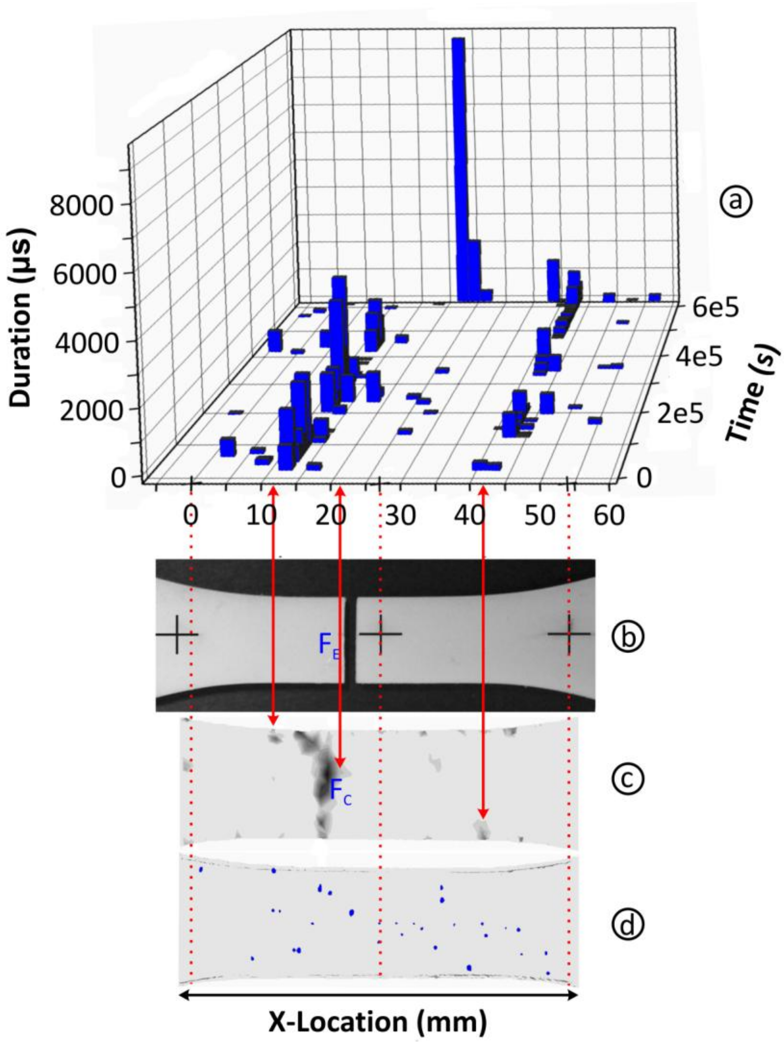

Figure 3.6: A comparison of AE location (a), specimen failure location (b), computational damage location (darker areas represent higher damage) (c) and the specimen defect field (d). All defects seen in (d) are $BaSO_4$ agglomerates. The experimental and computational failure locations (F_E and F_C) have been identified between three $BaSO_4$ agglomerates. Condition C was used when modelling $BaSO_4$.

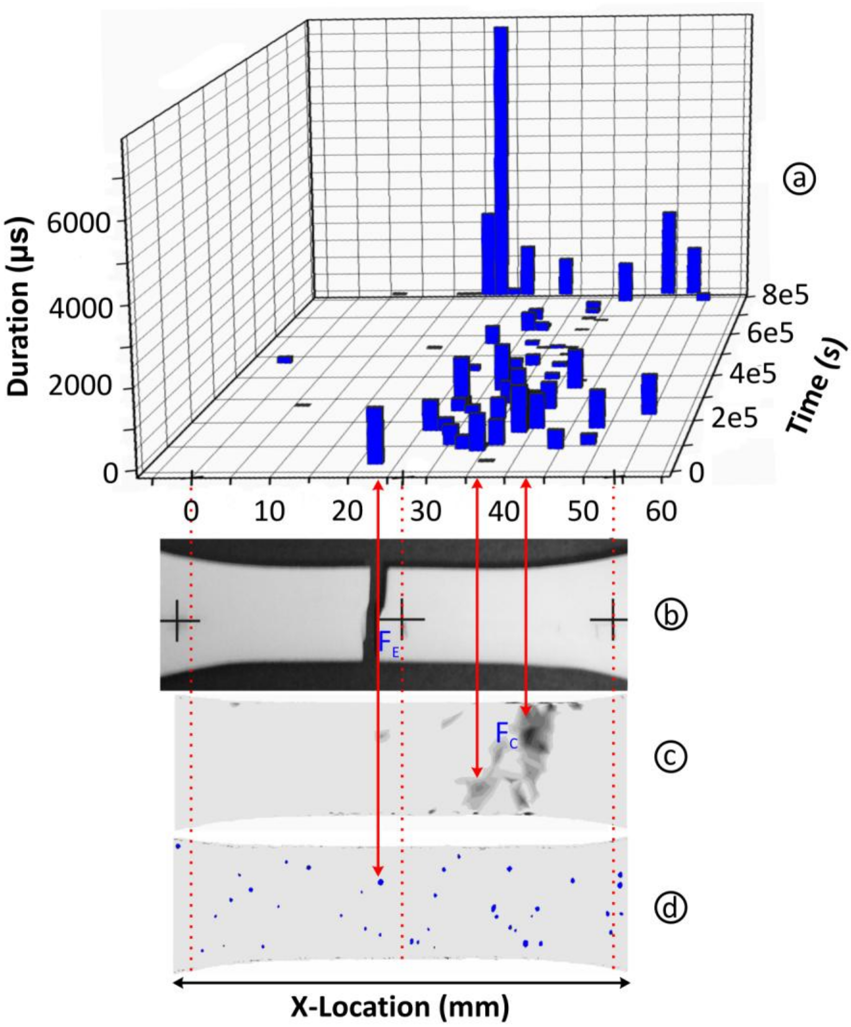

Figure 3.7: A comparison of AE location (a), specimen failure location (b), computational damage location (darker areas represent higher damage) (c) and the specimen defect field (d). The defects seen in (d) are all $BaSO_4$ agglomerates. Here the experimental and computational failure locations (F_E and F_C) were not conincident. Condition C was used when modelling $BaSO_4$.

3.4 Discussion

The most valuable aspect of this research is its novel capacity to compare bone cement fatigue life data obtained from experimental and computational methods. The formation of computational models from μCT scans has enabled good predictions of fatigue life to be made, and incorporated the variability of specimen fatigue life in simulations (Dunne and Orr, 2001). The current study demonstrates the effect of defects in dog-bone-shaped specimens of bone cement. In simulations, damage was seen to accumulate around internal defects where stress concentrations were created (in many cases at three or four locations), before one area dominated the damage pattern, resulting in failure (figure 3.8). This damage was compared with AE data, with the duration parameter used as a measure of damage (Roques et al, 2004b), showing good location agreement (figures 3.6 and 3.7). It is notable that the computational model could not replicate the discontinuous nature of damage progression identified by AE experimental specimens. In simulations, where elements became fully-damaged the reduction in stiffness created a stress-concentration in adjacent elements, which lead to failure of the specimen. However, the discontinuous damage pattern recorded with AE is likely to represent complex fatigue mechanisms consisting of crack initiation, craze formation, crack propagation and arrest: these mechanisms were not represented in simulations.

In the absence of large pores (larger than 0.7 mm^3 in volume), damage patterns were determined by surface porosity, smaller internal pores and $BaSO_4$ agglomerates. No relationship was found between the number of defects and specimen fatigue life, which suggests that the relative size and distribution of defects, rather than quantity, dictate failure.

The computational method correctly predicted the failure location in only four out of twelve samples, where larger pores occurred. However, non-critical damage was predicted at the experimental failure site in a further five specimens. This finding indicates more investigation is needed to clarify the effect on fatigue damage accumulation of pores, $BaSO_4$ agglomerates and other defects not captured in µCT scans, such as pre-load cracks created during cement polymerisation. It also signifies the inability of the current methodology to describe small inhomogenities in bone cement, and their effect on the fatigue failure process. This stems from the limited resolution of µCT scans, and the simplified fatigue mechanics laws employed here.

One can conclude from the AE in figures 3.6 and 3.7 that virtually all of the fatigue life is taken up by damage accumulation in some form, until the first high-energy events lead to rapid failure. This finding supports the theory of minimising fatigue crack initiation sites as a method of postponing specimen failure due to tensile fatigue loading. Figures 3.6 and 3.7 also show failure in a location which had previously seen little AE. The reasons behind this phenomenon are unknown. It is notable that the computational model did not replicate this discontinuous damage. This is further evidence that the failure process is not yet fully understood, and may account for the inability of the computational model to predict the failure location accurately in some specimens.

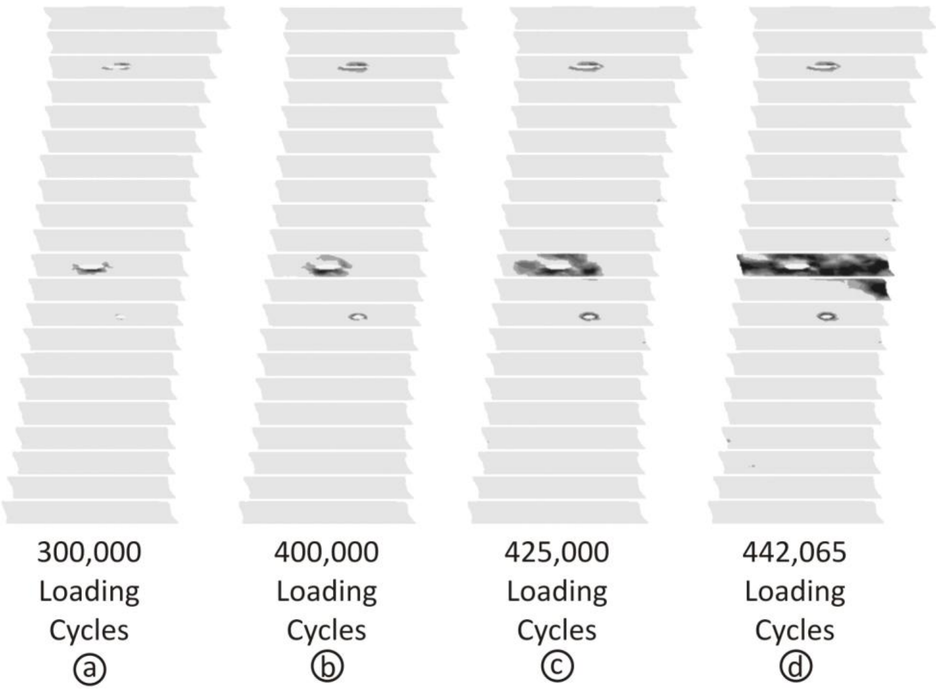

Figure 3.8: Damage (dark areas) in slices through a specimen at given number of loading cycles generated in a computational simulation. Damage takes many cycles to accumulate, occurring at several locations (a, b and c). Finally, damage rapidly accumulates at one location (the largest pore), leading to failure (d).

Varying the mechanical properties of $BaSO_4$ agglomerates in simulations assessed the effect of their presence on specimen response to tension fatigue loading. Figure 3.5 shows that the effect of this toggling on specimen fatigue life was negligible at a level of p=0.05. However, the $BaSO_4$ agglomerates did appear to influence the predicted damage pattern. Sinnett-Jones (2007) found that although $BaSO_4$ particles in agglomerates appear to be poorly bonded, they do support crack propagation, at a slower rate than the surrounding matrix. This was attributed to the compressive residual stresses of the surrounding matrix, generated on polymerisation. It appears that the presence of $BaSO_4$ agglomerates of the fatigue failure process is very small in practice.

There are some limitations to this study. McCormack et al (1996) and Roques et al (2004a) have shown that stresses created during bone cement polymerisation due to constraint by the mould can be large enough to produce cracks prior to loading. However, the resolution of μCT scans meant these pre-load cracks could not be detected and hence included in the simulations. Their inclusion may have reduced cement fatigue life in simulations, especially when one considers that the majority of specimen fatigue life is derived from crack initiation. The polymerisation process can also generate residual stresses in the cement. However, stress relaxation during ageing would have relaxed residual stress fields in the specimens in this study. The resolution of scans was also too coarse to define individual beads of polymethylmethacrylate in simulations, which can act to create stress concentrations that aid crack initiation and propagation (Sinnett-Jones et al, 2005). The CDM approach of modelling crack propagation by element death or elastic modulus reduction relies on many simplifications of fracture mechanics theories. However, if a large volume of cement is to be studied, which is likely to contain multiple cracks, the CDM method must be adopted. Other authors have presented a methodology where damage is resolved into three perpendicular tensors, allowing the direction of crack propagation to be represented by a directional loss of tensile stress transfer (Stolk et al, 2004). In this analysis, damage scalars were applied to elements in this analysis, meaning the magnitude of Von Mises stress dictated the loss of load-bearing capacity in all directions: this was assumed to be acceptable due to the uni-axial nature of loading. In addition, some simplifications were adopted; creep effects were not considered in this work, and a linear damage accumulation model was used whereas the mechanical properties of materials are known to be time-dependent (Callister, 1994).

In spite of these limitations, the correlation of experimental and computational fatigue life reported here is stronger than that previously noted (Stolk et al, 2004), which is thought to be due to the modelling of porosity. Fatigue life prediction is particularly accurate at low loads, where damage accumulation has been found to have a more linear relationship with the number fatigue cycles (Jeffers et al, 2005). Jeffers (2005) also found that accurate simulations of cement longevity could only be achieved by modelling porosity. Previous methods of modelling porosity have simulated porosity by assuming random stress concentrations in specimens. The method presented in the current study is recommended for improving finite element models of damage accumulation in cement undergoing fatigue loading. Also, the data presented in figure 3.4 enables the development of FE models of damage accumulation in bone cement, containing defect populations based on this sample data, using the methods of Janssen et al (2005b) or Jeffers et al (2005).

4 VERIFICATION OF CEMENT DAMAGE DETECTION BY ACOUSTIC EMISSIONS

4.1 INTRODUCTION

The dominant cause for failure in cemented total hip prostheses is aseptic loosening (NJR, 2007; Furnes et al, 2007; Karrholm et al, 2008). For the femoral component, the aseptic loosening process appears to involve the loosening of the stem in the cement mantle. Under further loading, Jasty et al (1991) and Kawate et al (1998) suggested that microcrack coalesce and propagation create through-cracks in the cement mantle, which allow micromotion and creates a pathway for wear debris to access the bone-cement interface, causing osteolysis and gross loosening. There is evidence that wear-induced osteolysis is a significant factor prior to cement mantle through-cracking (Schulte et al, 1993; Carrington et al, 2009), though there is no general consensus on this in the field.

To understand the aseptic loosening process, many researchers have attempted to characterise the fatigue failure process of bone cement. This may be achieved via mechanical testing of dog-bone-shaped specimens of bone cement under fatigue loading (Murphy and Prendergast, 2000; Roques et al, 2004b; Sinnett-Jones et al, 2005; Jeffers et al, 2005; Coultrup et al, 2009). Large cement pores and barium sulphate ($BaSO_4$) agglomerates have been implicated by several authors as fatigue crack initiation sites, particularly at the stress concentration between adjacent pre-polymerised polymethylmethacrylate (PMMA) beads (Sinnett-Jones et al, 2005). Observations of discontinuous growth bands and crack-spanning fibrils on specimen fracture surfaces have led authors to conclude that the fatigue failure process in bone cement consists of discontinuous crack growth through microcrack coalescence within a damage zone ahead of a principle crack (Topoleski et al, 1990; Molino et al, 1996; Murphy and Prendergast, 2000; Murphy and Prendergast, 2001, Sinnett-Jones et al, 2005).

The analysis of failed specimens gives a snapshot of the failure mechanism; however, the monitoring of specimen failure in real time is required to reveal the evolution of fatigue damage. Browne et al (2005) identified acoustic emission (AE) monitoring as a suitable technique to achieve this. Several authors have identified emissions of increasing duration and energy as fatigue tests progressed towards specimen failure (Roques et al, 2004b; Jeffers et al, 2005; Coultrup et al, 2009). These studies have confirmed fatigue damage events to be discontinuous in time, occurring in multiple locations. Roques et al (2004b) related AE durations exceeding 200 μs to critical events prior to catastrophic failure of specimens. However, Chapter 3 of this thesis revealed high-duration events which did not cause failure. While the ability of AE to describe failure events has been verified (Roques et al, 2004b; Jeffers et al, 2005), but the detection of non-catastrophic damage by AE has not; if fatigue failure in bone cement is considered to be a process of discontinuous damage, one must understand the contribution of pre-failure fracture events. AE data presented in chapter 3 suggest the presence of a damage process in specimens at some locations, which later stopped, leading to failure elsewhere. In this case, the failure location of the specimen could not be predicted in computational simulations. This phenomenon is not reported elsewhere. Therefore, the aim of this chapter was to relate non-catastrophic AE to microcracks within fatigue specimens. These microcracks were found by synchrotron tomography and scanning electron microscopy (SEM) of sectioned specimens.

4.2 MATERIALS AND METHODS

4.2.1 Specimen Preparation and Fatigue Testing

The majority of specimens used for this study were the same as those tested in Chapter 3. Additional (non-loaded) specimens were produced by the same methods to act as controls. The reader should consult Chapter 3 for information of specimen preparation, the fatigue test protocol and the configuration of the AE system.

4.2.2 Scanning Electron Microscopy

Four types of specimen were analysed; for each type, five repeat specimens were investigated:

Type-1: Surfaces where specimens failed under fatigue loading.

Type-2: Surfaces of specimens sectioned at locations where significant non-catastrophic AE were recorded.

Type-3: Surfaces of specimens sectioned at locations where no AE were recorded upon fatigue loading.

Type-4: Surfaces of sectioned specimens which had not been loaded at all (control).

Type-1 specimens were simply the fracture surfaces of fatigue specimens. Other specimen types were generated by sectioning. Section locations were determined with reference to profiles of AE duration variation along the gauge length span (54 mm). The span was split into individual 'AE regions' of 1 mm in length. The duration of all hits located within each AE region was summed (figure 4.1). An AE region was considered to contain significant non-catastrophic AE where the sum of AE duration exceeded 2000 µs over at least 10 hits, without causing failure of the specimen (i.e. the specimen failed elsewhere); specimens were sectioned at these locations to create type-2 specimens. For all specimens, there were regions where no AE were located; type-3 specimens were created at these locations by sectioning. Type-4 specimens were generated from unloaded specimens; section locations were chosen at random.

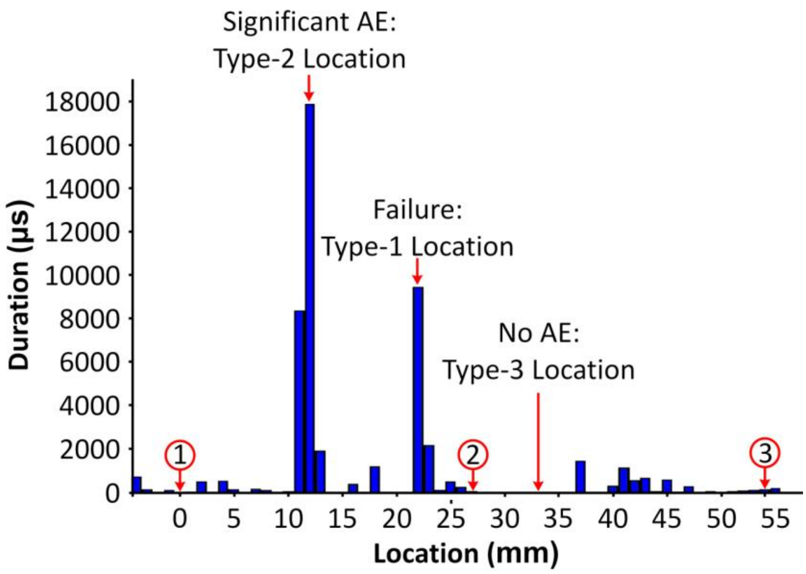

Figure 4.1: The linear location of acoustic emissions. Acoustic emission sensors are numbered.

Where applicable, a diamond saw lubricated with water was used for sectioning. Previous analyses have found this method does not create damage in control specimens (Sinnett-Jones et al, 2005). Scanning electron microscopy (SEM) was conducted with a field emission instrument (JEOL JSM6500F), at an accelerating voltage of 10 kV (resolution up to 1.5 nm). Specimen surfaces were splutter-coated with gold prior to imaging.

4.2.3 Synchrotron Tomography

Five type-2 specimens were sectioned to a suitable size for scanning (5 mm x 2 mm x 2 mm). A diamond saw was again used for sectioning. Synchrotron tomography was conducted in Beamline ID19 at the European Synchrotron Research Facility (ERSF) in Grenoble, France. An energy source of 20keV was used for scans, with an exposure time of 0.5s. Scans comprised 1500 radiographs at a resolution of 1.4 µm.

4.3 Results

4.3.1 Scanning Electron Microscopy Results

For type-1 specimens, a critical defect, such as a pore or a $BaSO_4$ agglomerate (figure 4.2a), was generally identified by the presence of local cracks. Cracks appear as white lines, and may be open in some locations (figure 4.2). The presence of fibrils behind the crack tip (figure 4.2b) suggests crazing-type crack propagation was occurring prior to failure.

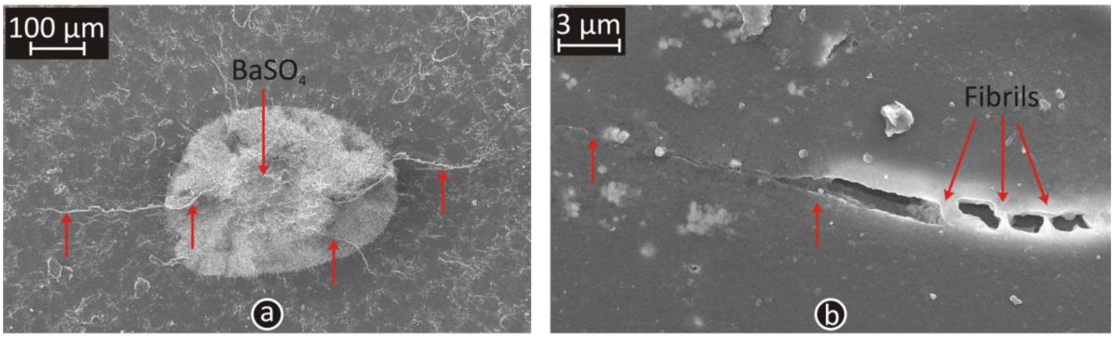

Figure 4.2: A barium sulphate agglomerate found on a type-1 specimen (a); an associated crack propagating from the agglomerate, revealing fibrils behind the crack tip (b). Where not labelled, cracks are identified by red arrows.

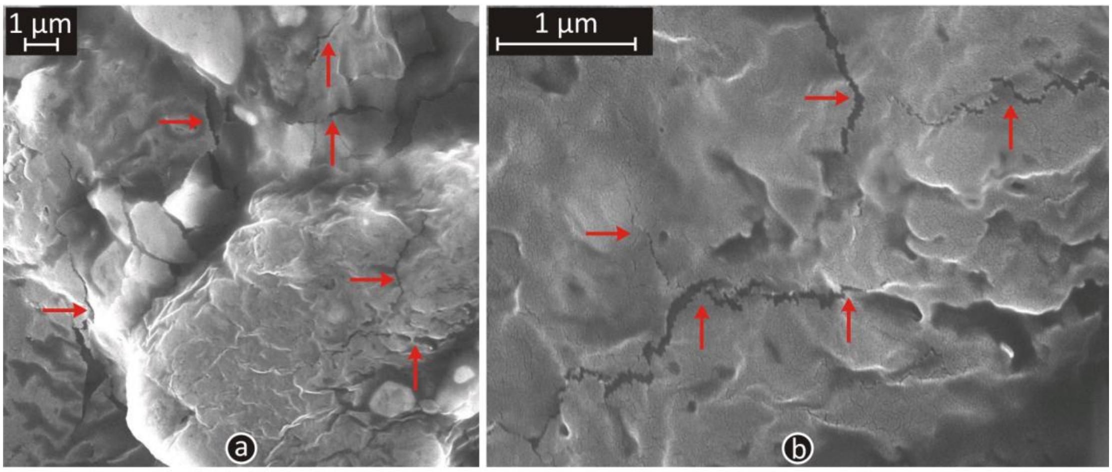

Figure 4.3: Cracks found on section faces of type-2 specimens. Microcracks of a few microns in length are identified by red arrows.

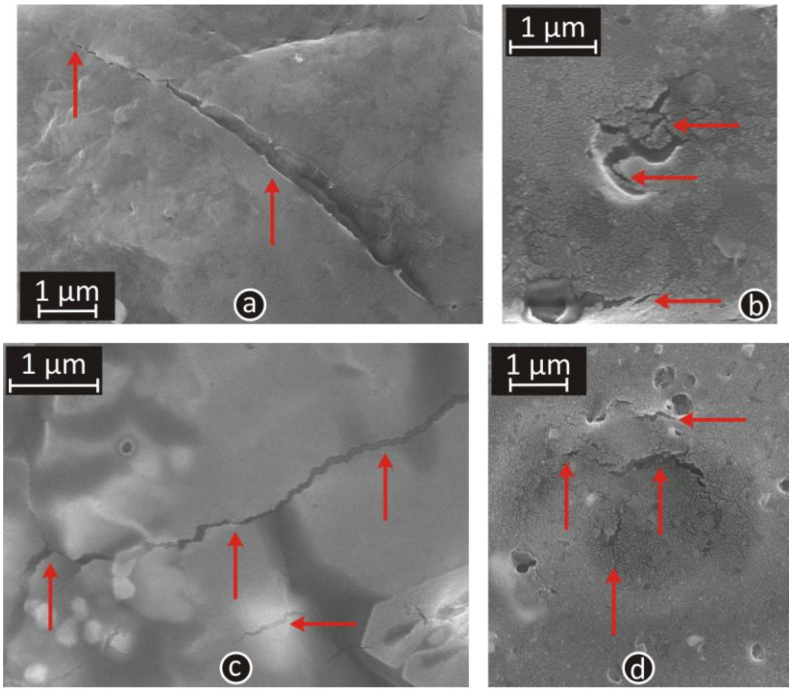

Figure 4.4: Further evidence of crack propagation through type-2 specimens (a and c); evidence of cement damage in circular patches, possibly within pre-polymerised beads, on type-2 specimens (b and d). Cracks are identified with red arrows.

For type-2 specimens, the majority of section area appeared to be undamaged; however, for every example, at least one area of concentrated, diffuse damage was apparent (figures 4.3 and 4.4). This damage is microscopic in scale, with a maximum crack thickness of 0.5 µm, and crack length of up to 6 µm. In many instances, the crack propagation direction was highly varied along the crack length, suggesting propagation occurs through local inhomogenities. In some cases, damage appears to have occurred in a small, circular patch (figure 4.4b and 4.4d). This may relate to defects within pre-polymerised beads, as noted by Sinnett-Jones et al (2005).

In type-3 specimens, no evidence of cement damage was found on the entire sectioned surface (figure 4.5b). Also for type-4 specimens, no damage was found to have resulted from polymerisation, even at large pores (4.5a).

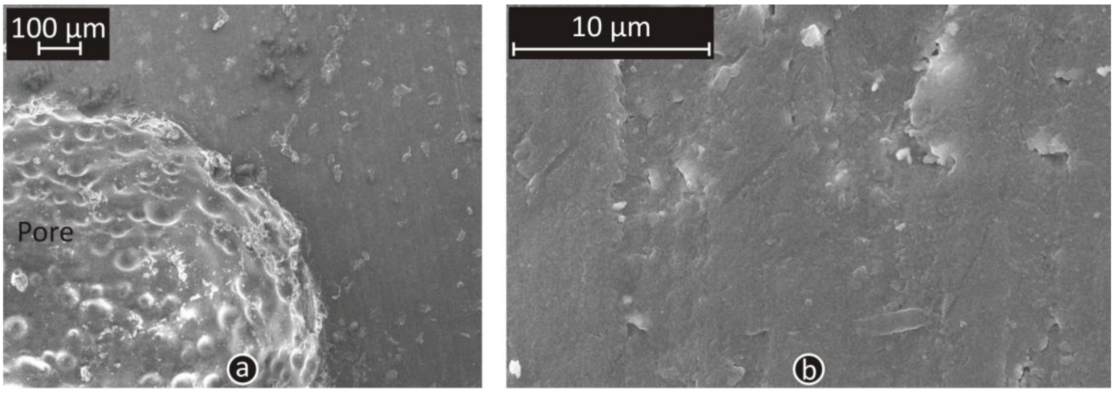

Figure 4.5: No evidence of cracking was found in fatigue type-3 specimens, even at large pores (a). Additionally, no cement damage was found in type-4 specimens (b).

4.3.2 Synchrotron Tomography

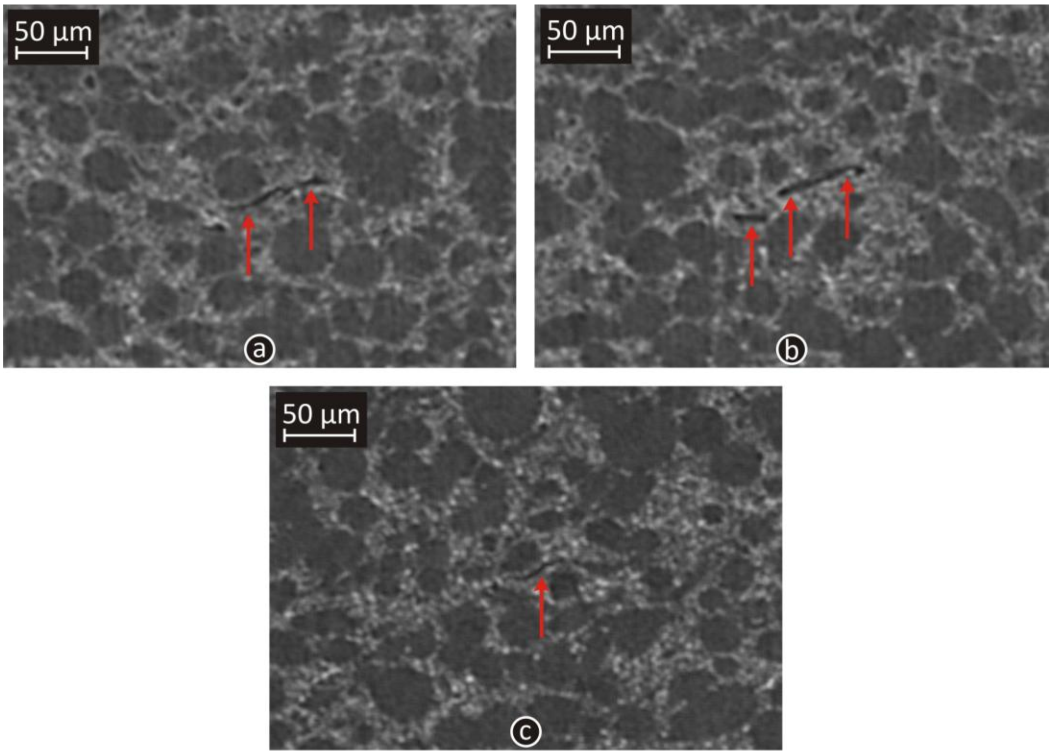

Figure 4.6: Matrix cracking (red arrows) within type-2 specimens at locations of recorded AE was detected with synchrotron tomography.

For synchrotron tomography the micro-structure of bone cement becomes more-readily apparent, with pre-polymerised beads discernable from the $BaSO_4$-filled matrix. The technique revealed evidence of cracking at the inter-bead matrix for type-2 specimens (figures 4.6a, 4.6b and 4.6c).

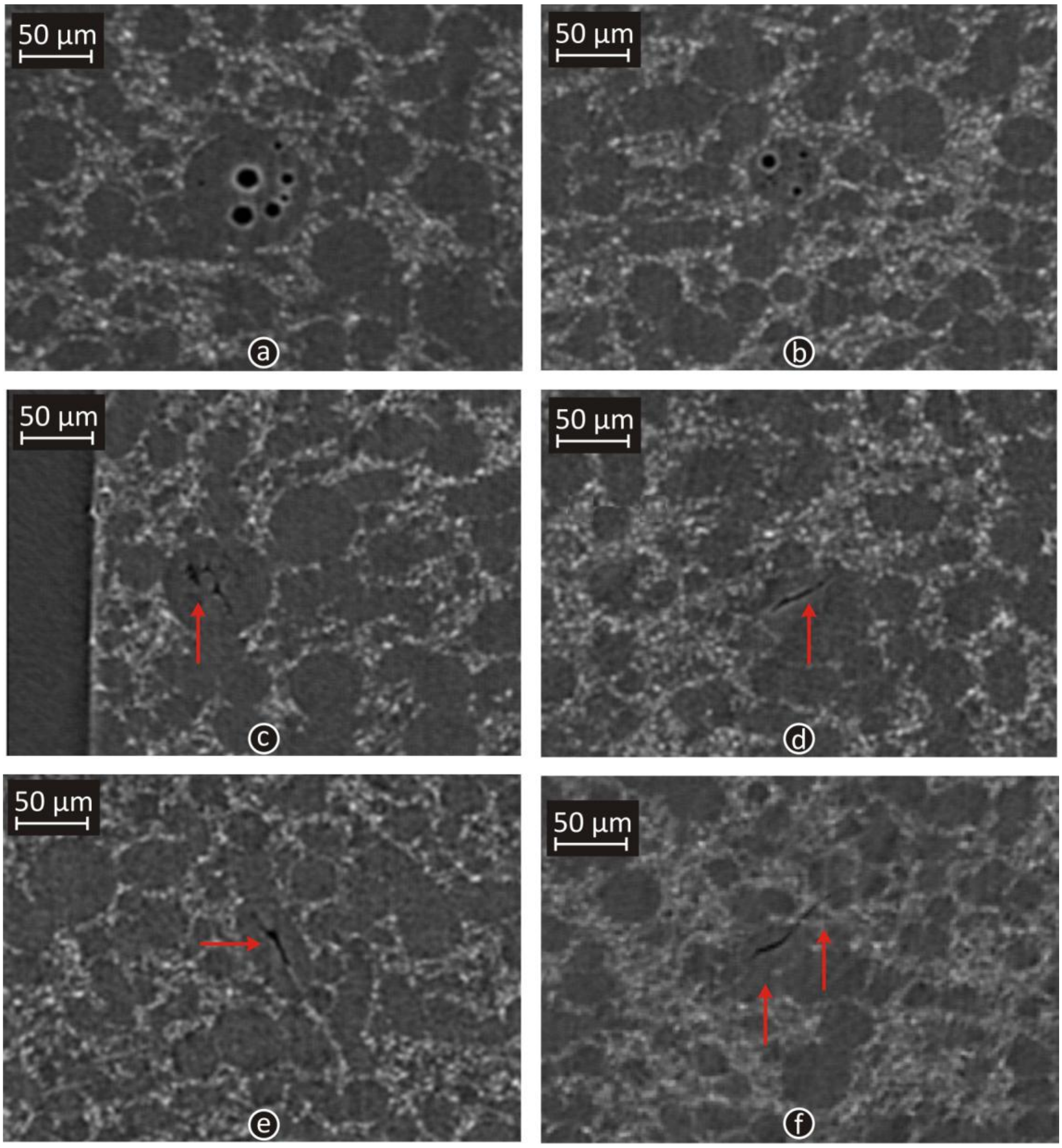

Figure 4.7: Damage features within synchrotron scans of type-2 specimens. Micro-pores with pre-polymerised beads (a and b); inter-pore damage within a pre-polymerised bead (c); cracking within pre-polymerised beads (d and e); break-out of a crack from a bead into the matrix (f).

As reported by Sinnett-Jones et al (2005), a small number of pre-polymerised beads contained small pores, of diameters up to 20 µm (figure 4.7a and b). In some cases cracks seemed to occur between these pores, with damage maintained within the bead (figure 4.7c). There were also multiple examples of crack-like defects within prep-polymerised beads, which may have initiated at internal defects (figures 4.7d and e). Additionally, there were limited examples of what appeared to be cement cracks breaking out of beads, and into the surrounding matrix (figure 4.7f).

Where larger pores (20 µm to 100 µm diameter) and barium sulphate agglomerates (up to 200 µm diameter) were found within type-2 specimens, no cement cracks could be associated with them in synchrotron scans at the resolution achieved in this investigation (figures 4.8a and 4.8b).

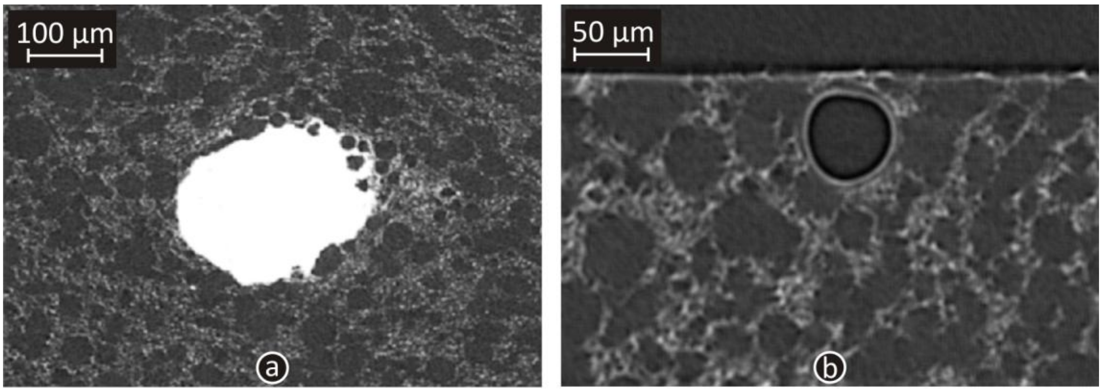

Figure 4.8: Cement cracks were not found at large $BaSO_4$ agglomerates (a) and pores (b) in synchrotron scans of type-2 specimens.

4.4 Discussion

This study presents evidence of bone cement fatigue damage at locations of non-catastrophic AE (type-2 specimens), and draws a comparison against locations where no AE was recorded (type-3 and type-4 specimens). Fracture surfaces (type-1 specimens) revealed cracks passing though pores and $BaSO_4$ agglomerates, with associated diffuse cracking and fibrils spanning cracks. In type-2 specimens, both synchrotron tomography and SEM have revealed small-scale damage, characteristic of that revealed in other studies (Topoleski et al, 1993; Sinnett-Jones et al, 2005). Cracks detected were up to a few µm in width, and 100 µm in length. There appears to be evidence of micro-cracking within pre-polymerised beads, and the deflection of cracks around pre-polymerised beads. The fact that no evidence of damage was found in type-3 and type-4 specimens suggests that located AE did relate to fatigue events. It was not, however, possible to relate specific micro-cracks to given AE.

SEM revealed small areas of concentrated damage on type-2 specimens, which may relate to the damage zones associated with craze formation, as described by Topoleski et al (1990). The small scale of these cracks (less than 1 µm wide) means that they were not visible on synchrotron scans, since the resolution of this imaging method was 1.4 µm. The larger-scale damage seen in synchrotron scans was not apparent with SEM, though this is not surprising considering that they were rarely seen in synchrotron scans and may be easily missed upon sectioning.

From the SEM, it is clear that many microcracks may occur in one location under fatigue loading, and one may postulate that they occur within a volume of several mm^3 in type-2 specimens, since they were consistently found by sectioning. This explains the detection of multiple locations of AE in fatigue specimens of bone cement (chapter 3; Roques et al, 2004b; Jeffers et al, 2005). It is suggested that for each type-2 location, there may be many more micro-cracks than received AE. This implies that the majority of cracking events produce low-energy AE below the rejection threshold (40 dB). However, AE which adheres to the selection criterion used here appears to relate to fatigue damage on some level. Unfortunately, the phenomenon of damage arrest in some locations of experimental specimens was not explained in this investigation.

Since cracking occurred within both pre-polymerised beads and the inter-bead matrix, and this damage was stable (as it did not cause failure), this suggests that high-energy rapid crack propagation is not exclusively responsible for causing cracking in pre-polymerised beads, as suggested by some other authors (Topoleski et al, 1993). It should be noted that the majority of damage observed from synchrotron tomography was associated with micro-pores within pre-polymerised PMMA beads, rather than larger pores or $BaSO_4$ agglomerates. This porosity has been identified as a possible crack initiation site elsewhere (Sinnett-Jones et al, 2005); it is likely that the relative locations of all pores significantly affect the failure process too (Taylor et al, 2006).

The observation of microcracks at the location of AE adds confidence in the use of AE as a non-destructive technique for monitoring fatigue damage in bone cement in real time. Since there was good agreement between the location of AE and simulated damage in computational specimens (chapter 3), this analysis partially backs-up the ability of the computational method to predict the location of microcracking in cement specimens.

5 THE EFFECT OF POLYETHYLENE CUP PENETRATION ON ACETABULAR CEMENT MANTLE STRESSES

5.1 INTRODUCTION

Bone cement is used for fixation in approximately half of all THA procedures in the UK (NJR, 2007). Despite advances in cementing techniques (Learmonth, 2005), aseptic loosening still accounts for approximately 75% of failures of cemented THAs (Furnes et al, 2007; Karrholm et al, 2008). Aseptic loosening is a long-term failure process, typically requiring at least ten years to occur. This failure mode is reported to be between two and four times more prevalent in the acetabular component than the femoral component (Schulte et al, 1993; Kobayashi et al, 1997; Madey et al, 1997; Callaghan et al, 1998; Callaghan et al, 2000). It is clear that one area of concentration for novel research should be ways to increase cup longevity beyond fifteen to twenty years.

For the femoral component, aseptic loosening occurs due to the failure of the stem-cement interface, followed by crack initiation and propagation in the cement mantle, and possibly bone resorption due to stress shielding and the presence of polyethylene wear debris. After cement mantle through-cracking, it appears that wear-induced osteolysis amplifies local stress concentrations to lead to gross loosening of the stem (Jasty et al, 1991; McCormack et al, 1999; Race et al, 2003). Clinical radiographs of the acetabular component report demarcation at the cement-bone interface as a pre-cursor to aseptic loosening (Garcia-Cimbrelo et al, 1997; Hodgkinson et al, 1989). There is a general consensus that initial demarcation at the cement-bone interface is caused by an auto-immune response to polyethylene wear debris (Schmalzried et al, 1992), which has been supported by the identification of polyethylene wear debris, macrophages and cytokines at the resorbed interface (Zicat et al, 1995; Mai et al, 1996; Jones et al, 1999). These observations lead one to consider why the failure processes for acetabular and femoral components are so different. Is it, in fact, possible that mechanical and biological stimuli contribute to aseptic loosening for both components (Wroblewski et al, 2004)?

There is clinical evidence of high polyethylene wear accompanying early acetabular aseptic loosening (Kobayashi et al, 1997; Callaghan et al, 2000; Wroblewski et al, 2004; Wroblewski et al, 2007), and bone-cement demarcation (Garcia-Cimbrelo et al, 1997). In one particular clinical study, patients were split into two groups: the first (a low-wear group) contained 190 patients with a rate of penetration of 0.02 mm/year or less, whilst the second (a high-wear group) comprised 149 patients with a rate of penetration of 0.2 mm/year or more. At an average follow-up time of 17 years, the cup survival rates for the low-wear and high-wear groups were 94% and 39% respectively (Wroblewski et al, 2004). As there was no statistical difference in survival for the femoral component for the two wear conditions, the authors reasoned that the high acetabular failure rate could not be linked solely to osteolysis.

Very few computational studies have been undertaken to reveal the failure process of the acetabular cement mantle. Experimental fatigue studies have confirmed that debonding at the bone-cement interface dominates acetabular aseptic loosening (Heaton-Adegbile et al, 2006; Tong et al, 2008). Zant et al (2007) and Tong et al (2008) have shown that the stress state in the acetabular cement mantle is multi-axial, with peak cement stresses at the cement-cup interface reaching 9MPa. Since this is not the location of failure in vivo, it appears that the process of aseptic loosening of the acetabular component is clearly not fully understood.

This author hypothesized that cup wear raises cement mantle stresses, which cause cement-bone demarcation either by mechanical overload of cancellous bone or because cement damage allows wear debris to access the cement-bone interface, causing osteolysis. This study explores the effect of various clinical variables on the magnitude of cement mantle stresses around the polyethylene acetabular cup, with particular focus on the effect of cup penetration. In light of the complexity of other finite element (FE) models of the pelvis (Dalstra et al, 1995; Dalstra and Huiskes, 1995; Thompson et al, 2002; Phillips et al, 2007), a simplified FE model was used to gather the majority of data, and a limited number of examples were corroborated with a more-realistic FE model. As such, this study also explores whether simplistic models of the in vivo case can yield large quantities of sufficiently useful data on prosthesis performance.

5.2 METHODS

This study utilised two static FE models: the *Simple Model* and the *Pelvis Model*. The computationally-inexpensive Simple Model (figure 5.1) allowed an automated full-factorial design-of-experiments analysis of independent variables to be swiftly conducted. The independent variables chosen were the thickness of the cement mantle, the depth of penetration of the femoral head into the cup, the quality of cancellous bone ('normal' or 'osteoporotic'), the size of the femoral head and acetabular cup, and the patient weight. The complex Pelvis Model (figure 5.2) was used to corroborate the Simple Model, since it was more representative of the in vivo condition. These two models were used to rank the independent variables chosen in terms of their effect on acetabular cement stresses.

5.2.1 The Simple Model

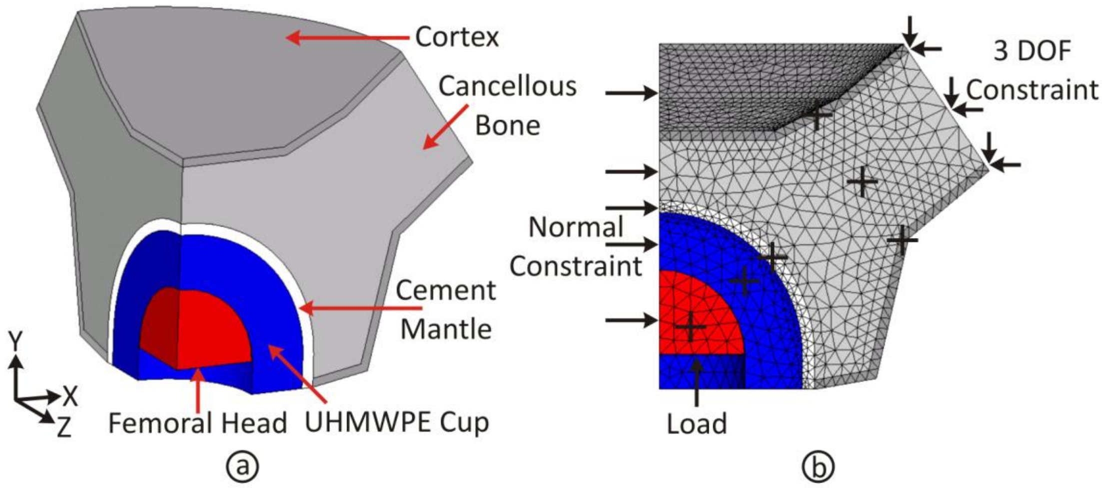

Figure 5.1: The geometry (a) and boundary conditions (b) of the Simple Model.

The Simple Model (figure 5.1) employed a simplified acetabular geometry (with a cortex thickness of 1.5mm) which was first published by Udofia et al (2004). This geometry was constructed within the FE solver ANSYS 11.0 (ANSYS Inc., Canonsburg, USA), allowing geometrical changes to the model to be automated. A quarter-model was used, with constraint applied at section areas to represent the full 3D case. The external cortical ridge was also constrained in all degrees of freedom (DOF) to represent the rest of the pelvis (figure 5.1b). The matrix of independent variable levels used is given in table 5.1. A full-factorial design-of-experiments analysis of these variables was conducted, requiring 720 simulations. The loading used was taken from Bergmann et al (2001), and represented normal walking loads in patients weighing 60 kg, 80 kg and 100 kg, applied through the pole of the cup. These values describe low, average and high population weights in the USA (US Department of Health and Human Services, 2004). Prosthesis geometry was taken from the DePuy Elite range (DePuy, Warsaw, USA), representing large and small cup-head combinations in the range (table 5.1).

Parameter	**Independent Variable Level**					
	1	**2**	**3**	**4**	**5**	**6**
Applied Load (N)	1398	1864	2330	-	-	-
Femoral Head Radius (mm)	11.060	11.060	13.950	13.950	-	-
Cup Internal Radius (mm)	11.215	11.215	14.100	14.100		
Cup External Radius (mm)	20.120	23.500	20.120	23.500		
Cancellous Elastic Modulus (MPa)	800	560	-	-	-	-
Cement Mantle Thickness (mm)	1	2	3	4	5	-
Cup Penetration Depth (mm)	0	1	2	3	4	5

Table 5.1: The independent variable levels used for the design-of experiments analysis of the Simple Model.

The material properties of cancellous bone have been found to be highly anisotropic (Dalstra et al, 1993), although Dalstra and Huiskes (1995) recommended using an elastic modulus of 800 MPa. The bulk elastic modulus of osteoporotic cancellous bone has been reported to be approximately 30% less than that of healthy bone (Li and Aspden, 1997) and therefore osteoporotic bone was represented with a modulus of 560 MPa. A minimum cement mantle thickness of 2 mm has been recommended by several authors, though mantles less than 1 mm and greater than 4 mm in thickness have been recorded in the literature (Dorr et al, 1983; Schmalzried et al, 1992; Kawate et al, 1998). Therefore, five levels of cement thickness were modelled, between 1 mm and 5 mm. Cup penetration rates exceeding 0.2 mm/year have been recorded in patient cohorts (Wroblewski et al, 1998; Chen and Wu, 2002), making cup penetration depths between 0 and 5 mm feasible after 20 years in vivo: this was represented in the six levels of cup penetration depth (table 5.1). Penetration was modelled by offsetting the femoral head a given distance towards to the pole of the polyethylene cup, and removing overlapping cup material.

A sliding contact model was used between the acetabular cup and the femoral head, assuming a coefficient of friction of 0.065 (Kurtz et al, 2000). The mechanical properties of the medical devices modelled are given in table 5.2.

Component / Material	Elastic Modulus (MPa)	Poisson's Ratio
Cortical Bone	17000	0.3
Normal Cancellous Bone	800	0.2
Osteoporotic Cancellous Bone	560	0.2
Bone Cement	2800	0.3
UHMWPE Cup	875	0.45
Steel Femoral Head	210000	0.3

Table 5.2: The mechanical properties of materials used in finite element simulations (Dalstra et al, 1995; Dalstra and Huiskes, 1995; Li and Aspden, 1997; Kurtz et al, 2000; Callister, 1994; Roques, 2003).

The model was meshed with eight-node first-order hexahedral elements, of an edge length of 1.8 mm (figure 5.1). A mesh sensitivity test of six sizes confirmed doubling the number of elements changed the maximum stress value by less than 3% for the thinnest cement mantle: hence, results were judged to be independent of the mesh size. Since aseptic loosening has been shown to be driven by the magnitude of cement stresses, the maximum value of stress in the cement mantle was recorded from each simulation.

5.2.2 The Pelvis Model

Many simplifications were made when defining the Simple Model, pertaining to the bone geometry, material properties, and load vector. The resulting loss in accuracy in simulations is partially vindicated by the speed of data assimilation. However, the accuracy of the Simple Model had to be assessed if data derived from it is to be considered reliable. As a corroboration step, specified cases modelled with the Simple Model were recreated with more-realistic bone geometry, material properties and gait data, with the Pelvis Model (figure 5.2a).

A pelvis was segmented from CT scan into steriolithography format using Amira 4.0 (ZIB, Berlin, Germany). Cement mantles and prostheses were generated using Solidworks 2006 SP4.1 (Solidworks Corp., Concord, USA). All parts of the model where then imported into Rhinoceros 4.0 (McNeel, Seattle, USA), where the cement and prostheses were positioned relative to anatomic landmarks with a cup angle of 42° and an anteverison angle of 14°, and the pelvis was cut. The pelvis was then meshed in ANSYS ICEM CFD 11.0 (ANSYS Inc., Canonsburg, USA) with four-node first-order tetrahedral elements, surrounded with three-node first-order triangular shell elements to represent the cortex. All elements had an edge length of 3 mm. A mesh sensitivity check showed it was unnecessary to use a second-order mesh for the cancellous and cortical bone. All other components were imported into ANSYS 11.0 (ANSYS Inc., Canonsburg, USA) and meshed with second-order 20-node brick elements and second-order 10-node tetrahedral elements with an edge length of 2 mm.

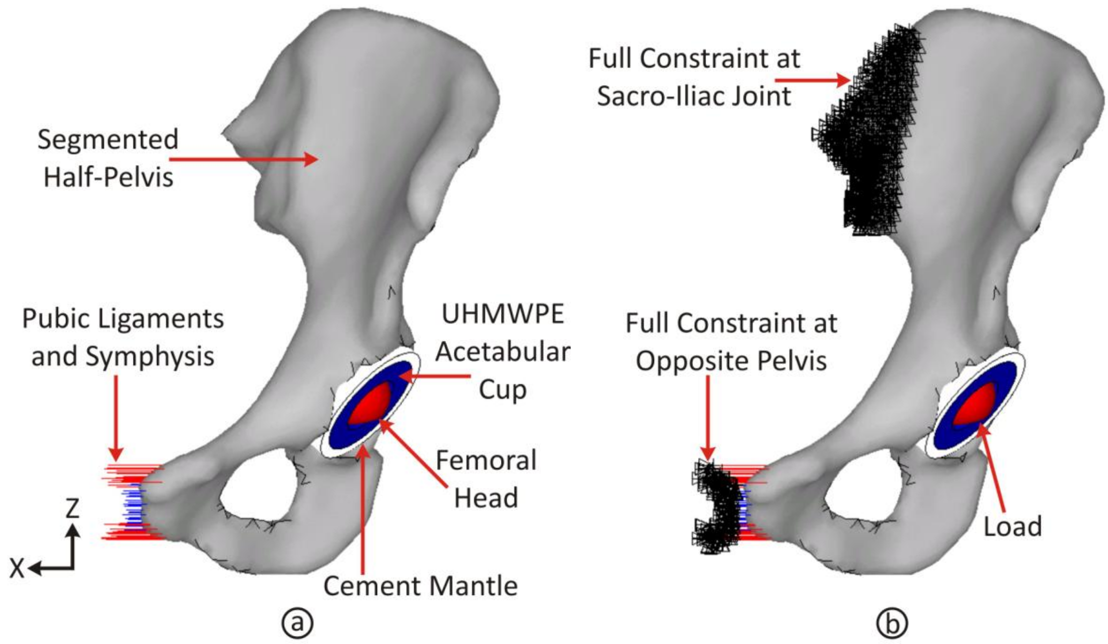

Figure 5.2: The geometry (a) and boundary conditions (b) of the Pelvis Model.

The mechanical properties of cancellous bone were modelled in three ways: as normal and osteoporotic with homogenous elastic modulus distributions (table 5.2), and additionally by calculating location-specific properties directly from the CT scan (Zannoni et al, 1998). This process averages bone densities over element volumes, and relates bone apparent density (ρ_{APP}) to bone elastic modulus (E, MPa) using equation 5.1. This resulted in location-specific elastic modulus values for cancellous bone elements, ranging between 130 MPa and 2112 MPa. The cortex thickness in the pelvis has been reported to vary between 0.7 mm and 3.2 mm (Dalstra et al, 1995). Since a mesh size of 3 mm was used for the bone, the high stiffness seen at the cortex was averaged out in many locations. This was the reason for adding exterior shell elements of thickness 1.5 mm to represent the cortex (Dalstra et al, 1995). A bonded contact model was used at the bone-cement interface, and a sliding contact model was used at the femoral head and cup, with a coefficient of friction of 0.065 (Kurtz et al, 2000). The material properties used are given in table 5.2.

$E = k \cdot \rho_{APP}^{3}$ Equation 5.1 (Zannoni et al, 1998)

Where $k=4249$ GPa $(g/cm^3)^{-3}$.

Independent Variables		Independent Variable Levels		
		1	2	3
Applied Load	F_X (N)	192	320	-
	F_Y (N)	312	520	-
	F_Z (N)	1350	2250	-
	F_{TOT} (N)	1398	2330	-
Cement Mantle Thickness (mm)		2	4	-
Cup Penetration Depth (mm)		0	2	5
Cancellous Bone Stiffness (MPa)		800	560	CT scans

Table 5.3: The independent variable levels used for analysis with the Pelvis Model.

The matrix of variable levels used for simulations used is given in table 5.3: these variable levels were intended to represent reasonable extremes of the patient condition. Two different load cases were simulated, representing the hip contact force during normal walking for patients weighing 60 kg and 100 kg (Bergmann et al, 2001). Two cement mantle conditions representing the minimum and maximum recommended thicknesses were simulated, while postoperative and long-term penetration depths were also considered (table 5.3). To model penetration, the femoral head was again offset by a given distance in the direction of the load vector, and overlapping cup material was removed. A full design-of-experiments analysis was conducted of these variables, requiring 36 simulations.

Anatomically, the pelvis transfers load from the spine to the legs via the bone and muscular structure. However, Phillips et al (2007) showed that the in vivo stress distribution at the acetabulum can also be created by fully constraining the pelvis at the joint with the sacrum, and at the pubis. Thus, the pelvis was fully-constrained at the sacro-iliac joint in all DOF. The superior and inferior pubic ligaments (tensile spring stiffness = 700 N/mm (Dakin et al, 2001)), and the pubic symphysis (compressive spring stiffness = 1500 N/mm (Dakin et al, 2001)) were modelled, and constrained in all DOF at nodes representing the contact points on the other half of the pelvis (figure 5.2). In all cases, the femoral head radius was 11.060 mm, the cup internal radius was 11.215 mm and the external cup radius was 20.120 mm. For each simulation, the maximum stress in the cement mantle was recorded.

5.3 RESULTS

Due to the design-of-experiments approach adopted in this study, the majority of results are presented in main effects plots. Main effects are average, additive effects which are associated with each particular level of each independent variable. A main effects plot graphs the average dependent variable response for each independent variable level. The steeper the graph, the greater effect the independent variable has on the dependent variable (Winer et al, 1991). Interactions can also occur when particular levels of independent variables combine to give a response in the dependent variable which is different from the sum of the corresponding main effects (Winer et al, 1991). The main effects and interactions for all independent variables were determined to rank variables in terms of their importance on the maximum cement mantle stress

5.3.1 Simple Model

The main effects plot for each independent variable used with the Simple Model is given in figure 5.3. Variables can be ranked in the following order of importance (starting with most important): cup penetration depth, cup outer radius, patient weight, cement mantle thickness, femoral head radius and cancellous bone stiffness. Indeed, the influence of changing the cup outer radius is comparable to that of penetration depth, suggesting that the overall cup thickness may be the driving factor: the rationale for this would be that a thicker cup distributes load over a greater surface area of cement. An increase from even 0 mm to 1 mm penetration gives a significant increase in the peak cement stress ($p<0.05$). There were significant interactions ($p<0.05$) between the cup external radius and penetration depth, the patient weight and penetration depth, and the patient weight and cup external radius.

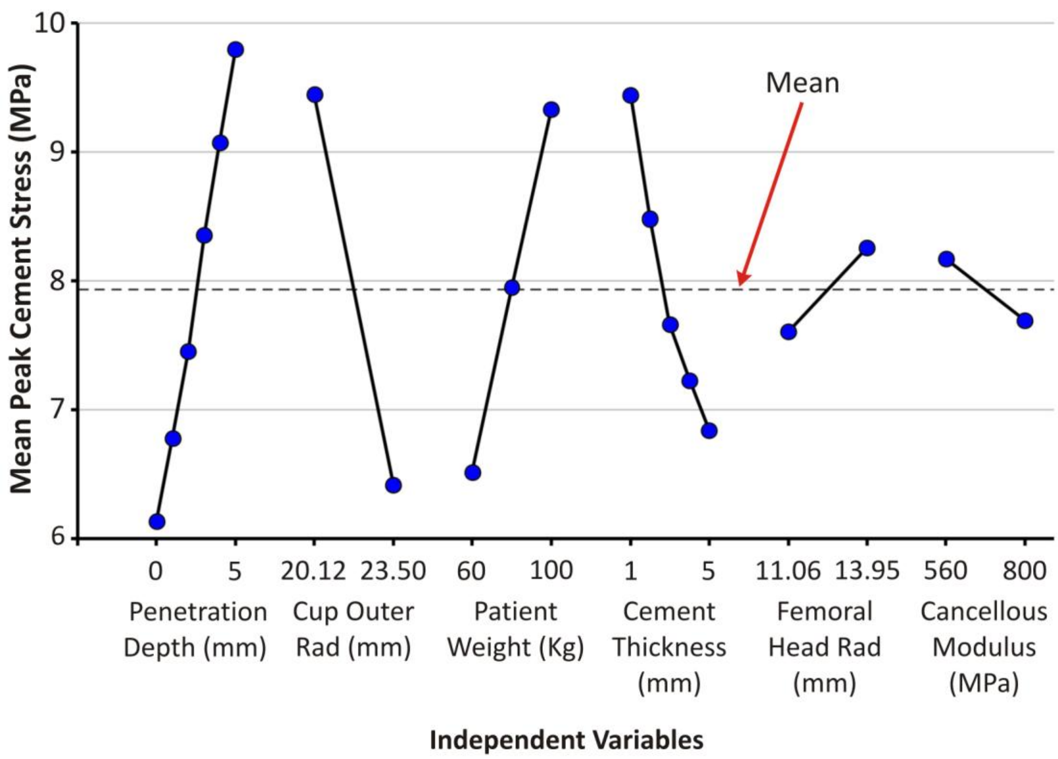

Figure 5.3: A plot of the main effect of each independent variable on the maximum cement mantle stress in the Simple Model.

5.3.2 Pelvis Model

As the Pelvis Model was used to corroborate the Simple Model, the results from the two models are presented here in comparison, normalised against the average maximum stress for each model (figure 5.4). The Pelvis Model did not rank the main effects of independent variables in the same order as the simple model, as it found, for the independent variable levels used, patient weight to have the most influence on the maximum cement stress. The pelvis model also predicted the effect of cup penetration to be more non-linear than the Simple Model. There is good agreement on the effect of cement thickness and homogenous bone elastic modulus.

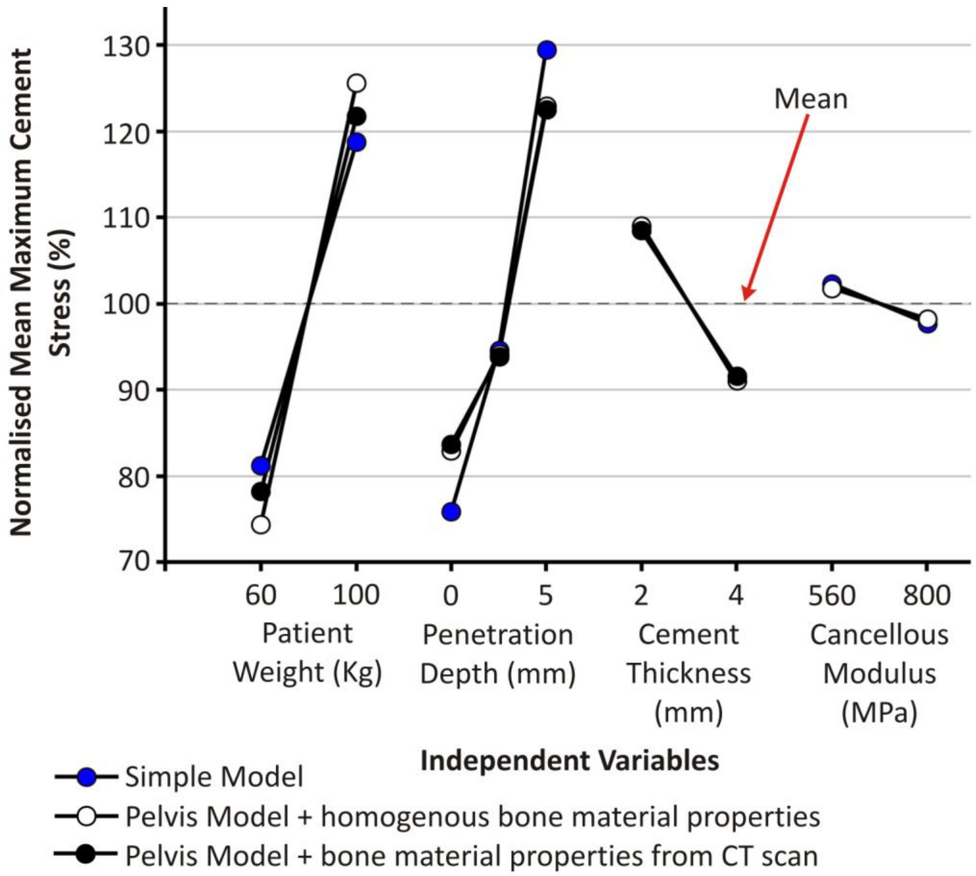

Figure 5.4: A comparison of the main effects on cement stresses generated in the Simple Model and the Pelvis Model. Maximum cement stresses are presented as percentages of the average maximum cement stress for each analysis type.

The stress distributions in two different cases for the Simple Model and the Pelvis Model are shown in figure 5.5. It can be seen that the region of highest stress occurs directly above the pole of the femoral head. High stresses are localised, meaning that most of the cement mantle experiences a relatively low stress. As highlighted by figure 5.5, the Simple Model consistently predicts higher cement stresses than the Pelvis Model. Cement mantle stresses are also consistently higher when cancellous bone material properties are found from the CT scan, which suggested this added complexity is necessary.

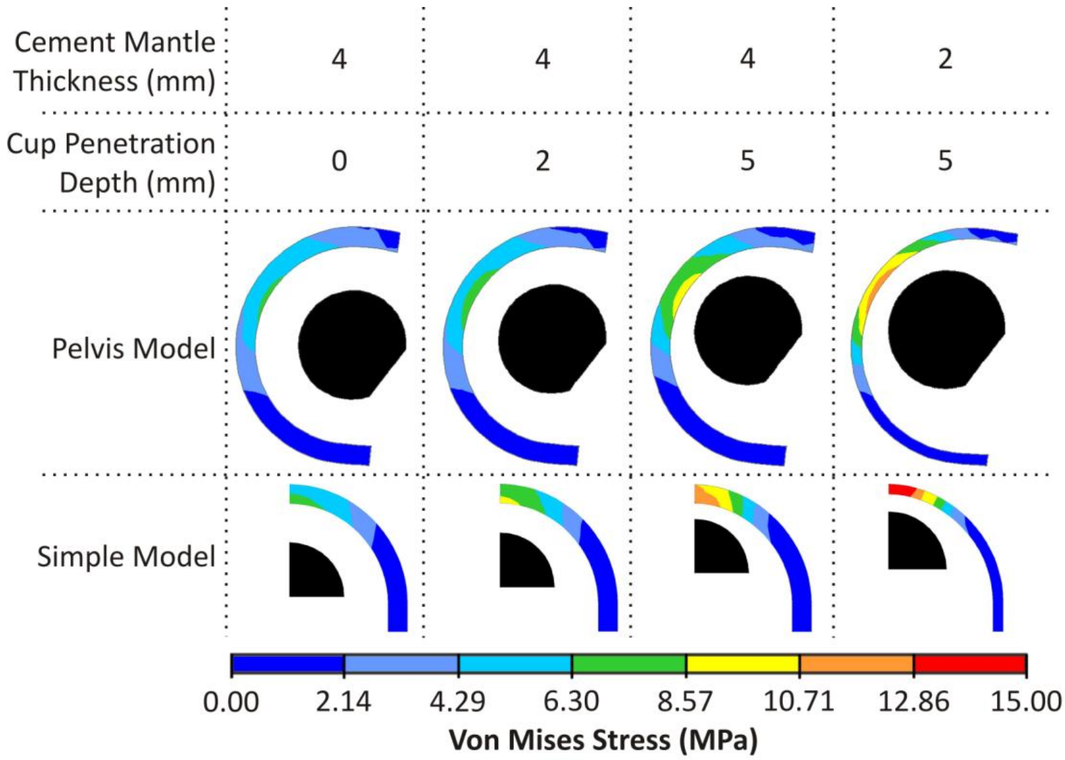

Figure 5.5: The Von Mises stress distribution found in the cement mantle for a range of independent variable levels, and a patient weight of 100 kg. Each section is taken through the pole of the femoral head (shown in black).

5.4 Discussion

This study has aimed to explore the mechanical effect of cup penetration on acetabular cement mantle stresses, and rank its effect against that of other variables using two FE methods. Both model types showed a significant increase in cement mantle stress for increasing cup penetration ($p<0.05$). Figure 5.4 also suggests that this stress amplification effect is non-linear with increasing penetration depth. Figure 5.5 shows that this maximum cement stress is manifested at the cement-cup interface, above the pole of the femoral head. This author speculates that cement stresses are initially reduced due to cement creep in vivo. However, as the number of loading cycles increases, polyethylene cup penetration progresses, causing cement stresses to steadily become augmented late in the fatigue life of the prosthesis. This may account for increased rates of aseptic loosening after 10 years in vivo for cups with a high penetration rate (Kobayashi et al, 1997; Callaghan et al, 1998; Callaghan et al, 2000; Wroblewski et al, 2004; Wroblewski et al, 2007). It should also be noted that impingement of the femoral stem on the cup becomes more likely as the cup penetration depth increases, which may cause the cup to be wrenched from the acetabulum (Wroblewski et al, 2009a).

The design-of-experiments approach showed that the cup penetration depth, cup outer radius, patient weight and cement mantle thickness respectively had the highest influence on cement mantle stress. Indeed, since the effects of varying the cup external radius and the polyethylene cup penetration depth appear to be the same, it may be the case that the effective cup thickness is the acting variable, since a thin cup will transfer load over a smaller area of cement. Data from fatigue testing of bone cement in other investigations (Murphy and Prendergast, 2000; Jeffers et al, 2005; Coultrup et al, 2009) reveal that a stress of 7MPa approximately equates to a fatigue life of 3 million cycles, while an endurance limit may exist below 6 MPa. Given the magnitude of stress amplification seen in this study (figure 5.5), this author supports the use of thick polyethylene cups and a thick cement mantle to minimise cement mantle stresses, especially when the confounding factors of patient weight (Wang et al, 2009) and high penetration depth are considered (Garcia-Cimbrelo et al, 1997; Wroblewski et al, 2004). This study also suggests that a high cup penetration rate may be a precursor for early acetabular aseptic loosening.

Another area of investigation at the start of this analysis was the use of simplified FE models of complex scenarios to acquire meaningful data. There was some disagreement between the two models over the ranking of independent variables. This author concludes that the Simple Model creates simplified boundary conditions for the cement mantle, causing some inaccuracy. However, agreement between the two models was generally good, suggesting that the data presented here still has value, and that the relevant important variables were identified by the Simple Model. Where simplified models are used, any data produced must be rigorously corroborated with representative computational or (ideally) experimental analyses.

The study of Tong et al (2008) predicted maximum cement stresses which were comparable to those determined in this study. However, they also reported that, despite evidence of demarcation at the bone-cement interface accompanying aseptic loosening (Garcia-Cimbrelo et al, 1997; Hodgkinson et al, 1989; Tong et al, 2008; Heaton-Adegbile et al, 2006), cement stresses at this interface were close to the endurance limit for bone cement, meaning cement cracking was unlikely. This may be the ideal post-operative case, but this study shows the independent variables investigated may cause cement stresses at the bone-cement interface to increase above the endurance limit for bone cement once the head has penetrated into the acetabular cup (figure 5.5). This study agrees that cement stresses are higher at the cement-cup interface. The prevalence of loosening at the cement-bone interface in vivo suggests that another factor makes it susceptible to failure. It is also worth noting that loosening at the cup-cement interface may not be discernable on radiographs, and may be a relevant occurrence in vivo, but this failure scenario has not been identified on autopsy specimens (Schmalzried et al, 1992).

There are several limitations to this study. The conditions modelled are idealised, and do not reflect the changing environment in vivo (e.g. bone remodelling, cement creep). The effect of penetration in particular is time-dependent: a cup penetration depth of 2 mm may take in excess of ten years to develop in vivo (Chen and Wu, 2002). The nature of design-of-experiment analyses can be a limitation itself: results can be misleading if inappropriate independent variable levels are adopted (e.g. if a disproportionately wide range of levels is used for one variable). This author accepts that computational models should be validated with data from experimental tests where possible; unfortunately, this was beyond the scope of this study.

While prosthesis fatigue lives cannot be adequately predicted from static simulations (Stolk et al, 2007), it is understood that the aseptic loosening process may be retarded by minimising cement stresses (Huiskes, 1993a). This study has shown that the surgeon may achieve this by using a thick polyethylene cup and thick cement mantle. Increasing cup penetration depth has been shown to significantly increase cement stresses, which may account for the high occurrence of aseptic loosening in patients exhibiting high polyethylene cup penetration rates (Kobayashi et al, 1997; Callaghan et al, 2000; Wroblewski et al, 2004; Wroblewski et al, 2007).

6 THE EFFECT OF POLYETHYLENE CUP WEAR RATE ON THE MECHANICAL FAILURE OF ACETABULAR CEMENT

6.1 INTRODUCTION

Bone cement is still commonly used to achieve acetabular prosthesis fixation in more than 50% of total hip arthroplasty (THA) procedures in the UK (NJR, 2007). Whilst arthroplasty registers report good long-term survival for cemented THAs (75% at 20 years), aseptic loosening is indentified as the indication for revision in approximately 75% of failed THAs (Furnes et al, 2007; Karrholm et al, 2008). Clinical studies have shown that the failure rate of the acetabular component is two to four times that of the femoral component after ten years in vivo (Schulte et al, 1993; Callaghan et al, 2000).

Clinically, aseptic loosening of the polyethylene cup is manifested as demarcation and the formation of fibrous tissue at the bone-cement interface. This demarcation patch is associated with symptomatic bone resorption and cup migration, and is a pre-cursor to long-term gross loosening of the cup (Hodgkinson et al, 1988; Garcia-Cimbrelo et al, 1997). This fibrous tissue was initially thought to result from mechanical overload of the cement or cancellous bone (Crowninshield et al, 1993). Schmalzried et al (1992) first provided an alternative biological loosening process: osteolytic bone resorption occurs at the cement-bone interface due to the ingress of polyethylene wear debris. This occurs initially at the exposed interface in the joint capsule, and propagates towards the dome of the cup as wear debris is entrained into resorbed soft tissue. Subsequent retrieval studies have identified polyethylene wear debris, macrophages and cytokines at the resorbed interface (Zicat et al, 1995; Mai et al, 1996; Jones et al, 1999). From a mechanical perspective, the cemented polyethylene cup appears to generally be a stable system (Mai et al, 1996). From this evidence, it appears that gross aseptic loosening of the polyethylene cup predominantly occurs due to an auto-immune response to wear debris causing chronic bone resorption. This does, however, raise the question of why the proposed failure methods for the acetabular and femoral components are so markedly different (Wroblewski et al, 2004)?

There is clinical evidence of polyethylene cup penetration accompanying aseptic loosening (Wroblewski et al, 2004; Wroblewski et al, 2007) and cement-bone demarcation (Garcia-Cimbrelo et al, 1997). One particular study discriminated between cups experiencing low wear (0.02 mm/year or less) and high wear (0.2 mm/year or more), showing the revision rate in the high-wear group was approximately eight times that of the low-wear group after seventeen years *in vivo* (Wroblewski et al, 2004). As there was no statistical difference in the survival of the femoral component for the two wear conditions, the authors concluded that some other effect must contribute to the failure process for polyethylene cups exhibiting a high wear rate. This leads one to the conclusion that failure is multi-factorial. The current author hypothesizes that in vivo loads contribute to cement-bone demarcation, either by mechanical overload of cancellous bone, or due to cement mantle damage providing a pathway for wear debris to access the cement-bone interface.

Porosity occurs in bone cement due to air entrainment on mixing, and thermal and density changes during polymerization (Gilbert et al, 2000). Pores have been identified a crack-initiators in dog-bone shaped specimens of bone cement (Jeffers, 2005; Coultrup et al, 2009), and vacuum mixing has been recommended to improve the fatigue performance in such tests (Dunne et al, 2003). However, a corresponding improvement in clinical performance with vacuum mixing has not been forthcoming (Ling and Lee, 1998); indeed, it has been suggested that clinical performance may be poorer after vacuum mixing (Malchau and Herberts, 1996). Jeffers et al (2007) suggested that pores must be located at stress singularities created by the prosthesis and bone geometries to significantly influence the aseptic loosening scenario.

Cement mantle thickness has been identified as critical to the longevity of femoral THA components, with thin cement areas allowing sooner through-cracking (Kawate et al, 1998). Good cement interdigitation and a pure cement thickness of at least 2-3 mm are recommended for fixation longevity (Dorr et al, 1983; Hodgkinson et al, 1993). As deep cement interdigitation is generally achieved by forcing the cup into acetabulum while cement cures, these two objectives are not trivial to achieve in reality (Lichtinger and Müller, 1998).

Despite suggestions that aseptic loosening of the cemented polyethylene cup is driven by biological processes (Schmalzried et al, 1992), several experimental studies have simulated the mechanical loading condition in the cement mantle, finding similar failure patterns and survival life as those reported clinically (Tong et al, 2008; Wang et al, 2009). Under mechanical loading, however, debonding starts at the dome of the cup (where stresses are highest), and propagates to the extremities. Unfortunately, the authors of these studies did not comment on whether debonding comprised of cement fracture, trabeculae fracture, or both. Corresponding computational analyses suggested that the highest cement stresses actually occurred at the cup-cement interface (Tong et al, 2008). These studies show that the construct may fail mechanically in principle, even though the failure mode is generally biological in vivo.

The current study computationally investigates the dependency of mechanical fatigue life of the acetabular cement mantle on the cement mantle thickness, cup penetration depth, and the presence of cement porosity. The aim is to discover if these factors make the cement mantle vulnerable to early mechanical fatigue failure and hence provide a potential path for wear debris. It was speculated that high cup penetration and a thin mantle would both elevate cement mantle stresses sufficiently to advance fatigue failure. The effects of these factors on cancellous bone stress amplification are also recorded, as this may promote cement-bone demarcation. This research is clinically relevant for two reasons. Firstly, if mechanical failure of the cement mantle is significantly accelerated, pathways for polyethylene debris to access the cement-bone interface may be created, aiding bone resorption at the cement-bone interface. Secondly, cement mantle cracking may impart sufficient loads to aid cancellous bone resorption at this interface.

6.2 METHODS

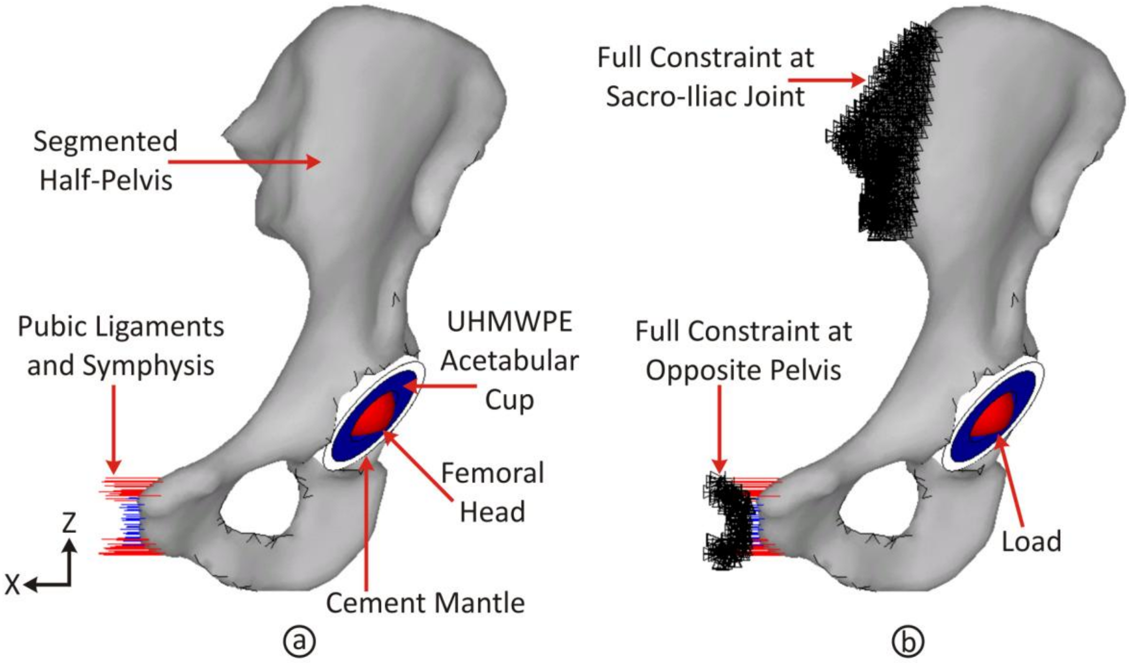

Figure 6.1: The geometry (a) and boundary conditions (b) of the FE model.

A hemi-pelvis geometry was segmented from a computed tomography (CT) scan and imported into Rhinoceros 4.0 (McNeel, Seattle, USA), where it was cut to accommodate the cement and prostheses (figure 6.1). These were positioned using anatomic landmarks with a cup angle of 42° and an anteversion angle of 14°. The pelvis was meshed with four-node first-order tetrahedral elements with an edge length of 5 mm. Location-based cancellous bone elastic modulus (E, MPa) was derived from the apparent element densities (ρ_{APP}) found in the CT scan, using equation 6.1 (Zannoni et al, 1998). The cortex was simulated with an external layer of first-order shell elements 1.5 mm thick. All medical devices were simulated with second-order tetrahedral elements, with an edge length of 2 mm or less. The material properties used are given in table 6.1 (Callister, 1994; Dalstra and Huiskes, 1995; Kurtz et al, 2000; Roques, 2003). The polyethylene cup and steel femoral head geometries were taken from the DePuy Elite Range (DePuy, Warsaw, USA). The hip contact force was applied to the femoral head from gait data (Bergmann et al, 2001), assuming a patient weight of 80 kg: this weight is close to the average weight for both males and females between the ages of 20 and 74 (US Department of Health and Human Services, 2004). The pelvis was fully-constrained at the sacro-iliac joint, and at the pubic symphysis (compressive spring stiffness 1500 N/mm) and the inferior and superior pubic ligaments (tensile spring stiffness 700 N/mm) (Dakin et al, 2001).

$$E = k \cdot \rho_{APP}^{\ 3}$$ Equation 6.1 (Zannoni et al, 1998)

Where k=4249 GPa $(g/cm^3)^{-3}$.

Component / Material	Elastic Modulus (MPa)	Poisson's Ratio
Cortical Bone	17,000	0.3
Cancellous Bone	From CT scan	0.2
Bone Cement	2,800	0.3
UHMWPE Cup	875	0.45
Steel Femoral Head	210,000	0.3

Table 6.1: The mechanical properties of materials used in finite element simulations (Dalstra and Huiskes, 1995; Dalstra et al, 1995; Li and Aspden, 1997; Callister, 1994; Harper and Bondfield, 2000; Kurtz et al, 2000; Roques, 2003).

A bonded contact model defined the cement-bone interface, while a sliding contact model (μ=0.065) was adopted at the bearing surface. Three different cup penetration rates were used, as were two different cement mantle thicknesses, making six types of simulation. For each type, four cases with different pore distributions were simulated; this number of repeats was found to give a 95% confidence interval range of 1% of the average cement mantle fatigue life. The number of pores in each cement mantle and the volume of each pore were assumed to be log-normally distributed and determined using a random number generator by means of the method of Jeffers (2005) (figure 6.2) and the pore population data of

Coultrup et al (2009). The centroid of each pore was selected from a 10,000 discrete points within the cement mantle, again using a random number generator. Where pore values overlapped cement, the overlapping cement material was subtracted prior to meshing, meaning pores were directly modelled in the cement mesh. Cement thicknesses of 2 mm and 4 mm were simulated.

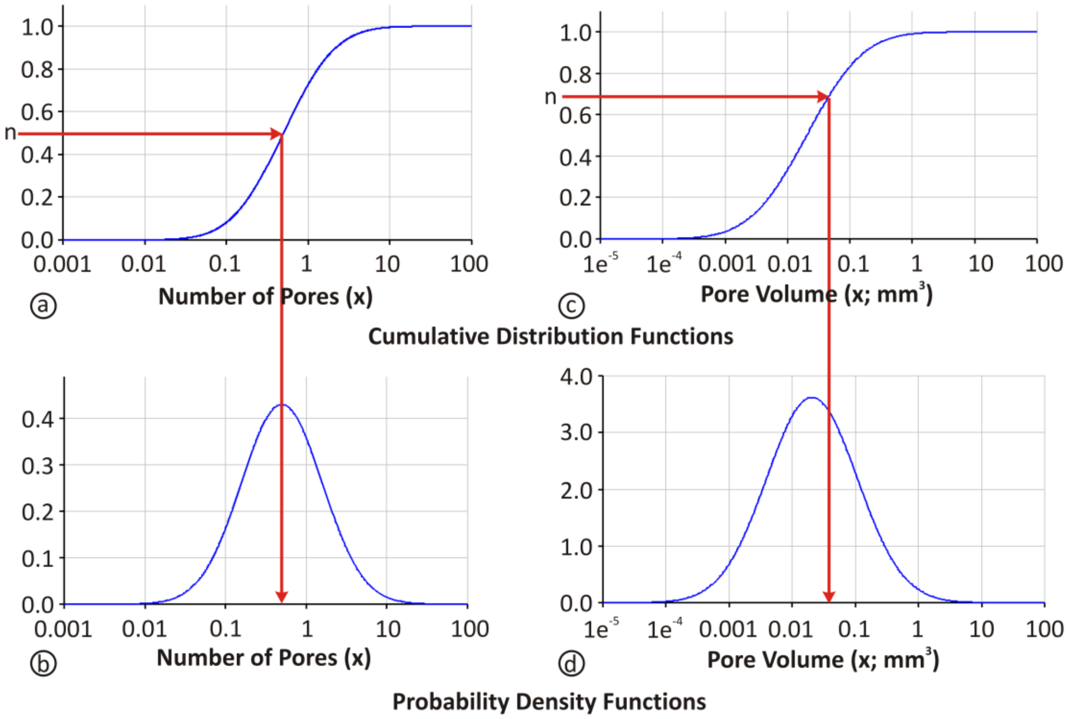

Figure 6.2: The procedure for calculating the number of pores (a and b) and the volume of each pore (c and d) from random numbers (n) between 0 and 1. Number of pores relevant for 2092.9 mm^3 of vacuum-mixed CMW-1 bone cement.

A damage accumulation routine, based on that published by Stolk et al (2004) was used to simulate fatigue failure of the cement mantle. Fatigue loading cycles were simulated incrementally in batches of thousands of cycles. For each element, the number of cycles to failure (N_F) was calculated from a theoretically pore-free S-N curve for bone cement (equation 6.2; Jeffers, 2005) considering the element stress (σ, MPa), with a damage scalar (D) accumulating in elements based on the number of cycles elapsed (N) (equation 6.3). When D exceeded 0.9 in any cement element, the element was assumed to be fully-damaged, so its elastic modulus was reduced 100 fold. Cement creep (ε_C) was also simulated using the same method as Stolk et al (2004) (equation 6.4).

$\log(N_F)=(78.39-\sigma)\cdot 11.22$ Equation 6.2

$$\Delta D = \frac{\Delta N}{N_F}$$ Equation 6.3

$$\varepsilon_C = 7.985\text{x}10^{7} \cdot N^{0.41130.116\log\sigma} \cdot \sigma^{1.9063}$$ Equation 6.4

Polyethylene cup penetration rates of 0.00, 0.45 and 0.90 mm/million cycles were chosen to achieve penetration depths upon failure of 0mm, 1-2mm and 3-4mm respectively (Madey et al, 1997; Callaghan et al, 2000; Wroblewski et al, 2004). Penetration was simulated using a mesh-morphing method. The femoral head was offset in each increment in the direction of load application, by a distance determined from the number of loading cycles simulated. Polyethylene cup nodes on the bearing surface were offset to account for this hew head location, and internal cup nodes were displaced so their proportional distance between the external surface and the bearing surface was maintained. The failure point for each cement mantle was arbitrarily chosen to be when 1% of the cement became fully damaged.

6.3 Results

In all simulations, a high-stress region was located in the cement above the femoral head, in line with the load vector (figure 6.3). At the start of fatigue simulations, the initial stresses in all elements were reduced due to cement creep (figures 6.3 and 6.4). As the simulations progressed, the creep rate diminished, but continued to reduce cement stresses throughout. The penetration of the acetabular cup increased the stress in elements directly above the femoral head (figure 6.3). After a given number of cycles, the effect of cup penetration became more significant than the stress-relaxing effect of creep, causing stress amplification in the high-stress region (figure 6.4). When elements became fully-damaged, high stresses were transferred to neighbouring elements, causing many elements to become fully damaged in quick succession. Failure consistently occurred at the cement-cup interface.

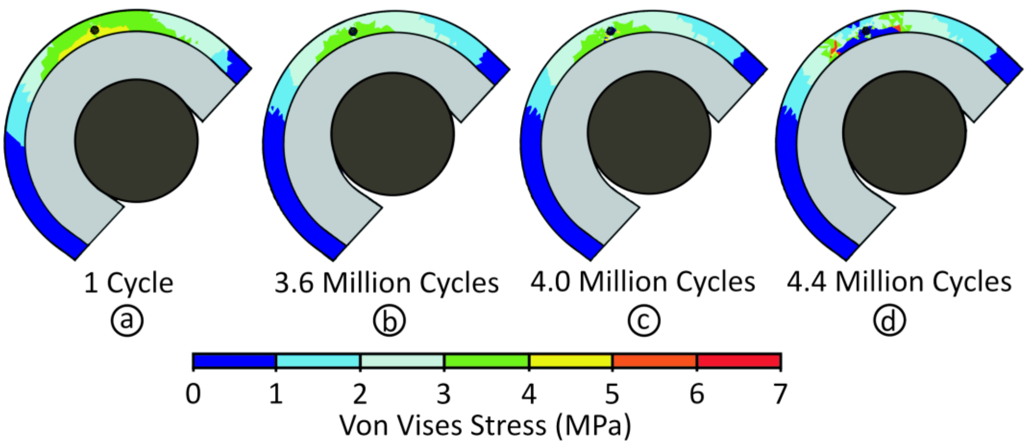

Figure 6.3: Cement mantle stress relaxation due to creep (a to b), the initial failure of elements at a pore (c), and the failure of cement elements at the cement-cup interface (d). Damaged elements may be identified by low stresses, due to the reduction in elastic modulus.

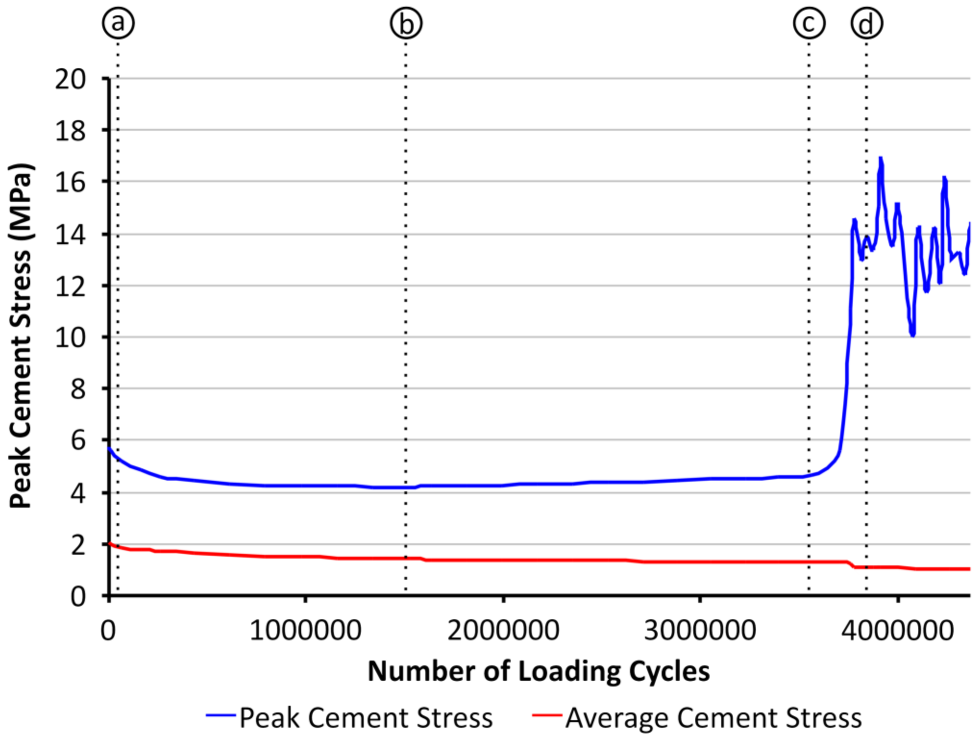

Figure 6.4: The variation of maximum cement stress during simulations. Cement stress reduction due to creep (a), stress augmentation due to cup penetration (b), initial cement failure (c) and variable peak stress due to chronic cement element failure (d) are marked.

Reducing the cement mantle thickness and increasing the rate of polyethylene cup penetration both reduced the number of cycles required to achieve failure of the cement mantle (figure 6.5). Using a cement mantle thickness of 2 mm instead of 4 mm reduced the fatigue life of the cement mantle by between 9 and 11%, depending on the cup penetration rate. Figure 6.5 shows that increasing the penetration rate from 0 mm/million cycles to 0.45 mm/million cycles and 0.9 mm/million cycles reduced the fatigue life of the cement mantle by 3-5 % and 9-11% respectively.

The number of pores in simulations varied between zero and sixteen. In some cases elements around pores in the high-stress cement region became damaged early. However, the effect of porosity on the predicted fatigue lives of the cement mantles was generally negligible (figure 6.5). UHMWPE cup stresses were found to be between 6 and 8MPa. Since this is well below the yield stress of the material (Callister, 1994), it was assumed that there was no permanent deformation or damage to the cup, other than simulated wear.

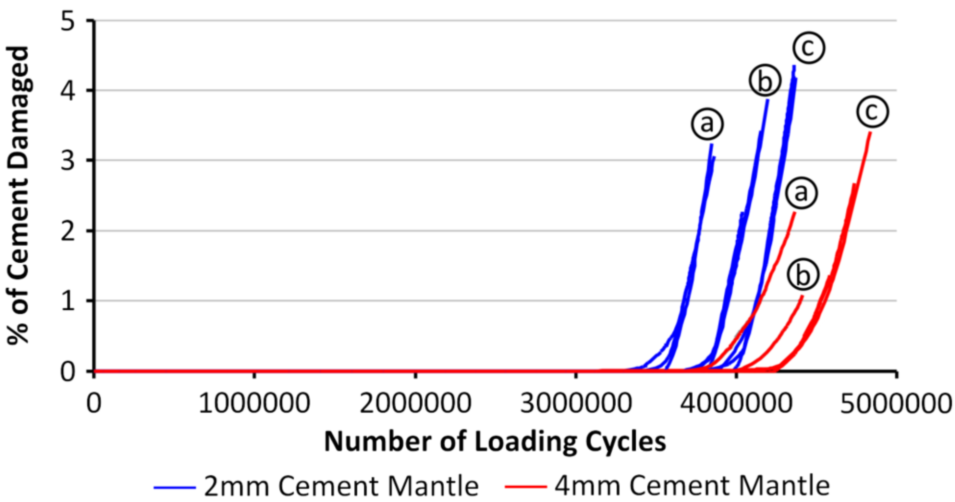

Figure 6.5: The accumulation of cement damage in all simulations. Polyethylene cup penetration rate is indicated by letters: (a) 0.90 mm / million loading cycles, (b) 0.45 mm / million load cycles, (c) 0.00 mm / million load cycles.

Cancellous bone stresses were heavily dependent on the cement mantle thickness (figure 6.6). Initial cancellous bone stresses were approximately 50% higher for the 2 mm cement mantle when compared to the 4 mm cement mantle. However, cup penetration and cement porosity had a negligible effect on cancellous bone stresses. Where cement elements became damaged, local cancellous bone stresses were markedly effected (figure 6.6), suggesting that cement cracking would have a critical effect on the long-term integrity of cancellous bone.

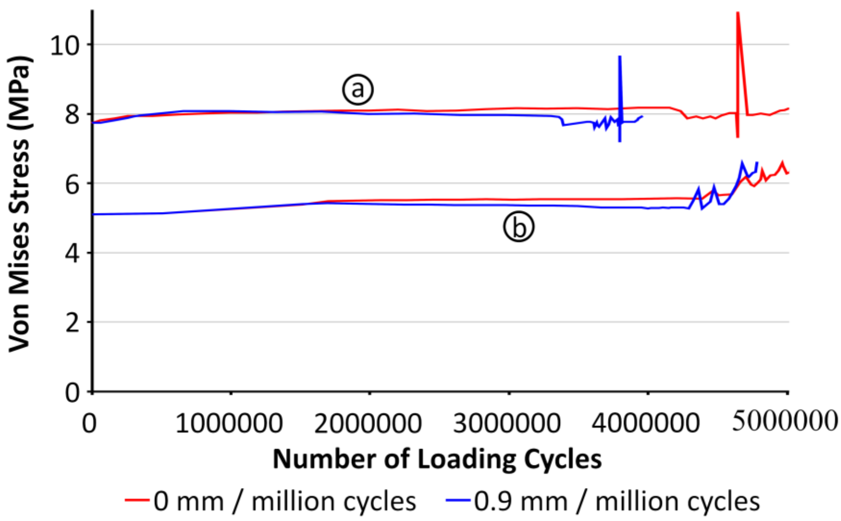

Figure 6.6: The profile of maximum cancellous bone stress during damage accumulation simulations. 2 mm cement mantle thickness (a) and 4 mm cement mantle thickness (b) are indicated.

6.4 Discussion

The principle objective of this study was to determine the effect of cup penetration, cement mantle thickness and cement porosity on long-term predictions of the mechanical failure of the polyethylene cup / cement / acetabular bone construct. Cement stresses are initially reduced by cement creep, but may be increased later in the life of the construct due to polyethylene cup penetration. A high penetration rate will result in faster fatigue failure of the cement mantle due to stress amplification. This appears to occur as a thin cement mantle spreads loading from the femoral head over a smaller volume of cement, thus raising the peak stress. However, polyethylene cup penetration had a negligible effect on cancellous bone stresses. Simulations of the thinner (2 mm) cement mantle resulted in a significantly shorter cement fatigue life due to the associated stress amplification, and also significantly higher cancellous bone stresses. The effect of porosity was negligible on cement mantle fatigue life and cancellous bone stresses.

There are a number of limitations to this study. The continuum damage mechanics method adopted greatly simplifies the process of fatigue crack initiation and propagation, though the complexity of fracture mechanics methods made them impractical for this study (Anderson, 2005). Damage in elements was described in via a scalar quantity derived from Von Mises stresses, meaning the directionality of cracking was not simulated in analyses. Stolk et al (2004) presented a methodology whereby damage tensors are recorded for all elements based on the principle stress direction, meaning the direction cracking and the perpendicular loss of stiffness in tension is simulated. This approach was not adopted here due to the high computational cost involved.

The fatigue lives predicted in figure 6.5 are far shorter than those reported clinically. This is because the fatigue data used was derived from mechanical testing at high stress (7 to 20 MPa), while the stresses predicted in this study were significantly lower (0 to 7 MPa). To determine fatigue life under lower stress, the fatigue data were extrapolated, though this ignores the existence of an endurance limit for cement. Also, fatigue data was manipulated to make it relevant to pore-free specimens. To account for the short fatigue lives, very high cup penetration rates were used to achieve clinically-relevant penetration depths.

To assess the effect of the limitation of this fatigue data computationally, additional simulations without porosity were conducted using the fatigue data of Murphy and Prendergast (1999) (equation 6.5). This data is derived from more specimens and has been used elsewhere to successfully rank the fatigue performance of four different cemented femoral stems in accordance with their clinical success (Stolk et al, 2007). Using this data, cement mantle fatigue lives between 17 and 24 million loading cycles were determined for the failure criterion: this represents 10 to 15 years postoperatively loading cycles (Silva et al, 2002), which is comparable to the survival times reported clinically (Wroblewski et al, 2004). In order to achieve the same cup penetration depths as before, a penetration rate of 0.18 mm/million load cycles was used for the 'high penetration rate' state. For these conditions, a change in cement mantle thickness from 2 to 4 mm resulted in a reduction in cement mantle fatigue life between 5 and 10%. A change from no penetration to a penetration rate of 0.18 mm/million loading cycles reduced the cement mantle fatigue life between 17 and 22%.

$\sigma=-4.736 \cdot \log(N_F)+37.8$ Equation 6.5 (Murphy and Prendergast, 1999)

Simulations of the mechanical failure of the cement mantle predicted damage initiation at the cement-cup interface, and subsequent through-cracking of the cement mantle (figure 6.3). However, clinical and experimental studies report failure of the construct at the cement-bone interface (Hodgkinson et al, 1988; Garcia-Cimbrelo et al, 1997; Tong et al, 2008; Wang et al, 2009). It is worth noting though that it is difficult to differentiate between cement and polyethylene on radiographs, so failure at the cement-polyethylene interface should not be completely discounted. The fact that failure was not identified at this interface in an autopsy study (Schmalzried et al, 1992) suggests it may not be a common occurrence though. From a purely-mechanical perspective, it may be that another factor makes the cement-bone interface prone to failure, such as weak trabeculae, poor apposition of cement into interstices or the presence of interfacial cement defects (Garcia-Cimbrelo et al, 1997; Tong et al, 2008). The theory of cancellous bone resorption and fibrous tissue formation to achieve aseptic loosening of the cemented polyethylene cup does not preclude the contribution of mechanical factors.

Cement stresses were initially found to be between 5 and 7 MPa, but are quickly attenuated by cement creep. Bone cement is projected to possess an endurance limit below 6 MPa (Coultrup et al, 2009; Suresh, 2004). A large proportion of elements in the cement mantle experienced a stress below this stress level for the majority of simulations, meaning the failure simulated here may not be clinically relevant in the absence of stress amplification by another factor. This supports the clinical finding that aseptic loosening for a polyethylene cup is not exclusively mechanical in origin (Schmalzried et al, 1992; Zicat et al, 1995; Mai et al, 1996; Jones et al, 1999). This study has shown that where there is high cup penetration and a thin cement mantle, the failure of the cement mantle due to fatigue loading may become a realistic scenario. Additionally, high wear of the polyethylene cup may lead to impingement of the stem neck on the cup, wrenching it from the acetabulum (Wroblewski et al, 2009).

Figure 6.6 shows that peak initial cancellous bone stress for a 4 mm cement mantle at approximately 5.1 MPa, and approximately 7.7 MPa for a 2 mm cement mantle, and located at the superior acetabular rim and in line with the load vector. These values increased for subsequent cement mantle failure. These stresses are much higher than those reported in the natural hip (Phillips et al, 2007), the reported yield stress of cancellous bone (Burgers et al, 2008) and the threshold required for bone resorption (Schmalzried et al, 1992). While retrieval studies have found polyethylene wear particles and macrophages, it is also possible that this mechanical stimulus contributes to the biological bone resorption process outlined by Schmalzried et al (1992).

A novel method was used in this study to model cement porosity in simulations, confirming that porosity has a negligible effect on the fatigue life of the cement mantle (Malchau and Herberts, 1996; Ling and Lee, 1998). This is thought to be because the highly-stressed region is very small, so the probability of it containing a pore was low. Therefore, the majority of pores did not contribute to the fatigue failure process (Jeffers et al, 2007). Where pores were found in the high-stress region, adjacent cement elements did fail earlier, but the resultant stress transfer was slow, meaning the failure criterion was achieved after a similar number of loading cycles. It should be noted that Jeffers et al (2007) reported a significant effect from including porosity in simulations of the femoral cement mantle. The reason for this discrepancy is not clear, but may be due to the different loading case.

In summary, this study has shown that pores have a negligible effect on the fatigue failure process of the acetabular cement mantle. By considering mechanical factors alone, both cement mantle thickness and cup penetration have a significant effect on the fatigue life of the cement mantle. A thick cement mantle appears to be important for achieving low cement and cancellous bone stresses, while deep cement interdigitation in cancellous bone is recommended to prolong the cement-bone interface (DePuy International Ltd, 2007): however it may be difficult to achieve both in practice. The author proposes that mechanical stress amplification by stress concentration, in tandem with biological effects, may account for the high clinical incidence of early aseptic loosening in cemented polyethylene cups with high wear rates.

7 THE QUANTIFICATION OF INTERDIGITATED BONE CEMENT STRESSES BY HOMOGENISATION

7.1 INTRODUCTION

Aseptic loosening is the dominant cause of failure in cemented THA femoral stems (Furnes et al, 2007; Karrholm et al, 2008), and is induced by fatigue loading. Clinically, stem-cement debonding and crack initiation at the bone-cement interface and pores appear to be key events. They allow cement through-cracking initially, and later osteolysis, stem pistoning and bone resorption prior to symptomatic gross loosening of the implant. There is no general consensus on the role of wear-induced osteolysis, though there is evidence that this process only has a significant effect on the failure process after through-cracking in the cement mantle (Jasty et al, 1991; Schulte et al, 1993; Kawate et al, 1998).

Modern force-closed cemented femoral stems are highly polished and tapered in two or three planes, allowing them to subside into the cement mantle and distribute load along their entire length (Huiskes et al, 1998; Shah, 2005). In France, the line-to-line cemented stem philosophy is both accepted and successful (Hamadouche et al, 2002; Langlais et al, 2003; Kerboull et al, 2004). In contrast to conventional approaches to cemented stem design, this procedure aims to remove as much mechanically-weak cancellous bone as possible by using the largest possible femoral broach, while the stem completely fills the cavity, forcing all cement into cancellous bone (Scheerlinck and Casteleyn, 2006). The longevity of these stems may result from direct stem-cortex contact and a large stem surface area (Janssen et al, 2007).

Many other authors have used continuum damage mechanics (CDM) computational models to predict the performance of given prosthesis designs under fatigue loading, and to understand the mechanical load transfer in the proximal femur and acetabulum (Stolk et al, 2004; Jeffers, 2005; Janssen et al, 2006; Stolk et al, 2007). As a result of this approach, the importance of limiting cement stress concentration is understood (Stolk et al, 2003b). To achieve computational efficiency, these analyses all assume that stress concentrations created by the trabecular structure are negligible; a pure cement region is assumed. Recent indications that the bone-cement interface is the preferable location for cement crack initiation (Kawate et al, 1998; Race et al, 2003; Jeffers et al, 2007; Leung et al, 2008) lead one to question the validity of this assumption.

Homogenisation provides a means for computationally modelling complex structures efficiently. A repeatable representative unit of the micro-scale structure is defined, and material properties for the structure are determined. A macro-scale model of the entire structure is defined, which contains Representative Volume Elements (RVEs). Each RVE represents one micro-structural model, and have the material properties determined from the micro-scale model. After the macro-scale model is solved, individual RVEs may be interrogated by applying solution nodal deflections to the micro-scale model (Hollister et al, 1991; Hollister et al, 1994). The architecture type and global apparent bone density for trabecular bone is known to vary significantly (Gibson, 1985), which in turn has been found to significantly affect the stiffness matrix of micro-scale models (Kowalzyck, 2003). Indeed, the elastic modulus of a composite (trabecular) bone-cement structure has recently been found to be less than or comparable to the elastic modulus of pure cement (2.1-3.0 GPa; Race et al, 2007). Because there is no chemical bonding between components, load transfer is achieved by mechanical interlock only, so strains occur due to relative sliding between cement and trabeculae, rather than by deformation (Miller et al, 2008). Using aluminium foam as a cancellous bone substitute, Leung et al (2008) reported cement crack initiation at the interface cement-trabeculae in four-point bend fatigue specimens, which may relate to this high local strain.

The objective of this study was to use a homogenisation method to determine the interdigitated bone cement stresses for femoral hip stems. Additionally, this study explores the effect of the apparent cancellous bone density, the cement-trabeculae bonding condition and trabeculae and the interdigitation depth on the magnitude of cement stresses. Analysis is conducted for force-closed and line-to-line femoral stems to determine if the success of the line-to-line philosophy can be explained from static stress distributions.

7.2 METHODS

7.2.1 Material Properties of Micro-Scale Models

Three micro-scale models were used to represent the repeatable structure of trabecular interdigitated with bone cement. The volumetric density of cancellous bone at the proximal femur is reported to vary between approximately 0.1 and 0.3 (average 0.2; Ulrich et al, 1999). To reflect this variation, three cancellous bone architectures were generated with volumetric densities of 0.1, 0.2 and 0.3, based on the study of Kowalzyck (2003). Observations of trabeculae architecture have revealed a transition from a bar-like structure to a plate-like structure when apparent volumetric density exceeds 0.2 (Gibson, 1985). Therefore, the parameters L_1, L_2, and R were varied to achieve this effect in the micro-scale models (figure 7.1; table 7.3). The unit cube size was 0.7mm, representative of trabecular spacing (Ulrich et al, 1999). The material properties applied to the structure are given in table 7.1. The trabecular bone and cement were meshed with tetrahedral first-order elements, with an edge length of 0.025mm and 0.075mm respectively. Two states of bonding between trabeculae and bone cement were considered: fully bonded, and a sliding contact with a coefficient of friction of 0.3 (Janssen et al, 2008).

Model	Material / Component	Elastic Modulus (GPa)	Poisson's Ratio
Micro-Scale Model	Individual Trabeculae	5	0.3
	Bone Cement	2.8	0.3
Macro-Scale Model	Steel Femoral Component	210	0.3
	Bone Cement	2.8	0.3
	Cortical Bone	17	0.3

Table 7.1: The material properties used in finite element simulations (Choi et al, 1990; Van Rietbergen et al, 1995; Roques, 2004).

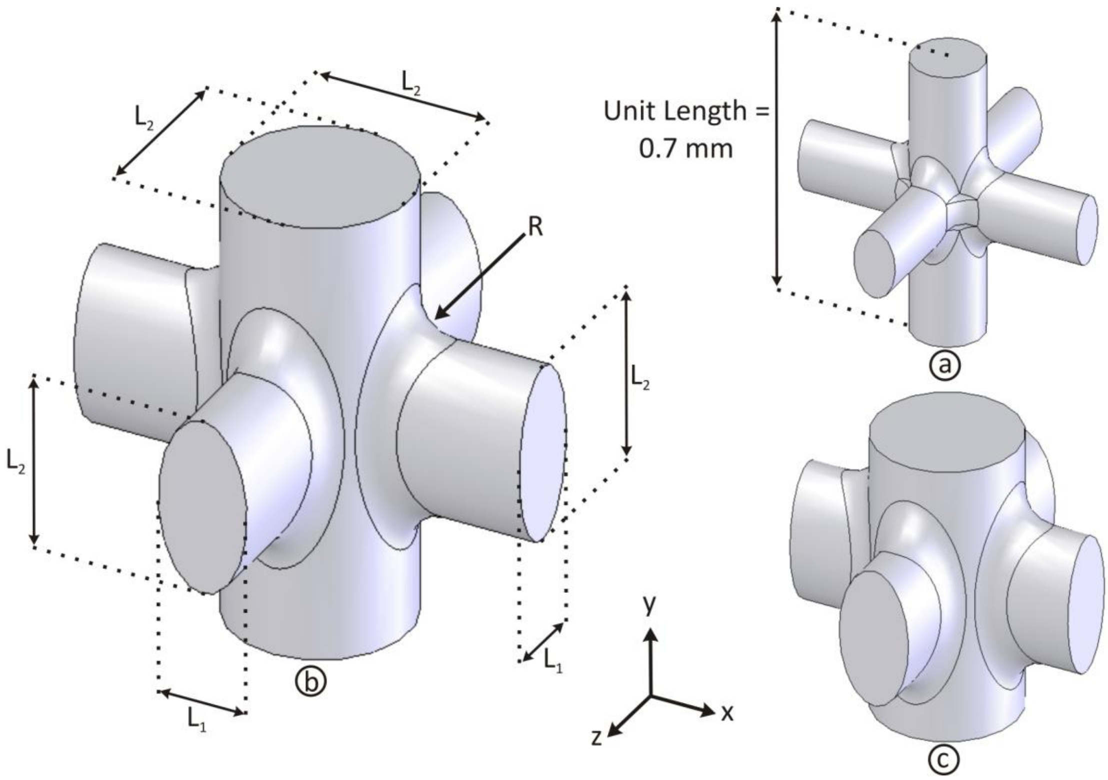

Figure 7.1: The trabeculae architectures for volumetric densities of 0.1 (a), 0.2 (b) and 0,3 (c). Image (b) is enlarged to show the architecture parameters L_1, L_2 and R. The x, y, z coordinate system adopted for material property calculation is given.

For any structure and loading condition, Hooke's Law may be used to relate the applied strain (ε_{ij}) to the resultant stress (σ_{ij}) using the compliance matrix for the structure (C) (equation 7.1). Since the micro-scale models adopted are symmetrical about two axes they may assumed to be orthotropic (Cowin, 1989); thus, the compliance matrix may be re-defined in terms of the elastic modulus (E), shear modulus (G) and Poisson's ratio (ν) component (equation 7.2). Material properties were determined by loading micro-scale models in pure tension (E_X, E_Y and E_Z), pure shear (G_{XY}, G_{YZ} and G_{XZ}) and multi-directional tension (ν_{XY}, ν_{YZ} and ν_{XZ}). In each case, elastic strains were applied to nodes on given faces of the unit cube, while the stress generated was determined from reaction forces.

$$\varepsilon = C \cdot \sigma \qquad \text{Equation 7.1}$$

$$\begin{Bmatrix} \varepsilon_X \\ \varepsilon_Y \\ \varepsilon_Z \\ \varepsilon_{XY} \\ \varepsilon_{YZ} \\ \varepsilon_{XZ} \end{Bmatrix} = \begin{bmatrix} 1/E_X & -\nu_{XY}/E_X & -\nu_{XZ}/E_Z & 0 & 0 & 0 \\ & 1/E_Y & -\nu_{YZ}/E_Y & 0 & 0 & 0 \\ & & 1/E_Z & 0 & 0 & 0 \\ & & & 1/G_{XY} & 0 & 0 \\ & sym & & & 1/G_{YZ} & 0 \\ & & & & & 1/G_{XZ} \end{bmatrix} \cdot \begin{Bmatrix} \sigma_X \\ \sigma_Y \\ \sigma_Z \\ \sigma_{XY} \\ \sigma_{YZ} \\ \sigma_{XZ} \end{Bmatrix} \qquad \text{Equation 7.2}$$

7.2.2 Macro-Scale Models

Macro-scale models were representative of force-closed and line-to-line cemented femoral stems (figure 7.2). All bone and cement volumes were symmetrical about the longitudinal axis of the stem. The interdigitated region was 2.1 mm thick, the cortex was 5 mm thick, and the cement mantle was 2 mm thick where it existed (DePuy International Ltd, 2007). The line-to-line model contained a distal void in keeping with the surgical technique (Scheerlinck and Casteleyn, 2006). Micro-scale models were represented as individual hexahedral RVEs, of edge length 0.7 mm: the mechanical properties determined for micro-scale models were applied to these elements (table 7.3). In all cases, the thickest trabeculae was assumed to orientated along the length of the cement mantle taper (y-axis), whilst thinner trabeculae were assumed to be aligned towards the centre of the stem (x-axis) and radially about the centre (z-axis).

Since the interdigitated region was effectively a tapered cylinder, typical hexahedral meshing would have resulted in highly skewed elements proximally. This skew would represent a change in trabecular spacing, making the model unrepresentative of true cancellous bone (Ulrich et al, 1999). To prevent the generation of highly skewed elements, the interdigitated region was split into 18 sections longitudinally, which were meshed individually and connected with bonded contact models. The cortex, stem, cement and distal cancellous bone were meshed with elements of a minimum edge length of 2 mm, 1 mm, 1 mm and 1 mm respectively, with the applied mechanical properties given in table 7.1. All models were constrained in all degrees of freedom at the distal cortex and cancellous bone (figure 7.2). Peak gait loads from "normal" walking were applied to the femoral head, assuming a patient weight of 80kg (Bergmann et al, 2001).

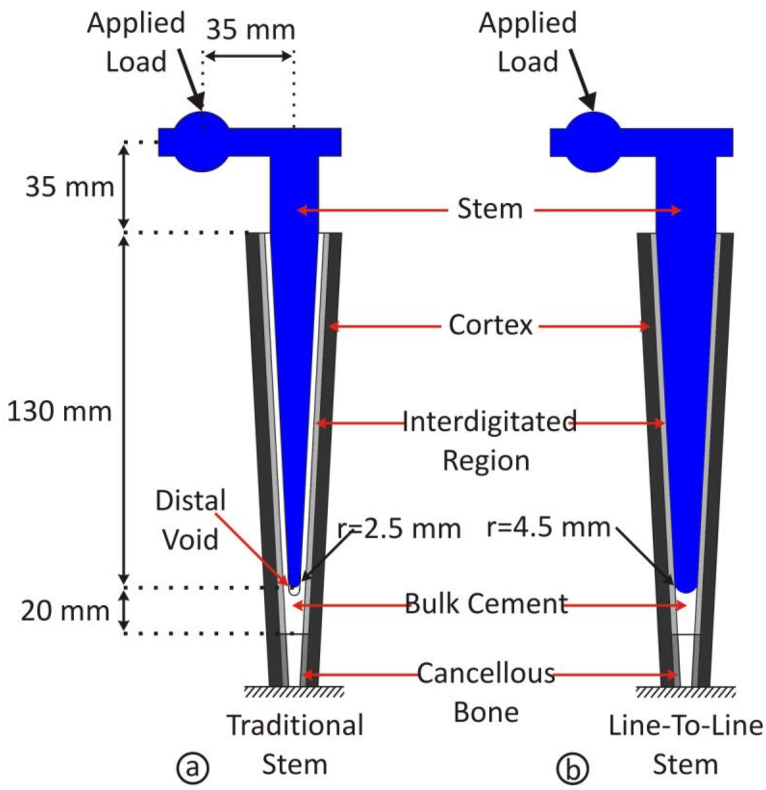

Figure 7.2: Cross sections of model geometries for the traditional (a) and line-to-line (b) cemented femoral stems.

Independent Variable	Levels			
	1	2	3	4
Homogenisation Simulations				
Stem Type	Force-Closed	Line-to-Line	-	-
RVE Apparent Density	0.1	0.2	0.3	-
Interdigitation Depth (mm)	0	0.7	1.4	2.1
Cement-Bone Bonding	Bonded	Un-Bonded	-	-
Control Simulations				
Stem Type	Force-Closed	Line-to-Line	-	-

Table 7.2: The independent variables and levels adopted for this study.

For homogenisation simulations, the effect of cement penetration depth, cement-bone bonding condition and cancellous bone apparent density were all varied by toggling the mechanical properties of elements prior to solving (table 7.2). Therefore, for an intermediate interdigitation depth, some elements in the interdigitated region represented interdigitated cancellous bone, while some represented pure cancellous bone. Additionally, two control analyses were conducted, which did not use homogenisation. Force-closed and line-to-line stems were simulated where the interdigitated region was considered to have the same mechanical properties as pure cement; this comparison against the conventional CDM damage accumulation method allowed the value of the homogenisation method to be assessed.

7.2.3 Interrogation of Representative Volume Elements

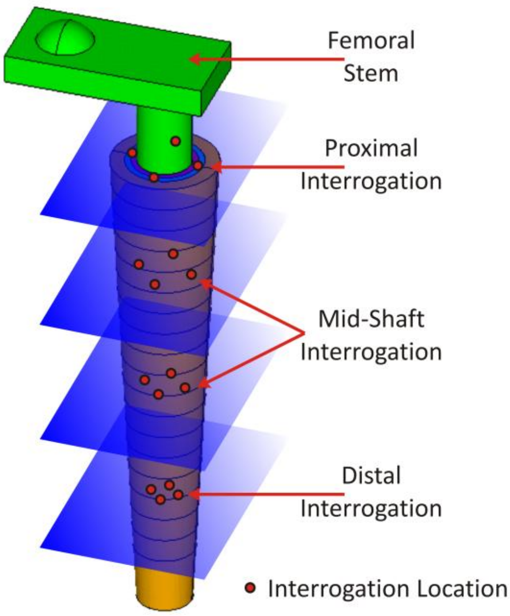

Figure 7.3: The traditional stem model with locations of RVE interrogation marked.

After the macro-scale models were solved, the stress state in selected RVEs was interrogated by applying RVE boundary conditions to micro-scale models. As mentioned in section 7.2.1, all RVEs were slightly skewed to form a tapered cylinder. To ensure micro-scale models incorporated this skew, the mesh of the micro-scale model was morphed to fit the corner nodes of RVEs. For each macro-scale model, 16 RVEs at constant locations were interrogated (figure 7.3), as was the RVE with the highest Von Mises Stress. In each case, the maximum Von Mises cement and trabeculae stresses were determined.

7.3 RESULTS

The material properties found from micro-scale models are reported in table 7.3. Interdigitation greatly increases the elastic and shear moduli of the structure. A sliding cement-trabeculae interface results in a lower stiffness than the bonded condition, as relative motion occurs between components under loading. Notably, an increase in bone apparent density resulted in reduced shear moduli in the x and z directions. As a full-factorial analysis of independent variables was conducted, results from homogenisation simulations are presented as mean effects plots. A discussion of the interpretation of these data is given in section 5.3.

Property	Cancellous Bone Only			Bonded Bone and Cement			Un-bonded Bone and Cement		
Density	0.1	0.2	0.3	0.1	0.2	0.3	0.1	0.2	0.3
R (mm)	0.105	0.140	0.175	0.105	0.140	0.175	0.105	0.140	0.175
L_1 (mm)	0.105	0.140	0.175	0.105	0.140	0.175	0.105	0.140	0.175
L_2 (mm)	0.175	0.280	0.350	0.175	0.280	0.350	0.175	0.280	0.350
E_X (MPa)	167	396	663	2964	3163	3350	2358	1891	1713
E_Y (MPa)	265	701	1131	2983	3216	3427	2699	2790	2918
E_Z (MPa)	167	396	663	2964	3163	3350	2358	1891	1713
G_{XY} (MPa)	8	57	153	1136	1212	1284	877	712	657
G_{YZ} (MPa)	8	57	153	1136	1212	1284	877	712	657
G_{XZ} (MPa)	3	14	42	1131	1197	1260	822	597	511
ν_{XY}	0.054	0.086	0.115	0.297	0.295	0.293	0.253	0.194	0.164
ν_{YZ}	0.086	0.152	0.197	0.299	0.299	0.299	0.265	0.214	0.172
ν_{XZ}	0.031	0.048	0.065	0.299	0.297	0.296	0.284	0.272	0.263

Table 7.3: The geometric and mechanical properties of micro-scale models.

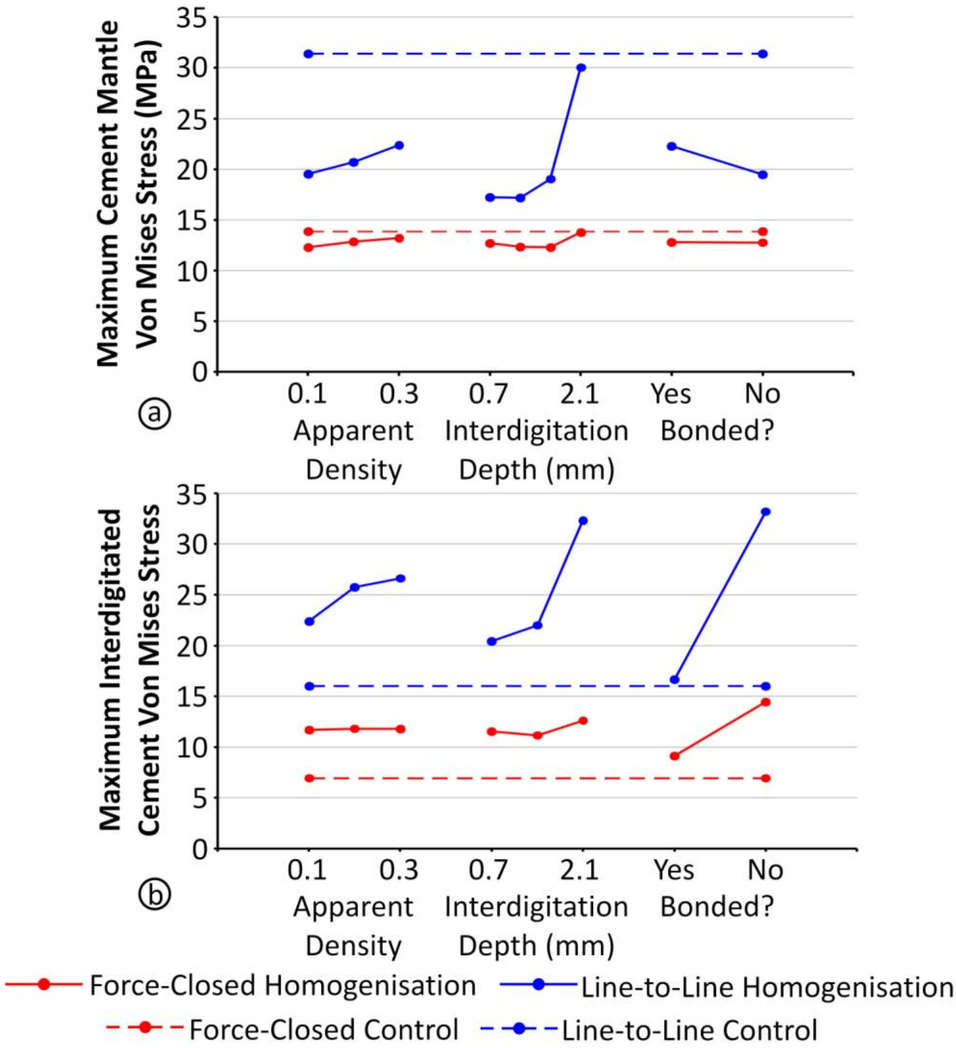

Figure 7.4: Maximum bulk cement mantle Von Mises stresses (a) and interdigited cement Von Mises stresses (b) for reported for both stem types, homogenisation and control methods. The bonded variable relates to the cement-trabeculae condition.

For the independent variables investigated, the maximum values of interdigitated cement stress and cement mantle stress are given in figure 7.4, with a comparison against the control simulations. It is clear from this figure that the maximum stress values found using homogenisation were much higher than those from the control simulations (where trabeculae were not modelled). In all cases, this peak stress was concentrated at the interface with trabeculae (figure 7.5). This concentration was more significant for sliding contact (figure 7.4). In all cases, the highest stresses in both the bulk cement mantle and interdigitated cement were found adjacent to the most distal contact area of the femoral stem (figure 7.6). For the force-closed stem this did not occur at the stem tip as the distal cement cavity ensured there was no contact at this location (figure 7.6). Peak interdigitated cement stresses were consistently found at the interface with pure cement (force-closed stem) or the stem (line-to-line stem).

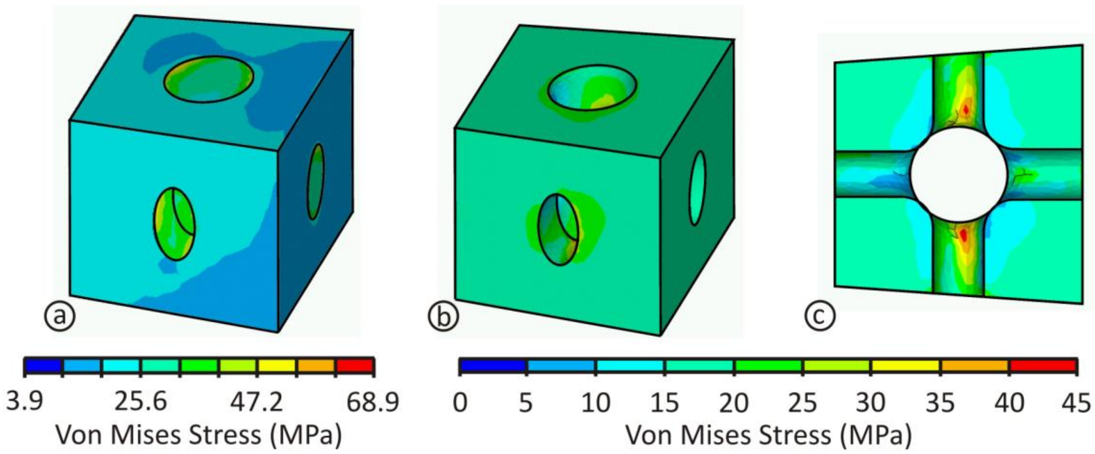

Figure 7.5: The stress distribution in an interrogated RVE, found adjacent to the distal tip of a force-closed stem (a). The sliding contact trabeculae-cement condition reveals high cement stresses (b), and localised stress concentration at the cement-bone interface, apparent on a cross-sectional view (c).

In the macro-scale model, the two different stem types imparted different stress patterns on the metaphysis; while stresses were lower for the line-to-line stem at some locations, the peak cement stress was consistently higher than for the force-closed stem (figure 7.4). An increase in interdigitation depth resulted in little change in the magnitude of stress in interdigitated cement and the cement mantle, until the interdigitation reached the cortex: in this case, a large increase in both stresses was apparent (figure 7.4). For a bonded trabeculae-cement model, the effect of apparent trabecular bone density on interdigitated cement stresses appears to be negligible. However, for a sliding contact model, this stress steadily increased for increasing bone apparent density (figure 7.4).

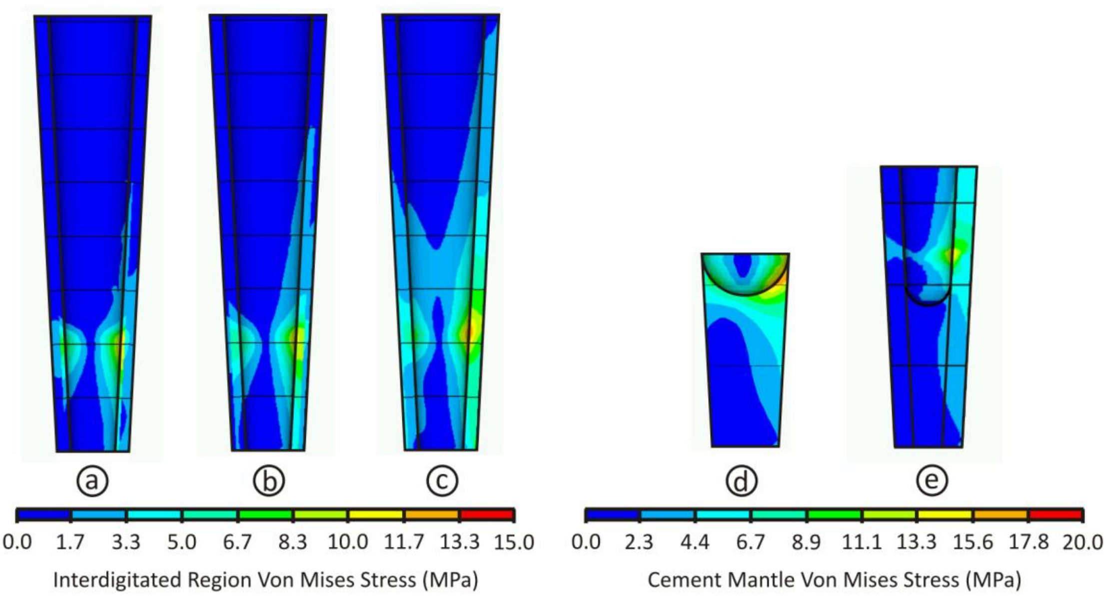

Figure 7.6: Plots of Von Mises stress in the distal interdigitated region for a force-closed stem, a sliding cement-bone interface and interdigitation depths of 0.7mm (a), 1.4mm (b) and 2.1mm (c). For (a) and (b) pure cancellous bone is included in results. Plots of cement mantle stress line-to-line (d) and a force-closed stems (distal region, e) show that cement stresses are highly concentrated at the distal stem tip for both stem types.

7.4 Discussion

This study has illustrated how a homogenisation method can be used to determine interdigitated cement stresses in computational models of the entire replaced proximal femur. Models of two different stem types were used to show how the method could distinguish the resulting stress distributions, and compute the effect of varying apparent trabecular bone density, interdigitation depth and trabeculae-cement bonding condition. The study attempted to reveal stress magnitudes in interdigitated cement, and elucidate the surprising success of the line-to-line cemented stem.

The mechanical properties for cement-bone microstructures are reported in table 7.3, and are comparable with those determined by other authors using experimental and computational methods (Majumdar et al, 1996; Ulrich et al, 1999; Kowalzyck, 2003; Race et al, 2007). It is not surprising that reinforcement of the cancellous structure with cement increases the shear and elastic modului of the structure. For a bonded trabeculae-cement contact model, the increase in elastic and shear moduli for increasing apparent bone density is due to the presence of more bone with relatively high moduli. However, for a sliding contact condition, relative motion allows the majority of strain to be taken up in the cement alone (Race et al, 2007). Increasing cancellous bone apparent density was modelled as the formation of plates aligned in the 'y' direction (figure 7.1); this ensured load was borne by an increasingly smaller cement cross-sectional area, resulting in inferior elastic and shear moduli in 'x' and 'z' directions. Since bone and cement are not physically bonded in vivo, the mechanical properties derived from the sliding contact model are probably more relevant to the clinical condition (Race et al, 2007; Janssen et al, 2008).

Figure 7.4 reveals that the interdigitation stresses calculated in these simulations are much higher than those in the control simulations. While the interdigitated trabecular bone structures and bulk cement have similar mechanical properties (tables 7.1 and 7.4), this increased stress results from stress concentrations created by the stiffer trabecular bone (figure 7.5). Given that a power law dictates the relationship between fatigue life and applied stress (Murphy and Prendergast, 2000; Jeffers et al, 2005), this increased stress may result in a dramatically reduced fatigue life. Again, this author believes that a higher stress results with sliding contact due to lower stress transfer to trabecular bone, and thus higher strain in adjacent cement. These observations of higher stresses in interdigitation than bulk cement back up ideas that cement crack formation may be caused due to stress concentrations caused at trabeculae (Kawate et al, 1998; Race et al, 2003; Leung et al, 2008).

For both stem types, the highest cement mantle and interdigitation stress was located adjacent to the tip of the stem contact. This is because the loading in vivo is chiefly axial, through the bending moment does cause some stress amplification in the medial proximal region. Peak stresses may well be higher for the line-to-line stem because there is no distal cement void, meaning stresses are less-well distributed across the taper (figure 7.6). Other authors have discussed the phenomenon of distal punch-out in shape-closed stems without a distal cavity: in vivo, this may occur for the line-to-line stem as a mechanism of sharing load across the structure better and prolonging the life of the construct (Jasty et al, 1991; Jeffers et al, 2007). This hypothesis, however, cannot be verified in these static simulations.

Perhaps one of the most interesting findings of this study is that where cement proliferates right through to the cortex, higher interdigitated cement stresses result than if proliferation is not complete (figures 7.4 and 7.6). Where proliferation was not complete, the elastic and shear moduli of remaining cancellous bone was low, accommodating significant strain. This agrees with Leung et al (2006), who recorded much higher load transfer for deeper cement penetration into cancellous bone. Where interdigitation was absent, the relatively soft cancellous bone shielded the interdigitated region from high load. However, where interdigitation reached the cortex, higher strain was generated in the interdigitated region, and higher stresses resulted. This finding goes against traditional practices of trying to achieve interdigitation right up to the cortex. Figure 7.6 reveals that a stress approaching 7MPa was generated in bulk cancellous bone where there was complete cement proliferation, which may be enough to cause fracture of trabeculae in vivo under fatigue loading (Burgers et al, 2008).

There are a number of limitations to this study. Where possible, the results of computational models should be experimentally verified; unfortunately this was beyond the scope of the study. Mesh dependency tests were conducted for all models to minimise simulation errors. The stem and femur geometry assumed in this study is a significant simplification, but was adopted to enable hexahedral meshing of the interdigitated region, and to ensure these elements displayed limited skew. Another assumption was that trabecular bone is a repeatable, cubic structure. Retrieval specimens reveal high variability in specimens; indeed, the structure at the femoral neck may be very different to that at the mid-shaft of the femur (Gibson, 1985; Ulrich et al, 1999). This study has considered cement stresses with a view to understanding aseptic loosening. This failure scenario should be considered as a process, not a single event, so its evolution may not be fully realised from an initial stress distribution. It has already been remarked that it is common for stresses to be re-distributed by distal punch-out of the cement mantle, while cement creep may also significantly reduce cement stresses postoperatively. A comparison of stem types and independent variables which influence their efficacy would be better-conducted using a quasi-static damage accumulation method (Stolk et al, 2007). Finally, the micro-scale models with sliding cement-bone contact were assumed to have the same mechanical properties in compression as tension: in practice, the load transfer mechanism in probably very different for these loading mechanisms.

This study has shown how the RVE homogenisation method may be used to solve large-scale models containing a complex, repeatable microstructure. This method has indicated that the peak stress in interdigitated cement is much higher than that previously predicted using established computational methods, as verified by control simulations in this study. The depth of interdigitation appears to affect the strain pattern in the replaced metaphysis. The RVE homogenisation method used in this study has suggested that peak stresses in both the cement mantle and interdigitated region are higher for the line-to-line stem type. Thus, the excellent long-term performance of cemented line-to-line stems (Hamadouche et al, 20002; Langlais et al, 2003) has unfortunately not been explained in static simulations of interdigitated cement.

8 THE SIMULATION OF DAMAGE FORMATION IN INTERDIGITATED BONE CEMENT

8.1 INTRODUCTION

Chapter 7 of this thesis described a homogenisation method to determine the magnitude of stresses in interdigitated cement for two different cemented total hip arthroplasties (THAs). Stresses in interdigitated cement were higher than those observed in the bulk cement mantle, due to stress singularities created at individual trabeculae, particularly when a sliding contact model was assumed between cement and trabeculae.

Other authors have used a continuous damage mechanics (CDM) method to simulate aseptic loosening in cemented THA prostheses (Stolk et al, 2004; Stolk et al, 2007; Coultrup et al, 2010; Janssen et al, 2006). These simulations assume that the cement mantle is homogenous, so represent the region of interdigitated cement in cancellous bone as pure cement. This simplification vastly shortens the solution time, since fewer elements are required. However, given that other authors have reported cement through-crack initiation in cement at the interface with trabeculae in autopsy (Jasty et al, 1991) and experimental studies (Race et al, 2003; Leung et al, 2008), one must question if the omission of individual trabeculae from models is an acceptable simplification.

This study explores the application of a homogenisation approach for simulating the fatigue failure of bone cement interdigitated in a trabeculae bone structure. In this approach the material properties for a repeatable micro-scale structure are determined, and used to solve a macro-scale model of the entire interdigitated cement region. Damage in interdigitated cement is represented in macro-scale models by the deterioration of mechanical properties of RVEs.

To the author's knowledge, this is the first time that such a method has been developed for use in this application. The first aim of this study is to determine whether the method described is suitable for use on a larger scale as a tool to predict the performance of cemented arthroplasties. The second aim was to assess the rationality of the failure process predicted via comparison with the failure mode for the CDM simulation, and also by comparison with clinical observations. In this manner, it is possible to determine if it is necessary to model individual trabeculae. The investigation also aims to provide constructive feedback to others in the research field on the suitability of adoption of this method.

8.2 METHODS

Two different types of simulation were conducted in this study: homogenisation damage accumulation analyses and CDM damage accumulation analyses.

8.2.1 Homogenisation Damage Accumulation Simulations

Homogenisation simulations used the same principles as the method outlined in chapter 7. The method involves solving a macro-scale model based on the solution of multiple micro-scale models. The macro-scale model was chosen as an idealised planar (non-cylindrical) section of a steel line-to-line femoral stem, surrounded by a region of trabecular bone completely interdigitated with bone cement, and a layer of cortical bone (figure 8.1a). An axial load of 25N was distributed across the stem to simulate gait loading: the magnitude of this load was found by matching the axial stem deflection with that seen distally in chapter 7. Since only a section of the stem-interdigitation-cortex geometry was modelled, only the axial loads in the interdigitated region were represented in models; bending and hoop stresses were omitted. Additionally, the cortex was constrained in all DOF at its extremity (figure 8.1b). A fully-bonded interface condition was assumed between the stem and interdigitated region, which is reported to be the postoperative case (Jasty et al, 1991).

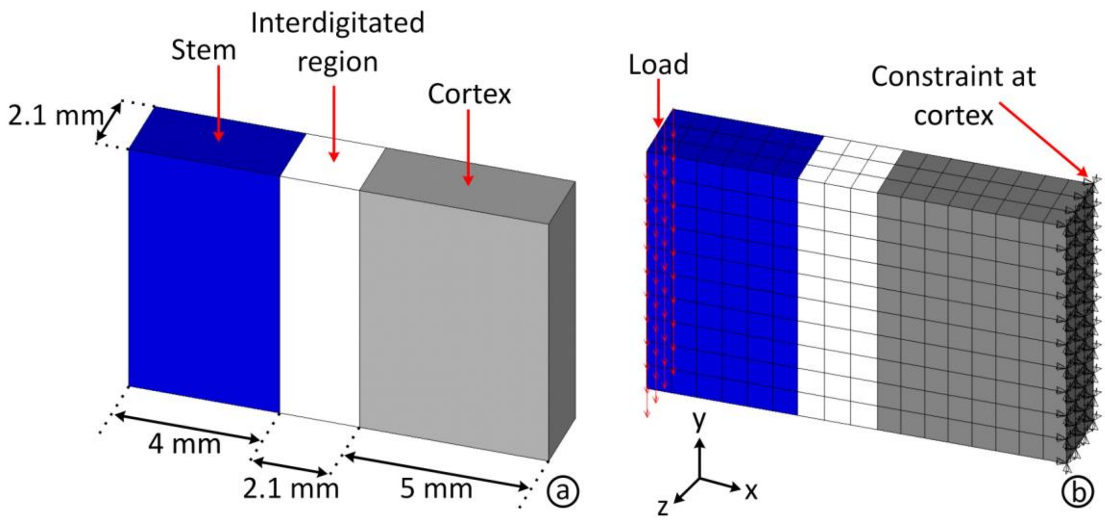

Figure 8.1: The planar macro-scale model adopted for simulations (a) and the applied boundary conditions and mesh size for homogenisation simulations (b). The local coordinate system is also indicated.

The macro-scale model was hex-meshed with an element size of 0.7mm; this represented the cubic size of the micro-scale model. Each element of interdigitated cancellous bone in the macro-scale model is therefore referred to as a representative volume element (RVE); there were 90 in total for the macro-scale model chosen. The macro-scale model was solved using the RVE material properties determined from micro-scale models, and the material properties given in table 8.1. A specific micro-scale model was associated with each RVE, comprising a repeatable trabeculae geometry (figure 8.2), surrounded by bone cement to form a cube. These micro-scale models were initially identical, though became unique as damage accumulated in the cement.

At the start of a given increment, the macro-scale model was solved, based on material properties determined in the previous increment. The number of loading cycles in each increment (ΔN) was arbitrarily chosen to be 125,000. For every RVE the resultant strains on corner nodes were found and stored in an array. Next, a loop was started where each micro-scale model was interrogated by applying interpolated resultant strains on external nodes (material properties given in table

8.1, mesh size 0.05 to 0.1 mm). The amount of damage occurring in each cement element in each micro-scale model within the increment was determined (ΔD), based on the number of cycles to failure (N_F) and the magnitude of stress (σ, MPa), using equations 8.1 and 8.2. Note fatigue data of Murphy and Prendergast (1999) is used in this study as cement porosity was not explicitly modelled. The increase in damage was added to any which existed previously for the cement element. A large array tracked the total damage in each cement element in each micro-scale model. For any cement element, where the total damage exceeded 0.9, the stiffness of the element was subsequently reduced 100 fold (Stolk et al, 2004; Coultrup et al, 2009). The mechanical properties of the trabeculae structure were assumed to be constant throughout the simulations.

Material / Component	Elastic Modulus (MPa)	Poisson's Ratio
Individual Trabeculae	5000	0.3
Steel Femoral Component	210000	0.3
Bone Cement	2800	0.3
Cortical Bone	17000	0.3

Table 8.1: The mechanical properties of materials used in simulations (Choi et al, 1990; Katsamanis et al, 1990; Van Rietbergen et al, 1995; Callister et al, 2004; Roques et al, 2004).

$$\sigma = -4.736 \cdot \log(N_F) + 37.8$$ Equation 8.1 (Murphy and Prendergast, 1999)

$$\Delta D = \frac{\Delta N}{N_F}$$ Equation 8.2

$$\begin{Bmatrix} \varepsilon_X \\ \varepsilon_Y \\ \varepsilon_Z \\ \varepsilon_{XY} \\ \varepsilon_{YZ} \\ \varepsilon_{XZ} \end{Bmatrix} = \begin{bmatrix} C_{11} & C_{12} & C_{13} & C_{14} & C_{15} & C_{16} \\ & C_{22} & C_{23} & C_{24} & C_{25} & C_{26} \\ & & C_{33} & C_{34} & C_{35} & C_{36} \\ & & & C_{44} & C_{45} & C_{46} \\ & sym & & & C_{55} & C_{56} \\ & & & & & C_{66} \end{bmatrix} \cdot \begin{Bmatrix} \sigma_X \\ \sigma_Y \\ \sigma_Z \\ \sigma_{XY} \\ \sigma_{YZ} \\ \sigma_{XZ} \end{Bmatrix}$$ Equation 8.3

After the new damage state was determined in all cement elements for all micro-scale models, the new global material properties for each micro-scale model were determined in compliance matrix format. Compliance matrix coefficients (C_{ij}) were calculated by applying strains (ε_{ij}) to micro-scale model faces and determining resultant stresses (σ_{ij}) (equation 8.3). In total, 21 simulations were required to fill the anisotropic compliance matrix; these are detailed in Chapter 11 (Appendix C). Once the compliance matrices for all 90 micro-scale models were determined, they were applied to the relevant RVEs, and a new increment was started.

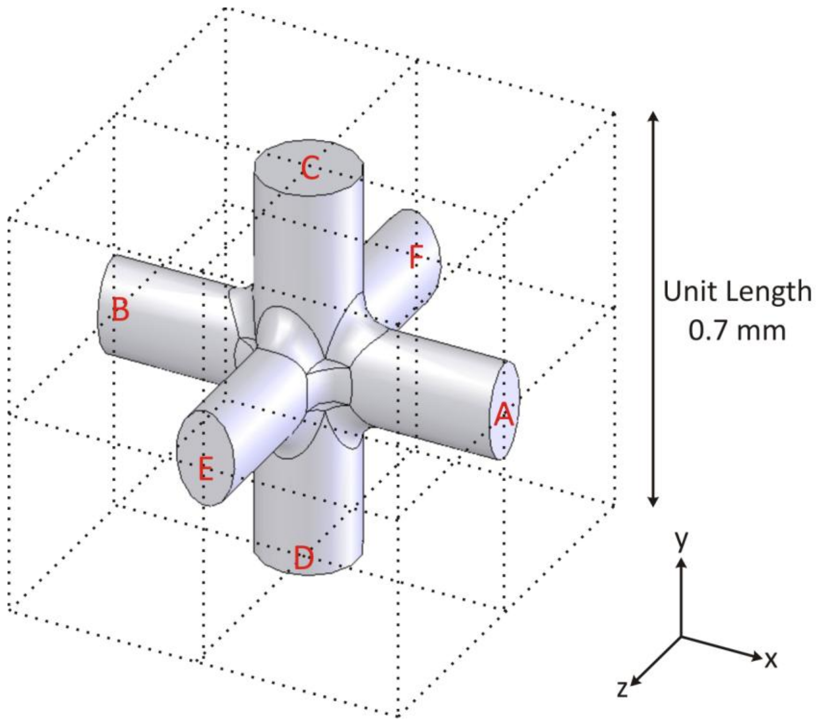

Figure 8.2: The micro-scale trabeculae geometry used for simulations (volumetric density = 0.1, see chapter 7). Cement fills the rest of the cubic structure. Cube faces are labelled A, B, C, D, E, F; this nomenclature relates to areas for load application to determine the mechanical properties for RVEs (Chapter 11, Appendix C).

Two different homogenisation simulations were run, assuming two different bonding conditions between cement and trabeculae. The first was a fully-bonded cased, and the second was a sliding contact with a coefficient of friction of 0.3 (Janssen et al, 2008). For both simulations, the interdigitated region was arbitrarily considered to have 'failed' when 1% of interdigitated cement was completely damaged.

8.2.2 CDM Damage Accumulation Simulations

In addition to homogenisation damage accumulation simulations, a further model used established methods to predict the longevity of the structure under fatigue loading, by omitting trabeculae (assuming the interdigitated region was composed of pure bone cement). This simulation used the established CDM damage accumulation method described by Stolk et al, 2004. This used the same cement fatigue life data as used for the homogenisation approach, which has been determined from experimental testing (equation 8.1). A mesh size of 0.2mm was adopted for the stem, interdigitated region and cortex; this mesh size was chosen by a mesh density test, which revealed that halving the mesh size resulted in a change in the maximum stress of elements of only 4%. It should be noted that mesh sizes for the homogenisation and CDM models were not consistent, since the mesh size in homogenisation simulations was driven by the size of micro-scale models. It is possible that the greater mesh refinement in the CDM models may result in more-accurate description of the stress distribution in the structure on a macro-scale level. The material properties used are given in table 8.1. Again, the interdigitated region was arbitrarily assumed to have 'failed' when 1% of the cement mantle became completely damaged.

8.3 RESULTS

Two different approaches are used here to evaluate the homogenisation method described: by comparing how damage accumulated within the interdigitated region for the two methods, and the predicted fatigue lives which resulted.

The stress fields predicted by the two methods are given in figure 8.3. It is clear that a more-significant stress concentration is initially apparent in the CDM model, which may well be related to the smaller mesh size used. This stress concentration is located at the boundary between the interdigitated region and the cortex. Once some cement elements became damaged, the reduction in cement element stiffness raised stresses in adjacent elements, causing progressive failure at this interface. In contrast, the homogenisation model shows some reduction in interdigitated material stresses in the same area, but the same stress concentration does not occur. This is probably the case because the trabeculae structure is not affected by loading, and because trabeculae allow load transfer to the remaining cement. These models appear to replicate the finding of damage initiation at the interdigitation-cortex interface as reported in chapter 7, but one must remember that bending and hoop stresses are not represented in this model, so the stress distribution may not present an accurate replication of the in vivo condition.

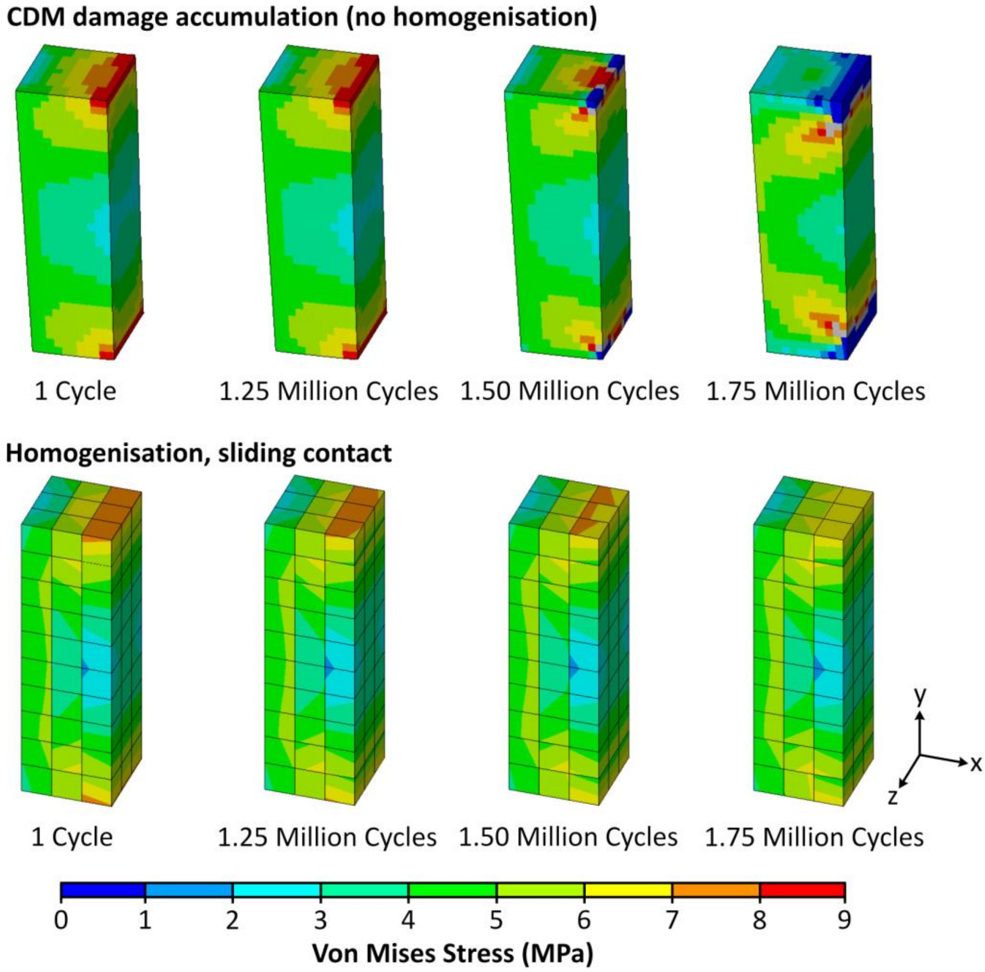

Figure 8.3: The evolution of damage in the interdigitated region during CDM simulations (a) and homogenisation simulations (b). Very low stress after prolonged loading may indicate cement damage, due to the stiffness reduction applied.

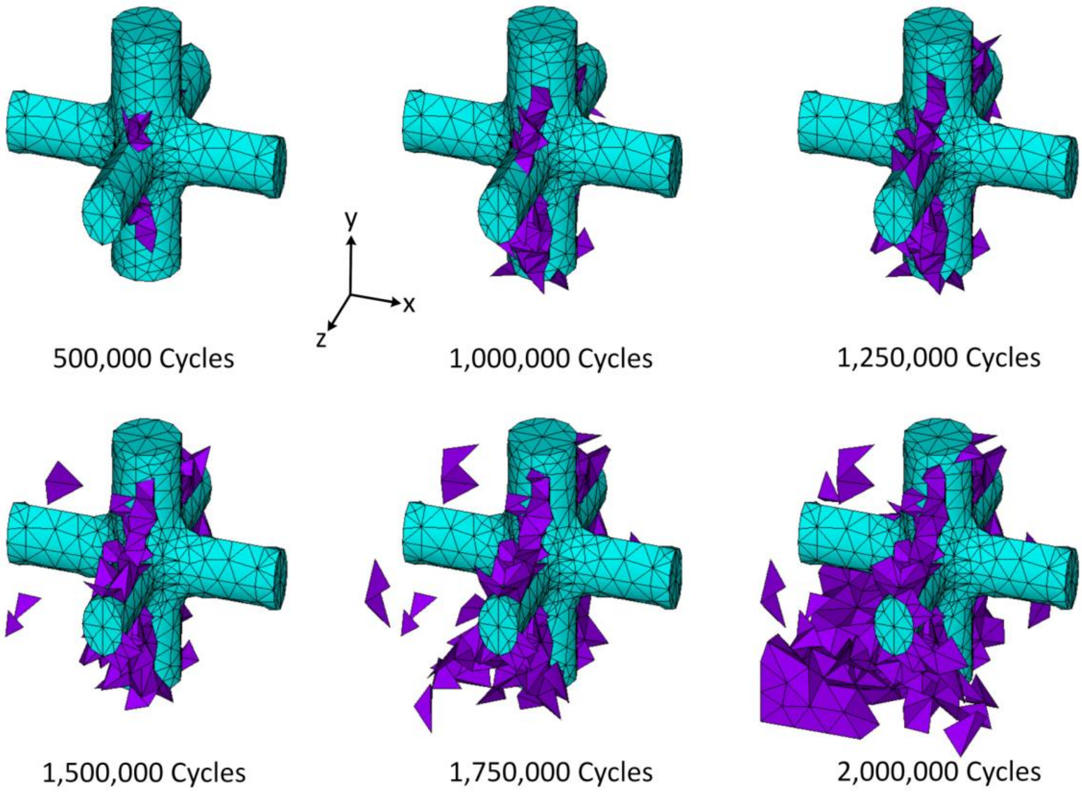

Figure 8.4: The progression of failure in one RVE adjacent to the cortex, assuming a sliding cement-trabecular interface. Bone is shown in light blue, whilst fully-damaged elements are shown as purple.

Further to the stress distributions in the macro-scale models, figure 8.4 reveals the damage accumulation process within one RVE located at the interdigitation-cortex interface. The principle loading mechanism in the structure is bending, perpendicular to the x-z plane. Damage initiates adjacent to trabeculae due to the location stress concentration created (chapter 7). Damage appears to propagate in the y-z plane due to the loading case, before remaining cement is damaged. The magnitude of loading is such that complete damage in interdigitated cement does not occur instantaneously, but over hundreds of thousands of loading cycles (figure 8.4).

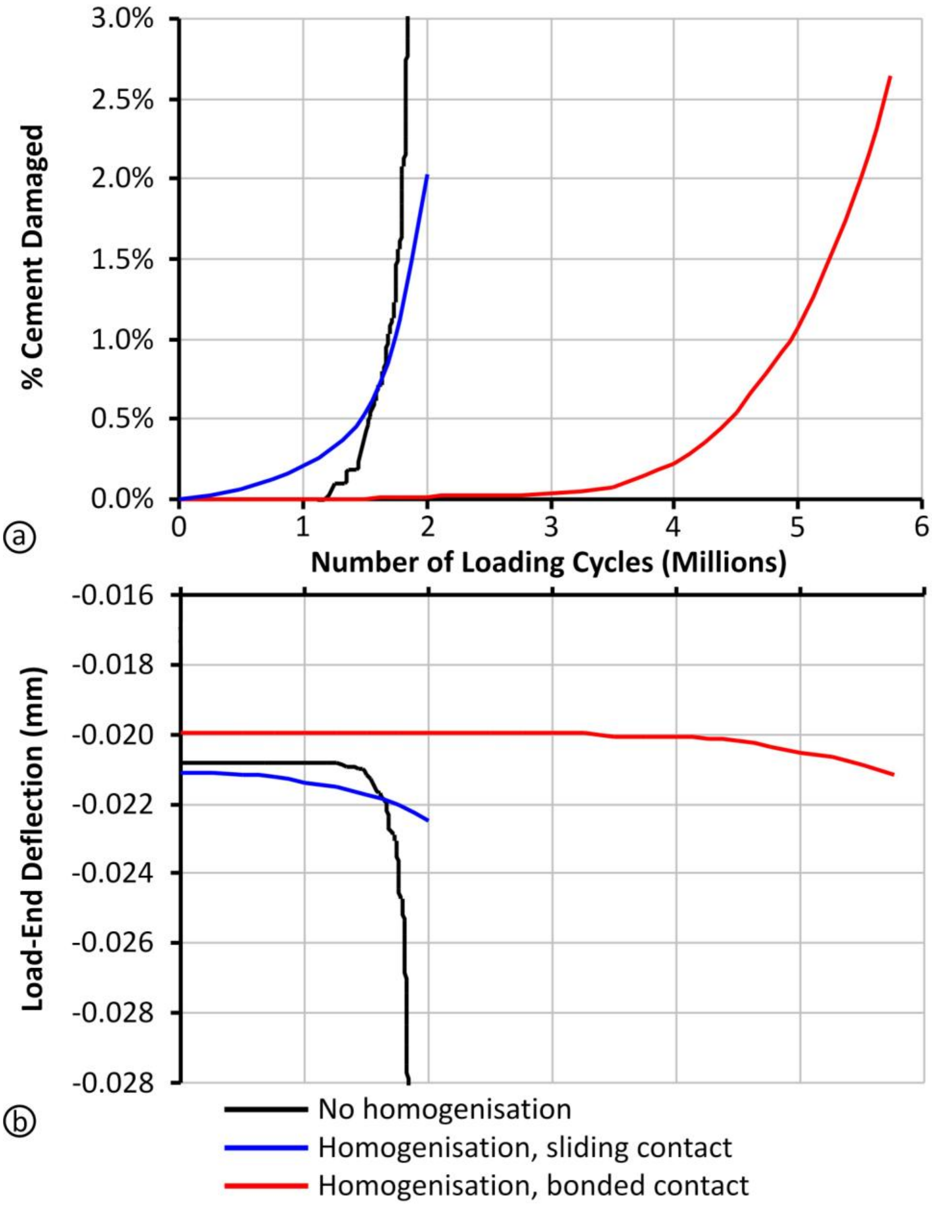

Figure 8.5: The failure of interdigitated bone cement, measured as the volume of failed cement (a) and the load-end deflection of the structure (b).

The second proposed manner of comparing the two computational methods was in terms of fatigue life. Figure 8.5a shows the change in damaged cement volume as simulations progress, revealing a sharp inflection point for the CDM simulation as a large number of cement elements become fully damaged in quick succession. For the homogenisation simulations, the rate of damage accumulation is more gradual. Failure of the interdigitated region was defined as when 1% of interdigitated cement became fully damaged: fatigue lives for all simulations are given in table 8.2. It may appear that the CDM and homogenisation methods agree well in terms of fatigue life where trabeculae and cement are assumed not to be bonded, but judging on the different damage patterns generated this may be coincidental. A clear difference in fatigue life is also revealed where the bonding condition between trabeculae and cement is varied. In particular, the predicted fatigue life was three times shorter where a sliding contact condition was assumed instead of a bonded contact condition. For completeness, figure 8.5b plots the load-end deflection of the stem as simulations progress. The failure of interdigitated material is clear for the CDM model as a significant change in load end deflection. The same was not true for homogenisation simulations, despite a comparable level of fully damaged cement. This again is probably because trabeculae are assumed to remain unchanged during simulations.

Simulation Type	Cycles to Achieve Failure Criterion
No homogenisation	1,683,963
Homogenisation, sliding contact	1,742,128
Homogenisation, bonded contact	4,936,634

Table 8.2: The number of cycles required to achieve the cement damage failure criterion in simulaitons.

Computational costs were significant for homogenisation simulations. For a sliding contact model between cement and trabeculae, the simulations took two weeks to reach a solution within 20 iterations. For a bonded interface, solution time was approximately four times shorter. In contrast, the CDM model took approximately 2 hours to solve within 100 iterations. All simulations were conducted on a Pentium 4 processor with 1GB of RAM.

8.4 DISCUSSION

Current methods of simulating the fatigue failure of cemented THA prostheses omit trabecular bone structures in order to achieve computational efficiency. The validity of simulations without interdigitated trabeculae has not been assessed, though laboratory testing and autopsy studies have revealed cement cracking at the interdigitated region (Jasty et al, 1991; Race et al, 2003). In particular, Leung et al (2008) used acoustic emission monitoring and micro computed tomography to reveal fatigue crack initiation at irregular trabeculae, and propagation into the cement mantle for four-point bend specimens.

This study has presented a novel homogenisation method for simulating the fatigue failure of a trabecular bone structure interdigitated with bone cement. This method breaks down the interdigitated region into a number of relatively simple analyses, allowing an iterative procedure to model the accumulation of damage in cement, and the failure of the interdigitated region. The main aim of this study was to assess the suitability of this homogenisation method for use in pre-clinical simulations of THA prostheses.

The homogenisation method used here outlined a failure pattern in keeping with observations of aseptic loosening in vivo (Jasty et al, 1991; Kawate et al, 1998). In contrast to the CDM approach, damage was found to accumulate more-steadily for the homogenisation method (figure 8.5), via crack initiation at the cement-bone interface, and progression towards adjacent trabeculae. This observation offers a better comparison with Jasty et al (1991), who suggested that the loosening process initiates early and progresses over tens of millions of loading cycles. Other authors have reported the CDM method to under-predict the fatigue life of femoral prostheses (Stolk et al, 2004), though the two methods used here report fatigue lives of the same order of magnitude. This suggests that the failure to model individual trabeculae is not responsible for the short fatigue lives predicted by the CDM method. However, the failure criterion used here is arbitrary, and one may also postulate that 1% of distributed damage in homogenisation simulations is not comparable to 1% of concentrated damage in CDM simulations. Therefore it is not possible to assess if the homogenisation process adds accuracy to prediction of the fatigue life of the interdigitated region. This may only truly be determined via comparison against experimental data.

However, the quantitative data generated here is of use to compare the effect of the bonding condition between cement and trabeculae for homogenisation simulations. Several studies (Kim et al, 2004a; Kim et al, 2004b; Miller et al, 2008) have reported that cement does not chemically bond to trabeculae, meaning load transfer occurs via mechanical interlock only. A computational and experimental study by Janssen et al (2008) has recommended using a coefficient of sliding friction of 0.3. The current study has revealed that this condition results in a significant reduction in fatigue life for the model considered (table 8.2). Assuming a bonded contact case may lead to over-predictions of fatigue lives.

There are a number of limitations to this study, which relate to both the accuracy of simulations and the ease of implementation of the homogenisation method. The first of these is the computational time required. The macro-scale model used here represented only a small portion of the proximal femoral metaphysis, yet the fatigue simulation required two weeks to reach a solution for the relevant sliding cement-trabeculae interface condition. This is because each micro-scale model must be solved 22 times in each increment, and the sliding contact patch makes simulations computationally expensive. It is clear that a very powerful processor would be required to model the entire replaced hip in an expedient time frame. Some processing time may be removed by determining new material properties only where at least one cement element has become completely damaged since the RVE material properties were last calculated. Since the increment sizes were large in the homogenisation simulations in this study, this approach would not reduce the solving time markedly. Additionally, one could assume that the failure of only a few cement elements does not significantly affect the mechanical properties of the RVE. This is analogous to the CDM method, where cement elements may possess a scalar damage value between 0 and 0.9, but maintain constant elastic modulus. Multiple characterisation analyses would be required to justify the efficacy and accuracy of this simplification, but it may be of use for reducing the computational cost of a series of large homogenisation simulations. In addition, the fatigue data used here (equation 8.1) relate to large-scale cement simulations, and have not been verified for the micro-scale required for homogenisation simulations.

For the CDM method, the computational cost is optimised by determining the number of cycles represented in iterations by considering the number of cycles to failure for each cement element. This ensures large iterations occur at the start of simulations where no damage occurs, but small iterations are simulated as elements become damaged. This approach was not used for homogenisation simulations, because sharp stress concentrations are created in each micro-scale model, meaning the number of increments required in one simulation, and therefore the computational cost, becomes huge. However, for large increment sizes, the CMD method loses accuracy (Stolk et al, 2004), and the same may be expected for homogenisation simulations.

The stress field modelled in this study features two sharp stress concentrations, which the homogenisation method does not appear to be able to capture accurately. This is because the size of RVEs is fixed by the size of the micro-scale model. Where boundary conditions are found from RVEs, they are interpolated between external nodes on micro-scale models. Thus, where a stress concentration occurs, it may not be accurately represented in the micro-scale model, and therefore not passed onto micro-scale models in the form of boundary conditions. It may be possible to reduce the mesh size to a fraction of the micro-scale model, and selectively pull out boundary conditions to apply to micro-scale models. This may overcome problems dealing with stress concentrations in the macro-scale model. Of further hindrance to the current method is the requirement for RVEs to be cubic. For a complex shape to be modelled, the method must be modified to allow for non-cubic micro-scale models.

There are several further assumptions which may affect the relevance to the in-vivo case. Firstly, the mechanical properties of trabeculae are assumed to be constant during simulations, but it is possible that they will fracture or become remodelled due to the applied loading (Mann et al, 2009). Also, creep was not modelled in cement, even though it is known to result in significantly longer fatigue lives (Jeffers, 2005); this is because no relationship for anisotropic cement creep in a multi-axial stress state had been published at the time of writing. Finally, the failure criterion for the interdigitated region was chosen arbitrarily due to the lack of comparable experimental data, and may have a significant effect on the fatigue lives predicted.

This study assesses a method for including individual trabeculae in simulations of interdigitated cement. It has shown that the fatigue failure process resulting from its use may be more relevant to the in vivo condition than the prevailing CDM method. In particular, it has outlined the sharp reduction in structure fatigue life for a sliding cement-trabeculae interfacial condition over a bonded condition. However, the method outlined is computationally-expensive, and requires further development and verification before it may be used to assess new cemented joint prostheses prior to clinical release.

9 Conclusions and Further Work

9.1 Motivation

The motivation for this study is described in Chapter 1 to stem from the need to improve quality of life for total hip arthroplasty (THA) patients, and the need to reduce the revision burden on health care services to allow more primary procedures. While the clinical performance of THAs is excellent (Furnes et al, 2007; Karrholm et al, 2008), patient scoring studies reveal that survival and patient quality of life are not mutually inclusive (Britton et al, 1996; Garellick et al, 1998). Additionally, the excellent performance of THA has led to the procedure being offered to increasingly young patients who place higher demands on medical devices (Learmonth, 2006). While surgical approaches and cementing techniques have improved significantly over the last 50 years (Learmonth, 2005), improvements in medical device design have been less significant; indeed, the performance of the Charnley femoral stem remains the 'gold standard' for THA (Huiskes, 1993a). Improved medical devices are required to address the revision burden and improve patient long-term quality of life. Currently, approximately 5,800 revision procedures are conducted annually in the UK, at a total projected cost of £53 million (Iorio et a, 1999). Additionally, with limited operating room time available, a high number of revision procedures mean fewer primaries can be conducted, increasing the waiting time for patients suffering from painful and debilitating conditions.

The design of new medical devices is commonly led by surgeons based on observations from patients. Short clinical trials cannot, unfortunately, indicate the long-term performance of novel medical devices. The result of this is that new devices may not perform better than their predicates, or may even perform worse (Huiskes, 1993a). Two examples of this are the 3M Capital Hip (Massoud et al, 1997) and Boneloc cement (Abdel-Kadar et al, 2001). Through the careful design of tests, laboratory experiments may be used to evaluate the long-term performance of devices over an accelerated timescale. However, such testing can be time-consuming and expensive, while differences in results due to prosthesis design features may be difficult to identify. These disadvantages may be overcome by using computational analyses, which offer fast computation and good control of independent variables (Huiskes, 1993a).

The research group at the University of Nijmegen developed a computational method to simulate the fatigue failure of cemented femoral stems, and showed it to be successful enough to indentify clinically successful prostheses (Verdonschot and Huiskes, 1997a; Stolk et al, 2004; Stolk et al, 2007). Further work at the University of Southampton has identified that the method over-predicted the long-term survival of cement, and showed that the omission of cement pores and residual stresses may be the cause (Jeffers et al, 2007).

The aim of this study was to improve the predictive power of computational models for use as pre-clinical tools for assessing the efficacy of novel cemented hip prostheses. Fatigue monitoring and tomography methods were used to better-understand the fatigue failure process of bone cement and the effect of internal defects, and to also allow improved predictions of the fatigue lives of specimens. Since clinical studies have shown that the aseptic loosening rate is higher for acetabular cups than femoral stems (Schulte et al, 1993; Kobayashi et al, 1997; Madey et al, 1997; Callaghan et al, 1998; Callaghan et al, 2000), this study also aimed to identify the key variables for the longevity of the acetabular component, and use the methods developed at the Universities of Nijmegen and Southampton to help reveal the genesis of failure in this component. Finally, concerns about the assumption that interdigitated trabecular bone may be modelled as pure bone cement in simulations provided the motivation for developing a novel homogenisation method to test the validity of this assumption.

9.2 Summary of Research

This research began by investigating the fatigue failure mechanisms in simple dog-bone-shaped specimens of bone cement. Previous research had described the

Wöhler curve for different brands of this material (Murphy and Prendergast, 2000; Jeffers et al, 2005), and used acoustic emission (AE) monitoring to reveal a discontinuous fatigue crack initiation process. Chapters 3 and 4 built on this by using a novel tomographic method to form computational models of experimental fatigue specimens, incorporating internal defects. This method allowed direct comparison of experimental and computational results for the first time and allowed improved predictions of fatigue life to be made, reproducing the variability seen in experimental specimens. For both types of specimen, damage was found to form at multiple locations by internal defects, before catastrophic failure occurred at one location. As seen before (Wang et al, 1996), where large pores (>0.7mm^3) were present they were found to dominate failure. In their absence, both experimental specimens and simulations showed failure incidence at small internal defects. This confirms the theory that internal porosity must be modelled to accurately simulate the fatigue failure of bone cement (Jeffers et al, 2007).

These studies combine experimental, tomographic and computational methods to outline a holistic process of fatigue failure in bone cement. The agreement between computational and experimental damage location and the verification of cement cracking at locations of AE adds confidence in the suggested failure process. However, other authors have reported less accuracy in predicting the fatigue lives of novel medical devices (Stolk et al, 2004; Jeffers, 2005; Stolk et al, 2007). This may be because, in reality, the stress state in the cement mantle is multi-axial, while the geometry of cement results in areas of significant stress concentration. In addition, FE models of the replaced metaphysis generally make multiple assumptions about geometry, material properties and boundary conditions. These include using idealised bone geometry, not modelling soft tissues, using homogenous material properties for bone, not modelling trabecular architecture, cement defects and porosity, and generalising applied muscle forces (Huiskes, 1993b; Phillips et al, 2007).

The real power of computational methods lies in the rapid simulation of multiple in-vivo conditions, with a high level of control over independent variables.

Simplifications in models may be necessary for computational efficiency, but should not diminish the accuracy of results. Chapter 5 explored aspects of solving time and accuracy using simple and complex models to determine the effects of various parameters on the magnitude of stresses in the acetabular cement mantle. The complex model was assumed to be more relevant to the in vivo condition, as the material properties, geometry and boundary conditions were more representative. This analysis showed that the simple model effectively described the effects of these parameters, though the magnitudes of predicted stresses were higher than those expected in vivo. Since the results of these finite element analyses were not verified with in vivo specimens, the only way the data could be analysed was by the comparison of the effects of variables. The good agreement between the ranking achieved from the simple and complex models reveals the potential for using appropriate simplifications in finite element models to efficiently assess novel medical devices. The industrial sponsors of this thesis, DePuy International Ltd, may use the simple model for future analyses to compare the effect of cup design features on cement stresses. But they would not use the complex model, because the added complexity appears to not be necessary for a full-factorial analysis of parameters, and also because it involves significant set-up time and high potential for operator error. If computational methods are to be transferred to industry for use in the design process, they must minimise computational expense and the potential for operator error, and must be verified to be accurate enough for the scenario considered. Chapter 5 has shown that a computational model does not necessarily require high complexity to allow a meaningful analysis of a structure.

Chapter 6 presented simulations of the fatigue failure of the acetabular cement mantle. This chapter revealed that stresses in the acetabular cement mantle are generally close to the projected endurance limit for bone cement, though a thin cement mantle or high cup penetration may elevate stresses to the level where fatigue failure of the cement mantle becomes a possible scenario. This means that aseptic loosening of the polyethylene cup is probably largely driven by biological processes, but mechanical processes may also contribute. A valuable extension to this work would be to attempt to model the biological failure processes in conjunction with the cement fatigue failure process, to validate this conclusion. Additionally, the current study lacks evidence of fatigue failure in the acetabular cement mantle in autopsy specimens, and requires better validation with in vitro analyses, such as those conducted at the University of Portsmouth (Tong et al, 2008; Wang et al, 2009).

The study in chapter 6 also revealed a major problem with the current CDM damage accumulation method. This author believes that the major reason that simulations currently cannot accurately predict the longevity of prostheses is that the Wöhler curve does not adequately describe the fatigue performance of bone cement for the relevant range of cement mantle stresses. At the acetabulum these were mostly between 0 and 7 MPa, and were reduced during simulations due to cement creep (Chapter 6). The fatigue data used, however, was generated from experimental loading between 7 and 20 MPa. By extrapolating phase 2 of Wöhler curve (figure 22.2) down to low stress levels, one effectively assumes that bone cement does not exhibit an endurance limit. However, since an endurance limit exists for PMMA (Suresh, 2004), this author expects one will also exist for bone cement. This would explain why the CDM method is accurate for simulations of dog-bone-shaped specimens with applied loads between 7 and 20 MPa, but not accurate for lower load conditions. Additionally, this author is not yet satisfied that bone cement performs comparably for uni-axial loading as it does for multi-axial loading, the in-vivo case. More testing is required to obtain data for low, multi-axial stress states.

In the last two chapters of this thesis, a method of representing cancellous bone interdigitated with cement in large static and fatigue simulations was trialled. This method was effectively used in chapter 7 to determine the magnitude of stresses in interdigitated bone cement, finding them to be higher than those in the bulk cement mantle and highly concentrated at the cement-trabeculae interface. This supports observations of cement crack initiation at this location (Jasty et al, 1991; Race et al, 2003). This author attempted to use this method in simulations of the fatigue failure of a stem-interdigitation-cortex construct in chapter 8. The method revealed a failure method which compared well with that seen experimentally (Race et al, 2003). However, the computational time required meant that simulations of only a small part of the replaced femur took several weeks to solve. This brings one back to the discussion of computational solution time, the benefits of computational simulations, and ease of adoption of computational methods into industry; the solution time involved was clearly not appropriate to solve large numbers of simulations expediently. It appears this is the cost of representing individual trabeculae in macro-scale models. However, there may be alternative ways of representing the bone-cement interface in simulations which can vastly reduce the computational time, yet retain most of the accuracy. One possible approach may be to use cohesive elements to represent the cement-interdigitation interface, as proposed by Waanders et al (2010). By this rationale, the local condition of the interface is defined in terms of a stiffness; this stiffness may reduce as damage occurs at the interface. A similar method has already been adopted successfully by other authors to describe debonding at the stem-cement interface (Verdonschot et al, 1997b; Perez et al, 2006).

In summary, this thesis has explored a number of methods for improving the pre-clinical computational assessment of novel THA prostheses. It has characterised the fatigue failure of bone cement, and used resulting data to conduct analyses of entire femoral and acetabular THA prostheses. These analyses have helped this author to investigate proposed failure processes for cemented implants, and explore the effects of various parameters by closely controlling independent variables. Finally, novel methods for improving simulations have been critiqued in terms of accuracy and suitability for use in industry. Further verification via experimental testing and investigation of ex-vivo specimens has been proposed to assess the accuracy of the methods presented. Additionally, more work is required to provide industry with a methodology for using efficient computational models with validated simplifications, which give the user a high degree of control over independent variables while restricting the possibility for operator error.

10 References

Abdel-Kader KFM, Allcock S, Walker DI and Chaudhry SB, 2001. Boneloc bone–cement: Experience in hip arthroplasty during a 3-year period. The Journal of Arthroplasty 16(7): 811-819.

Alfaro-Adrian J, Gill HS, Marks BE and Murray DW, 1999. Mid-term migration of a cemented total hip replacement assessed by radiostereometric analysis. International Orthopaedics 23(3): 140-144.

Amstutz HC, Beaulè PE, Dorey FJ, Le Duff MJ, Campbell PA and Gruen TA, 2004. Metal-on-metal hybrid surface arthroplasty: two to six-year follow-up study. Journal of Bone and Joint Surgery 86: 28-39.

Anderson TL, 2005. Fracture mechanics: fundamentals and applications. Taylor & Francis Group, Boca Raton, USA.

Anderson AE, Peters CL, Tuttle BD and Weiss JA, 2005. A subject-specific finite element model of the pelvis: development, validation and sensitivity studies. Journal of Biomechanical Engineering 127: 364-373.

Anthony PP, Gie GA, Howie CR and Ling RS, 1990. Localised endosteal bone lysis in relation to the femoral components of cemented total hip arthroplasties. Journal of Bone and Joint Surgery (Br) 72(6):971-979.

ARC, 2004. Osteoporosis: an information booklet. The Arthritis Research Campaign, Chesterfield, UK. Retrieved Jan 201 from www.arc.org.uk.

ARC, 2005. Osteoarthritis: an information booklet. The Arthritis Research Campaign, Chesterfield, UK. retrieved Jan 2010 from www.arc.org.uk.

ARC, 2006. Rheumatoid arthritis: an information booklet. The Arthritis Research Campaign, Chesterfield, UK. retrieved Jan 201 from www.arc.org.uk.

ASTM, 2000. Standard guide for computed tomography (CT) imaging. Designation: E1441-00 1-33.

Beattie AG, 1983. Acoustic emission: principles and instrumentation. Journal of Acoustic Emission 2: 95-128.

Bergmann G, Graichen F and Rohlmann A, 1993. Hip joint loading during walking and running measured in two patients. Journal of Biomechanics 28(8): 969-990.

Bergmann G, Graichen F and Rohlmann A, 1995. Is staircase walking a risk for the fixation of hip implants? Journal of Biomechanics 28(5): 535-553.

Bergmann G, Deuretzbacher G, Heller M, Graichen F, Rohlmann A, Strauss J and Duda GN, 2001. Hip contact forces and gait patterns from routine activities. Journal of Biomechanics 34: 859-871.

Bishop NE, Ferguson S and Tepic S, 1996. Porosity reduction in bone cement at the cement-stem interface. Journal of Bone and Joint Surgery 78(B): 349-357.

Brandt K, 2004. Non-surgical treatment of osteoarthritis: a half-century of "advances". Annals of the Rheumatic Diseases 63(2): 117-122.

Britton AR, Murray DW, Bulstrode CJ, McPherson K and Denham RA, 1996. Long term comparison of the Charnley and Stanmore design total hip replacements. Journal of Bone and Joint Surgery - British Volume 78(B): 802-808.

Browne M, Roques A and Taylor A, 2005. The acoustic emission technique in orthopaedics – a review. Journal of Strain Analysis 40(1): 59-79.

British Standard EN 1330-9, 2000. Non-destructive testing terminology, part 9: Terms used in acoustic emission testing. British Standards Institution.

Burgers TA, Mason J, Niebur G and Ploeg HL, 2008. Compressive properties of trabecular bone in the distal femur. Journal of Biomechanics 41: 1077-1085.

Callaghan JJ, Forest EE, Olejniczak JP, Goetz DD and Johnston RC, 1998. Charnley total hip arthroplasty in patients less than fifty years old: a twenty to twenty-five-year follow-up note. Journal of Bone & Joint Surgery (Am) 80 (5): 704-714.

Callaghan JJ, Albright JC, Goetz DD, Olejniczak JP and Johnston RC, 2000. Charnley total hip arthroplasty with cement. Journal of Bone & Joint Surgery (Am) 82 (4): 487-497.

Callister WD, 1994. Materials science and engineering: an introduction, third edition. John Wiley and Sons, New York.

Carrington NC, Sierra RJ, Gie GA, Hubble MJ, Timperley AJ and Howell JR, 2009. The Exeter Universal cemented femoral component at 15 to 17 years: an update on the first 325 hips. Journal of Bone and Joint Surgery (Br) 91(6): 730-737.

Chen CQL, Scott W and Barker TM, 1999. Effect of metal surface topography on mechanical bonding at simulated total hip stem-cement interfaces. Journal of Biomedical Materials Research, 48(4): 550-556.

Chen J-H and Wu JS-S, 2002. Measurement of polyethylene wear: a new three-dimensional methodology. Computer Methods & Programs in Biomedicine 68: 117-127.

Choi K, Khun J, Ciarelli MJ and Goldstein SA, 1990. The elastic moduli of human subchondral, trabecular and cortical bone tissue and the size-dependency of cortical bone modulus. Journal of Biomechanics 23(11): 1103-1113.

Chwirut DJ, 1984. Long-term compressive creep deformation and damage in acrylic bone cements. Journal of Biomedical Materials Research, 18: 25-37.

DePuy-CMW, 2007. CMW-1 bone cement data sheet. Supplied with CMW-1 bone cement, DePuy-CMW, Blackpool, UK.

Collis DK and Mohler CG, 1998. Loosening rates and bone lysis with rough finished and polished stems. Clinical Orthopaedics and Related Research 355: 113-122.

Coombs RR and Thomas RW, 1994. Avascular necrosis of the hip. British Journal of Hospital Medicine 51(6): 275-280.

Coultrup OJ, Browne M, Hunt C and Taylor M, 2009. Accounting for inclusions and voids allows the prediction of tensile fatigue life of bone cement. Journal of Biomechanical Engineering 131(5).

Coultrup OJ, Hunt C, Wroblewski BM and Taylor M, 2010. Computational assessment of the effect of polyethylene wear rate, mantle thickness and porosity on the mechanical failure of the acetabular cement mantle. Journal of Orthopaedic Research 28(5): 565-570.

Cowin SC, 1989. Bone Mechanics. CRC Press, Boca Raton, FL.

Crowninshied RD, Brand RA and Pedersen DR, 1983. A stress analysis of the acetabular reconstruction in pertrusio acetabuli. Journal of Bone & Joint Surgery 65(4): 495-499.

Crowninshield R, 2001. Femoral hip implant fixation within bone cement. Operative Techniques in Orthopaedics, 11(4): 296-299.

Dakin GJ, Arbelaez RA, Molz IV, Alonso JE, Mann KA and Eberhardt AW, 2001. Elastic and viscoelastic properties of the human pubic symphysis joint: effects of lateral impact loading. Journal of Biomechanical Engineering 123: 218-226.

Dalstra M, Huiskes R, Odgaard L and van Erning L, 1993. Mechanical and textural properties of pelvic trabecular bone. Journal of Biomechanics 26(4-5): 523-535.

Dalstra M, Huiskes R and van Erning L, 1995. Development and validation of a three-dimensional finite element model of the pelvic bone. Journal of Biomechanical Engineering 117: 272-278.

Dalstra M and Huiskes R, 1995. Load transfer across the pelvic bone. Journal of Biomechanics 28 (6): 715-724.

DePuy-CMW Ltd, 2007. In-house data generated by DePuy-CMW Ltd, Blackpool, UK.

DePuy International Ltd, 2007. C-StemTM triple tapered stabilised hip: surgical technique. Distributed by DePuy International Ltd, Leeds, UK.

DLS, 2009. About synchrotrons. Diamond Light Source Ltd., retrieved Aug 2009 from http://www.diamond.ac.uk/Home/About.html.

Dorr LD, Takei GK and Conaty JP, 1983. Total hip arthroplasties in patients less than forty-five years old. Journal of Bone & Joint Surgery (Am) 65: 474-479.

Dunne NJ and Orr JF, 2001. Influence of mixing techniques on the physical properties of acrylic bone cement. Biomaterials 22(13): 1819-1826.

Dunne NJ, Orr JF, Mushipe MT and Eveleigh RJ, 2003. The relationship between porosity and fatigue characteristics of bone cements. Biomaterials 24(2): 239-245.

Ebied A and Journeaux S, 2002. Metal-on-metal hip resurfacing. Current Orthopaedics 16(6): 420-425.

Engelbrecht DJ, Weber FA, Sweet MBE and Jakim I, 1990. Long term results of revision total hip arthroplasty. Journal of Bone and Joint Surgery (Br) 72 (1): 41-45.

ERSF, 2008. The European light source. European Synchrotron Research Facility, retrieved Aug 2009 from http://www.esrf.fr/AboutUs. Accessed November 2009.

Furnes O, Havelin LI, Espehaug B, Steindal K and Soras TE, 2007. Report 2007. The Norwegian Arthroplasty Register.

Garcia-Cimbrelo E, Diez-Vasques V, Madero R and Munuera L, 1997. Progression of radiolucent lines adjacent to the acetabular component and factors influencing migration after Charnley low-friction total hip arthroplasty. Journal of Bone and Joint Surgery (AM) 79(A): 1373-1380.

Garellick G, Malchau H and Herberts P, 1998. Specific or general health outcome measures in the evaluation of total hip replacements. Journal of Bone and Joint Surgery (Br) 80: 600-606.

Gibson LJ, 1985. The mechanical behaviour of cancellous bone. Journal of Biomechanics 18(5): 317-328.

Gilbert JL, Hasenwinkel JM, Wixson RL and Lautenschlager EP, 2000. A theoretical and experimental analysis of polymerisation shrinkage of bone cement: A potential major source of porosity. Journal of Biomedical Materials Research 52(1): 210-218.

Ginebra MP, Albuixech L, Fernandez-Barragain E, Aparicio C, Gil FJ, San Roman J, Vazquez B and Planell JA, 2002. Mechanical performance of acrylic bone cements containing different radiopacifying elements. Biomaterials 23: 1873-1882.

Gray H, 1997. Gray's anatomy; classic first edition. Reed Editions.

Hamadouche M, Boutinm P, Daussange J, Bolander ME and Sedel L, 2002. Alumina-on-alumina total hip arthroplasty: A minimum 18.5-year follow-up study. Journal of Bone and Joint Surgery (Am) 84(1): 69-77.

Harper EJ and Bonfield W, 2000. Tensile characteristics of ten commercial acrylic bone cements. Journal of Biomedical Materials Research 53: 605-616.

Harris WH, 1969. Traumatic arthritis of the hip after dislocation and acetabular fractures: Treatment by mould arthroplasty: An end-result study using a new method of result evaluation. Journal of Bone and Joint Surgery (Am) 51(4): 737-755.

Heaton-Adegbile P, Zant NP and Tong J, 2006. In vitro fatigue behaviour of a cemented acetabular reconstruction. Journal of Biomechanics 39(15): 2882-2886.

Hertzler J, Miller MA and Mann KA 2002. Fatigue crack growth rate does not depend on mantle thickness: an idealized cemented stem constructed under torsional loading. Journal of Orthopaedic Research 20(4): 676-682.

Hodgkinson JP, Shelley P and Wroblewski BM, 1989. The correlation between the roentgenographic appearances and operative findings at the bone-cement junction of the socket in Charnley low friction arthroplasties. Clinical Orthopaedics 228: 105-109.

Hodgkinson JP, Maskell AP, Ashok P and Wroblewski BM, 1993. Flanged acetabular components in cemented Charnley hip arthroplasty. Journal of Bone & Joint Surgery (Br) 75: 464-467.

Hodgkinson JP, Shelley P and Wroblewski BM, 1988. The correlation between the roentgenographic appearance and operative findings at the bone-cement junction of the socket in Charnley low friction arthroplasties. Clinical Orthopaedics and Related Research 228: 105-109.

Hollister SJ, Fyhrie DP, Jepsen KJ and Goldstein SA, 1991. Application of homogenisation theory to the study of trabecular bone mechanics. Journal of Biomechanics 24(9): 825-839.

Hollister SJ, Brennan JM and Kikuchi N, 1994. A homogenisation sampling procedure for calculating trabecular bone effective stiffness and tissue level stress. Journal of Biomechanics 27(4): 433-444.

Hook S, Moulder E, Yates PJ, Burston BJ, Whitley E and Bannister GC, 2006. The Exeter Universal stem: a minimum ten-year review from an independent centre. Journal of Bone and Joint Surgery (Br) 88: 1584-1590.

Huiskes R, 1993a. Mechanical failure in total hip arthroplasty with cement. Current Orthopaedics 7(4): 239-247.

Huiskes R, 1993b. Failed innovation in total hip replacement. Acta Orthopaedica Scandinavica 64(6): 699-716.

Huiskes R, Verdonschot N and Nivbrant B, 1998. Migration, stem shape, and surface finish in cemented total hip arthroplasty. Clinical Orthopaedics and Related Research 355: 103-112.

Iorio R, Healy WL and Richards JA, 1999. Comparison of the hospital cost of primary and revision total hip arthroplasty after cost containment. Orthopedics 22(2): 185-189.

Jacobs ME, Koeweiden EMJ, Slooff TJJH, Huiskes R and van Horn JR, 1989. Plain radiographs inadequate for evaluation of the cement-bone interface in the hip prosthesis. Acta Orthopaedica Scandinavica 60(5): 541-543.

Jacobs JJ, 2008. Metallic wear debris: biological responses. Proceedings of the American Academy of Orthopaedic Surgeons 2008, San Francisco, USA.

James SP, Schmalzried TP, McGarry FJ and Harris WH, 1993. Extensive porosity at the cement-femoral prosthesis interface: a preliminary study. Journal of Biomedical Materials Research 27(1): 71-78.

Janssen D, Aquarius R, Stolk J and Verdonschot N, 2005a. The contradictory effect of pores on fatigue cracking of bone cement. Journal of Biomedical Materials Research 74(2): 747-753.

Janssen D, Stolk J and Verdonschot N, 2005b. Why would cement porosity reduction be clinically irrelevant, while experimental data show the contrary? Journal of Orthopaedic Research 23(4): 691-697.

Janssen D, Aquarius R, Stolk J and Verdonschot N, 2005c. Finite-element analysis of failure of the Capital Hip designs. Journal of Bone and Joint Surgery (Br), 87: 1561-1567.

Janssen D, Stolk J and Verdonschot N, 2006. Finite element analysis of the long-term fixation strength of cemented ceramic cups. Proceedings of the Institute of Mechanical Engineers 220: 533-539.

Janssen D, van Aken J, Scheerlinck T and Verdonschot N, 2007. The 'French paradox' exposed: a finite element analysis of cement philosophy on implant stability and crack formation in the cement mantle. Conference Proceedings of Engineers and Surgeons: Joined at the Hip, London. Published by the Institute of Mechanical Engineers.

Janssen D, Mann KA and Verdonschot N 2008. Micro-mechanical modelling of the cement-bone interface: The effect of friction, morphology and material properties on the micromechanical response. Journal of Biomechanics 41(15): 3158-3163.

Jasty M, Maloney WJ, Bragdon CR, O'Connor DO, Haire T and Harris WH, 1991. The initiation of failure in cemented femoral components of hip arthroplasties. Journal of Bone and Joint Surgery - British Volume 73(B): 551-558.

Jeffers JRT, 2005. In silico simulation of long term cement mantle failure in total hip replacement. PhD Thesis, University of Southampton, UK.

Jeffers JRT, Browne M and Taylor M, 2005. Damage accumulation, fatigue and creep behaviour of vacuum mixed bone cement. Biomaterials 26(27): 5532-5541.

Jeffers JRT, Browne M, Lennon AB, Prendergast PJ and Taylor M, 2007. Cement mantle fatigue failure in total hip replacement: experimental and computational testing. Journal of Biomechanics 40(7): 1525-1533.

Jones LC, Frondoza C and Hungerford DS, 1999. Immunohistochemical evaluation of interface membranes from failed cemented and uncemented acetabular components. Journal of Biomedical Materials Research 48(6): 889-898.

Kapandji IA, 1987. The physiology of the joints. Churchill-Livingstone, New York, USA.

Karrholm JGG, Rogmark C and Herberts P, 2008. Annual report 2007. Swedish Hip Arthroplasty Register.

Katsamanis F and Raftopoulos DD, 1990. Determination of mechanical properties of human femoral cortical bone by the Hopkinson bar stress technique. Journal of Biomechanics 23(22): 1173-1184.

Kawate K, Maloney WJ, Bragdon CR, Biggs SA, Jasty M and Harris WH, 1998. Importance of a thin cement mantle: autopsy studies of eight hips. Clinical Orthopaedic Related Research 355: 70-76.

Kerboull L, Hamadouche M, Courpied JP and Kerboull M, 2004. Long-term results of Charnley-Kerboull hip arthroplasty in patients younger than 50 years. Clinical Orthopaedics, 418: 112-118

Kim D-G, Miller MA and Mann KA, 2004a. A fatigue damage model for the cement-bone interface. Journal of Biomechanics 37(10): 1505-1512.

Kim D-G, Miller MA and Mann KA, 2004b. Creep dominates tensile fatigue damage of the cement-bone interface. Journal of Orthopaedic Research 22(3): 633-640

Klassbo M, Larsson E and Mannevik E, 2003. Hip disability and osteoarthritis outcome score: An extension of the Western Ontario and McMaster Universities Osteoarthritis Index. Scandinavian Journal of Rheumatology 32(1): 46-51.

Kobayashi S, Takaoka K, Saito N and Hisa K, 1997. Factors affecting aseptic failure of fixation after primary Charnley total hip arthroplasty: multivariate survival analysis. Journal of Bone & Joint Surgery (Am) 79 (11): 1618-1627.

Kohn D, 1995. Acoustic emission and nondestructive evaluation of biomaterials and tissues. Critical Reviews in Biomedical Engineering 22(3/4): 221-306.

Kowalczyk P, 2003. Elastic properties of cancellous bone derived from finite element models of parameterized microscructure cells. Journal of Biomechanics 36(7): 961-972.

Kurtz S, Giddings V, Muratoglu O, O'Connor D, Harris W and Krevolin J, 2000. Stress in a highly crosslinked acetabular component for total hip replacement. Transactions of the Orthopaedic Research Society 25: 222.

Kurtz SM, Villarraga ML, Zhao K and Edidin AA, 2005. Static and fatigue mechanical behaviour of bone cement with elevated barium sulphate content for treatment of vertebral compression fractures. Biomaterials 26: 3699-3712.

Langlais F, Kerboull M, Sedel L and Ling RSM, 2003. The 'French paradox'. Journal of Bone and Joint Surgery (Br) 85(1): 17-20.

Le Vay D, 1990. The history of orthopaedics. The Parthenon Publishing Group, Carnforth, UK.

Learmonth ID, 2005. The evolution of contemporary cementing techniques. Orthopaedics 28(8): 831-832.

Learmonth ID and Cavendish VJ, 2005. Outcome assessment following total hip replacement Orthopaedics 28(8): 827-830.

Learmonth ID, 2006. Total hip replacement and the law of diminishing returns. Journal of Bone and Joint Surgery (Am), 88: 1664-1673.

Lee AJC, Ling RSM, Gheduzzi S, Simon JP and Renfro RJ, 2002. Factors effecting the mechanical and viscoelastic properties of acrylic bone cement. Journal of Materials Science - Materials in Medicine 13(8): 723-733.

Lennon AB and Prendergast PJ, 2002. Residual stress due to curing can initiate damage in porous bone cement: experimental and theoretic evidence. Journal of Biomechanics 35: 311-321.

Lennon AB, McCormack BAO and Prendergast PJ, 2003. The relationship between cement fatigue damage and implant surface finish in proximal femoral prostheses. Medical Engineering & Physics 25: 833-841.

Leung SY, New A and Browne M, 2006. Modelling the mechanics of the cement-bone interface. Journal of Biomechanics, 39 (Supplement 1): 2248.

Leung SY, New AM and Browne M, 2008. The use of complementary non-destructive evaluation methods to evaluate the integrity of the bone-cement interface. Proceedings of the Institute of Mechanical Engineers, Part H 223(1): 75-86.

Lewis G, 1997. Properties of acrylic bone cement: state of the art review. Journal of Biomedical Materials Research 38: 155-182.

Lewis G, 1999. Effect of mixing method on storage temperature of cement constituents on the fatigue and porosity of acrylic bone cement. Journal of Biomedical Materials Research 48(2): 143-149.

Lewis G, 2003. Fatigue testing and performance of acrylic bone-cement materials: state-of-the-art review. Journal of Biomedical Materials Research 66: 457-486.

Li B and Aspden RM, 1997. Material properties of bone from the femoral neck and calcar femorale of patients with osteoporosis or osteoarthritis. Osteoporosis International 7: 450-456.

Lichtinger TK and Müller RT, 1998. Improvement of the cement mantle of the acetabular component with bone-cement spacers: a retrospective analysis 200 cemented cups. Archives of Orthopaedic Trauma Surgery 118: 75.

Ling R, 1992. The use of a collar and precoating on cemented femoral stems is unnecessary and detrimental. Clinical Orthopaedic Related Research 285: 73-83.

Ling RSM and Lee AJC, 1998. Porosity reduction on acrylic cement is clinically irrelevant. Clinical Orthopaedics and Related Research (355): 249-253.

MacDonald SJ, 2008. Hip resurfacing: yet to be proven. Orthopedics, 31(9): 879-881.

Madey SM, Callaghan JJ, Olejniczak JP, Goetz DD and Johston RC, 1997. Charnley total hip arthroplasty with use of improved techniques of cementing. Journal of Bone and Joint Surgery (AM) 79(1): 53-64.

Mai MT, Schmalzried TP, Dorey FJ, Campbell PA and Amstutz HC, 1996. The contribution of frictional torque to loosening at the bone-cement interface in Tharies hip replacements. Journal of Bone & Joint Surgery (Am) 78(4): 505-511.

Majumdar SKM, Augat P, Newitt DC, Link TM, Lin JC, Lang T, Lu Y and Genant HK, 1998. High-resolution magnetic resonance imaging: three-dimensional trabecular bone architecture and biomechanical properties. Bone 22(5): 445-454.

Malchau H and Herberts P, 1996. Prognosis of total hip replacement - surgical and cementing technique in THR: a revision risk study of 134,056 primary operations. Proceedings of the Academy of Orthopaedic Surgeons.

Mann KA, Bartel DL, Wright TM and Ingraffea AR, 1991. Mechanical characteristics of the stem-cement interface. Journal of Orthopaedic Research 9(6): 798-808.

Mann KA, Bartel DL, Wright TM and Burstein AH, 1995. Coulomb frictional interfaces in modelling cemented total hip replacements: a more realistic model. Journal of Biomechanics 28(9): 1067-1078.

Mann KA, Mocarski R, Damron LA, Allen JA and Ayers DC, 2001. Mixed-mode failure response of the cement-bone interface. Journal of Orthopaedic Research 19(6): 1153-1161.

Mann KA, Gupta S, Race A, Miller MA, Cleary RJ and Ayers DC, 2004a. Cement microcracks in thin-mantle regions after in vitro fatigue loading. Journal of Arthroplasty 19(5): 605-612.

Mann KA, Damron LA, Race A and Ayers DC, 2004b. Early cementing does not increase debond energy of grit blasted interfaces. Journal of Orthopaedic Research 22(4): 822-827.

Mann KA, Miller M, Verdonschot N and Eberhardt A 2009. Micro-mechanics of post-mortem retrieved cement-bone interfaces: influence of interface morphology. Proceeding of the ASME Summer Bioengineering Conference 2009, Lake Tahoe, USA.

Masonis JL, Bourne RB, Ries, MD, McCalden RW, Salehi A and Kelman DC, 2004. Zirconia femoral head fractures: a clinical and retrieval analysis. Journal of Arthroplasty 19(7):898-905.

Massoud SN, Hunter JB, Holdsworth BJ, Wallace WA and Juliusson R, 1997. Early femoral loosening in one design if cemented hip replacement capital hip. Journal of Bone and Joint Surgery (Br) 79(4): 603-608.

Mavrogordato M, Taylor A, Taylor M and Browne M, 2008. Combined non-destructive-evaluation of cement shrinkage effects in a total hip replacement model. Proceedings of the 54th Annual Meeting of the Orthopaedic Research Society, San Francisco, USA.

McCormack BAO, Prendergast PJ and Gallagher DG, 1996. An experimental study of damage accumulation in cemented hip prostheses. Clinical Biomechanics 11(4): 214-219.

McCormack BAO, Prendergast PJ and O'Dwyer B, 1999. Fatigue of cemented hip replacements under torsional loads. Fatigue and Fracture of Engineering Materials and Structures 22(1): 33-40

McCormack BAO and Prendergast PJ, 1999. Microdamage accumulation in the cement layer of hip replacements under flexural loading. Journal of Biomechanics 32(5): 467-475.

McCormick RK, 2010. Images downloaded from mccormickdc.com/osteoporosis.

McLaughlin JR and Harris WH, 1996. Revision of the femoral component of a total hip arthroplasty with the calcar-replacement femoral component: results after a mean of 10.8 years postoperatively. Journal of Bone and Joint Surgery (Am) 78 (3): 331-339.

Merle d'Aubigne R and Postel M, 1954. Functional results of hip arthroplasty with acrylic prosthesis. Journal of Bone and Joint Surgery (Am) 36: 451-475.

Miller MA, Race A, Verdonschot N and Mann K, 2008. On the fatigue behaviour of the cement-bone interface loaded in shear. Journal of Biomechanics 41(1): S328.

Molino LN and Topoleski LDT, 1996. Effect of BaSO4 on the fatigue crack propagation rate of PMMA bone cement. Journal of Biomedical Materials Research 31(1): 131-137.

Murphy SB, Walker PS, Schiller AL, 1984. Adaptive changes in the femur after implantation of an Austin Moore prosthesis. Journal of Bone and Joint Surgery (AM) 66: 437-443.

Murphy BP and Prendergast PJ, 1999. Measurement of non-linear microcrack accumulation rates in polymethylmethacrylate bone cement under cyclic loading. Journal of Materials Science 10: 779-781.

Murphy BP and Prendergast PJ, 2000. On the magnitude and variability of fatigue strength of acrylic bone cement. International Journal of Fatigue 22: 855-864.

Murphy BP and Prendergast PJ, 2001. The relationship between stress, porosity, and nonlinear damage accumulation in acrylic bone cement. Journal of Biomedical Materials Research 59: 646-654.

Nicholson PHF, Cheng XG, Lowet G, Boonen S, Davie MWJ, Dequeker J and Van der Perre G, 1997. Structural and material mechanical properties of human vertebral cancellous bone. Medical Engineering & Physics 19(8): 729-737.

NJR, 2007. National joint registry for England and Wales: 4th annual report. Available at www.njrcentre.org.uk.

Parvizi, 2008. Hip resurfacing as an alternative to hip arthroplasty. Orthopedics, 31(7): 668-670.

Perez MA, Garcia-Aznar JM, Doblare M, Seral B and Seral F, 2006. A comparative FEA of the debonding process in different concepts of cemented hip implants. Medical Engineering & Physics 28(6): 525-533.

Phillips ATM, Pankaj P, Howie CR, Usmani AS and Simpson AHRW, 2007. Finite element modelling of the pelvis: inclusion of muscular and ligamentous boundary conditions. Medical Engineering & Physics 29(7): 739-748.

Poss R, 1992. Editorial comment. Clinical Orthopaedics and Related Research, 274: 2.

Qi G, Li J, Mann KA, Mouchon WP, Hamstad MA, Salehi A and Whitten SA, 2004. 3D real time methodology monitoring cement failures in THA. Journal of Biomedical Materials Research Part A, 71A(3): 391-402.

Raab S, Ahmed AM and Provan JW, 1982. Thin film PMMA pre-coating for improved implant bone-cement fixation. Journal of Biomedical Materials Research 16(5): 679-704.

Race A, Miller MA, Ayers DC, Cleary RJ and Mann KA, 2002. The influence of surface roughness on stem-cement gaps. Journal of Bone and Joint Surgery (Br) 84: 1199-

Race A, Miller MA, Ayers DC and Mann KA, 2003. Early cement damage around a femoral stem is concentrated at the cement / bone interface. Journal of Biomechanics 36(4): 489-496.

Race A, Mann KA and Edidin AA, 2007. Mechanics of bone/PMMA composite structures: an in vitro study of human vertebrae. Journal of Biomechanics 40: 1002-1010.

Reading AD, McCaskie AW and Gregg PJ, 1999. The inadequacy of standard radiographs in detecting flaws in the cement mantle. Journal of Bone and Joint Surgery (Br), 81(1): 167-170.

Rho JY, Ashman RB and Turner CH, 1993. Young's modulus of trabecular and cortical bone material: ultrasonic and microtensile measurements. Journal of Biomechanics 26(2): 111-119.

Roques A, 2003. Novel approaches to the structural integrity assessment of acrylic bone cement as part of the bone / cement / stem construct. PhD Thesis, University of Southampton, UK.

Roques A, Browne M, Taylor A, New A and Baker D, 2004a. Quantitive measurement of the stresses induced during polymerisation of bone cement. Biomaterials 25(18): 4415-4424.

Roques A, Browne M, Thompson J, Rowland C and Taylor A, 2004b. Investigation of fatigue crack growth in acrylic bone cement using the acoustic emission technique. Biomaterials 25(5): 769-778.

Rydell NW, 1966. Forces acting on the femoral head-prosthesis: A study on strain gauge supplied prostheses in living persons. Acta Orthopaedica Scandinavica 37(88): 1-132.

Sasov JA and Van Dyck D, 1998. Desktop x-ray microscopy and microtomography. Journal of Microscopy 191(151-158).

Scheerlinck T and Casteleyn P-P, 2006. The design features of cemented femoral hip implants. Journal of Bone and Joint Surgery (BR) 88-B(1): 1409-1418.

Schmalzried TP, Kwong LM, Jasty M, Sedlacek RC, Haire TC, O'Connor DO, Bragdon CR, Kabo JM, Malcolm AJ and Harris WH, 1992. The mechanism of loosening in cemented acetabular components in total hips arthroplasty: analysis of specimens retrieved at autopsy. Clinical Orthopaedics and Related Research 274: 60-78.

Schmalzried TP and Callaghan JJ, 1999. Current Concepts Review - Wear in Total Hip and Knee Replacements. Journal of Bone and Joint Surgery (Am) 81: 115-136.

Schulte RK, Callaghan JJ, Kelley SS and Johnston RC, 1993. The outcome of Charnley total hip arthroplasty with cement after a minimum twenty-year follow-up: the results of one surgeon. Journal of Bone and Joint Surgery (Am) 75: 961-975.

Shah N and Porter M, 1995. Evolution of Cemented Stems. Orthopaedics 28(8): 819-825.

Sherk HH, Pasquariello PS, and Watters WC, 1981. Congenital dislocation of the hip: a review. Clinical Pediatrics 20(8): 513-520.

Silva M, Shepherd EF, Jackson WO, Dorey FJ and Schmalzried TP, 2002. Average patient walking activity approaches 2 million cycles per year. Journal of Arthroplasty 17(6): 693-697.

Sinnett-Jones PE, Browne M, Ludwig W, Buffière JY and Sinclair I, 2005. Microtomography assessment of failure in acrylic bone cement. Biomaterials 26(33): 6460-6466.

Sinnett-Jones PE, 2007. Micromechanical aspects of fatigue failure in conventional and carbon nanotube-reinforced acrylic bone cement. University of Southampton, PhD Thesis.

Spitzer AI, 2005. The cemented femoral stem: selecting the ideal patient. Orthopedics 28(8, Sup): 841-848.

Stauffer RN, 1982. Ten-year follow up study of total hip replacement. Journal of Bone and Joint Surgery (Am) 64(7): 983-990.

Stolk J, Verdonschot N, Cristofolini L, Toni A and Huiskes R, 2002. Finite element and experimental models of cemented hip joint reconstructions can produce similar bone and cement strains in pre-clinical tests. Journal of Biomechanics 35(4): 499-510.

Stolk J, Verdonschot N, Mann KA and Huiskes R, 2003b. Prevention of mesh-dependent damage growth in finite element simulations of crack formation in acrylic bone cement. Journal of Biomechanics 36(6): 861-871.

Stolk J, Maher SA, Verdonschot N, Prendergast PJ, and Huiskes R, 2003a. Can finite element models detect clinically inferior cemented hip implants? Clinical Orthopaedic Related Research 409: 138-150.

Stolk J, Verdonschot N, Murphy BP, Prendergast PJ, and Huiskes R 2004. Finite element simulation of anisotropic damage accumulation and creep in acrylic bone cement. Engineering Fracture Mechanics 71: 513-528.

Stolk J, Janssen D, Huiskes R and Verdonschot N, 2007. Finite element-based preclinical testing of cemented total hip implants. Clinical Orthopaedic Related Research 456: 138-147.

Stulberg SD and Dolan M, 2008. The short stem: a thinking man's alternative to surface replacement. Orthopedics 31(9): 885-886.

Suresh S, 2004. Fatigue of materials. Cambridge University Press, Cambridge.

Szmukler-Moncler S, Salama H, Reingewirtz Y and Dubruille JH, 1998. Timing of loading and effect of micromotion of bone-dental implant interface: review of experimental literature. Journal of Biomedical Materials Research 43(2): 192-203.

Taylor D, Hoey D, Sanz L and O'Reilly P, 2006. Fracture and fatigue of bone cement bone cement: the critical distance approach. Proceedings of the European Conference of Fracture, Alexandroupolis, Greece.

Thompson MS, Northmore-Ball MD and Tanner KE, 2002. Effects of acetabular resurfacing component material and fixation on the strain distribution in the pelvis. Proceedings of the Institute of Mechanical Engineers 216 (4): 237-245.

Timoshenko SP and Goodier JN, 1970. Theory of Elasticity: 3rd Edition. McGraw-Hill: 396-398.

Tong J, Zant NP, Wang J-Y, Heaton-Adegbile P and Hussel JG, 2008. Fatigue in cemented acetabular replacements." International Journal of Fatigue 30: 1366-1375.

Topoleski LDT, Ducheyne P and Cuckler JM, 1990. A fractographic analysis of the in vivo poly(methylmethacrylate) bone cement. Journal of Biomedical Materials Research 24: 135-154.

Topoleski LDT, Ducheyne P and Cuckler JM, 1993. Microstructural pathway of fracture in poly(methyl methacrylate) bone cement. Biomaterials 14(15): 1165-1172.

Udofia IJ, Yew A, and Jin ZM, 2004. Contact mechanics analysis of metal-on-metal hip resurfacing prostheses. Proceedings of the Institute of Mechanical Engineers 28: 293-305.

Ulrich D, Van Rietbergen B, Laib A and Rüegsegger P, 1999. The ability of three-dimensional structural indices to reflect mechanical aspects of trabecular bone. Bone 25(1): 55-60.

US Department of Health and Human Services, 2004. Mean body weight, height and body mass index, United States 1960-2002. Advance Data from Vital and Health Statistics, 347.

Van Rietgergen B, Weinans H, Huiskes R and Odgaard A, 1995. A new method to determine trabecular bone elastic properties and loading using micromechanical finite-element models. Journal of Biomechanics 28(1): 69-81.

Verdonschot N and Huiskes R, 1994. The creep behaviour of hand-mixed Simplex P bone cement under cyclic tensile loading. Journal of Applied Biomaterials 5: 235-243.

Verdonschot N and Huiskes R, 1995. Dynamic creep behaviour of acrylic bone cement. Journal of Biomedical Materials Research 29: 575-581.

Verdonschot N and Huiskes R, 1996. Subsidence of THA stems due to acrylic cement creep is extremely sensitive to interface friction. Journal of Biomechanics 29(12): 1569-1575.

Verdonschot N and Huiskes R, 1997a. The effects of cement-stem debonding in THA on the long-term failure probability of cement. Journal of Biomechanics 30(8): 795-802.

Verdonschot N and Huiskes R, 1997b. The effects of cement-stem debonding in THA on the long-term failure probability of cement. Journal of Biomechanics 30 (8): 795-802.

Verdonschot N and Huiskes R, 1997c. Acrylic cement creeps but does not allow much subsidence of femoral stems. Journal of Bone and Joint Surgery (Br)79: 665-669.

Verdonschot N and Huiskes R, 1998. Surface roughness of debonded straight-tapered stems in cemented THA reduces subsidence but not cement damage. Biomaterials 19(19): 1773-1779.

Vidal FP, Letang JM, Piex G and Cloetens P, 2005. Investigation of artefact sources in synchrotron microtomography via virtual x-ray imaging. Nuclear Instruments & Methods in Physics Research, Section B 234(3): 333-348.

Waanders D, Janssen D, Bertoldi K, Mann KA and Verdonschot N, 2010. Mixed-mode behaviour of the cement-bone interface: a finite element study. Proceedings of the Annual Symposium on Computational Methods in Orthopaedic Biomechanics, New Orleans, USA.

Wang JS, Toksvig-Larsen S, Müller-Wille P and Franzen H, 1996. Is there any difference between vacuum mixing systems in reducing bone cement porosity? Journal of Biomedical Materials Research 33: 115-119.

Wang K, Jingshen W, Lin Y and Zeng H, 2003. Mechanical properties and toughening mechanisms of polypropylene / barium sulphate composites. Composites Part A: Applied Science and Manufacturing 34(12): 1199-1205.

Wang J-Y, Heaton-Adegbile P, New A, Hussel JG and Tong J, 2009. Damage evolution in acetabular replacements under long-term physiological loading conditions. Journal of Biomechanics 42: 1061-1068.

Williams JL and Johnson WJH, 1989. Elastic constants of composites formed from PMMA bone cement and anisotropic bovine tibial cancellous bone. Journal of Biomechanics 22(6-7): 673-682.

Winer BJ, Brown DR and Michels KM, 1991. Statistical principles in experimental design: third edition. McGraw-Hill Inc., New York, USA.

Wolff J, 1892. Das Gesetz der Transformation der Knochen. A. Hirschwald: Berlin, 1892, Translated by Manquet, P. and Furlong, R. as The Law of Bone Remodelling. Springer: Berlin, 1986

Wroblewski BM, 1989. Long-term results of total joint replacement. Taken from Joint Replacement: state of the art, pg 43-50. Published by Butler and Tanner, London, UK.

Wroblewski BM, Siney PD and Fleming PA, 1998. Wear and fracture of the acetabular cup in low-friction arthroplasty. Journal of Arthroplasty 13 (2): 132-137.

Wroblewski BM, Siney PD and Fleming PA, 2004. Wear of the cup in the Charnley LFA in the young patient. Journal of Bone & Joint Surgery (Br) 86-B: 498-503.

Wroblewski BM, Siney PD and Fleming PA, 2005. Triple tapered polished cemented stem (C-Stem™) in total hip arthroplasty, follow-up to 10 years. Journal of Bone and Joint Surgery (Br) 88 (Supplement 2): 234

Wroblewski BM, Siney PD and Fleming PA, 2007. Charnley low friction arthroplasty: survival patterns to 38 years. Journal of Bone & Joint Surgery (Br) 89-B: 1015-1015.

Wroblewski BM, Siney PD and Flemming PA, 2009a. Effect of reduced diameter neck stem on incidence of radiographic cup loosening and revisions in Charnley low-frictional torque arthroplasty. Journal of Arthroplasty, 24(1): 10-14.

Wroblewski BM, Siney PD and Flemming PA, 2009b. Charnley low-frictional torque arthroplasty: Follow-up for 30 to 40 years. Journal of Bone and Joint Surgery, 91-B(4): 447-450.

Young L, Duckett S and Dunn A, 2009. The use of the cemented Exeter Universal femoral stem in a district general hospital: a minimum ten-year follow-up. Journal of Bone and Joint Surgery (Br) 91: 170-175.

Zannoni C, Mantovani R and Viceconti M, 1998. Material properties assignment to finite element models of bone structures: a new method. Medical Engineering & Physics 20: 735-740.

Zant NP, Wong CKY and Tong J, 2007. Fatigue failure in the cement mantle of a simplified acetabular replacement model. International Journal of Fatigue 29(7): 1245-1252.

Zicat B, Engh CA and Gokcen E, 1995. Patterns of osteolysis around total hip components inserted with and without cement. Journal of Bone & Joint Surgery (Am) 77(3): 432-439.

11 APPENDICES

11.1 APPENDIX A: LIST OF PUBLICATIONS

The research enclosed within this thesis has also been disseminated in the following publications:

Coultrup OJ, Browne M, Hunt C and Taylor M, 2007. In silico evaluation of the effects of internal defects of fatigue damage accumulation. Proceedings of the International Congress on Computational Bioengineering, Isla Margarita, Venezuela.

Coultrup OJ, Browne M, Hunt C and Taylor M, 2008. Computational evaluation of the effects of internal defects on fatigue damage accumulation in bone cement. Proceedings of the Orthopaedic Research Society Annual Meeting, San Francisco, USA.

Coultrup OJ, Browne M, Hunt C and Taylor M, 2008. Acoustic emission monitoring of non-critical fatigue damage in bone cement. Proceedings of the Acoustic Emission Working Group, Memphis, USA.

Coultrup OJ, Browne M, Hunt C and Taylor M, 2009. Accounting for inclusions and voids allows the prediction of tensile fatigue life of bone cement. Journal of Biomechanical Engineering 131(5).

Coultrup OJ, Hunt C and Taylor M, 2009. The effect of polyethylene cup penetration on acetabular cement fatigue life. Proceedings of the ASME 2009 Summer Bioengineering Conference, Lake Tahoe, USA.

Browne M, Coultrup OJ, Hunt C and Taylor M, 2009. Combined non-destructive evaluation techniques for the assessment of bone cement microcracking during fatigue. Proceedings of the International Society for Technology in Arthroplasty Annual Congress, Hawaii, USA.

Coultrup OJ, Hunt C, Wroblewski BM and Taylor M, 2010. Computational assessment of the effect of polyethylene wear rate, mantle thickness and porosity on the mechanical failure of the acetabular cement mantle. Journal of Orthopaedic Research 28(5): 565-570.

11.2 Appendix B: Full Results Table for Chapter 3

Specimen	Load (MPa)	Experimental Fatigue Life	Computational Fatigue Life				Failure Locations (mm From Specimen Base)			Failure Defect
			A	B	C	D	Experimental	AE	Computational	
1	20	310,993	52,080	87,871	118,359	58,079	73 mm	72 mm	58 mm	$BaSO_4$
2	20	25,982	56,836	65,675	67,661	60,005	56 mm	56 mm	82 mm	None
3	20	21,634	12,780	20,200	27,674	13,779	76 mm	77 mm	75 mm	$BaSO_4$
4	20	6,984	26,490	28,558	28,696	27,333	74 mm	73 mm	62 mm	None
5	20	3,478	Failure Outside Scanned Volume				50 mm	-	-	$BaSO_4$
6	20	930	Failure Outside Scanned Volume				98 mm	-	-	Pore
7	15	815,671	236,472	209,517	209,886	208,371	85 mm	84 mm	71 mm	$BaSO_4$
8	15	613,250	265,386	285,414	285,650	272,746	53 mm	53 mm	83 mm	None
9	15	540,491	147,103	154,715	154,616	155,342	77 mm	76 mm	94 mm	Pore
10	15	75,577	Failure Outside Scanned Volume				51 mm	-	-	None
11	15	61,622	Failure Outside Scanned Volume				48 mm	-	-	Pore
12	15	16,524	41,032	41,795	41,339	41,408	68 mm	69 mm	68 mm	Pore
13	11	3,000,000*	458,119	539,041	544,598	465,891	78 mm*	80 mm*	59 mm	None
14	11	1,870,331	343,317	430,435	586,459	353,301	72 mm	72 mm	79 mm	None
15	11	771,382	430,479	442,065	442,880	443,011	74 mm	74 mm	74 mm	Pore
16	7	3,000,000*	1,645,126	1,673,580	1,716,066	1,645,080	79 mm*	80 mm*	81 mm	$BaSO_4$

Table 11.1: A comparison of experimental fatigue life and computational fatigue life for the specimens in chapter 3. The four $BaSO_4$ modelling conditions are listed as A, B, C and D. Fatigue lives are given in terms of the number of loading cycles. The failure defect on fracture surfaces is given in the final column. *Specimens 13 and 16 did not fail within the 3 million cycle limit, so the loading magnitude was doubled to give a failure location for comparison with the simulated failure location.

11.3 Appendix C: Table of Simulations for Chapter 8

#	Directional Deflections on Micro-Scale Model Faces						Output Strain	Compliance Coefficient
	A	B	C	D	E	F		
1	ε_X=0.01	ε_X=0	-	-	-	-	ε_X	C_{11}
2	-	-	ε_Y=0.01	ε_Y=0	-	-	ε_Y	C_{22}
3	-	-	-	-	ε_Z=0.01	ε_Z=0	ε_Z	C_{33}
4	ε_Y=0.01	ε_Y=0	ε_X=0.01	ε_X=0	-	-	ε_{XY}	C_{44}
5	-	-	ε_Z=0.01	ε_Z=0	ε_Y=0.01	ε_Y=0	ε_{YZ}	C_{55}
6	ε_Z=0.01	ε_Z=0	-	-	ε_X=0.01	ε_X=0	ε_{XZ}	C_{66}
7	ε_X=0.01 ε_Y=0.01	ε_X=0 ε_Y=0	-	-	-	-	ε_X	C_{12} C_{14}
8	ε_X=0.02 ε_Y=0.01	ε_X=0 ε_Y=0	-	-	-	-	ε_X	
9	ε_X=0.01 ε_Z=0.01	ε_X=0 ε_Z=0	-	-	-	-	ε_X	C_{13} C_{16}
10	ε_X=0.02 ε_Z=0.01	ε_X=0 ε_Z=0	-	-		-	ε_X	
11	-	-	ε_Y=0.01 ε_X=0.01	ε_Y=0 ε_X=0	-	-	ε_Y	C_{24}
12	-	-	ε_Y=0.01 ε_Z=0.01	ε_Y=0 ε_Z=0	-	-	ε_Y	C_{23} C_{25}
13	-	-	ε_Y=0.02 ε_Z=0.01	ε_Y=0 ε_Z=0	-	-	ε_Y	
14	-	-	-	-	ε_Z=0.01 ε_X=0.01	ε_Z=0 ε_X=0	ε_Z	C_{36}
15	-	-	-	-	ε_Z=0.01 ε_Y=0.01	ε_Z=0 ε_Y=0	ε_Z	C_{35}
16	ε_X=0.01	ε_X=0	ε_Y=0.01	ε_Y=0	ε_Z=0.01	ε_Z=0	ε_X	C_{15}
17	ε_Z=0.01	ε_Z=0	ε_Y=0.01	ε_Y=0	ε_X=0.01	ε_X=0	ε_Y	C_{26}
18	ε_Y=0.01	ε_Y=0	ε_X=0.01	ε_X=0	ε_Z=0.01	ε_Z=0	ε_Z	C_{34}
19	ε_Z=0.01	ε_Z=0	ε_Z=0.01	ε_Z=0	ε_Y=0.01 ε_X=0.01	ε_Y=0 ε_X=0	ε_{XY}	C_{45} C_{46}
20	ε_Z=0.02	ε_Z=0	ε_Z=0.01	ε_Z=0	ε_Y=0.01 ε_X=0.02	ε_Y=0 ε_X=0		
21	ε_Z=0.02	ε_Z=0	ε_Z=0.01	ε_Z=0	ε_Y=0.01 ε_X=0.02	ε_Y=0 ε_X=0	ε_{YZ}	C_{56}

Table 11.2: The boundary strains (ε_{ij}) applied to macro-model faces (figure 8.1) to determine the anisotropic compliance matrix coefficients (C_{ij}) in chapter 8. The output strains used in caluclations of anisotropic material properties (equation 8.3) are also given. X, Y and Z indicate the coordinate system.